Post-fabrication tuning of Hybrid Plasmonic Nanostructures with VO_2

A PhD Thesis

by:

Stephen Cunningham

Supervisor:

Prof. Louise Bradley

School of Physics
Trinity College Dublin
January 2023

Declaration

I declare that this thesis has not been submitted as an exercise for a degree at this or any other university and is entirely my own work. Any assistance or collaboration is recognised in the acknowledgements and throughout the thesis where applicable.

I agree to deposit my thesis in the University's open access institutional repository or allow the library to do so on my behalf, subject to Irish Copyright Legislation and Trinity College Library conditions of use and acknowledgement.

I have read and I understand the plagiarism provisions in the General Regulations of the University Calendar for the current year, found at `http://www.tcd.ie/calendar`.

I have also completed the Online Tutorial on avoiding plagiarism 'Ready Steady Write', located at `http://tcd-ie.libguides.com/plagiarism/ready-steady-write`.

Stephen Cunningham

Abstract

The development of hybrid plasmonic nanostructures and metamaterials to control electromagnetic radiation on the nanoscale has been at the centre of scientific research for the past few decades. Utilising the surface plasmon resonances arising from noble metal nanoparticles is attractive due to the diverse range of applications within the field of nanophotonics. However, the plasmonic response of these nanostructures is heavily dependent on factors set during the fabrication process, such as the combination of materials used as well as there structural dimensions. The inability to dynamically tune the optical response of such nanostuctures post-fabrication imposes serious limitations on potential applications within optoelectronic systems. To overcome this, tunable plasmonic elements consisting of metallic nanoparticles on a thin layer of vanadium dioxide VO_2, a phase change material, are considered. VO_2 is an attractive option as a phase change material due to its large reversible transition from a semiconducting phase to a metallic phase at the critical temperature of 68° C, close to room temperature.

The VO_2 phase change is used to dynamically tune the plasmonic response of coupled nanoparticles within the visible and near IR spectral regions.

The modulation of the reflectance, transmittance and absorptance spectra of VO_2 thin films with thicknesses between 5 nm - 200 nm is investigated with significant blueshifts in the optical response within the visible spectral range. By implementing a metallic backreflecting layer a larger contrast in the optical spectra of the VO_2 thin film is demonstrated with a large change in the CIE colour in each case. Plasmon resonance wavelength shifts of over 600 nm are observed in the near-IR spectral region upon the transition of the VO_2 layer from the semiconducting phase to the metallic phase. This is significantly larger than the wavelength shifts reported in this spectral range using other phase change materials. Additionally, significant increases in the scattering cross sections are observed for VO_2 film thicknesses between 30 - 50 nm as well as enhancement of the plasmonic hotspots surrounding Au nanoparticles. Au Bowtie Dimer structures demonstrate a 3.6-fold increase in the E-field intensity within the dimer gap accompanied by a reshaping of the spatial profile of the E-field enhancement providing a mechanism for tunable metasurfaces.

Finally, a method to dynamically tune luminescence enhancement in the near infrared spectral range by coupling metal nanostructures to VO_2 thin films. A numerical model is employed to calculate the emission of quantum emitters in a hybrid system comprising a single silver (Ag) nanodisc on top of a thin layer of VO_2. Through the optimisation of this system, a luminescence enhancements greater than 4 can be seen in the metallic VO_2 compared to the semiconducting phase allowing for compensa-

tion of thermal quenching of up to 70% between room temperature and 70° C. This renders the hybrid system a promising candidate for improved photon management in optoelectronic devices where elevated temperatures minimize the efficiency of such devices.

The research presented in this thesis demonstrates how hybrid plasmonic nanostructures, incorporating a thin layer of VO_2, can allow for dynamic modulation of reflectance, transmittance, absorptance and scattering spectra as well as enhancement of the localised E-field and emission of coupled quantum emitters.

Acknowledgements

Firstly, I would like to acknowledge my supervisor Prof. Louise Bradley for providing me the opportunity to undertake research in her group. It was truly a pleasure to work in her group alongside so many amazing people. Her support and guidance along the way was instrumental to the completion of my research.

I would also like to extend my gratitude each member of the group. Without the help and support of Dr. John Gough, Dr. Keith Wilson and Dr. Jorge Garcia, the early days of my research would've been considerably more difficult so I'd like to thank them for quickly making me feel like part of the group. I'd like to thank Dr. Calin Hrelescu for all his assistance and advice, whether it be in the lab or over pints at the Pav. Thanks to all of the other members of the group, Dr. Xia Zhang, Carolyn Elliott, Fionnuala McGrath, Jing Qian and Sara Pelivani. It was truly a pleasure to work alongside them for these few years.

I'd also like to thank Dr. Stephen Barry Porter and Dr. Gwenael Atcheson for their expertise and assistance in training me in fabrication and characterisation techniques. My thanks to Chris Smith for ellipsometry measurements, as well as all technical staff in the School of Physics, CRANN and the AML for all their help over the years.

I also want to thank my family and friends for all of their support despite not understanding a word of what I do!

Lastly, I want to thank my girlfriend Julia (and our cat Mia) for all of her love and support.

List of Publications and Conference Contributions

Publications

1. Stephen Cunningham, Calin Hrelescu, and A. Louise Bradley, "Plasmonic nanodiscs on vanadium dioxide thin films for tunable luminescence enhancement," Opt. Express 29, 22288-22298 (2021)

2. Stephen Cunningham and A. Louise Bradley, "Tunable plasmonics with Au nanoparticles coupled to thin film vanadium dioxide," Opt. Mater. Express 12, 3638-3647 (2022)

Conference Contributions

1. S. Cunningham, J. J. Gough, C, Hrelescu, S. B. Porter, P. Stamenov and A. L. Bradley, "VO_2 as a phase change material for tunable plasmonic structures", Photonics Ireland 2018, 3rd - 5th September 2018, Cork, Ireland. (Oral Presentation)

2. S. Cunningham, J. J. Gough, C. Hrelescu, S. B. Porter, P. Stamenov and A. L. Bradley, "Dynamic Tuning of Plasmonic Structures using Phase Change Materials", E-MRS 2019 Spring Meeting, May 27th - 31st 2019, Nice, France. (Oral Presentation)

3. S. Cunningham, J. J. Gough, S. B. Porter, P. Stamenov, C. Hrelescu and A. L. Bradley, "Light Manipulation with Plasmonic Structures using Phase Change Materials", CLEO/Europe-EQEC 2019, June 23rd - 27th 2019, Munich, Germany. (Poster)

4. S. Cunningham, C. Hrelescu and A. L. Bradley, "Photoluminescence Modification using Plasmonic Nanodiscs Coupled to Thin Film Vanadium Dioxide", Photonics Ireland 2021, September June 14th - 16th 2021, Online. (Poster)

5. S. Cunningham, C. Hrelescu, G. Atcheson, P. Stamenov, A. L. Bradley, "Photoluminesce Modification using Plasmonic Nanoparticles Coupled to Vanadium

Dioxide", OSA Optical Design and Fabrication Congress 2021, June 27th - July 1st 2021, Online. (Poster)

6. S. Cunningham, C. Hrelescu, G. Atcheson, P. Stamenov and A. L. Bradley, "Tunable luminescence enhancement using hybrid plasmonic nanostructures on thin film vanadium dioxide", Nano Today 2021, November 15th - 18th 2021, Online. (Poster)

7. S. Cunningham, C. Hrelescu, G. Atcheson, P. Stamenov and A. L. Bradley, "Dynamic Tuning of Coupled Emitter-Plasmonic Systems using Thin Film Vanadium Dioxide", EUROMAT 2021, September 12th - 16th 2021, Online. (Oral presentation)

8. S. Cunningham and A.L. Bradley, "Manipulation of Light-Matter Interaction of the Nanoscale", CIMTEC 2022, June 20th - 24th 2022, Perugia, Italy. (Oral Presentation)

9. S. Cunningham and A. L. Bradley, "Large Reversible Plasmon Shift with Au Nanodisc Dimers", July 24th - 28th 2022, Maastricht, Netherlands. (Oral Presentation)

Contents

1 Introduction

Between 1959, when the concept of nanoscience and nanotechnology was first introduced by Nobel Prize laureate Richard Feynman in his seminal lecture "There's Plenty of Room at the Bottom",[1] and today, the world has seen an explosion in scientific advancement in all areas of nanoscience. In particular, the development of new fabrication and synthesis techniques have paved the way for the development of numerous novel nanostructures allowing for the manipulation of light on the nanoscale and the development of technologies unimaginable at the beginning of the last century.

As a consequence of the reduced size of nanomaterials, which have dimensions on the order of 1 - 100 nm,[2] considerably smaller than the wavelength of visible light, the chemical and physical properties can be remarkably different from properties seen in the bulk material.[3] Combinations of these nanoscale materials has allowed for the development of hybrid structures which can have material properties that greatly differ from their constituent materials.[4]

The advancement in material growth and fabrication techniques that have led to the development of novel nanomaterials come in the form of both the "top-down" and the "bottom-up" approach.[5,6] Advances in the "top-down" approach, which involve the fabrication of nanostructures through processing of the bulk material, have come in the form of lithographic techniques such as photolithography, electron beam lithography and nano-imprint lithography.[7] Methods such as mechanical exfoliation have also allowed for the growth of 2D materials,[8] a class of materials characterised by their single atomic layer thickness.[9] The "bottom-up" approach, characterised by the self-assembly of atoms and molecules,[6] has seen the emergence of numerous growth methodologies including various chemical and physical deposition techniques allowing for the growth of novel materials on the nanoscale. Both of these kinds of fabrication techniques are crucial in the fabrication of the hybrid nanostructures discussed in this work.

Just as the size of electronic components moves towards smaller sizes, advances in nanoscale light manipulation has seen the size of optical components shrink as well. Recent advances have promised the miniaturisation of optical components by replacing bulky systems of lenses with flat optical meta lenses for example. This year, flat optical

components have been deployed within consumer devices for the first time with the release of a direct time-of-flight sensor developed by Metalenz.[10] This kind of optical sensor module can be integrated into smartphones, drones, robots and vehicles and is intended to point towards the improvements in performance, power, size and cost that meta-optics can offer over traditional optics. The market for these kinds of flat optical devices is expected to be worth several billion dollars by 2030[11] and from this it can be seen that nano optical devices will play an increased role in our lives and in the technology we use as times goes on.

For optical responses in the visible regime, plasmonics and in particular the phenomenon of localised surface plasmon resonances (LSPRs) is of particular interest. Gold (Au) and silver (Ag) nanoparticles are commonly used in this field as these metals support resonances within the visible regime, which can be adjusted by altering the size of the nanoparticle or by selection of the dielectric environment surrounding the nanoparticle. While plasmonic effects in fabricated materials can be seen in the Lycurgus Cup,[12] a Roman artifact dating back to the 4th Century, not until the last few decades has plasmonics been applied in a wide range of applications. These applications include, surface enhanced Raman Spectroscopy,[13–15] LEDs[16–18] and biosensing[19–21] among others. The strong enhancement of the electromagnetic field by a plasmonic nanoparticle at "hotspots" surrounding a plasmonic particle has also recieved much attention due to applications in optical trapping,[22] solar cells[23] and emission enhancement.[24]

Despite the growing use of plasmonics and metamaterials for on-chip integration,[25] the inability to dynamically tune their response post-fabrication imposes serious limitations on potential optoelectronic applications. Much research in the last few years has therefore focused on various methodologies to achieve active tuning of the optical response of metamaterials and metasurfaces to greatly expand the potential applications within optoelectronic devices.[26–28] Much of this research has focused on longer wavelengths in the range between 1 - 10 μm,[29,30] with a particular focus at telecom wavelengths such as the wavelength band around $\lambda = 1550$ nm.[31] Dynamic tuning within the visible and near infrared spectral range has previously been explored though the transition of liquid crystals from nematic state to isotropic state,[32,33] however in these cases there is a minimal shift in the peak wavelength response. Single layers of 2D materials such as graphene have also demonstrated the ability to tune the response of plasmonic nanoparticles within the visible through application of a bias voltage through an ionic liquid.[34] However, this also shows a minimal shift in the plasmonic response. On the other hand, phase change materials such as $Ge-Sb-Te$ (GST) and $Ag-In-Sb-Te$ (AIST) have also been employed to dynamically tune the optical response of metamaterials.[35–38] However these materials are noted as requiring a high temperature or

current to switch between the crystalline and amorphous phase.[39]

To produce devices that demonstrate a large change in optical properties, are low-cost, fast switching and energy efficient another phase change material, VO_2 must be considered. VO_2 is well known to transition at 68° C and is therefore advantageous over GST and AIST, due to reduced energy needed to reach this transition point. Previous studies have shown VO_2 used in IR waveguides,[40,41] IR sensing[42,43] and other THz applications[44] as well as in so called "smart windows".[45,46] The incorporation of VO_2 into hybrid nanostructures to modify response in the visible has seen less study due to the smaller change in the dielectric function at these wavelengths, however, as seen in this work, these changes are significant enough to cause large changes in the optical response of a hybrid nanostructure. In fact the change in optical response is large enough that the phase transition can be observed by the naked eye due to the modulation in thin film reflectance without the addition of plasmonic elements.

The aim of this thesis is to investigate hybrid nanostructures incorporating the VO_2 phase change material. As mentioned, VO_2 is an attractive material for dynamic tuning and through numerical simulation and experimental fabrication and characterisation, this work aims to find optimised hybrid structures for various optoelectronic applications including photoluminescence enhancement. This application is of particular interest as quantum emitters are known to suffer from thermal quenching so incorporation of VO_2 is investigated as a method to compensate for these kind of losses to increase the efficiency of devices such as solar concentrators. This kind of application is of increasing importance in a world where energy consumption is one of the most important issues facing humanity today.

In **Chapter 2** the background theory and concepts behind the work presented in this thesis are introduced. This includes the theory behind localised surface plasmons, an important aspect of this work as it's the modification of this interaction that drives the shifts and enhancements seen in **Chapters 5** and **6**. The theory behind fluorescence is also discussed with regards to radiative and nonradiative rates and fluorescent lifetime as well as a discussion of the impact of thermal quenching, an important factor to consider when the VO_2 phase change is thermally driven. Background theory on quantum dot and dye fluorophores is also given in this chapter. Finally, within this chapter there is a discussion on the phase change material VO_2 as this material and its phase changing property is central to the work presented in the forthcoming chapters. Formulation of effective medium theory is also presented.

Chapter 3 provides an overview of the fabrication and characterisation techniques used in the production of thin film VO_2. In addition to techniques used for confirmation of the VO_2 oxide phase, an overview of the optical techniques used to demonstrate how

the optical properties are modified through the actuation of the VO_2 phase transition is given. FDTD simulations are used as tool throughout this work to demonstrate how changing various parameters within the hybrid structures presented effects the optical response. Within this chapter, the theory and implementation of FDTD methods in Lumerical are discussed alongside the refractive index data used for each material within FDTD simulations. The methodology behind conversion of simulated spectra to colour is also shown. Lastly, the methodology behind the sample fabrication by physical vapour deposition techniques is shown, with the parameters used for VO_2 film growth. Nanostructure fabrication by EBL and fluorescent molecule attachment is also discussed.

In the following three chapters, the hybrid nanostructure is gradually built up with **Chapter 4** focusing on planar VO_2. Within this chapter, Finite Difference Time Domain (FDTD) simulations are used to show the reflectance,transmittance and absorptance properties of thin film VO_2 on a c-plane sapphire substrate as a function of film thickness. The optical properties off the nanoscale thin film are seen to vary significantly with film thickness particularly when the simulated spectra are converted to their RGB values. The impact of the addition of a a gold backreflector layer is seen to dramatically expand the colour gamut with large colour changes across the phase change. Experimentally, the characterisation of fabricated VO_2 films is shown as formation of the VO_2 oxide phase isn't trivial. Demonstrations of the switching effects using various stimuli are presented with a particular focus on the dynamics of the smaller area of metallic VO_2 formed when the transition is electrically actuated.

Chapter 5 expands on the previous chapter, adding plasmonic nanostructures on top of thin film VO_2. Through FDTD methods, large shifts in the peak plasmonic response for a wide range of naoparticle morphologies, including single nanoparticles and dimers are observed and discussed. The effects of various structural parameters on the response and the change in response are investigated and large changes in response, previously unreported are noted. Experimental shifts for fabricated nanostructures are also discussed and compared to the simulated case.

Finally in **Chapter 6** a model for calculating enhancement of quantum emitters coupled to plasmonic nanoparticles on thin film VO_2 is discussed and implemented. The impact of the hybrid material's various structural parameters and how they effect the degree of enhancement seen for the coupled quantum emitters is investigated.

To conclude, **Chapter 7** will discuss overall conclusions drawn from the work down in the preceding chapters with a discussion on future work regarding the implementation of VO_2 in hybrid nanostructure devices.

2 Background

2.1 Plasmons

The optical response of the hybrid nanostructure systems explored in this work rely on the unique optical properties seen when electromagnetic radiation interacts with structures on the order of or smaller than the wavelength of visible light ($\lambda = 380 - 700$ nm). At this length scale the optical response of a system becomes strongly dependent on structural geometry, material composition and the surrounding dielectric environment due to the excitation of the plasmon resonance. The two fundamental excitations of surface plasmons are namely Localised Surface Plasmon Resonance (LSPRs) and Surface Plasmon Polaritons (SPPs). The significant near field enhancement surrounding a metallic nanostructure is fundamental to the work presented in future chapters as it can modify the emission of emitters[47,48] in close proximity, by either enhancing[49,50] or quenching[51,52] the emitter's photoluminescence.

2.1.1 Localised Surface Plasmon Resonance

When electromagnetic radiation interacts with a metallic nanostructure, the incident electric field acts as a driving force for conduction electrons within the metallic nanostructure. As shown in Fig. 2.1, the oscillating electric field of the incident light drives a coherent oscillation of the conduction electrons. As the electron cloud is displaced from its equilibrium position, the Coulomb force acts as a restoring force between the electron cloud and atomic nuclei. The frequency of the oscillation is determined by many factors including the electron density, effective electron mass as well as the size

and shape of charge distribution. As a non-propagating form of plasmon excitation, electrons are confined by the boundary of the nanoparticle, unlike the case for SPPs where the plasmon propagates along the interface of a bulk metal. Interaction of the electromagnetic field with the plasmonic nanoparticle allows for numerous phenomena including subwavelength localisation of electromagnetic energy, significant enhancement of the electric field at the surface of the nanoparticle and modification of the absorption and scattering properties of such structures.

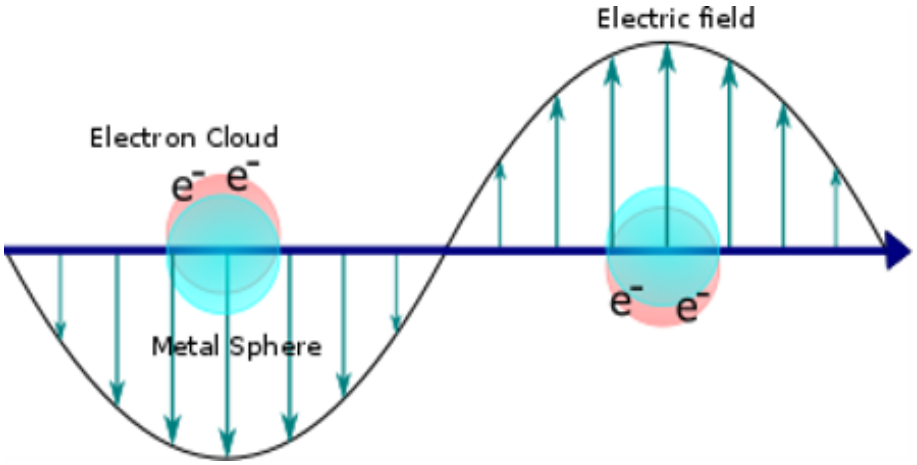

Figure 2.1: Schematic of LSPR in a metallic nanoparticle.

By considering the simplest case of a metallic sphere the resonance condition can be derived from the dipole moment given by

$$P = \alpha \varepsilon_H \varepsilon_0 E_0 \tag{2.1.1}$$

where ε_0 is permittivity of free space, ε_H is the permittivity of the surrounding host dielectric, E_0 is the applied electric field and α is the polarizability given by

$$\alpha = 4\pi r^3 \frac{\varepsilon_m - \varepsilon_H}{\varepsilon_m + 2\varepsilon_H} \tag{2.1.2}$$

where r is particle radius and ε_m is the spheres permittivity.

In this case, we consider the nanoparticle diameter to be considerably smaller than

the wavelength of the incident electromagnetic radiation, meaning the particle can be treated as being in an electrostatic field, allowing the dipole moment to be given as in Eq 2.1.1.

The resonance condition is when α is largest i.e. when $\varepsilon_m = -2\varepsilon_H$, otherwise known as the Fröhlich condition.

From this, the absorption cross-section σ_{Abs} and scattering cross-sections σ_{Sca} are defined as follows

$$\sigma_{Abs} = kIm[\alpha] = 4\pi kr^3 Im[\frac{\varepsilon_m - \varepsilon_H}{\varepsilon_m + 2\varepsilon_H}] \tag{2.1.3}$$

$$\sigma_{Sca} = \frac{k^4}{6\pi}|\alpha|^2 = \frac{8\pi}{3}k^4 r^6 [\frac{\varepsilon_m - \varepsilon_H}{\varepsilon_m + 2\varepsilon_H}]^2 \tag{2.1.4}$$

where $k = \dfrac{2\pi}{\lambda}$

The extinction cross-section is given by $\sigma_{Ext} = \sigma_{Abs} + \sigma_{Sca}$

As the scattering and absorption cross-sections scale with the radius to the 6th power and 3rd power respectively, the relative contributions to the extinction are highly dependent on nanoparticle radius as well as material composition and shape. It's noted from the scattering cross-section equations, the magnitude of the cross-section increases with nanoparticle radius. The effective cross-section of a plasmonic particle can be up to 12 times larger than the size of the nanoparticle itself.[53,54] This allows the nanoparticle, which has dimensions below the optical diffraction limit, to be visualised under dark field microscopy.

Noble metals such as gold and silver are typically employed in plasmonic systems due their strong response at visible wavelengths. This response arises from the significant negative permittivity exhibited at these wavelength ranges allowing for fulfillment of the Fröhlich condition. For metals like Au and Ag, the real part of the permittivity ($Re(\varepsilon)$) decreases and the imaginary part ($Im(\varepsilon)$) increases with increasing wavelength

around the resonance. The dielectric functions of Au[55] and Ag[56] are depicted in Fig. 2.2 (a) and (b) respectively demonstrating the negative real permittivity in the visible spectral region.

The complex dielectric function, given as $\varepsilon = \varepsilon_1 + i\varepsilon_2$ is related to the complex refractive index, given as $\tilde{n} = n + i\kappa$ by the following equations[57]

$$n = \sqrt{\frac{|\varepsilon| + \varepsilon_1}{2}} \tag{2.1.5}$$

$$\kappa = \sqrt{\frac{|\varepsilon| - \varepsilon_1}{2}} \tag{2.1.6}$$

where $|\varepsilon| = \sqrt{\varepsilon_1^2 + \varepsilon_2^2}$

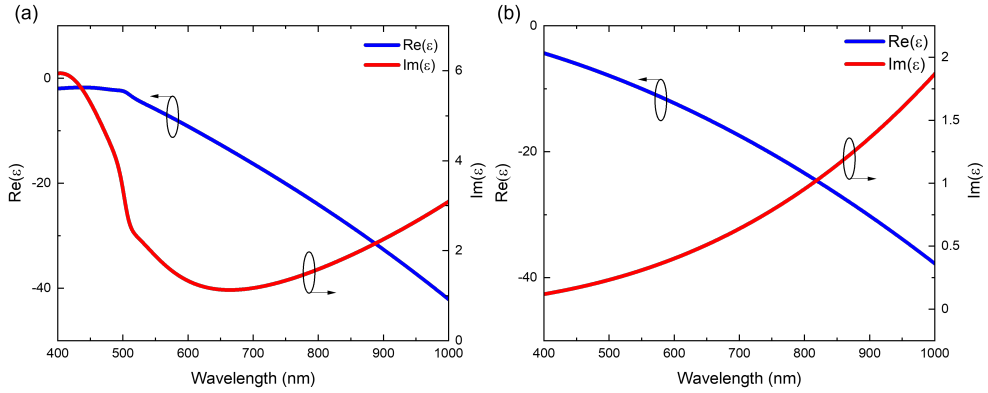

Figure 2.2: Real and imaginary parts of (a) Au[55] and (b) Ag[56] dielectric function in the visible and NIR spectral region.

Elongated nanoparticles such as rods or cuboids offer further possibilities in optical property modification as their anisotropic shape allows for the support of multiple plasmonic modes at different spectral positions relating to oscillation over their long axis (longitudinal mode) and their short axis (transverse mode).[58] Further examples of anisotropic multi-resonant plasmonic nanoparticles can be found in Maiers "Plasmonic Nanoantennas: Fundamentals and Their Use in Controlling the Radiative Properties of Nanoemitters" and the references therein. Metal nanoparticles in ordered arrays with periods comparable to the wavelength of visible light further demonstrate unique coupling properties depending on orientation and periodicity. Additionally, dimer struc-

tures and other structures with a nanogap between elements allow for the formation of a "plasmonic hot spot" where there is a large enhancement in the local E-field. This highly localised enhancement can also be observed in particles with pointed tips such as bipyramids.[59]

2.2 Thin Film Interference

In this work, particularly in **Chapter 3** where the optical response of thin film VO_2 on a Au backreflecting layer is considered, the spectral response of the thin film is due to interference effects. Interference effects arise when multiple light waves interact with each other and the resultant wave can be described as a superposition of the individual waves. These effects are highly dependent on the thickness of thin film layers and phase differences induced by reflection from an interface.

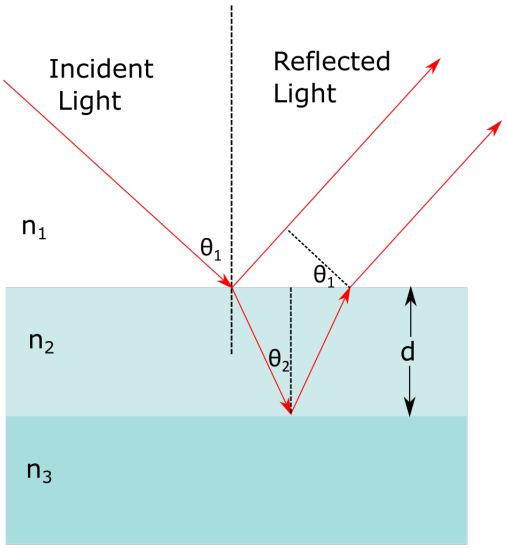

Figure 2.3: Schematic demonstrating the optical path difference between light reflected from the upper and lower interfaces of a thin film with n indicating the different refractive indices within the thin film structure.

Using Snell's law $n_1 sin(\theta_1) = n_1 sin(\theta_2)$ where n_1 and n_2 are the refractive indices at each layer and θ_1 and θ_2 are the angles of incidence at each interface (as shown in Fig.

2.3), the optical path difference can be calculated as

$$2n_2 dcos(\theta_2) \tag{2.2.1}$$

Constructive interference occurs when the difference in the optical path length between the waves reflected by each interface is equal to an integer multiple (m>0) of the wavelength of the incident light (λ) i.e

$$2n_2 dcos(\theta_2) = m\lambda \tag{2.2.2}$$

This relation applies when the refractive indices are as follows $n_1 > n_2 > n_3$. In most cases it can be assumed that $n_1 = 1$ as the thin film structure is in air. There is a π phase shift in the reflected light when it reflects from a medium with a higher refractive index. In the case where $n_2 < n_3$, there is no phase shift induced upon reflection at the lower interface, so the dependency becomes

$$2n_2 dcos(\theta_2) = (m - \frac{1}{2})\lambda \tag{2.2.3}$$

For destructive interference effects the relations given for the constructive interference are shifted by half an integer number of wavelengths.

From these interference conditions, thin films can demonstrate structural colour in reflectance, highly dependent on film thickness. In the case of VO_2, as the thin films optical constants are altered upon the phase transition, large reversible changes in the structural colour from thin film interference can be demonstrated. These large changes in structural colour, as shown in **Chapter 4**, have applications in smart windows and mirrors and in display technology[60]

2.3 Fluorescence

Photoluminescence is the process in which a molecule absorbs electromagnetic radiation of a particular energy and subsequently emits a photon, typically at a longer wavelength and therefore lower energy than the absorbed radiation.[61] When a photon is absorbed, one of the weakly bound electrons of the fluorophore (fluorescent molecule) is promoted to a higher energy level above the ground state. This excited state is metastable, meaning the fluorophore will quickly return to the ground state. This return to the ground state occurs either through a radiative process, where a photon is emitted, or a non-radiative process such as internal conversion, vibrational relaxation and intersystem crossing.[62–65] The average period of time the molecule remains in an excited state is known as the fluorescence lifetime (τ_{PL}) and is typically on the order of 10^{-8} s. In phosphorescent materials these lifetimes are significant longer ranging from 10^{-3} s up to minutes. A Jablonski diagram, as shown in Fig. 2.4, demonstrates the various radiative and nonradiative pathways a molecule in an excited state can use to return to the ground state. For the case of fluorescence the de-excitation is through the lowest vibrational energy level of the 1st excited singlet state (S1) following Kasha's rule.[66] The singlet state refers to energy levels that can be populated by weakly bound electrons without a spin flip. In the case of the phosphorescence, as indicated in the Jablonski diagram (Fig. 2.4), the lifetime is much longer due to intersystem crossing into a triplet state. Singlet and triplet states are defined by the spin of the electron. In a singlet state, all electrons in the molecule are spin paired while in a triplet state there is a set of unpaired electron spins. The transition from the triplet state back to the singlet ground state is a known as a forbidden transition, meaning that under usual approximations this transition cannot occur. However, at a higher level of approximation this transition can occur albeit at a significantly lower rate, resulting in the longer phosphorescent lifetime.[67,68]

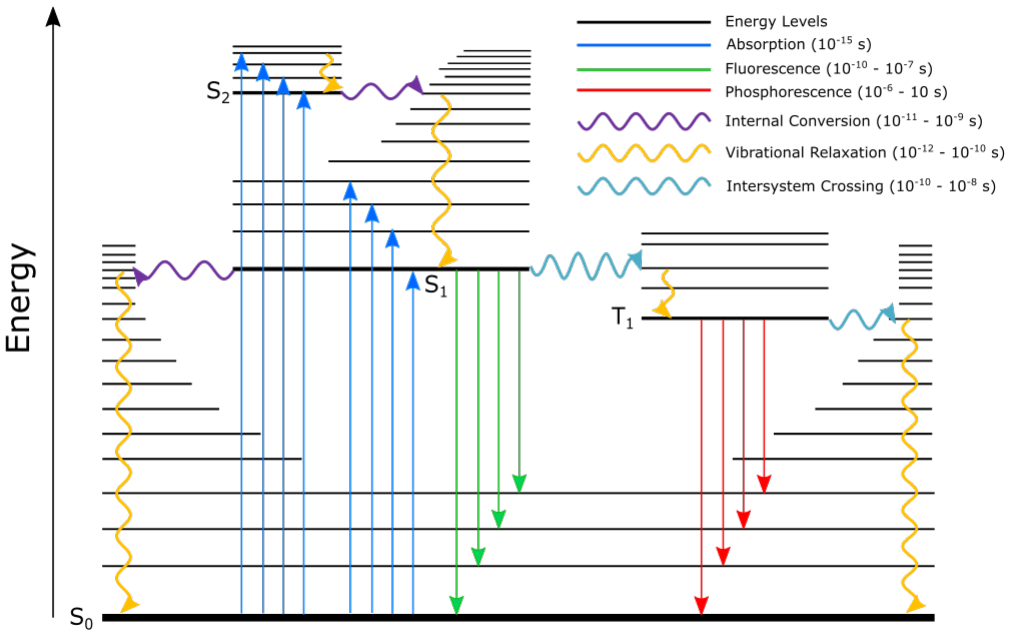

Figure 2.4: A typical Jablonski diagram showing possible radiative and non-radiative transition pathways. Figure adapted from Ref.[69]

The fluorescence lifetime can be related to a radiative (γ_R) and nonradiative rate (γ_{NR}) by the following equation

$$\tau_{PL} = \frac{1}{\gamma_R + \gamma_{NR}} \tag{2.3.1}$$

The nonradiative rate itself can be divided into constituent parts so that

$$\gamma_{NR} = \gamma_{IC} + \gamma_{ISC} \tag{2.3.2}$$

where γ_{IC} and γ_{ISC} represent internal conversion and intersystem crossing respectively.

The natural lifetime is given as $\tau_0 = \gamma_R^{-1}$. This lifetime can be thought of as the fluorophores longest possible lifetime i.e when $\gamma_{NR} = 0$.

The radiative rate γ_R of a fluorophore is related to its absorption and fluorescence spectra and is a function of the refractive index of the surrounding medium and can be given by the equation[70,71]

$$\gamma_R = \frac{1}{\tau_0} = \frac{8000\pi c}{N_A} \frac{n_{fl}^3}{n_{abs}} \frac{g_{ex}}{g_{gr}} \langle \tilde{v}^{-3} \rangle^{-1} \int \frac{\varepsilon(\tilde{v})}{\tilde{v}} d\tilde{v} \tag{2.3.3}$$

where c is the speed of light in vacuum, N_A is Avogadro's number, n_{fl} is the mean refractive index over the emission spectrum, n_{abs} is the mean refractive index over the absorption spectrum. g_{ex} and g_{gr} are the multiplicities (related to the spin of the electron of the excited state, g = 1 for a singlet state, g = 3 for a triplet state) for the excited state and the ground state respectively. ε is the extinction co-oefficient and $\tilde{v}$ is the wavenumber. $\langle \tilde{v}^{-3} \rangle^{-1}$ is the reciprocal of the mean value of $\tilde{v}^{-3}$ in the fluorescence emission spectrum, independent of the fluorescence intensity or quantum yield and given by

$$\langle \tilde{v}^{-3} \rangle^{-1} = \frac{\int F(\tilde{v}) d\tilde{v}}{\int F(\tilde{v}) \tilde{v}^{-3} d\tilde{v}} \tag{2.3.4}$$

where F is the fluorescence emission spectrum. This equation is known as the Strickler-Berg equation[72] and for $n_{fl} = n_{abs}$ and $g_{ex} = g_{gr} = 1$ can be given as

$$\gamma_R = 2.88 \times 10^{-9} n^2 \frac{\int I(\tilde{v}) d\tilde{v}}{\int I(\tilde{v}) \tilde{v}^{-3} d\tilde{v}} \int \frac{\varepsilon(\tilde{v})}{\tilde{v} d\tilde{v}} \tag{2.3.5}$$

The fluorescence quantum yield (Φ) defined as the ratio of fluorescence photons emitted to the number of photons absorbed is given by the equation

$$\Phi = \frac{\tau_{PL}}{\tau_0} = \frac{\gamma_R}{\gamma_{NR} + \gamma_R} = \frac{1}{1 + \frac{\gamma_{NR}}{\gamma_R}} \tag{2.3.6}$$

The rate equation for fluorescence is given as follows

$$dN = (\gamma_R + \gamma_{NR})N(t)dt \tag{2.3.7}$$

$$\implies F(t) = F_0 e^{\frac{-t}{\tau_{PL}}} \tag{2.3.8}$$

where F_0 is the fluorescence intensity at at a t = 0 and τ_{PL} is the fluorescence lifetime. This means the fluorescence lifetime can be defined as the amount of time it takes for the fluorescence intensity to decay from the peak intensity to $\frac{I_{Peak}}{e}$ or $\approx 37\%$ of the peak intensity.

In the previous equation (2.3.6) given for the quantum yield of an fluorescent molecule there is a dependence on γ_R and γ_{NR}, intrinsic properties of the quantum emitter. However, when a fluorescent emitter is in close proximity to a plasmonic nanoparticle additional nonradiative de-excitation pathways become available. By taking this into account the above equation can be modified to include a modified radiative (γ_{R^*}) rate and an additional nonradiative ($\gamma_{NR_{NP}}$) rate due to the presence of the nanoparticle.

$$\Phi_{NP} = \frac{\gamma_{R^*}}{\gamma_{NR} + \gamma_{NR_{NP}} + \gamma_{R^*}} \tag{2.3.9}$$

In the case where a fluorescent molecule is very close to the metallic nanoparticle ($\sim$5 nm) the nonradiative de-excitation pathways results in a decreased fluorescence lifetime which can now be expressed as

$$\tau_{NP} = \frac{1}{\gamma_{NR} + \gamma_{NR_{NP}} + \gamma_{R^*}} \tag{2.3.10}$$

where τ_{NP} is the fluorescence lifetime modified by the presence of a nanoparticle.

In the case of the hybrid systems considered in this work, systems containing a quantum emitter and a nanoparticle on a phase change material, the impact of the underlying substrate layer must also be considered with regards to additional radiative and nonra-

diative pathways it offers. The previous equation for τ_{NP} is further modified to account for this

$$\tau_{Hyb} = \frac{1}{\gamma_{NR} + \gamma_{NR_{NP}} + \gamma_{NR_{Film}} + \gamma_{R^{**}}} \tag{2.3.11}$$

where τ_{Hyb} is the lifetime of the fluorescent molecule in the hybrid system, $\gamma_{NR_{Film}}$ is an additional nonradiative rate added due the presence of the substrate film and $\gamma_{R^{**}}$ is the modified radiative rate due to the nanoparticle and the substrate.

For calculations of the lifetime within numerical simulations all of the nonradiative terms arising from the loss pathways due to the nanoparticle and the VO_2 thin film are collected together and only the total effect of the hybrid system are considered i.e $\gamma_{Loss} = \gamma_{NR_{NP}} + \gamma_{NR_{Film}}$.

The expression for the fluorescence lifetime can be finally simplified into

$$\tau = \frac{1}{\gamma_R + \gamma_{Loss} + \gamma_{NR}} \tag{2.3.12}$$

2.3.1 Photoluminescence Thermal Quenching

In this work the emission of quantum emitters is modified through the phase transition of VO_2. As this phase change is usually actuated thermally, the impact of temperature on the emission of quantum emitters must be discussed.

The fluorescence intensity of quantum emitters is known to decrease with increasing temperature. This thermal quenching effect has been shown to be a reversible process in quantum dots[73] provided the temperature does not exceed a threshold where permanent damage occurs. A 60 - 80% permanent loss in emission intensity has been reported when quantum dots are heated to 210° C,[74] attributed to the formation of permanent surface defects. However, this temperature regime is far above the critical temperature of VO_2. The thermal quenching of fluorescent emitters can be attributed to surface

trap states or thermally activated carrier trapping and phonon-assisted non-radiative decay.[75] Trap states near the conduction band arise due to the increased displacement of surface atoms from their equilibrium positions with increased temperature. Additionally, increased temperature increases non-radiative relaxations through increased decay via phonons resulting in a decrease in PL intensity. The emission wavelength is also noted to slightly redshift at higher temperature.

2.4 Quantum Emitters

As seen in the excitation of plasmons, the interaction of electromagnetic radiation with matter at the nanoscale differs greatly from typical interactions seen at the macroscale. At the nanoscale limit, photon interactions are with discrete internal (electronic) energy levels within a molecular system. Quantum emitters can be treated as effective two-level systems, i.e. by considering electronic levels that differ in energy matches the energy of interacting photon energy.[76] The quantum emitters considered within this work fall into two categories namely semiconductor quantum dots and fluorescent dye molecules.

2.4.1 Semiconductor Quantum Dots

Quantum dots (QD) or semiconductor crystals are structures on the order of 1-10 nm in diameter and as such act as quasi zero dimensional objects i.e. they are spatially confined in 3 dimensions. Due to this confinement, the quantum mechanical "particle in a box" description can be applied to excitons (bound electron and hole states) within the QD. The electronic structure is therefore described in terms of discrete energy levels. A QD is capable of absorbing a photon if the photon energy, E_{Ph}, is greater than the bandgap energy E_g of the QD. The quantum confinement in the quasi zero dimensional QD means the energy gap corresponding to the first electronic transition follows the "particle in a box" description i.e $E \propto \frac{1}{L^2}$. As a result of this, increasing the QD diameter results in a redshift in the energy of absorbed photons and subsequently

emitted photons. Likewise decreasing the diameter has the effect of blueshifting the luminescence response.A schematic indicting this effect is shown in Fig. 2.5(a). As quantum dots have broadband absorption spectra (Fig. 2.5 (b)), a range of laser excitation wavelengths can be used as an excitation source. Additionally, a single laser excitation source is capable of exciting a range of differently sized QDs emitting at a range of wavelengths. The high quantum yield, photostability and resistance to photobleaching have allowed QDs to be used in applications such as display technology, biomedicine and photodetectors.

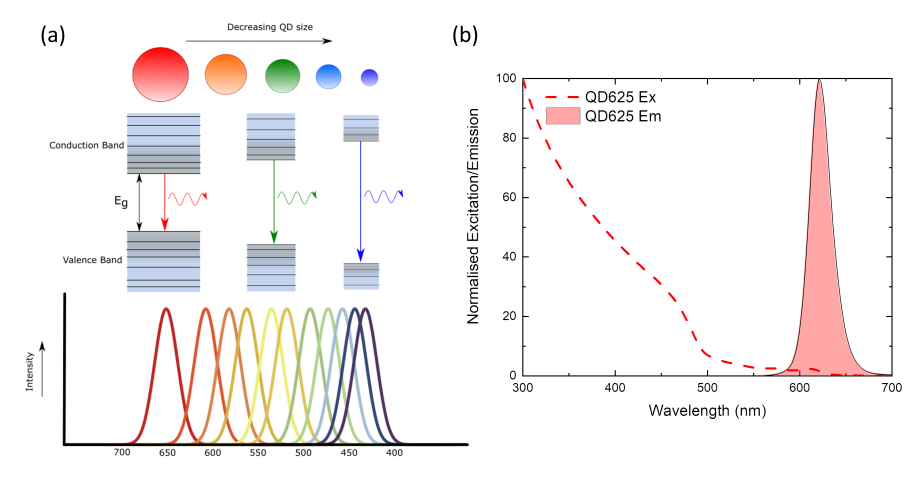

Figure 2.5: (a) Diagram demonstrating larger bandgap with decreasing quantum dot size and subsequently emission at a lower wavelength. (b) Normalised excitation (dotted line) and emission (solid line with fill) spectra for QD625.

2.4.2 Dye Molecules

Dye molecules are fluorescent molecules that contain extended systems of conjugated double bonds. The emission from organic dyes typically comes from either an optical transition delocalised over the molecule or from intramolecular charge transfer transitions.[77] For the dyes considered in this work, the emission is the former case characterised by comparatively narrow absorption and emission bands with close separation. These dyes are also characterised by high molar absorption co-efficients, and moderate to high fluorescence quantum yields.

Alexa Fluor

Alexa Fluor are a family of fluorescent dyes widely used as fluorescent labels in fluorescent microscopy and cell biology. The excitation and emission spectra of the Alexa Fluor series extends over the visible and near infrared (NIR) spectral range. Compared to the dyes from which the Alexa Fluor series dyes are synthesised from (fluorescein, rhodamine) Alexa Fluor dyes offer greater photostabilty and less sensitivity to pH with greater brightness in conjugates due to decreased self-quenching. Alexa Fluor dyes have a range of quantum yields (QY) with Alexa Fluor 488 having a quantum yield of 0.92. It is noted that generally the quantum yield of Alexa Dye molecules decreases as the emission redshifts with Alexa 700 and Alexa 750 having quantum yields of 0.25 and 0.12 respectively.[55] The excitation and emission spectra of several Alexa dyes are given in Fig. 2.6.

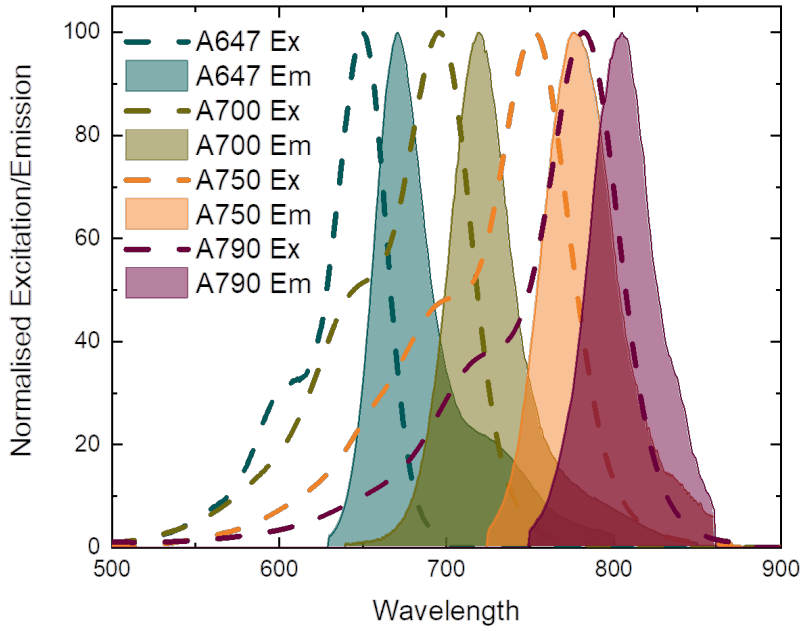

Figure 2.6: Normalised excitation (dotted lines) and emission (solid lines with fill) spectra for Alexa Fluor 647, Alexa Fluor 700, Alexa Fluor 750 and Alexa Fluor 790

2.5 Phase Change Material - Vanadium Dioxide (VO_2)

Phase change materials (PCMs) are a class of material in which a reversible physical change can be induced by the application of an external stimulus such as heat or an external electric field. For the purpose of fabricating hybrid plasmonic systems, a phase change material that remains in the solid phase in both material states is required. The phase change material VO_2 is considered as a route towards the development of highly tunable plasmonic components. VO_2 is well known to undergo an abrupt, reversible structural and electronic phase transition at the critical temperature (T_c) of 68°C.[78,79] Through this phase transition VO_2 goes from a semiconducting monoclinic phase to a rutile metallic phase with an accompanying decrease in electrical resistivity of over four orders of magnitude demonstrated.[80,81] The hysteresis associated with the thermal phase transition of VO_2 is on the order of 10 K for a polycrystalline film[82] with reported switching times on the order of 1 ns.[83]

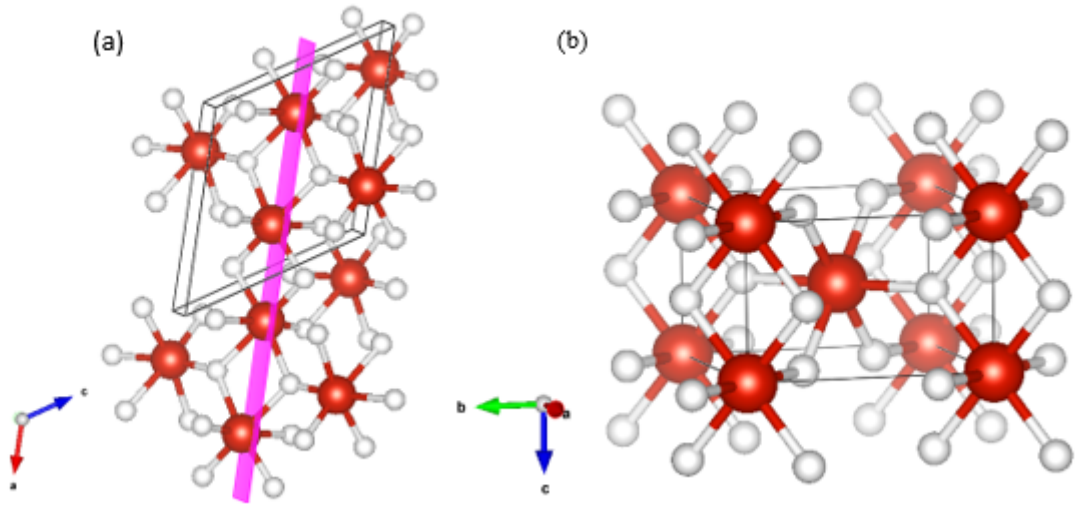

Figure 2.7: (a) Semiconducting Monoclinic Phase VO_2 (a = 5.74Å, b = 4.52Å, c = 5.38Å,$\alpha = \gamma = 90°$, $\beta = 122.6°$),[84] pink plane highlights alternating V-V distances (b) Metallic Rutile Phase VO_2 (a = b = 4.53Å, c = 2.87Å, $\alpha = \beta = \gamma = 90°$).[85]

The VO_2 structural phase change from the rutile (tetragonal) phase to the monoclinic phase is driven by the dimerization of vanadium chains along the c-direction of the rutile phase and twisting of the V-V axis. The symmetry of the monoclinic structure belongs

to the $P2_1/c$ space group[84] while the rutile structure belongs to the $P4_2/mmm$ space group.[85] The formation of vanadium dimers results in the distance between subsequent vanadium atoms moving from a fixed value of 2.87 Å in rutile phase to alternating distances of 3.12 Å and 2.65 Å in the monoclinic phase. As a result, the monoclinic VO_2 phase has effectively twice the unit cell volume of the rutile phase, 117.47 $Å^3$ to 58.87 $Å^3$. The molecular structure of VO_2 in its monoclinic phase and its rutile phase are demonstrated in Fig. 2.7. Lattice distortion effects and electron correlation effects in the low symmetry monoclinic phase cause the $3d_{||}$ band to split into two separate bands, a lower energy filled $3d_{||}$ and a higher energy, empty antibonding $3d^*_{||}$. Additionally, the antibonding $3d^*_\pi$ is pushed to a higher level above the Fermi energy. This opens a band gap with $E_g \sim 0.6 - 0.7eV$ resulting in the increased resistivity seen in the monoclinic phase (Fig. 2.8).

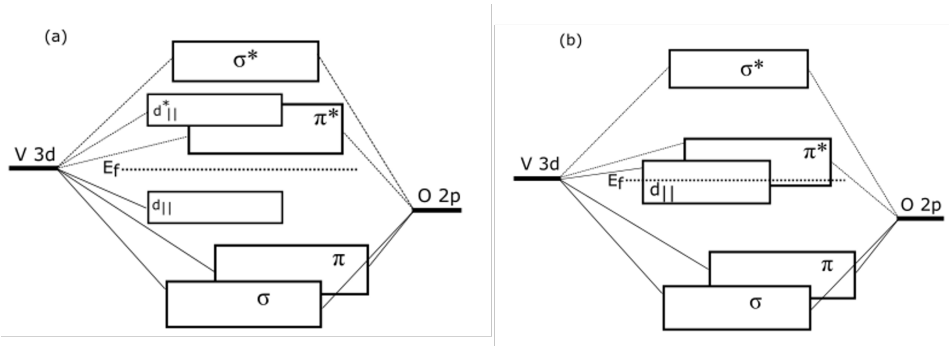

Figure 2.8: Band diagrams for (a) monoclinic semiconducting VO_2 and (b) rutile metallic VO_2.

The precise nature of the VO_2 transition mechanism is still a topic of much debate with competing ideas of what drives the transition: a Mott-like transition driven by electron correlation effects or a Peierls-like transition driven by lattice distortion effects.[86] Recent theoretical and experimental studies suggest that both effects are required to obtain an accurate picture of the transition mechanism.[87]

VO_2 offers a number of distinct advantages over other PCM options previously explored. The phase transition can be thermally actuated at the critical temperature (T_c) of 68 °C, relatively close to room temperature, and significantly lower than the T_c of other material options Ge-Sb-Te (GST) and Ag-In-Sb-Te (AIST) which transition

near 150°C[88–90] and 170°C,[91] respectively. Additionally, the VO_2 T_c can be further tuned through the inclusion of dopants. The inclusion of high valence transition metal cations such as W^{6+}, Nb^{5+}, Ta^{5+}, Mo^{6+} or Ru^{4+} allows significant reduction of the T_c.[78] At a doping level of 7% the T_c of Mo-doped VO_2 decreases to 24°C,[92] and at a doping level of $\sim$ 2%, the T_C of W-doped VO_2 decreases to room temperature.[93] Conversely the T_c can be increased with inclusions of low valence cations such as Al^{3+}, Cr^{3+} or Fe^{3+} with a 1-3 °C increase per %.[94–96]

In addition to thermal actuation, the VO_2 phase transition can be triggered electrically or optically. The reported threshold electric field required for phase transition is on the order of 10^6 V/m, an order of magnitude lower than the values of 5.6 x 10^7 V/m and 1.9 x 10^7 V/m reported for GST and AIST, respectively.

Studies of crystalline VO_2 thin films have shown that the phase change occurs on the order of $\sim$ 100 fs.[97,98] Other studies have demonstrated that a current driven VO_2 switch is capable of operating over 260 million cycles without failure.[99] Fast switching speed coupled with stability over many cycles make VO_2 an ideal candidate for applications in optoelectronics.

VO_2 also offers advantages in that there are many viable synthesis methods that have been employed for thin film growth including pulsed laser deposition (PLD), magnetron sputtering, sol-gel coating, chemical vapour deposition (CVD), electron beam evaporation and ion beam deposition. However, as vanadium is a transition metal, it has many valence states meaning there is a large range of stable vanadium oxide phases including Magneli phases (V_nO_{2n-1})[100–102] and Wadsley phases ($V_{2n}O_{5n-2}$).[101,103] Due to large number of vanadium oxide phases, growth of VO_2 that demonstrates large switching properties is extremely sensitive to the parameters used during film growth, in particular temperature and partial pressure. The mechanisms of VO_2 thin film growth will be further discussed in **Chapter 3**.

2.6 Maxwell Garnett Effective Medium Theory

While the optical properties of hybrid VO_2 nanostructures are tunable through the phase change of an underlying VO_2 layer, in order to understand how the optical properties of the system evolve through the VO_2 phase change at intermediate temperatures an effective medium approach is taken. The Maxwell Garnett effective medium approach allows for calculation of intermediate VO_2 phases by treating the effective medium as a host medium of semiconducting VO_2 with metallic VO_2 inclusions. The calculation of the effective medium is given as follows

$$\varepsilon_{eff} = \varepsilon_m \frac{2\delta_i(\varepsilon_i - \varepsilon_m) + \varepsilon_i + 2\varepsilon_m}{2\varepsilon_m + \varepsilon_i - \delta_i(\varepsilon_i - \varepsilon_m)} \tag{2.6.1}$$

where ε_{eff} is the dielectric function of the effective media , ε_i is the dielectric function of the inclusions, ε_m is the dielectric function of the matrix and δ_i is the volume fraction of inclusions.

The Maxwell Garnett effective medium equation can be derived from the Clausius-Mossotti relation, an expression where the dielectric function of a medium is expressed in terms of the polarizability of constituent atoms or molecules.[104]

The local electric field $\vec{E}_{loc}$ acting on a spherical electric dipole can be approximated as

$$\vec{E}_{loc} = \vec{E} + \frac{\vec{P}}{3_{\varepsilon_0}} \tag{2.6.2}$$

where $\vec{P}$ is the electric polarization and ε_0 is the permittivity of free space.

If the local dipole moment $\vec{p}$ induced in a single molecule is considered, it's clear that the magnitude of p depends on the local field $\vec{E}_{loc}$ and in dielectrics the molecular charge separation is directly proportional to, and in the same direction as the local field.[105] Therefore, the dipole moment can be expressed as

$$\vec{p} = \alpha \vec{E}_{loc} = \alpha(\vec{E} + \frac{\vec{P}}{3_{\varepsilon_0}}) \tag{2.6.3}$$

where α is a constant known as the molecular polarizability The dipole moment per unit volume is then given as

$$\vec{P} = N\vec{p} = N\alpha \vec{E}_{loc} = N\alpha(\vec{E} + \frac{\vec{P}}{3_{\varepsilon_0}}) \tag{2.6.4}$$

where N is the number of molecules per unit volume

From the definition of electric displacement $\vec{D} = \varepsilon_0 \vec{E} + \vec{P}$ and given that $\vec{D} = \varepsilon_0 \varepsilon_r \vec{E}$ the polarization can be expressed as

$$\vec{P} = \vec{D} - \varepsilon_0 \vec{E} = \varepsilon_0 \varepsilon_r \vec{E} - \varepsilon_0 \vec{E} \tag{2.6.5}$$

$$\vec{P} = \varepsilon_0(\varepsilon_r - 1)\vec{E} \tag{2.6.6}$$

where ε_r is the relative permittivity. If the above expression for P is substituted into the equation derived previously the following relation is obtained.

$$\varepsilon_0(\varepsilon_r - 1)\vec{E} = N\alpha(\vec{E} + \frac{\varepsilon_r - 1}{3}\vec{E}) \tag{2.6.7}$$

which can be rearranged to give the expression for the Clausius-Mossotti relation:

$$\frac{(\varepsilon_r - 1)}{(\varepsilon_r + 2)} = \frac{N\alpha}{3\varepsilon_0} \tag{2.6.8}$$

and when the dielectric is a compound consisting of a number of different molecules or atoms

$$\frac{(\varepsilon_r - 1)}{(\varepsilon_r + 2)} = \frac{1}{3\varepsilon_0} \sum_i N_i \alpha_i \tag{2.6.9}$$

where N_i and α_i are the appropriate quantities for the ith type of molecule or atom.

This equation is rewritten with the polarizabilty α in cgs units as polarizability volume

$$\frac{(\varepsilon_r - 1)}{(\varepsilon_r + 2)} = \frac{4\pi}{3} \sum_i N_i \alpha_i \tag{2.6.10}$$

The static polarization is given by the formula below

$$\alpha = a^3 \frac{(\varepsilon_r - 1)}{(\varepsilon_r + 2)} \tag{2.6.11}$$

and combined with the expression for the volume fraction

$$\delta_i = \frac{4\pi}{3} \frac{a^3}{V} \tag{2.6.12}$$

gives the following expression relating the dielectric function to the inclusions

$$\frac{\varepsilon_{eff} - 1}{\varepsilon_{eff} + 2} = \delta_i \frac{\varepsilon_i - 1}{\varepsilon_i + 2} \tag{2.6.13}$$

This expression, when solved for ε_{eff} gives the relation used for the effective medium calculation given earlier. This effective medium calculation is used within the numerical model to calculate the scattering cross-section of coupled nanoparticles and the photoluminescence intensity of coupled emitters at intermediate temperatures at different points on the VO_2 thermal hysteresis.

2.7 Conclusion

In this chapter, the theoretical concepts underpinning the work done throughout this thesis are presented. Nanoscale light-matter interactions are discussed, in particular the LSPRs that occur when light interacts with metallic nanostructures. The dynamic tuning of these resonances is discussed, in detail, in **Chapter 5** and also in **Chapter**

6 as a platform for photoluminescence enhancement. Thin film interference effects are discussed as they pertain to the reflectance, transmittance and absorptance spectra presented in **Chapter 4** and **Chapter 5**. A discussion of fluorescence and various fluophores is presented in this chapter as this forms the basis of the work presented in **Chapter 6** where enhanced emission of quantum emitters is presented. Finally, the phase change material VO_2 has been introduced. This material forms the basis for all of the results presented in this thesis and is a fundamental part of all hybrid nanostructures discussed in this work. The optical properties and the fabrication of VO_2 is further discussed in the next chapters.

3 Methods

3.1 Summary

This chapter contains a brief overview of the standard techniques used to fabricate and characterise the hybrid nanostructures considered in this work. The two physical vapour deposition techniques used to fabricate VO_2 thin films are discussed alongside the background theory of the characterisation techniques used to determine VO_2 thin film quality including Raman spectroscopy, X-ray reflectivity, X-ray diffraction. How some of these techniques are specifically applied to VO_2 is expanded on in **Chapter 4**. The theory behind the FDTD simulation methods used throughout this work is discussed. Finally, additional fabrication techniques for the fabrication of the hybrid plasmonic nanoparticle - quantum emitter structure are discussed.

3.2 Raman Spectroscopy

Raman Spectroscopy is an optical, non destructive spectroscopic technique based on the inelastic scattering of monochromatic laser light by molecules excited to a higher energy vibrational or rotational level. Due to the inelastic nature of the interaction, the scattered light is of a different frequency to the incident light. Inelastic scattering events are significantly less likely to occur (1 in every 10^7 incident photons) compared to elastic or Rayleigh scattering, where the energy of the scattered photon matches the energy of the incident photon. This necessitates the use of a high intensity, monochromatic laser source. Raman scattering can be divided into Stokes and

anti-Stokes scattering based on whether the energy of the scattered photons is lower or higher than the energy of the incident laser. Quantum mechanically, Stokes and anti-Stokes scattering are equally likely to occur, but in an ensemble of molecules, the majority of molecules are in the ground vibrational level making Stokes scattering the more likely process. Due to this, the Stokes Raman scattering signal is more intense than the anti-Stokes signal and is generally the one measured in Raman spectroscopy. As the wavelength of Raman scattered light is dependent on the wavelength of the laser excitation source, the Raman shift is given in terms of wavenumber ($\tilde{\nu}$) in units of cm^{-1}. The wavenumber is related to the excitation laser wavelength (λ_0) and the scattered wavelength (λ_1) by the following equation:

$$\tilde{\nu} = \frac{1}{\lambda_0} - \frac{1}{\lambda_1} \tag{3.2.1}$$

As the vibrational energy levels of a molecule are highly dependent on atomic structure and bond strength, a Raman spectra can be used as a fingerprinting technique to identify a fabricated thin film. Given the low probability of inelastic scattering occurring, Raman signals are generally weak meaning long integration times coupled with the use of the high intensity laser source are required. Throughout this work Raman spectra are used as an identifier of the semiconducting VO_2 phase. Additionally, Raman mapping is a technique used to obtain spectral information across a larger sample area. The variation in Raman spectra across a larger sample area allows determination of the uniformity of the vanadium oxide phase across the sample. Fig. 3.1 illustrates the energy level transitions for Rayleigh, Stokes and anti-Stokes Raman scattering.

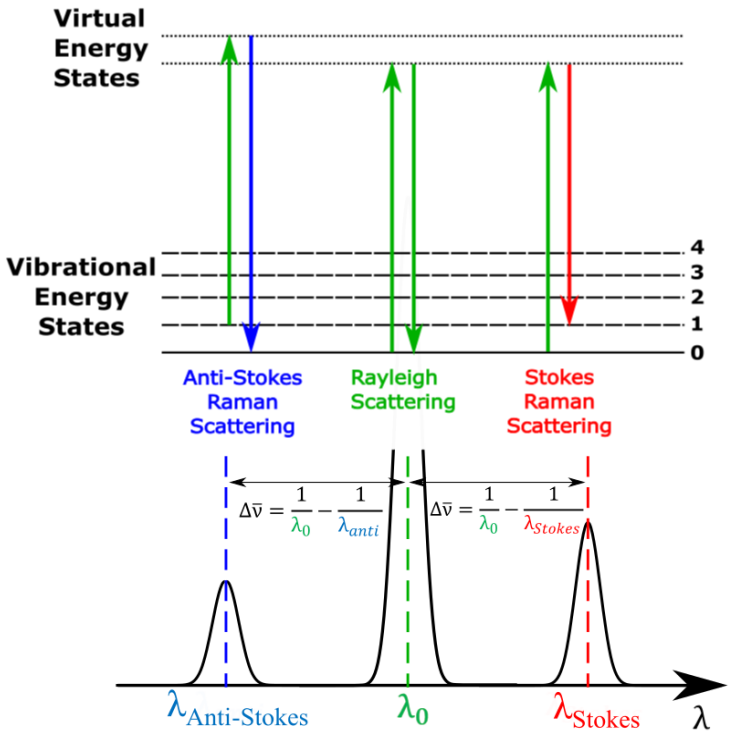

Figure 3.1: Diagram illustrating Rayleigh, Stokes and anti-Stokes scattering.

3.3 X-Ray Reflectivity

X-Ray reflectivity (XRR) is a non-destructive reflectivity technique applicable to crystalline and amorphous materials and can be used to determine the thickness, density and roughness of material layers within a thin film system. XRR can give layer thicknesses to Angstrom resolution making it ideal technique for determination of thicknesses of thin films to high resolution. When X-rays are incident on a flat material surface at a grazing angle of incidence, total internal reflection occurs at or below a critical angle (θ_c). For thin films deposited on a substrate, the electronic density changes at the material interface. Reflected X-rays from this interface can constructively or destructively interfere with reflections from the material surface, resulting in an oscillatory pattern forming when the scattered intensity is measured as a function of angle. These oscillations observed at low angles are known as Kiessig fringes.[106] The scattered intensity is proportional to the square of the modulus of the Fourier

transform of the electron density. As a result layer thickness can be determined by fitting the oscillation pattern using thickness, density and surface roughness as fitting parameters. The film thickness is determined by the periodicity of the oscillation in the measured XRR intensity pattern. The position of the fringes within the oscillatory pattern are related to the film thickness by a modified Bragg equation

$$sin^2\theta_i = \theta_c^2 + (n_i + \Delta n)^2\lambda^2/4t^2 \tag{3.3.1}$$

where θ_i is the position of the maximum or minimum of the ith interference fringe, θ_c is the critical angle, n_i is an integer, $\Delta n = 1/2$ for maximum and 0 for minimum, λ is the X-ray wavelength and t is the thickness.

3.4 X-Ray Diffraction

X-ray diffraction (XRD) is a nondestructive technique that provides detailed information about the crystallographic structure, chemical composition, and physical properties of materials. The technique is based on constructive interference of diffracted monochromatic x-rays from adjacent lattice planes occurring when conditions satisfy Bragg's law

$$n\lambda = 2dsin\theta \tag{3.4.1}$$

where n an integer, λ is the wavelength of the x-ray, d is the perpendicular distance between adjacent lattice planes and θ is the angle of the incident x-ray. Peak position, relative intensity and full-width at half maximum (FWHM) are characteristics of the material and crystallinity. Schematics demonstrating the Bragg condition and illustrating an X-ray diffractometer are given in Fig. 3.2.

The Scherrer equation can be used to relate the size of crystallites in a solid to the peak broadening in an XRD spectra and is given as

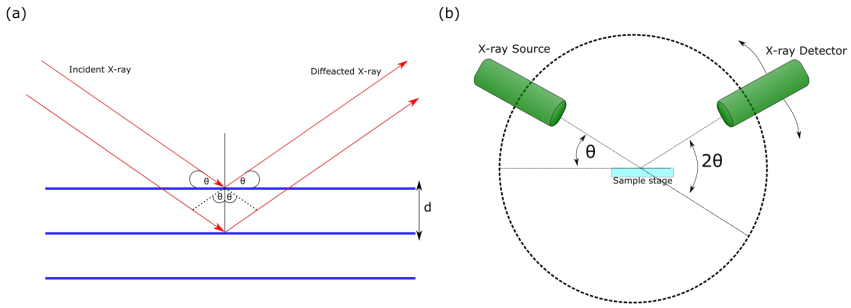

Figure 3.2: (a)Schematic of Bragg's law demonstrating the path length difference between waves subsequent lattice planes separated by distance d (b) Simplified schematic of an X-ray diffractometer used for XRR and XRD measurements.

$$n\tau = \frac{K\lambda}{\beta cos\theta} \tag{3.4.2}$$

where τ is the mean size of crystalline domains, K is a dimensionless shape factor with a typical value of 0.9, λ is the wavelength of the x-ray source, β is the line broadening of the FWHM given in radians and θ is the Bragg angle.

3.5 X-ray photoelectron spectroscopy

X-ray photoelectron spectroscopy is a surface sensitive technique based on the photoelectric effect, the emission of electrons when electromagnetic radiation is incident on a sample. The technique allows analysis of a material's surface chemistry i.e. elemental composition and electronic state of the atoms within a material. To acquire the XPS spectra the sample is irradiated with X-rays and the kinetic energy of the electrons emitted from the top surface of the material are measured. The energies and intensities of the photoelectron peaks gives a characteristic spectrum enabling identification of the material phase.

The binding energy of the emitted electrons is determined by the photoelectric effect equation

$$E_{binding} = E_{photon} - (E_{kinetic} + \Phi) \tag{3.5.1}$$

where $E_{binding}$ is the binding energy (BE) of the electron measured relative to the chemical potential, E_{photon} is the energy of the incident X-ray and Φ is the materials work function.

3.6 Ellipsometry

Ellipsometry is a spectroscopic technique that can be used to determine the optical constants of a material of known thickness or to determine the layer thickness of a sample from known optical constants. The optical constants used in numerical simulations of VO_2 thin films were obtained by fitting data from ellipsometry measurements. A simplified schematic of an ellipsometer is given in Fig. 3.3. The basic principle behind the method is that the amplitude and phase of s and p polarized light incident on a sample plane will be altered upon reflection. By measuring the change in the reflected light beam two parameters can be established; Psi (Ψ) and Delta (Δ), where $\tan(\Psi)$ defines the magnitude of the reflectivity ratio for s and p polarized light and (Δ) the phase difference between the reflected s and p polarized light. These parameters are related by following equation;

$$tan(\Psi)e^{i\Delta} = r_p/rs \tag{3.6.1}$$

where r_p and r_s are the complex reflection coefficients for p and s polarized light, respectively. The values of psi and delta are acquired as a function of wavelength allowing for an optical model to be built to fit acquired data. The measurements and fitting to acquire the VO_2 optical constants used in numerical simulation were acquired on a Sopra GESP5 ellipsometer. A Woollam's Alpha SE Ellipsometer was used for thickness measurements of further samples with fits made based on refractive index data acquired from the Sopra GESP5 ellipsometer. A simplified schematic of an

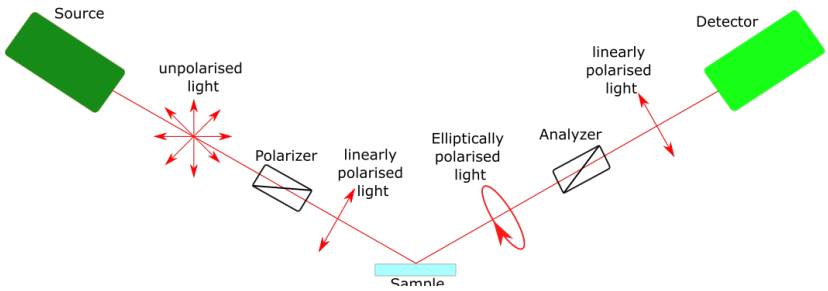

Figure 3.3: Simplified schematic of an ellipsometer

ellipsometer is given in Fig. 3.3.

3.7 Scanning Electron Microscopy

The resolution of any microscope has a fundamental, far-field, wavelength-dependent limit. This limit is known as the Abbe diffraction limit and is approximated as

$$d = \frac{\lambda}{2nsin\theta} = \frac{\lambda}{2NA} \tag{3.7.1}$$

where λ is the wavelength of light, n is the refractive index of the medium ,θ is the half-angle of the converging light and NA is the numerical aperture. For visible light this gives an effective limit of d $\approx \frac{\lambda}{2}$. As the visible light spectrum lies between 380 and 700 nm, the best possible resolution for an optical microscope is in the order of hundreds of nanometers. The fabricated nanostructures and thin films have physical dimensions on the order of tens of nanometers, meaning in order to image a subwavelength structure an alternative to optical microscopy is needed.

The nanostructures fabricated in this work were imaged using electron microscopy. Electron microscopy utilises high energy electrons, as opposed to photons, to obtain high enough resolution to image nanostructures. For electrons the imaging resolution is related to the de Broglie wavelength of the particle which is given by

$$\lambda = \frac{h}{mv} = \frac{h}{E} \tag{3.7.2}$$

where h is Planck's constant ($\sim 6.626 \times 10^{-34} m^2 kg/s$), m is the mass of the electron ($\sim 9.1 \times 10^{-31} kg$) and v is the velocity of the electron. From this it's clear that the de Broglie wavelength is inversely proportional to the electron's velocity ($\lambda \propto \frac{1}{v}$). The kinetic energy of the electron can also be expressed in terms of the accelerating voltage V and the electron charge (1.6×10^{-19} C)

$$\frac{1}{2}mv^2 = eV \tag{3.7.3}$$

the de Broglie wavelength can now be given as

$$\lambda = \frac{h}{\sqrt{2meV}} \tag{3.7.4}$$

indicating that to achieve higher resolution imaging an increased accelerating voltage is required.

SEM imaging was achieved using a Carl Zeiss Ultra Plus SEM with a LaB_6 source. Imaging for the purposes of electron beam lithography was achieved with a Carl Zeiss Supra 40 FESEM. A schematic of an SEM is given in Fig. 3.4(a). For imaging purposes the SEM was operated with an accelerating voltage of 5 kV at a working distance of between 5-6 mm. SEM images were taken using the in-lens detector due to the greater resolution of the sample surface. An example of the same image taken with the inlens detector and the SE2 (secondary electron) detector is given in Fig. 3.4.

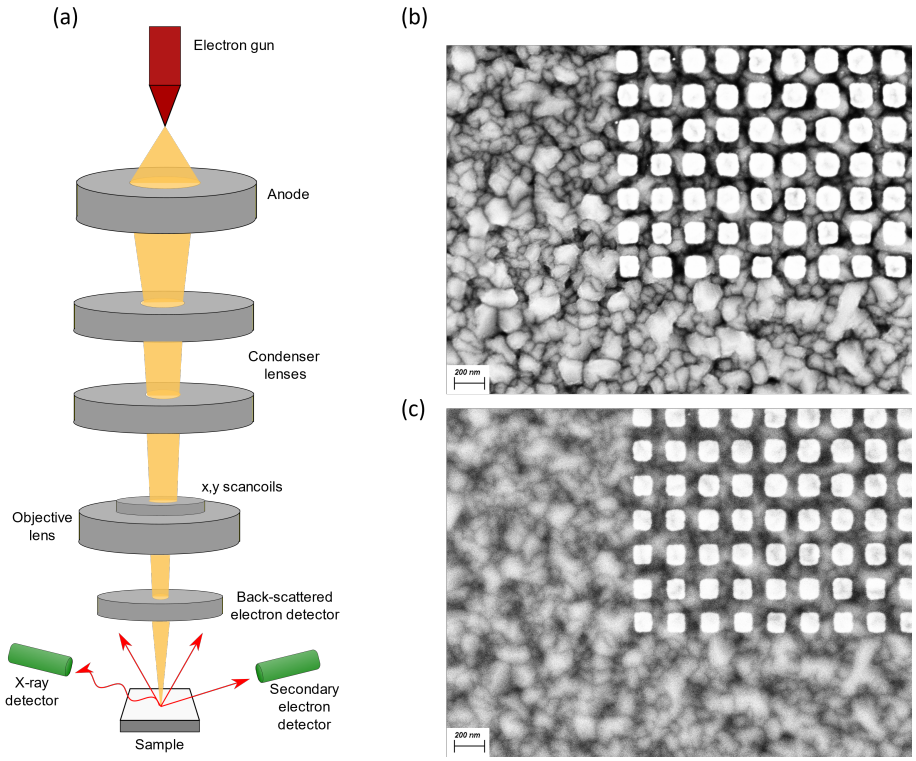

Figure 3.4: (a) Schematic of scanning electron microscope. SEM image of Au nanoboxes on VO_2 taken with (b) InLens detector and (c) SE2 detector

3.8 Optical Measurements

Normal Reflectance

Normal reflectance was measured with a custom-built set-up as shown in Fig. 3.5. A Xenon lamp is used as an illumination source with a 50:50 beam splitter used to direct light towards samples mounted on a sample stage. A 40x lens was mounted on an adjustable x,y stage to allow the sample image to be focused onto the fibre coupler. The fibre coupler allowed the reflected light to be directed into an Andor 230i spectrometer with Andor CCD camera

To obtain the reflectance spectra of a sample the raw data was treated as follows

$$R = \frac{R_s - Dark}{\frac{R_r}{0.2} - Dark} \tag{3.8.1}$$

where R_s is the raw counts reflected from the sample and R_r is the reflected counts from

a reference. The reference counts are taken from a double side polished Al_2O_3 substrate. This value is adjusted by dividing by 0.2 to compensate for the combined reflectance from the Al_2O_3 and the ceramic holder. Dark represents the dark counts from the spectrometer and any stray light from when the white light source is blocked.

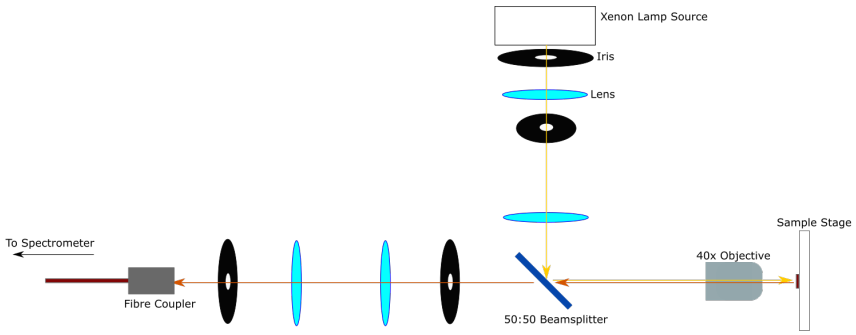

Figure 3.5: Schematic of normal reflection setup

Bright and Dark Field

Reflectance and scattering spectra were measured using an Olympus upright microscope in brightfield and darkfield mode, respectively. The spectra presented in this work were taken using MPlanFL N 50x and 100x objective lenses capable of working in bright and darkfield mode. A simplified schematic of the objective lenses' operation is given in Fig. 3.6. In dark field mode the sample is illuminated with a cone of light and collects the scattered light, i.e. the non-0-order reflection. An example of images taken in bright and dark field mode are given in Fig. 3.6 (c) and (d), respectively.

Reflectance and scattering data taken using the Olympus microscope was treated similarly to the normal reflectance case. A ceramic diffuser was used for obtaining the reference spectra in the scattering case.

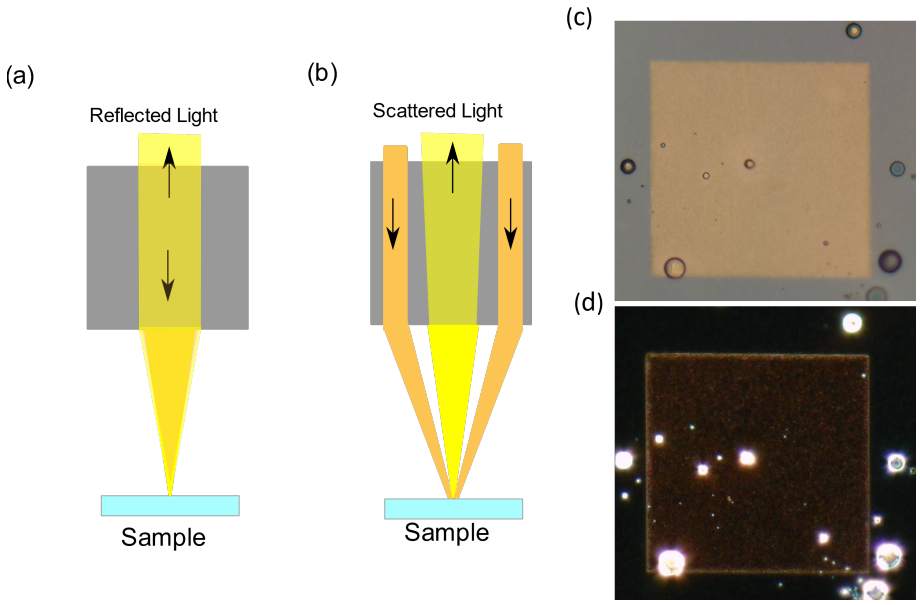

Figure 3.6: (a) Schematic of objective and sample under bright field illumination (b) objective and sample under dark field illumination. 50 μm x50 μm nanoparticle array imaged with 100x objective lens in (c) bright field and (d) dark field.

3.9 Finite Difference Time Domain Simulation

Due to the multitude of parameters to consider when designing hybrid VO_2 - plasmonic structures coupled with the complexity and cost in the fabrication of structures at the nano-scale, numerical simulations are a vital tool for the development of hybrid VO_2 - plasmonic nanostructures with optimised optical responses.

Finite Difference Time Domain (FDTD) is a computational modelling methodology designed to solve Maxwell's equations for complex 3D geometries. Simulations are built within Lumerical FDTD solutions software using a CAD interface.

FDTD solves Maxwell's curl equations in non-magnetic materials

$$\frac{\partial \vec{D}}{\partial t} = \nabla \times \vec{H} \tag{3.9.1}$$

$$\vec{D}(\omega) = \varepsilon_0 \varepsilon_r \vec{E}(\omega) \tag{3.9.2}$$

$$\frac{\partial \vec{H}}{\partial t} = -\frac{1}{\mu_0} \nabla \times \vec{E} \tag{3.9.3}$$

where $\vec{E}$ is the electric field strength vector, $\vec{H}$ is the magnetic field strength vector and $\vec{D}$ is the electric displacement vector, respectively, and $\varepsilon_r(\omega)$ is the complex relative dielectric constant.

From these equations it can be seen that the change in the E-field in time is dependent on the curl of the H-field (the change in the H-field across space). This means that value of the E-field at each time step at any point in space is dependent on the previous value of E-field and the numerical curl of the local distribution of the H-field in space.

Similarly, it can be seen that that change in H-field in time is dependent on the curl of the E-field. Therefore, the value of the H-field at each time step at any point in space is dependent on the previous value of the H-field and numerical curl of the local distribution of the E-field in space.

The FDTD method solves the equations on a discrete spatial and temporal grid. Each field component is solved at different location within a grid cell (Yee cell). In this Cartesian coordinate system, Maxwell's equations have six components, three electric (E_x, E_y, E_z) and three magnetic (H_x, H_y, H_z).

From the equation for Faraday's law given above, the partial differentials for each component can be described as:

$$\frac{\partial \vec{H_x}}{\partial t} = -\frac{1}{\mu_0}\left(\frac{\partial \vec{E_z}}{\partial y} - \frac{\partial \vec{E_y}}{\partial z}\right) \tag{3.9.4}$$

$$\frac{\partial \vec{H_y}}{\partial t} = -\frac{1}{\mu_0}\left(\frac{\partial \vec{E_x}}{\partial z} - \frac{\partial \vec{E_z}}{\partial x}\right) \tag{3.9.5}$$

$$\frac{\partial \vec{H_z}}{\partial t} = -\frac{1}{\mu_0}\left(\frac{\partial \vec{E_y}}{\partial x} - \frac{\partial \vec{E_x}}{\partial y}\right) \tag{3.9.6}$$

Similarly, from the equation for Ampere's law, the partials differentials for each component are given as:

$$\frac{\partial \vec{E}_x}{\partial t} = \frac{1}{\varepsilon_0 \varepsilon_r}(\frac{\partial \vec{H}_z}{\partial y} - \frac{\partial \vec{H}_y}{\partial z}) \tag{3.9.7}$$

$$\frac{\partial \vec{E}_y}{\partial t} = \frac{1}{\varepsilon_0 \varepsilon_r}(\frac{\partial \vec{H}_x}{\partial z} - \frac{\partial \vec{H}_z}{\partial x}) \tag{3.9.8}$$

$$\frac{\partial \vec{E}_z}{\partial t} = \frac{1}{\varepsilon_0 \varepsilon_r}(\frac{\partial \vec{H}_y}{\partial x} - \frac{\partial \vec{H}_x}{\partial y}) \tag{3.9.9}$$

In FDTD simulations time and space are discretised, so derivatives can be approximated by finite differences. The derivative of an arbitrary time function $f(t)$ is given as,

$$f'(t) = \lim_{\Delta t \to 0} \frac{f(x + \Delta t) - f(t)}{\Delta(t)} \tag{3.9.10}$$

As in FDTD schemes δx and δt take finite values the derivative can approximated using a forward difference approximation, meaning a linear interpolation between the current data value and the next data value.

$$f'(x) \approx \frac{f(t + \Delta t) - f(t)}{\Delta t} \tag{3.9.11}$$

Alternatively a backwards difference approximation may be used. In this case the approximation is made using a linear interpolation between the current data value and the previous data value.

$$f'(x) \approx \frac{f(t) - f(t - \Delta t)}{\Delta t} \tag{3.9.12}$$

These approximations have an error of $O(\Delta x)$. If a linear interpolation between the previous data value and the next data value is made instead the approximation be-

comes,

$$f'(x) \approx \frac{f(t+\Delta t) - f(t-\Delta t)}{2\Delta t} \tag{3.9.13}$$

This central difference approximation has an error of $O(\Delta(t^2))$ therefore is the preferred method for solving partial differential equations where the forward and backward data values are available.

In FDTD the electric and magnetic field components are sampled a time intervals of Δt offset by $\frac{\Delta t}{2}$ with the electric field components sampled at integers of Δt and the magnetic field components sampled at half integer times of Δt.

From examining the Yee cell (Fig. 3.7, Fig. 3.8), it can be seen that for the calculation of the E and H fields information from neighbouring cells is required.

Applying the central difference method to the derivatives given previously the following equation is gotten for the E_x component of the E field;

$$\frac{E_x^{i,j,k}\mid_{t+\Delta t} - E_x^{i,j,k}\mid_t}{\Delta t} = \frac{1}{\varepsilon_0 \varepsilon_r}\left[\frac{H_z^{i,j,k}\mid_{t+\frac{1}{2}\Delta t} - H_z^{i,(j-1),k}\mid_{t+\frac{1}{2}\Delta t}}{\Delta y} - \frac{H_y^{i,j,k}\mid_{t+\frac{1}{2}\Delta t} - H_y^{i,j,(k-1)}\mid_{t+\frac{1}{2}\Delta t}}{\Delta z}\right] \tag{3.9.14}$$

This dependence on the neighbouring H-field components can be clearly seen in the figure of the Yee Cell given in Fig. 3.7. The other derivatives of the other components are given in a similar way.

Applying the same method to the H_x component of the H-field results in the following equation

$$\frac{H_x^{i,j,k}\mid_{t+\frac{1}{2}\Delta t} - H_x^{i,j,k}\mid_{t-\frac{1}{2}\Delta t}}{t} = -\frac{1}{\mu_0}\left[\frac{E_z^{i,(j+1),k}\mid_t - E_z^{i,j,k}\mid_t}{\Delta y} - \frac{E_y^{i,j,(k+1)}\mid_t - E_y^{i,j,k}\mid_t}{\Delta z}\right] \tag{3.9.15}$$

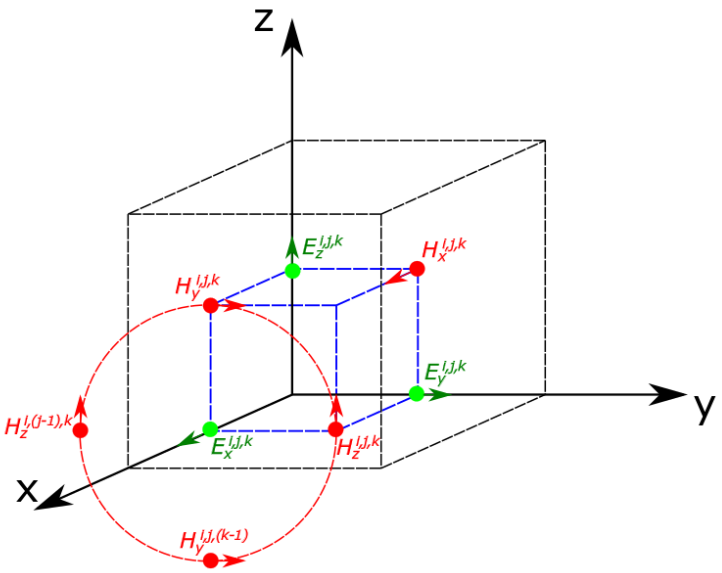

Figure 3.7: A Yee Cell with highlighted H-field components $(H_y^{i,j,k}, H_z^{i,j,k}, H_y^{i,j,(k-1)}, H_z^{i,(j-1),k})$ for the calculation of $\nabla \times \vec{H}$ and E_x. The x,y and z coordinates of the Yee cell are denoted by i,j and k respectively

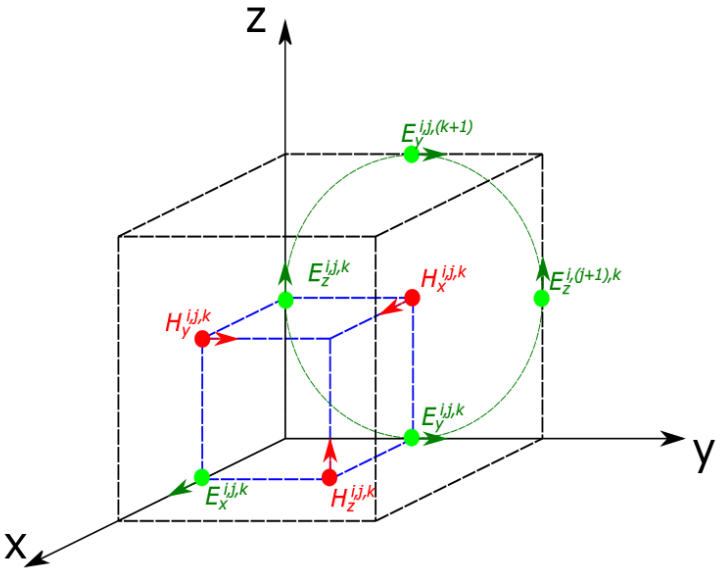

Figure 3.8: A Yee Cell with highlighted E-field components$(E_y^{i,j,k}, E_z^{i,j,k}, E_y^{i,j,(k+1)}, E_z^{i,(j+1),k})$ for the calculation of $\nabla \times \vec{H}$ and E_x. The x,y and z coordinates of the Yee cell are denoted by i,j and k respectively

FDTD uses a rectangular, Cartesian mesh. As fundamental simulation quantities are calculated at each mesh point, for high accuracy simulations, a suitably small mesh size is required particularly when simulating curved geometries as insufficient mesh size can lead to staircasing effects. However, as simulation time scales with $\frac{1}{x^4}$ where x is mesh unit length, small mesh sizes can require a large amount of computational

time and resources. However, a major advantage of the FDTD simulation scheme is that broadband response can be seen for a single simulation. To reduce simulation time, a fine mesh is only applied to simulation regions where it is necessary to produce accurate spectra.

3.9.1 Simulation Dielectric Permittivity data

The complex refractive index data for materials used in FDTD simulations, with the exception of VO_2, have been taken from the Lumerical FDTD Material library. The material data for substrates (Al, Al_2O_3, SiO_2) was taken from Palik.[56] The data for Ag is also taken from Palik,[56] while Au is taken from Johnson and Christy.[55] Finally the material data for VO_2 in both semiconducting and metallic phase is obtained from in-house ellipsometry measurements performed by Chris Smith on a VO_2 thin film (30 nm). The measured material data and the fitted data for the FDTD simulations for VO_2 in semiconducting phase and metallic phase are given in Fig. 3.9.

The VO_2 FDTD model material fits are adjusted to best match experimental material data in the wavelength range between 400 nm - 1000 nm. The parameters for the fits are given in the Table. 3.1

	Semiconducting	Metallic
fit tolerance	0.1	0.1
max coefficients	5	4
imaginary weight	1	1
fit range	390 - 1300 nm	390 - 1300 nm
RMS error	0.130676	0.15313

Table 3.1: Parameters used for fitting semiconducting and metallic VO_2 from material data for use in FDTD numerical simulations

3.10 Spectral Colour Conversion

Throughout this work reflectance spectra for various metasurfaces are generated using FDTD simulation methods. As the reflectance spectra encompass the visible spectral region they can be interpreted by the human eye, a series of equations is used in order

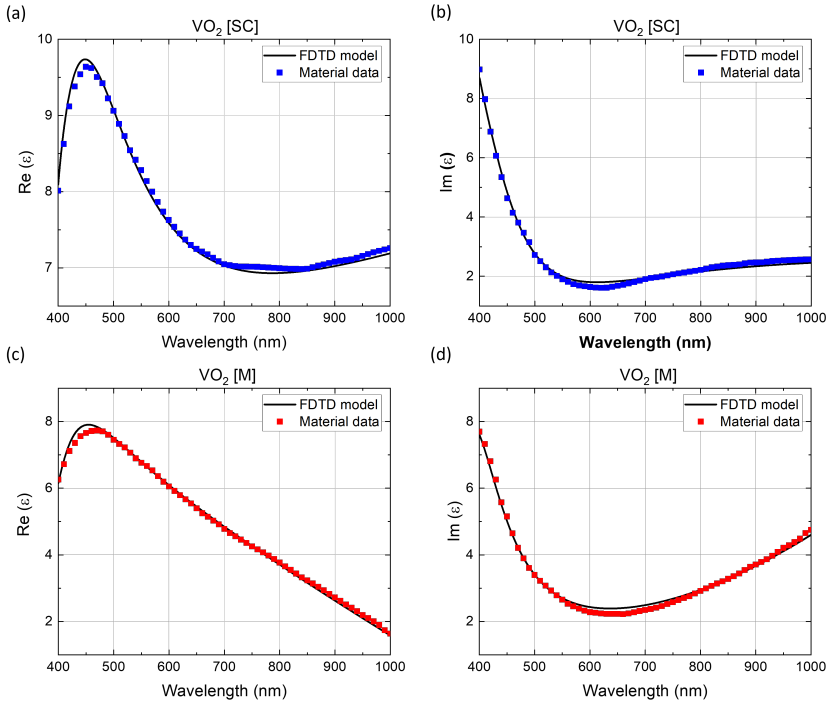

Figure 3.9: (a) Real component of the dielectric permittivity VO_2 material data and FDTD fit for VO_2 in semiconducting phase. (b) Imaginary component of the dielectric permittivity VO_2 material data and FDTD fit for VO_2 in semiconducting phase (c) Real component of the dielectric permittivity VO_2 material data and FDTD fit for VO_2 in metallic phase. (d) Imaginary component of the dielectric permittivity VO_2 material data and FDTD fit for VO_2 in metallic phase

to convert the reflectance spectra to a corresponding standard RGB value colour. This is done as tunable structural colour has applications in display technology.

To determine the colorimetric characteristics of a reflecting material, the material must be irradiated by a source. A spectral power density S(λ) function is used to emulate theoretical source called illuminant. To represent average daylight illumination, CIE standard illuminant D65 is used.[107] This illuminant has a correlated colour temperature of 6500 K. To determine the x chromaticity coordinate on the CIE 1931 chromaticity diagram the following equation is used

$$x_D = \frac{-4.6070 \times 10^9}{(T_{cp})^3} + \frac{2.9678 \times 10^6}{(T_{cp})^2} + \frac{0.09911 \times 10^3}{(T_{cp})} + 0.244063 \qquad (3.10.1)$$

where T_{cp} is the correlated colour temperature of the phase of daylight. As the standard D65 illuminant $T_{cp} = 6500K$, x^D has a value of 0.3127.

The corresponding y_D can then be calculated using the following equation

$$y_D = -3.000x_D^2 + 2.870x_D - 0.275 \tag{3.10.2}$$

giving $y_D = 0.329$ for the standard illuminant.

The spectral power density (SPD) of a daylight sample can be approximated by using a linear combination of three fixed SPDs; the mean S_0 and the first two characteristic vectors S_1 and S_2 corresponding to changes in colour temperature due to presence or absence of clouds or direct sunlight and variation caused by the presence of water vapour respectively. The characteristic vectors S_0, S_1 and S_2 are shown in Fig. 3.10(a). The linear combination of these vectors is given by the following equation

$$S(\lambda) = S_0(\lambda) + M1S_1(\lambda) + S_2(\lambda) \tag{3.10.3}$$

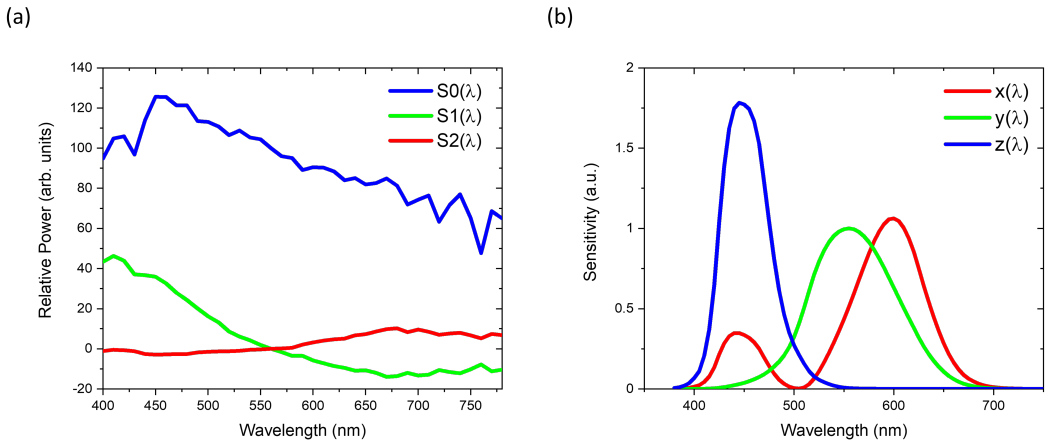

Figure 3.10: (a) Characteristic vectors $S_0(\lambda)$(blue), $S_1(\lambda)$(green), $S_2(\lambda)$(red) used for the calculation of S(λ) (b) CIE 2° observer colour matching functions or the numerical description of the average human's chromatic response.

Based on the x_D and y_D chromaticity coordinates for the standard illuminant D65, M1 and M2 factors can be calculated as follow

$$M_1 = \frac{1.3515 - 1.7703x_D + 5.9114y_D}{0.0241 + 0.2562x_D - 0.7341y_D} \tag{3.10.4}$$

$$M_2 = \frac{0.0300 - 31.4424x_D + 30.0717y_D}{0.0241 + 0.2562x_D - 0.7341y_D} \tag{3.10.5}$$

with M1 and M2 having final values of -0.29707 and -0.68797, respectively.

With the calculated spectral power distribution of the D65 illuminant, the CIE XYZ values can be calculated by weighting the reflectance spectra against the CIE 2° standard observer function[108] x(λ),y(λ) and z(λ) given in Fig. 3.10(b). These functions determine colour chromaticity and luminosity by representing the response of the cones receptors within the eye. The X, Y and Z values are calculated from the following

$$X = \frac{100}{K}\int_{400}^{780} R(\lambda)x(\lambda)S(\lambda)d\lambda \tag{3.10.6}$$

$$Y = \frac{100}{K}\int_{400}^{780} R(\lambda)y(\lambda)S(\lambda)d\lambda \tag{3.10.7}$$

$$Z = \frac{100}{K}\int_{400}^{780} R(\lambda)z(\lambda)S(\lambda)d\lambda \tag{3.10.8}$$

where K is a normalising function based on the luminosity of a perfect reflectance diffuser and is given as

$$K = \int_{400}^{780} y(\lambda)S(\lambda)d\lambda \tag{3.10.9}$$

therefore $\frac{100}{K} = 0.009464$

These calculated XYZ primary values can be mapped onto the CIE 1931 chromaticity diagram by the functions

$$x = \frac{X}{X + Y + Z} \tag{3.10.10}$$

$$y = \frac{Y}{X + Y + Z} \tag{3.10.11}$$

To convert the XYZ values to RGB, the XYZ values must be expressed as decimals which is done by dividing each value by 100, i.e. $X_d = X/100$ etc.

The conversion to RGB values requires a matrix operation in the form

$$\begin{bmatrix} R \\ G \\ B \end{bmatrix} = \begin{bmatrix} 3.2406 & -1.5371 & -0.4985 \\ -0.9693 & 1.8706 & 0.0416 \\ 0.0556 & -0.2040 & 1.0572 \end{bmatrix} \begin{bmatrix} X \\ Y \\ Z \end{bmatrix} \tag{3.10.12}$$

This outputs RGB values with values between 0 and 1, which are then gamma corrected, with any values below 0 set to 0.

A gamma correction is applied to the RGB values to account for the non-linear response of photoreceptors in the human eye.[109] The gamma correction function, as applied to the linear RGB values can be described by the following

$$R_{sRGB} \begin{cases} 12.92 R_{linear} & R_{linear} \leq 0.0031308 \\ (1.055 R_{linear}^{\frac{1}{2.4}}) - 0.055 & R_{linear} > 0.0031308 \end{cases} \tag{3.10.13}$$

$$G_{sRGB} \begin{cases} 12.92 G_{linear} & G_{linear} \leq 0.0031308 \\ (1.055 G_{linear}^{\frac{1}{2.4}}) - 0.055 & G_{linear} > 0.0031308 \end{cases} \tag{3.10.14}$$

$$B_{sRGB} \begin{cases} 12.92 B_{linear} & B_{linear} \leq 0.0031308 \\ (1.055 B_{linear}^{\frac{1}{2.4}}) - 0.055 & B_{linear} > 0.0031308 \end{cases} \tag{3.10.15}$$

In this way, the reflected colour of hybrid nanostructures for various structural param-

eters and the difference in colour for these structures when VO_2 is in semiconducting and metallic phase can be demonstrated.

3.11 Sample Fabrication

3.11.1 Thin Film Growth

In addition to the well known vanadium oxide phases VO_2, V_2O_3 and V_2O_5 there are a multitude of vanadium oxide phases that exist between these principal phases generally following the formula V_nO_{2n+1} or V_nO_{2n-1} (Magnéli phases). Due to the number of distinct phases gaining precise control of the oxide phase formed during thin film growth isn't trivial. During the last few decades numerous methods have been employed to grow thin films of purely the VO_2 phase. The most commonly used methods include metal-organic chemical vapour deposition (MOCVD),[110] sputtering,[111,112] sol-gel[113] and pulsed laser deposition (PLD).[114,115]

The VO_2 thin films presented throughout this work were grown on c-plane sapphire (c - Al_2O_3 {0001}) by two physical vapour deposition techniques, reactive sputtering and pulsed laser deposition. There are four commonly used face terminations of sapphire as substrates, namely c-plane (0006), r-plane ($10\bar{1}1$), m-plane ($1\bar{1}00$) and a-plane ($11\bar{2}0$). While r-plane, c-plane and m-plane sapphire have been used for VO_2 growth, c-plane Al_2O_3 was selected as a suitable substrate. Despite its hexagonal structure it offers a low lattice mismatch with VO_2. The lattice parameters of Al_2O_3 are given as follows a = b = 4.761Å, c = 12.994Å, $\alpha = \beta = 90.0°$, $\gamma = 120 = 120.0°$.[116] This gives lattice mismatch of $< 5\%$ between the rutile metallic VO_2 phase and the Al_2O_3 substrate facilitating epitaxial growth as well as minimising strain effects which can have significant impact on the temperature, magnitude and hysteresis of the VO_2 phase transition. Al_2O_3 is an insulator with a band gap of 9 eV at room temperature.[117] This facilitates testing grown vanadium oxide samples for continuous film growth as in cases where there are discontinuities in the film resistance, measurements across Al_2O_3 are outside of the range of a digital multimeter.

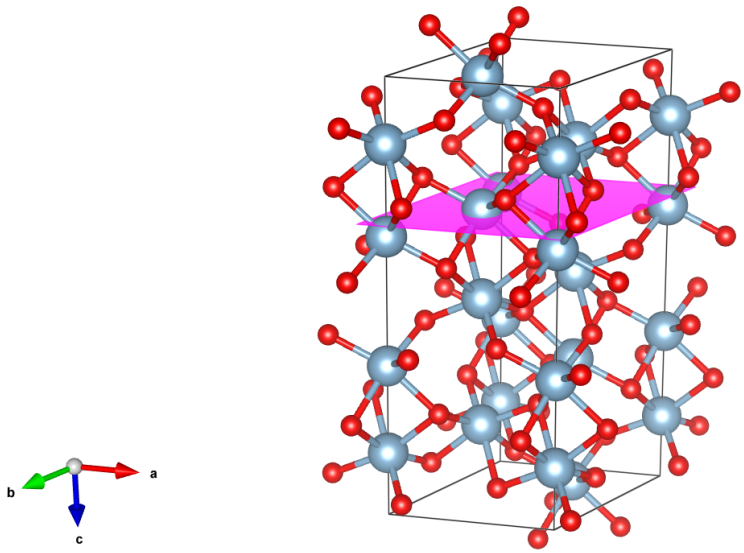

Figure 3.11: Atomic structure of hexagonal Al_2O_3.[116] Blue spheres represent the Al^{3+} and the red spheres represent the O^{2-} atoms. The pink plane represents the [001] atomic plane.

Pulsed Laser Deposition (PLD)

Pulsed laser deposition (PLD) is a deposition method that is relatively simple in its application, though the kinetics involved in the ablation process can be complex. The method employs a high powered pulsed laser in a high vacuum environment to ablate a target consisting of the material to be deposited. Material ablated from the target surface is deposited on a heated substrate through a highly directed plasma plume. Through repetition of laser shots there is an accumulation of matter on the substrate surface driving the formation of a thin film. From the microstructure of the VO_2 thin films grown, the growth is determined to grow in a Volmer-Weber (island growth mode) or a Stranski-Krastanov mode (hybrid 2D-3D mode). Growth mode is determined by the relative surface energy and lattice match between thin film and substrate. From literature the surface energy of VO_2 (011) is reported to be 0.29 J/m^2.[118]The surface energy of c-Al_2O_3 is 1.85 J/m^2,[119] lower than energies for the other Al_2O_3 planes. While often in PLD the target contains the same stochiometry as the intended film, for the preparation of VO_2 a pure vanadium target was used. This target was pressed and sintered from vanadium powder (-100 mesh, 99.9% trace metal basis, Sigma Aldrich).

PLD can be performed under high vacuum or in cases where oxide growth is required, a controllable oxygen environment. The configuration used for the fabrication of the thin films used throughout this work is show in Fig. 3.12.

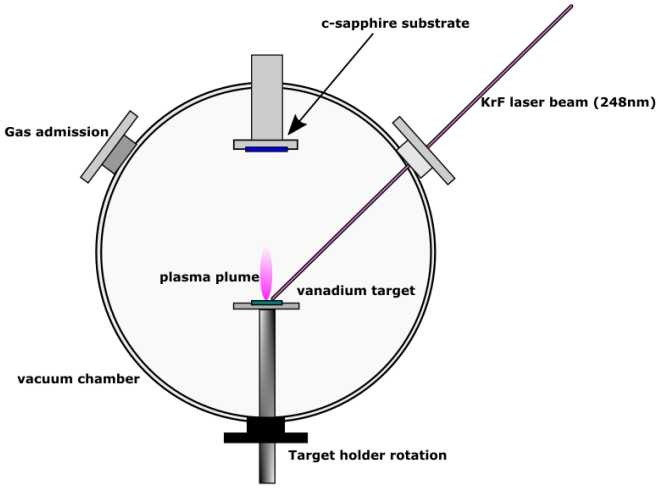

Figure 3.12: Schematic of setup used for VO_2 thin film growth.

For the growth of VO_2 thin films a focused KrF pulsed excimer laser (248 nm (5eV) , 10Hz repetition rate) is incident onto a vanadium target in O_2 partial pressure of between 15 - 20 μbar. A KrF laser is used as short wavelength photons are strongly absorbed by the target and have sufficient energy to induce photochemical reactions and ablate the material target. Laser power was controlled through tuning of the high voltage required for laser pulse generation and an attenuator placed in the path of the laser. The attenuator consists of an enclosed prism with an adjustable angle to reduce laser power. Laser spot size was determined by placing a metal razor in the vacuum chamber and measuring the size of the area ablated by the laser. A power meter placed within the vacuum chamber was used to determine laser power at each attenuator angle. Coupled with the measured spot size of 0.016 cm^2 values for the laser fluence was calculated. Frequent monitoring of the laser fluence was vital for the production of high quality VO_2 thin films, as fluence values lower than $1.5 Jcm^{-1}$ proved too low to produce an adequate plasma plume required for material deposition. A pre-ablation step is taken before each deposition to remove any oxide layers formed on the surface of the vanadium target.

The target-substrate distance was maintained at 7 cm with substrate temperatures of 550 - 600 $^{\circ}C$ producing the highest quality films. The deposition rate was $\sim$ 1.05 nm per minute allowing film thicknesses to be controlled purely by deposition time. No post annealing step was required to achieve VO_2 films demonstrating strong switching properties near the critical temperature of 68 $^{\circ}C$.

RF Sputtering

In addition to PLD, magnetron sputtering was also employed as a physical deposition technique to grow VO_2 thin films.

The principle behind sputtering is as follows: A sputtering target consisting of the material to be deposited is bombarded with highly energetic ions of an inert gas. For the growth of VO_2 thin films a reactive sputtering method was utilised meaning, similar to the PLD method, a pure vanadium target was used in an oxygen environment for precise control of the vanadium oxide phase grown. Argon was used in the system as the sputtering gas. The forceful collision of energetic ions causes the target metal atoms to be ejected from the target and directed towards a substrate placed a distance from the target. The substrate was heated to temperatures around 550$^{\circ}C$ to promote adhesion of the ejected material to the Al_2O_3 substrate. The substrate holder is rotated during the sputtering process to ensure uniformity in the VO_2 thin film growth. Within the sputtering system a magnetron is utilised creating lines of magnetic flux that run parallel to the surface of the target. This allows confinement of charged plasma particles close to the target surface by the strong electric and magnetic fields. This provides additional ionizing collisions to occur near the target surface in effect enhancing ion bombardment without an increase in operating pressure. This in turn leads to a higher sputtering rate and therefore an increased deposition rate. A simplified schematic of the sputtering chamber is provided in Fig. 3.13.

Sputtering of VO_2 thin films was achieved using the Trifolium Dubium (TD) (Fig. 3.14 Platform, a multi-technique cluster tool, located in a class 10000 cleanroom.

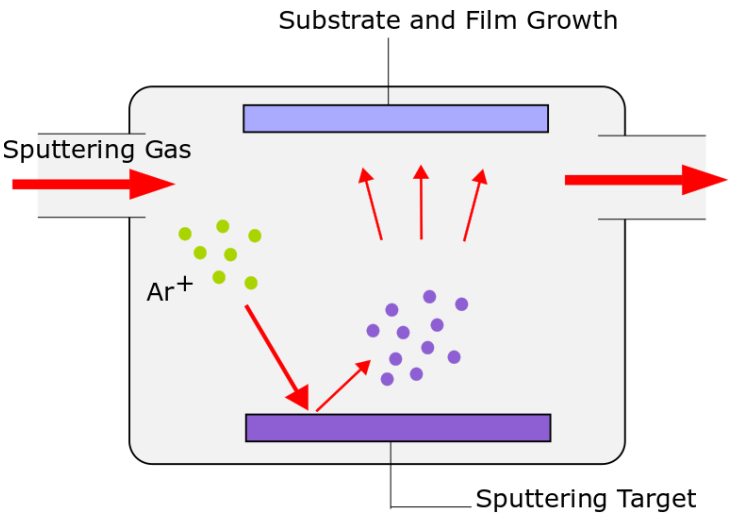

Figure 3.13: Simplified schematic of sputtering setup used for VO_2 thin film growth.

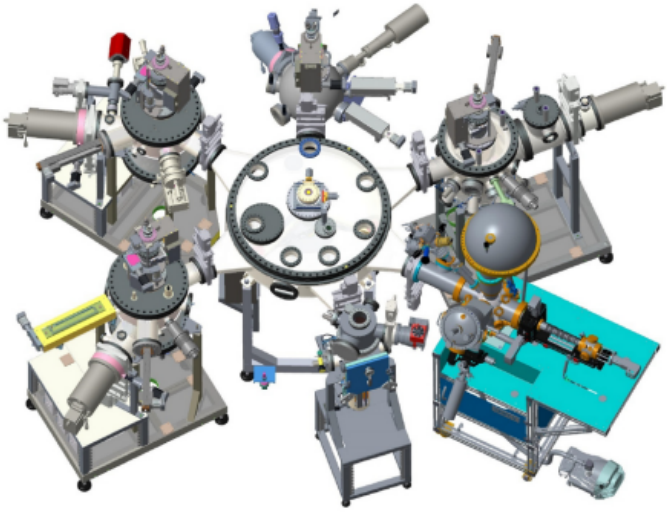

Figure 3.14: Schematic of Trifolium Dubium (TD) platform

To grow thin film VO_2, 10 mm x 10 mm double side polished c-plane Al_2O_3 substrates were first loaded into Inconel carriers and blown with a nitrogen gun to remove surface particles. After the samples are loaded into the load-lock chamber an in-built heater system allows substrates to be baked out at 200 $°C$, reducing water vapour introduced to the system. The substrate is then transferred to Sputter chamber 2 (used for reactive sputtering) containing six 2" MEIVAC MAK2 magnetrons with adjustable angles to increase sputter uniformity. For VO_2 film growth a substrate temperature of 550 $°C$ was used. The RF magnetron power was set to 200 W and the Load and Tune capacitors positions manually tuned to maximize forward power and minimize reflected power to

the magnetrons. A pre-sputter step was done before each deposition to remove any oxide layer formed on top of the vanadium target to ensure the VO_2 phase is grown in each deposition. To ensure film uniformity the substrate holder is rotated at 1 Hz. For a magnetron power of 200 W a deposition rate of $\sim$ 0.106 nm/s was observed. The VO_2 phase was successfully grown with a 20:1.85 $Ar : O_2$ ratio. These growth parameters are summarised in Table. 3.2.

Temperature	550°C
RF power	200 W
Deposition Rate	0.106 nm/s
Ar : O_2	20 : 1.85

Table 3.2: Reactive Sputtering Parameters for VO_2 thin film growth.

3.11.2 Electron Beam Lithography (EBL)

The fabrication of metallic nanostructures on thin film VO_2 was achieved through electron beam lithography (EBL). This method employs electrons in high vacuum accelerated at high voltage (15kV). EBL allows high resolution periodic structures to be made with precise dimensional control as the electron wavelength, at high voltages, is significantly smaller than the target feature sizes. The degree of controllability makes EBL an invaluable technique for the fabrication of the plasmonic nanoantenna and metallic contacts used in research presented in this work.

The basic principle behind EBL is that a positive tone resist on the sample is exposed to an electron beam allowing for removal of the exposed area in a developer material. Evaporation of metal onto the thin film fills these gaps with a lift off step to remove excess metal leaving only the patterned structures.

In order to fabricate well-formed plasmonic nanoparticles with the correct dimensions and periodicity, precise exposure parameters were selected through dose tests.

To fabricate high quality nanoparticles, the resist material (PMMA 950K A3) is spin coated (750 RPM for 5s, 2000 RPM for 60s) onto the surface of the thin film and prebaked at 180° for 90s. After PMMA baking, a thin removable layer of Espacer is

applied to the sample. The Espacer layer is applied by spin coating with the same parameters used for the PMMA layer. Espacer is highly conductive, allowing for the dissipation of electrons. This prevents sample charging and therefore drift induced positional errors during the patterning process. A small scratch in the PMMA is made with tweezers near the sample corner to allow ease of focusing before patterning. Selective exposure to an electron beam (Zeiss SUPRA 40 - Scanning Electron Microscope (SEM)) allows nanoarrays or single nanoparticles to be patterned onto the PMMA, as the exposed long chain PMMA molecules are broken into short chained molecules. Use of the 7 μm lens with a beam current of approximately 13.8 pA allowed the patterning of high quality nanostructures on the sample. Raith Elphy Quantum software is used for CAD layout, control of exposure parameters, automation and precision control of the microscope.

The exposed short chained molecules are removed in a development step. The samples are first washed in H_2O for 30 seconds to remove the Espacer layer. After drying using a nitrogen gun, the samples are exposed to the developer solution methyl-isobutyl ketone (MIBK) and isopropyl alcohol (IPA) in a 1:3 ratio (MIBK:IPA) for 45 seconds followed directly by a 30 second IPA stopper rinse. A metallic layer was deposited by an electron beam evaporation system (Temescal FC-2000). A thin titanium (Ti) adhesion layer (1-5 nm) is used with a noble metal layer of between 35 - 40 nm.

Excess PMMA and metal was removed by immersion of the sample in acetone heated to 40°C in a standard lift-off process.

3.12 Conclusion

In conclusion, this chapter introduces the simulation, fabrication and characterisation techniques necessary for the hybrid nanostructures presented in this work. FDTD simulation methods are described with specific configurations for simulations given later in their prospective sections. FDTD is the primary simulation tool used for all structures presented in **Chapter 4,5 and 6** as the optical response and the near field enhance-

ment can be examined using Lumerical commercial simulation software. The method of converting spectra to xyY colour space is described with the colour response of various thin film VO_2 samples shown in **Chapter 4** and **Chapter 5** An overview of both growth techniques used for VO_2 thin film fabrication is made, with the optimal parameters for both growth methods is given. An overview of the various characterisation techniques, including Raman Spectroscopy, XRD and XPS, used to confirm the phase of thin film samples, is given with additional data on sample characterisation given in **Chapter 4**. The principles of SEM and EBL are discussed as they pertain to the fabrication of nanoparticles on the fabricated VO_2 thin films. Finally, the techniques used to acquire optical spectra of fabricated nanoparticles on the VO_2 thin film samples is given.

4 VO_2 thin films

4.1 Summary

As the basis for dynamic tuning of hybrid nanostructures, it is important to consider how the optical properties of planar VO_2 films are altered between the two material phases as well as the how the application of different stimuli used to actuate the transition impacts the characteristic phase change. In this chapter, the optical properties of thin film VO_2, with thicknesses of up to 200 nm, are simulated using VO_2 fits generated from ellipsometry data acquired from a fabricated VO_2 thin film sample. The reflectance, transmittance and absorptance of VO_2 on Al_2O_3 is calculated from FDTD simulation with the resulting spectra converted to RGB values to determine the colour change. Additionally, the impact of a metallic backreflecting layer and a hybrid VO_2 - Au planar film are considered. As VO_2 films play a significant role in the plasmonic tuning and photoluminescence modification discussed in future chapters, this chapter discusses various aspects of the thin film characterisation including phase, thickness and roughness characterisation as these film qualities play a significant role in the degree of dynamic modification in a real device. Lastly the phase change characteristic of fabricated thin films is explored though different phase change actuation methods including thermal and electrical.

4.2 Planar VO_2

In this section, the simulated optical properties of thin film VO_2 are examined in the wavelength range 400 - 1000 nm in the low temperature semiconducting phase and the high temperature metallic phase to determine their optical response before the addition of plasmonic structures to the system. The commercial FDTD solver Lumerical is used to determine the reflectance, transmittance and absorptance properties of VO_2 thin film layers of varying thickness on an Al_2O_3 substrate. It's important to analyse the impact of film thickness on the optical properties of the VO_2 film and the change in optical properties upon the VO_2 phase change in order to optimise the system for various applications in optoelectronics. Furthermore, within the VO_2 research space there isn't extensive data on the impact of thickness on the optical response of VO_2 films. The complex refractive index for VO_2 used in all simulations is as described in **Chapter 3**.

For FDTD simulations on planar thin film structures, the simulation space spans 246 nm in the x and y direction and 1800 nm in the z direction with periodic boundary conditions along the x and y directions and PML boundary above and below the planar structure. As shown in the schematic in Fig. 4.1, a plane wave source is placed at the plane z = 500 nm above the VO_2 surface with a Bloch/periodic wave injected in the negative z-direction (indicated by the purple arrow in the schematic), normal to the VO_2 surface. As the wave is normally incident on a planar structure, all wave polarizations are equivalent. A polarization angle of 0 (along the x axis) is selected for all VO_2 planar simulations. For planar VO_2 simulations, the wavelength start and stop are set at 400 and 1000 nm, respectively, to cover the response in the visible and NIR. A 2D Z-normal DFT (discrete Fourier transform) monitor, acting as a reflection monitor, is placed at the plane z = 700 nm above the plane wave injection. Similarly, a DFT monitor is placed at the plane z = -600, below the VO_2 surface, which acts a transmission monitor. As the plane wave is injected in the negative z-direction, power radiated back through the reflection monitor is treated as positive and power

transmitted through the transmission monitor is treated as negative. When considering the transmittance through a given structure the absolute value of the monitor data is taken when plotting spectra. Each monitor uses the same wavelength limits as the plane wave source and uses a wavelength spacing with 601 frequency points so that data is recorded at 1 nm intervals.

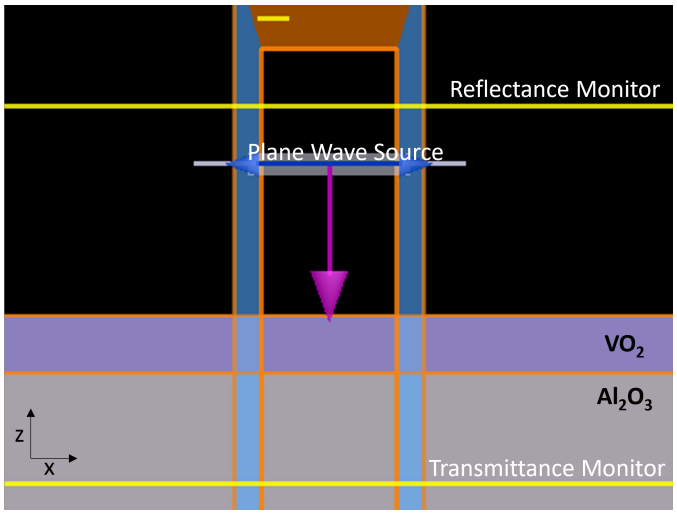

Figure 4.1: Schematic of FDTD simulation space for planar VO_2 simulations.

For the presented VO_2 spectra, optical properties were considered at 5 nm intervals up to a thickness of 200 nm. These thin films layers are simulated on an Al_2O_3 substrate to match fabricated VO_2 samples. As discussed in the previous chapter, $c - Al_2O_3$ is selected due to the lattice match with VO_2 facilitating growth of the VO_2 oxide phase.

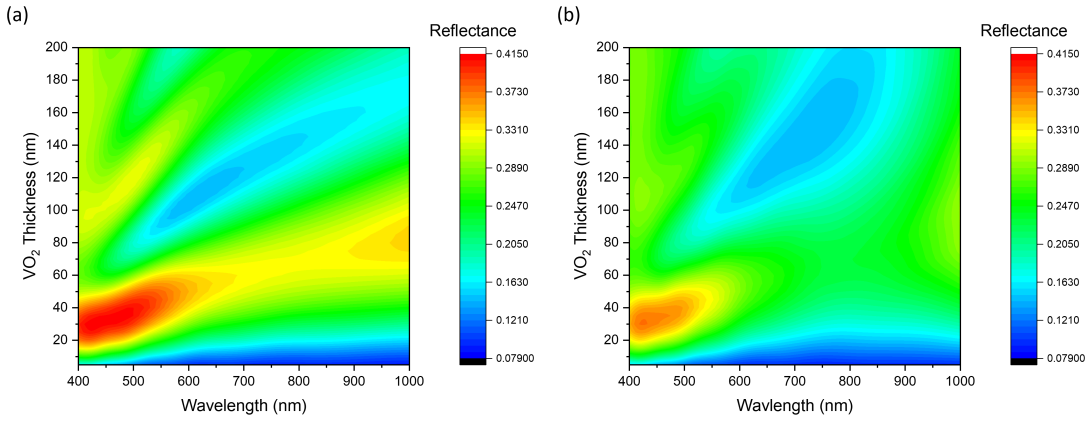

Figure 4.2: VO_2 reflectance in (a) semiconducting phase and (b) metallic phase

The reflectance of the planar VO_2 film as a function of wavelength and thickness in semiconducting and metallic phase is presented in Fig. 4.2. In general, the reflectance of a planar VO_2 film is shown to decrease when the film transitions from the semiconducting phase to the metallic phase. In the semiconducting phase, the reflectance is at a maximum of approximately 0.4 at $\sim$ 450 nm for a film thickness of 30 - 35 nm. Above 50 nm, a position of minimum reflectance arises at 440 nm which redshifts with increasing thickness as shown in the light blue region in Fig. 4.2 (a). The redshifting oscillatory pattern seen in the reflectance spectrum with increased thickness is due to a thin film effect caused by interference effects within the thin VO_2 layers.

In the metallic phase, the reflectance is at a maximum of approximately 0.37 at 425 nm for a film thickness of 30 - 35 nm. Similar to the semiconducting phase, a position of minimum reflectance arises at film thicknesses above 50 nm, which redshifts with increasing VO_2 thickness. However, it can be clearly seen from Fig. 4.2 (b) that the redshift of the minimum value is significantly reduced in the metallic phase when compared to the shift seen in semiconducting phase.

When the reflectance in both phases is considered, for the VO_2 films of thicknesses up to 50 nm, there is a drop in reflectance across the visible spectrum which increases to a maximum of a 28.8% change in reflectance at approximately 760 nm. In the regime above 50 nm, a region where there is an increase in reflectance in metallic phase emerges. This region redshifts with increasing VO_2 film thickness. The raw reflectance change (ΔR), i.e. the difference between the reflectance in the metallic phase and the semiconducting phase ($R_M - R_{SC}$), and the percentage change ($\Delta R\%$), i.e. the raw reflectance change divided by the reflectance in the semiconducting phase ($\Delta R/R_{SC}$), are demonstrated in Fig. 4.3 with the area of increased reflectance highlighted. Additionally, the change in reflectance in the region around 760 nm reaches a maximum between 50 - 70 nm. A second region of maximum ΔR occurs when the VO_2 film thickness is $\geq$ 140 nm. However, despite large values for ΔR seen for thicker VO_2, the damping effect of thicker VO_2 on plasmon resonance features limits the usefulness of these large ΔR values for many optoelectronic applications.

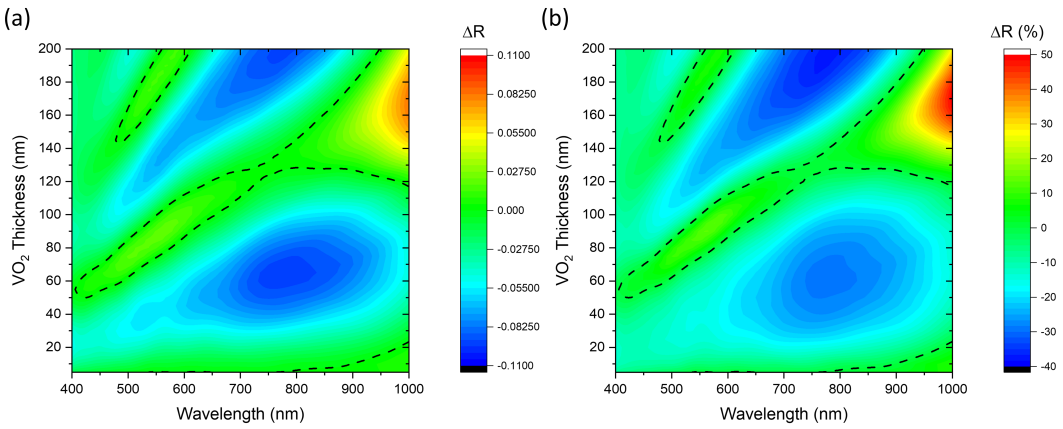

Figure 4.3: (a) VO_2 thin film $\Delta R(R_M - R_{SC})$ for varying film thickness. (b) VO_2 thin film $\Delta R\%((R_M - R_{SC})/R_{SC})$ for varying film thickness. In both graphs the black dashed line indicates the contour where $\Delta R = 0$, therefore the bounded area represents increased reflectance in the metallic phase.

Due to the distinct change in the reflectance spectra as a function of VO_2 thickness, there is a large change in the generated CIE colour as indicated in Fig. 4.4(a). The position of minimum reflectance within the visible spectrum oscillates with thin film thickness resulting in the oscillation in the colour as the CIE colour points move around the central point in the CIE colour map (Fig. 4.4(b)). It is noted that in the metallic phase, the points on the CIE colour map are closer to the central point resulting in less difference in the colour as a function of thickness.

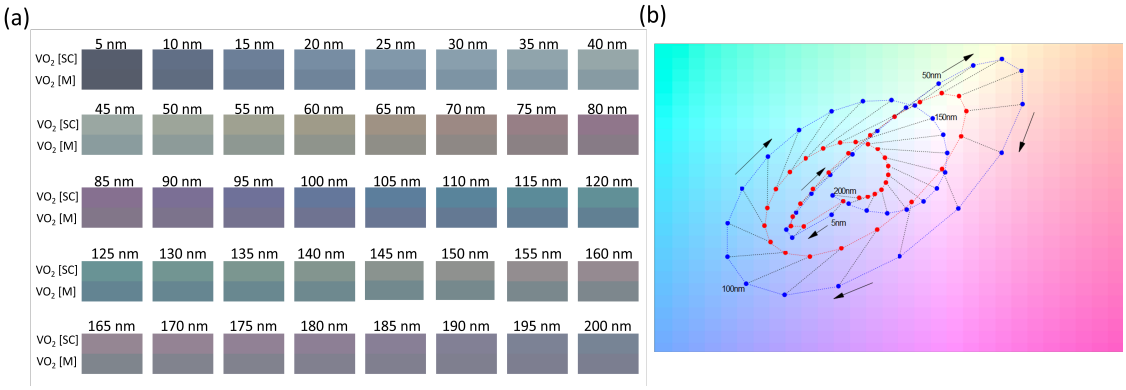

Figure 4.4: (a) Reflectance colour for VO_2 of thickness between 5 - 200 nm in 5 nm steps. For each thickness the CIE colour in the semiconducting phase is on top and the CIE colour in the metallic phase is on the bottom. (b) Partial CIE colour map indicating the reflected colour in semiconducting phase (blue) and metallic phase (red). Arrows indicate direction of increasing VO_2 thickness and black lines connect points of equal VO_2 thickness.

The transmittance spectra of the planar VO_2 film in both material phases (Fig. 4.5) indicate a drop in transmittance from the semiconducting phase to the metallic phase across all VO_2 thicknesses up to 200 nm. As expected the transmittance decreases with increasing VO_2 thickness. From Fig. 4.5, there is a sharp decrease in the transmittance with increasing thickness up to $\sim$ 50 nm for VO_2 in both phases. The transmittance drop from $\sim$ 0.86 for a 5 nm thick film to $\sim$ 0.46 for a 50 nm film in the spectral region around 600 nm. However, in the visible spectral region, there is minimal change in the transmittance with a modulation of < 0.05 as VO_2 transition from semiconducting to metallic phase. For a 50 nm VO_2 film a raw change in transmittance of approximately 0.05 can be seen. This observed drop in transmittance increase to 0.1 at $\sim 80nm$ within the visible spectral region. When the spectral region up to 1 μm is considered a decrease in transmittance up to 0.25 is observed with for $\sim$ 150 nm VO_2 thin films.

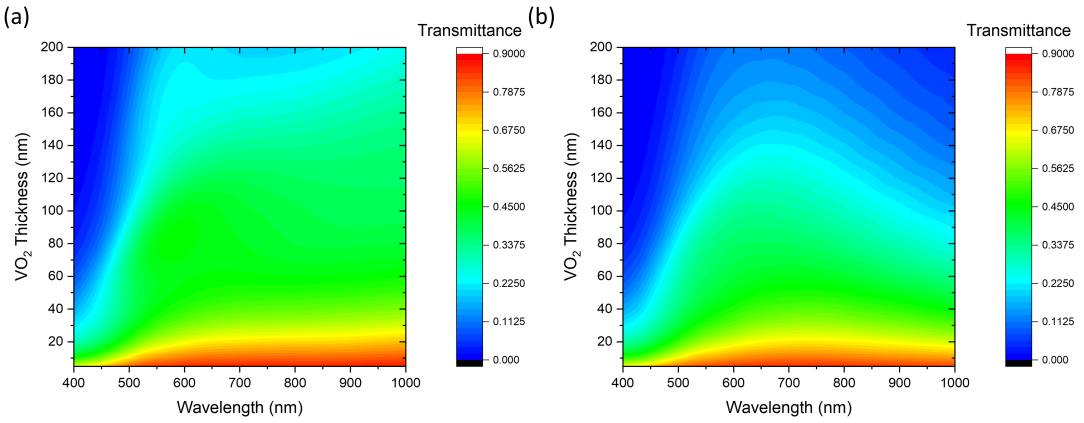

Figure 4.5: VO_2 transmittance in (a) semiconducting phase and (b) metallic phase

The change in transmittance between the two VO_2 phases is more clearly demonstrated in Fig. 4.6 (a) and (b) which show the raw transmittance change (ΔT) i.e the difference between the transmittance in the metallic phase and the semiconducting phase ($T_M - T_{SC}$) and the percentage change ($\Delta T\%$) i.e the raw transmittance change divided by the transmittance in the semiconducting phase ($\Delta T/T_{SC}$) respectively. From these figures it can be clearly seen that the transmittance change is negligible for thin films under 60 nm, and is $\sim$ 0.1 for the majority of thicknesses and wavelengths. As the transmittance for a 150 - 200 nm thick VO_2 layer is on the order of 0.2 a transmittance modulation

of 0.1 accounts for an 50% decrease in transmittance as shown in Fig 4.6(b).

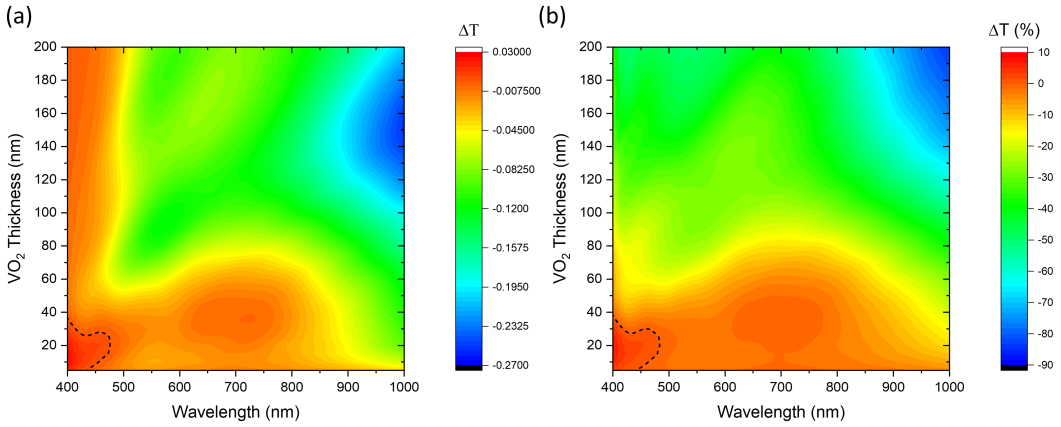

Figure 4.6: (a)VO_2 thin film $\Delta T(T_M - T_{SC})$ for varying film thickness. (b) VO_2 thin film $\Delta T\%((T_M - T_{SC})/T_{SC})$ for varying film thickness. In both graphs the black dashed line indicates the contour where $\Delta T = 0$, therefore the small bounded area in the bottom left represents a region of increased transmittance in the metallic phase.

In transmission, VO_2 thin films displays less contrast between colours at thickness below 50 nm due to the negligible difference in transmittance at visible wavelengths. While this difference becomes more pronounced at larger film thicknesses, the oscillation in the displayed colour, seen in the reflectance case, isn't seen. The points on the CIE colour map move away from the central point towards the edge of the gamut with increasing thickness as demonstrated in Fig. 4.7(b).

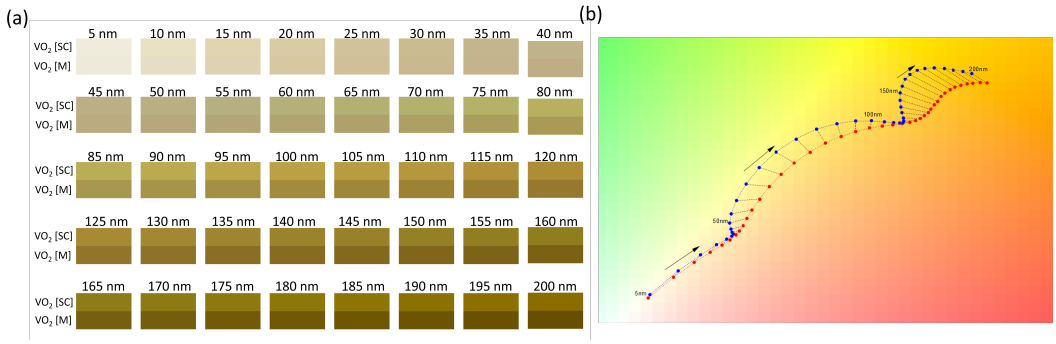

Figure 4.7: (a) Transmitted colour for VO_2 of thickness between 5 - 200 nm in 5 nm steps. For each thickness the CIE colour in the semiconducting phase is on top and the CIE colour in the metallic phase is on the bottom (b) Partial CIE colour map indicating the transmitted colour in semiconducting phase (blue) and metallic phase (red). Arrows indicate direction of increasing VO_2 thickness and black lines connect points of equal VO_2 thickness.

The absorptance spectra of planar VO_2 films in both material phases (Fig. 4.8) is calculated indirectly using the previously calculated values for the reflectance and transmittance of the VO_2 film using the formula

$$Absorptance = 1 - Reflectance - Transmittance \tag{4.2.1}$$

as the sum total of the VO_2 thin films reflectance, transmittance and absorptance must equal unity.

In both VO_2 phases, increasing the VO_2 film thickness results in an increased absorptance. In the semiconducting phase the thin film absorptance increases from ~ 0.1 at 5 nm to ~ 0.5 - 0.7 for the 200 nm thick film at wavelengths between 400 - 1000 nm. For a film in metallic phase, the thin film absorptance increases from ~ 0.1 to ~ 0.72 - 0.76 for the 200 nm thick film at wavelengths between 400 - 1000 nm.

When the raw change in absorptance (ΔA), i.e. the difference between the absorptance in the metallic phase and the semiconducting phase ($A_M - A_{SC}$)(Fig. 4.9(a)), is considered, it's seen that for thin films < 20 nm thick and near 400 nm there is a minimal increase in the absorptance. However, a ΔA of up to 0.23 is observed near 1000 nm for films with thicknesses between 80 - 140 nm. Despite the smaller change in absorp-

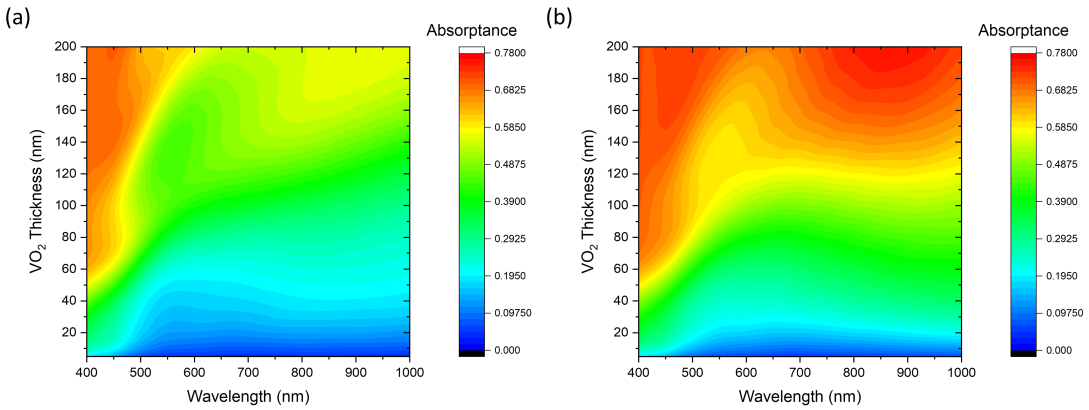

Figure 4.8: VO_2 absorptance in (a) semiconducting and (b) metallic phase

tance at lower wavelengths and thinner films, when the percentage change ($\Delta A\%$), i.e. the raw absorptance change divided by the absorptance in the semiconducting phase ($\Delta A/A_{SC}$), is considered, a significant modulation of the absorptance of $\sim 45\%$ can be seen.

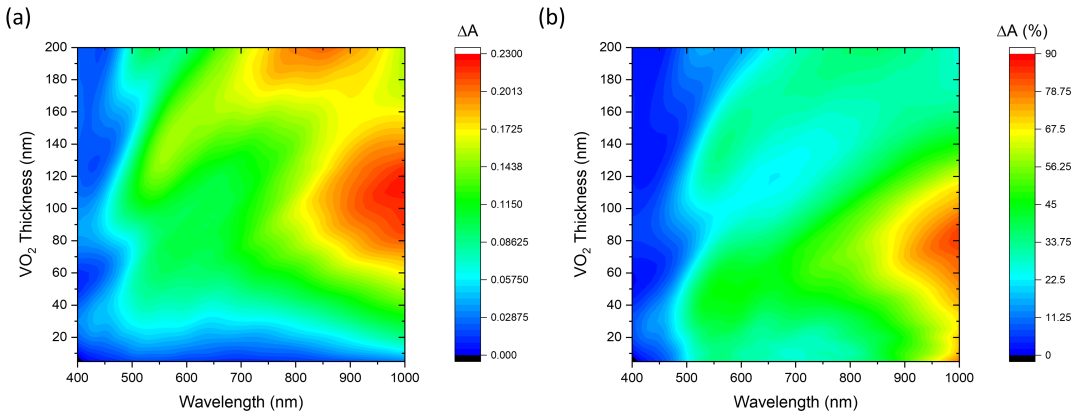

Figure 4.9: (a)VO_2 thin film $\Delta A(A_M - A_{SC})$ for varying film thickness. (b) VO_2 thin film $\Delta A\%((A_M - A_{SC})/A_{SC})$ for varying film thickness.

4.3 Planar VO_2 with back reflector

Next, the optical properties of a planar VO_2 film with varying thickness on an optically thick back reflecting metallic layer of Au was considered. The use of a metallic layer underneath the VO_2 film provides both high reflectance within the visible spectrum and as a bottom contact for electrical actuation of the VO_2 phase change. The FDTD simulation parameters are identical to the ones used in planar VO_2 simulations but with the addition of a 200 nm, optically thick Au metallic back reflecting layer.

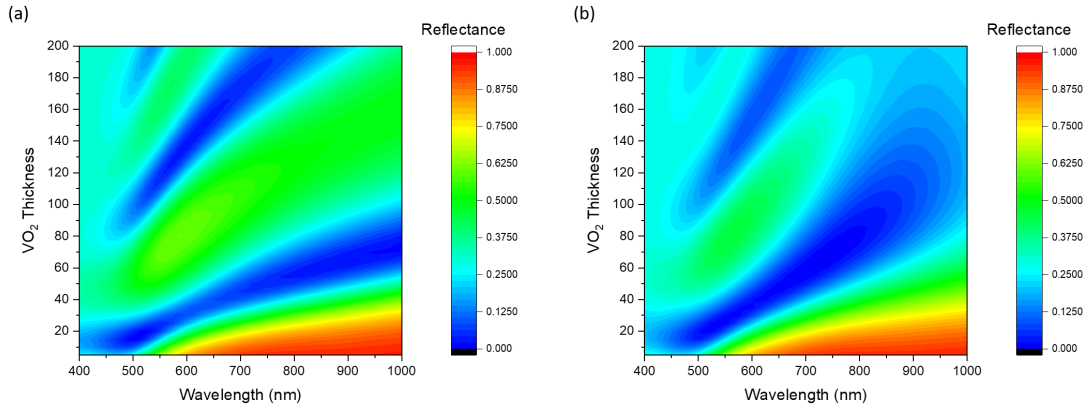

Figure 4.10: VO_2 reflectance on an optically thick Au back reflecting layer (200 nm) for varying VO_2 film thickness in (a) semiconducting phase and (b) metallic phase.

A back reflecting metallic layer introduces significant thin film interference effects due the reflection of incident light at the air - VO_2 interface and at the VO_2 - back reflecting metallic layer. As varying the thickness of the VO_2 layer changes the path length light travels within the VO_2 film, thickness dependent maximum and minimum reflectance values emerge. The magnitude of these minimum and maximum values decrease with VO_2 film thickness as VO_2 has a non-zero attenuation coefficient in both semiconducting and metallic phase.

Unlike the case with no back reflecting layer, the minimum values are significantly closer to 0 indicating regions where there is complete destructive interference as seen in the dark blue regions in Fig. 4.10 (a) and (b). As with the case with no backreflecting layer the positions of the minimum values redshift with increasing thickness in both VO_2 phases. For films with thickness < 20 nm the large reflectance from the Au backre-

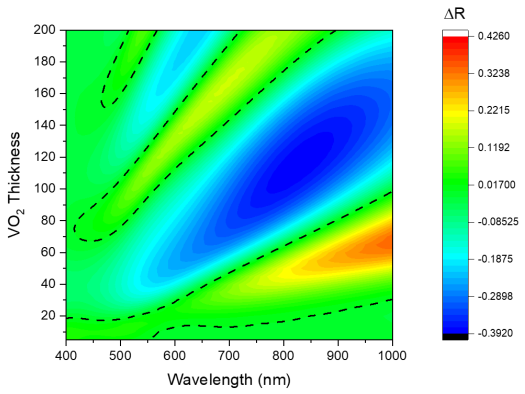

Figure 4.11: VO_2 thin film with Au back reflector ΔR ($R_M - R_{SC}$) for varying film thickness. The black dashed line indicates the contour where $\Delta R = 0$, therefore the bounded area represents increased reflectance in the metallic phase.

flecting layer dominates with almost all incident light reflected for VO_2 in both phases. However, for films $>$ 20 nm, a maximum reflectance of $\sim$ 0.75 emerges at 550 - 600 nm for films between 60 - 100 nm thick in semiconducting phase. A similar reflectance feature is seen for metallic phase VO_2, albeit with a decreased magnitude.

Fig. 4.11 depicts ΔR, i.e. the difference between the reflectance when the VO_2 film is in metallic phase and in semiconducting phase ($R_M - R_{SC}$). Like the Δ R case without the backreflecting layer, regions where Δ R is positive and negative emerge. In this case a gain in reflectance can be seen for thin film thicknesses $<$ 50 nm, a contrast to the planar VO_2 case where there is no reflectance gain for $<$ 50 nm films. Additionally, the increase in reflectance reaches up to 0.4 contrasting with maximum gains of 0.1 seen previously in Fig. 4.3

The reflectance spectra of the VO_2 with Au backreflecting layer with thicknesses up to 200 nm cover a significantly larger colour gamut due to the thin film effects induced by the backreflecting layer. A larger colour contrast is also seen for VO_2 in semiconducting and metallic phases at each thickness as demonstrated in Fig. 4.12.

As the back reflecting layer is optically thick, meaning that a negligible amount of incident light is transmitted ($<$ 0.02%) the absorptance of the VO_2 - Au thin film structure can be treated as Abs = 1 - R. Therefore, the absorptance spectra (Fig. 4.13) are an inverse of the reflectance spectra (Fig. 4.10) as regions of minimum reflectance

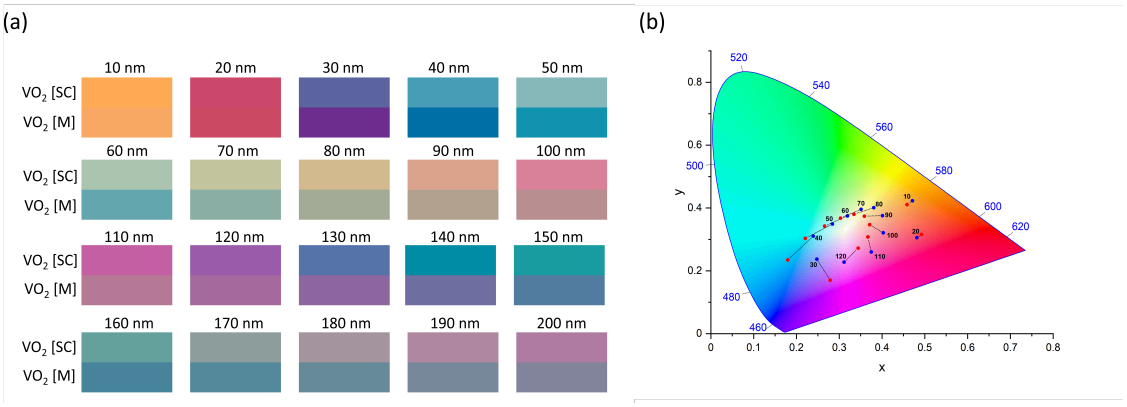

Figure 4.12: (a) Reflectance colour for VO_2 of thickness between 10 - 200 nm in 10 nm steps on a Au back reflecting layer. For each thickness the CIE colour in the semiconducting phase is on top and the CIE colour in the metallic phase is on the bottom (b) CIE 1931 colour map for VO_2 with thicknesses between 10 - 120 nm on an optically thick back reflecting Au layer. The blue and red points indicate CIE colour for VO_2 in semiconducting and metallic phase, respectively.

correspond to regions of maximum absorptance. As in the case of the reflectance, the VO_2 phase transition blueshifts the peak response. The magnitude of the peak shift is thickness dependent with an example given for the 30 nm, 50 nm and 70 nm case in the Fig. 4.13. For the 30 nm case a blueshift of 20 nm is observed. This shift increases to 85 nm and 205 nm for the 50 nm and 70 nm case, respectively. The absorptance of the VO_2 film with the Au backreflector show peak values > 0.99 indicating near perfect absorption.

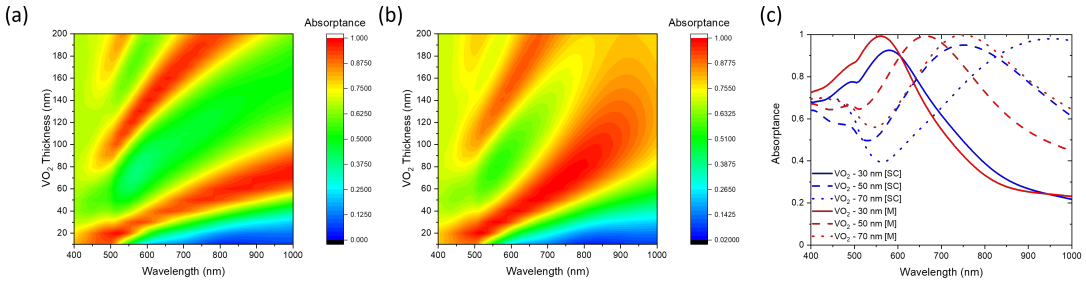

Figure 4.13: (a) VO_2 absorptance on an optically thick Au back reflecting layer (200 nm) for varying VO_2 film thickness in (a) semiconducting phase and (b) metallic phase (c) Absorptance spectra of 20 nm, 50 nm and 70 nm VO_2 film on 200 nm Au backreflecting layer, demonstrating blueshift in peak wavelength upon phase transition.

A hybrid VO_2 - Au planar thin film structure is also considered, consisting of planar VO_2 with a varying proportion of embedded planar Au. The simulation space consists of a 250 nm x 250 nm area with periodic boundary conditions. The reflectance of the VO_2 - Au film is considered for Au inclusions of equal length and width and thickness equal to the VO_2 film thickness, up to a thickness of 200 nm. The impact of the inclusions is considered at 25 nm intervals representing Au Volume fractions between 1 - 81%. A schematic of the VO_2 - embedded Au film is demonstrated in Fig. 4.14.

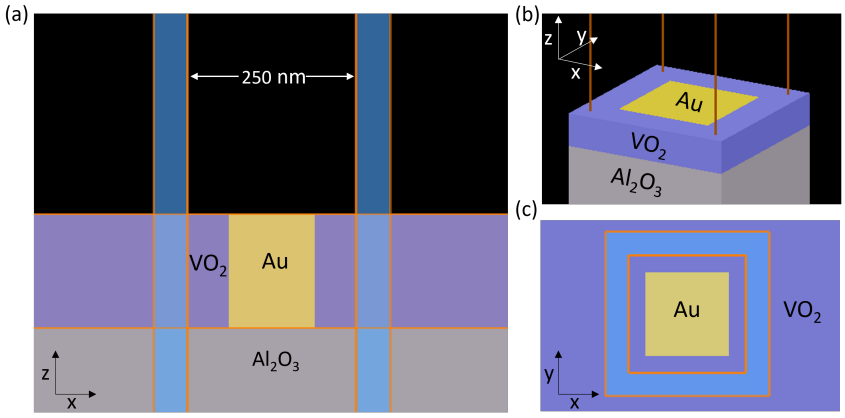

Figure 4.14: Schematic of VO_2 - Au planar films. (a) Cross-section of film demonstrating 250 nm simulation space in x-direction with periodic (blue) boundary conditions. Source is normally incident to the plane, in the -z direction (b) 3D perspective view of the planar structure (c) top-down XY view of the planar structure.

From Fig. 4.15 and Fig. 4.16 depicting the reflectance of the VO_2 - Au film with increasing Au volume fractions it can be seen that there is a significant impact of the reflectance profiles for both VO_2 phases and from Fig. 4.17, it can be seen that inclusion

of Au regions within a planar VO_2 thin film has a significant impact on ΔR and in particular the spectral position of regions where reflectance is increased for metallic phase VO_2. For the Au inclusion with side length 25 nm representing 1 % of the total volume of the periodic structure unit cell, the ΔR colour map is functionally identical to the case with no Au inclusions. However, for the 50 nm case, representing a 4 % volume Au inclusion, the ΔR colour map shows a distinct change from the 25 nm case. The 100 nm inclusion demonstrates the largest percentage ΔR of $\sim$ 60%, representing a 0.15 change in raw reflectance, in the wavelength range between 700 - 900 nm. Significant ΔR in the visible spectral region is observed for the 150 nm and 175 nm cases. In particular, for the 175 nm case, reflectance gains of up to 30 % are observed for film between 30 and 60 nm. The figure demonstrates that, through inclusions of differing amounts of metallic reflecting material, the planar thin film has a range of reflectance profiles that demonstrate large changes at different VO_2 thicknesses and wavelength ranges. The raw change in reflectance (ΔR) is presented in the Appendix.

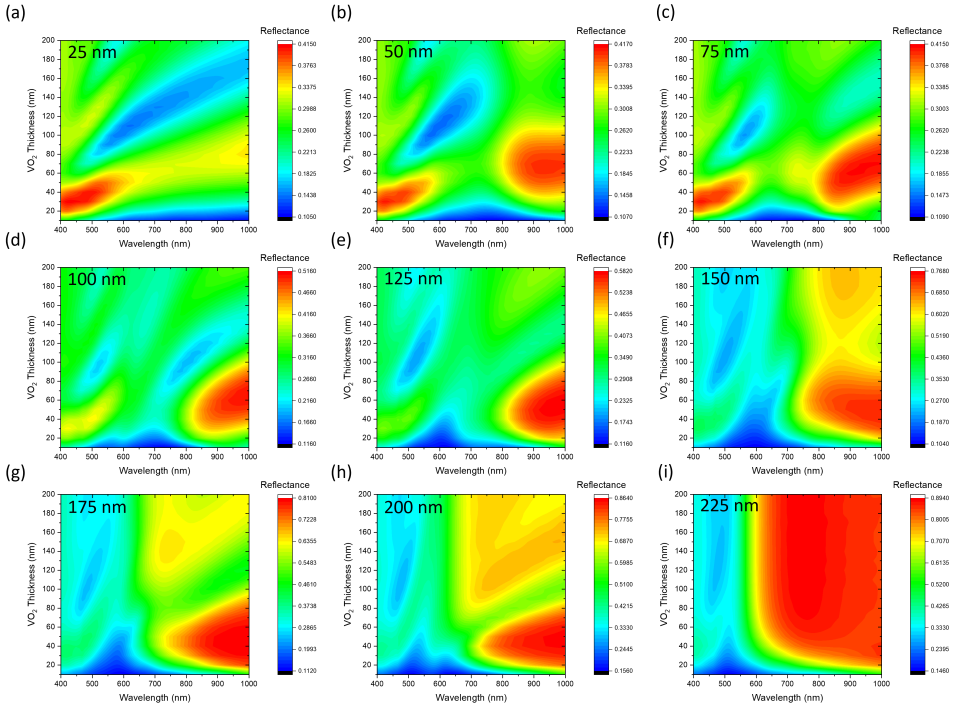

Figure 4.15: (a-i) VO_2 - Au film reflectance for VO_2 in semiconducting phase for varying film thickness and side length of the embedded Au.

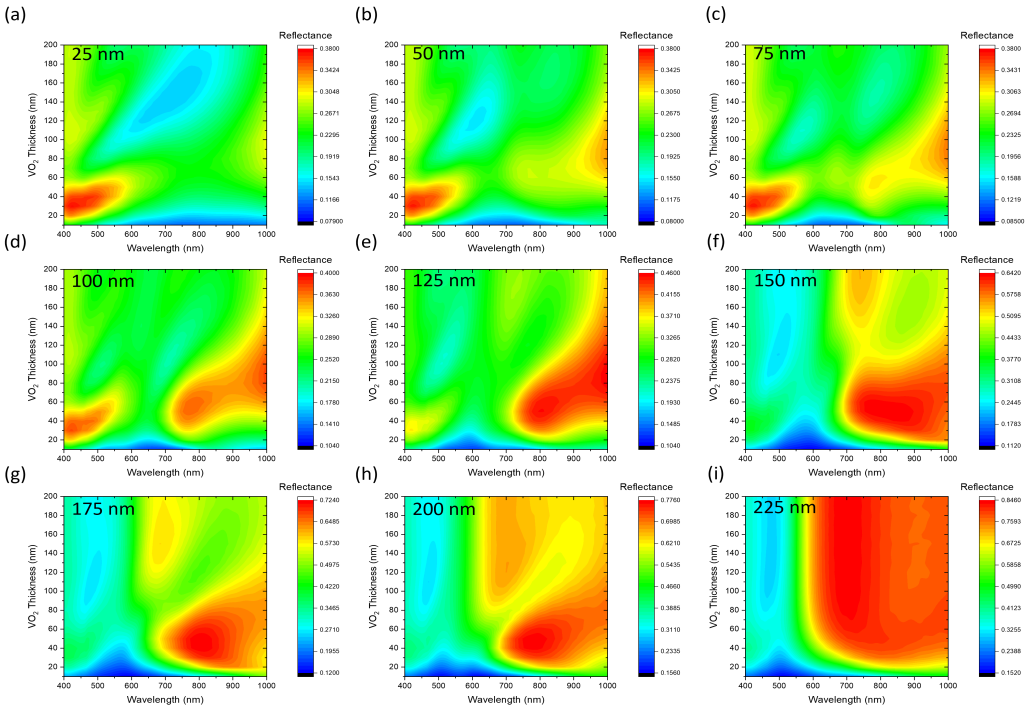

Figure 4.16: (a-i) VO_2 - Au film reflectance for VO_2 in metallic phase for varying film thickness and side length of the embedded Au.

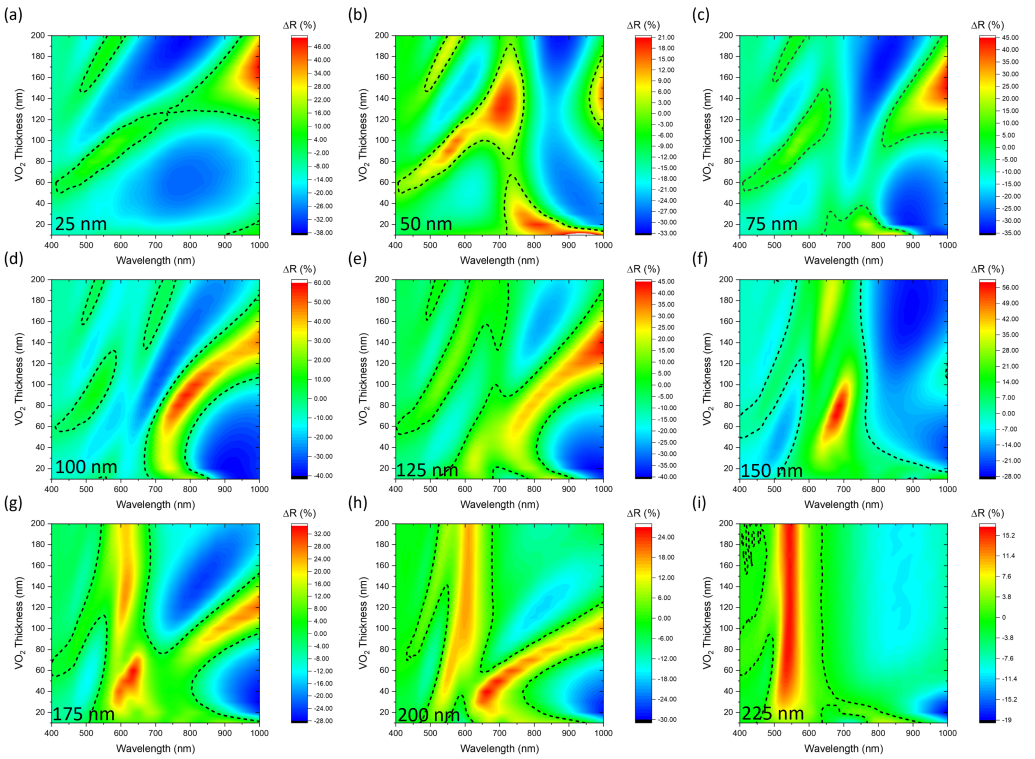

Figure 4.17: (a-i) VO_2 - Au film $\Delta R\%((R_M - R_{SC})/R_{SC})$ for varying film thickness and side length of the embedded Au. Black dashed line represents region where $\Delta R\% = 0$, therefore the bounded areas represent an increased reflectance for VO_2 in metallic phase.

4.4 Thin Film Characterisation

After deposition, fabricated VO_2 thin films were characterised with numerous techniques to determine the exact oxide phase of the grown film, the thickness of the thin film and the surface quality. Optical characterisation of the films transitioned from the semiconducting and metallic phase through thermal or electrical methods is achieved, and spectra are compared to those calculated using FDTD simulation. Immediately after deposition by PLD, fabricated thin films were tested by measuring a resistance across the sample and by demonstrating the presence of any phase switching properties upon heating the sample above the critical temperature of 68°. This initial characterisation is used as a relatively quick way to ascertain which deposition parameters produced continuous oxide films for optimisation purposes before further characterisation techniques were applied.

4.4.1 VO_2 Phase Characterisation

X-Ray Diffraction (XRD)

Characterisation of the VO_2 oxide phase was carried out using X-Ray diffraction (XRD) measurements. Standard $\theta-2\theta$ XRD scans were carried out using a PANalytical X'Pert Pro X-ray Diffractometer. Manual control of the stage in the Z direction allowed samples to be aligned to the X-ray source and detector arms of the system. As fabricated VO_2 samples were deposited on $c-Al_2O_3$ substrates, the apparatus was aligned to the known Al_2O_3 (0006) peak at 41.68°. XRD scans of samples displaying phase transition properties demonstrate an intensity peak at $\approx$ 39.8 - 40 °. Values taken from literature support this peak angle as the 020 peak associated with the formation of the VO_2 oxide phase.[120,121] For each scan, XRD data points were taken for a scan range between 20 - 100 °with a scan step size of 0.0167113 °. Typical XRD spectra for phase switching VO_2 samples are given in Fig 4.18. Slight variations in peak position, intensity and FWHM are attributed to variations between VO_2 samples including strain and crystallite size.

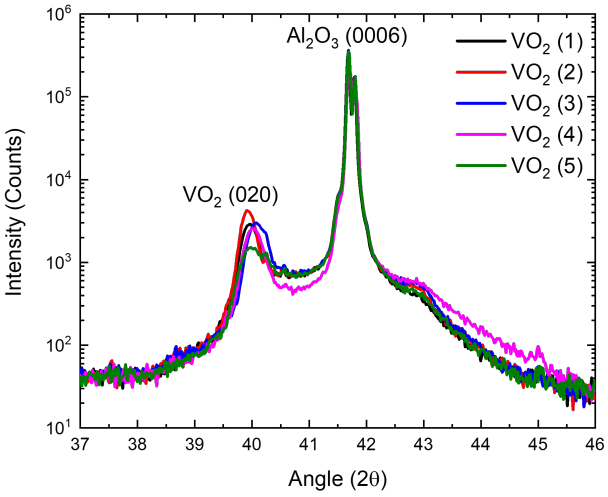

Figure 4.18: $\theta - 2\theta$ XRD scans of VO_2 samples grown on $c - Al_2O_3$. The characteristic Al_2O_3 peak and VO_2 peak are at 41.68°and 39.8 °- 40°, respectively. Peak width can be used to determine crystallite size

Raman Spectroscopy

Raman Spectroscopy was used as an additional characterisation tool to confirm the presence of the VO_2 oxide phase. The Raman spectra used for confirmation of the VO_2 oxide phase were acquired using two separate Raman systems. Measurements were performed using a Horiba Jobin Yvon LabRAM HR800 Spectrometer under ambient conditions. Before performing measurements on fabricated samples, the Raman spectrometer was calibrated using a Si sample. The acquired spectra from the Si sample was set to align with the known peak at 520 cm^{-1}. Raman emission was collected using a 100x objective lens (N.A. = 0.8) and dispersed by a grating with 2400 gr/mm. A 532 nm laser excitation source was used for all measurements, which was allowed to stabilise for 10 mins before acquisition of Raman spectra. A camera allowed for coarse focusing and selection of specific areas on fabricated samples under white light illumination. Fine focus adjustment was achieved with using the image of the laser on the sample. An adjustable filter was used to control the intensity of the laser beam on the sample with a 10% filter used for regular measurements.

Raman measurements were also carried out using a WITec Alpha 300R confocal Raman

microscope. In this case the signal was collected by a 100 x objective lens (N.A = 0.95) and dispersed by a 1800 line/mm grating. The advantage of this Raman system is the capability to acquire Raman maps. As many spectra can be automatically taken over a given area, Raman maps were used to determine VO_2 film quality over a particular area. In the semiconducting phase, the monoclinic (M1) VO_2 structure is associated with 18 Raman-active vibrations $9A_g + 9B_g$. The spectral location of these modes as given in the literature[122] are shown in the table 4.1

$A_g(cm^{-1})$	$B_g(cm^{-1})$
137	143
194	224
224	262
310	393
340	442
393	450*
499	484
612	582
663	820

Table 4.1: Raman modes for semiconducting monoclinic (M1) VO_2 phase. *This mode hasn't been experimentally confirmed.

In the metallic, rutile (R) phase, there are four weak Raman-active modes A_{1g}, B_{1g}, B_{2g} and E_g appearing 240, 390, 510 and 625 cm^{-1}, respectively.

For experimental confirmation of the VO_2 oxide phase, the semiconducting phase was examined due to ease of measurement, having strong well-resolved bands and not requiring external stimulus to induce the phase transition.

In Fig 4.19 characteristic peaks associated with the VO_2 A_g modes are observed confirming the grown films are the desired vanadium oxide phase. In particular, the strong peaks at 194,224, and 612 cm^{-1} indicate the growth of the VO_2 (M1) phase. Additional peaks associated with the Al_2O_3 substrate are observed at 418, 575 and 751 cm^{-1}. For VO_2 sample D, sample shown in Fig 4.19 (a), the weak VO_2 signal and the strong Al_2O_3 signal shown at 418 cm^{-1} is consistent with the samples discontinuous film growth indicated by the inability to obtain a resistance reading across the sample. In Fig 4.19 (b) Raman spectra for thin films grown by reactive sputtering with different

O_2 partial pressures is shown with the strong VO_2 peaks for the $O_2 : Ar - 1.85 : 50$ sample indicating good VO_2 growth conditions.

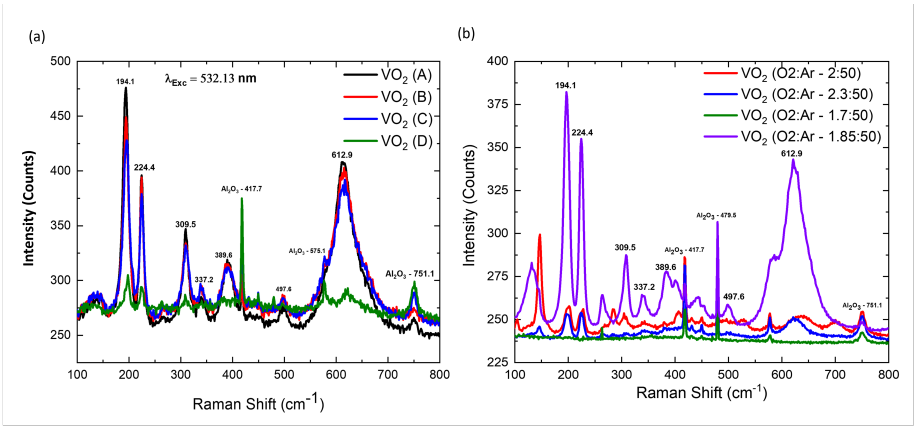

Figure 4.19: (a) Acquired Raman Spectra for VO_2 thin films fabricated by PLD. The spectra for samples A, B and C are representative of the deposition of VO_2, The weak VO_2 signal from sample D is indicative of the formation of a thin, discontinuous film. (b) Acquired Raman Spectra for thin films fabricated by reactive sputtering. The strong VO_2 Raman peaks for the sample grown with O2:Ar - 1.85:50 indicate this partial pressure is suitable for growth of the VO_2 phase. The FWHM of Raman peaks can be used to determine crystallinity of the thin film.

XPS

For VO_2 samples deposited by magnetron sputtering, X-ray photoelectron spectroscopy (XPS) was used as an additional characterisation technique. In this case the, the sample could be easily transfered from the deposition chamber to the XPS chamber within the TD system. As the binding energies for V2p and O1s are relatively similar for the various vanadium oxidation states (V^{5+}, V^{4+} and V^{3+}) the values of each are quoted in Table. 4.2[123]

Material	$V2P_{3/2}$ BE (eV)	O1s BE (eV)	Δ BE (eV)
V_2O_5	517.3	530	12.7
VO_2	516.3	530	13.7
V_2O_3	515.4	530	14.6

Table 4.2: $V2p_{3/2}$ and O1s binding energy for various vanadium oxide phases.[123]

Typical XPS spectra for sputtered samples are given in Fig. 4.20. It is noted that for each sample the spectra are adjusted so that the O1 peak is at 530 eV and can act as a reference. The vanadium oxide phase is characterised by the position of the $V2p_{3/2}$

peak. The pure VO_2 phase is characterised by the peak binding energy of 516.3 eV or a ΔBE of 13.7 eV between the O1 peak and the $V2p_{3/2}$.

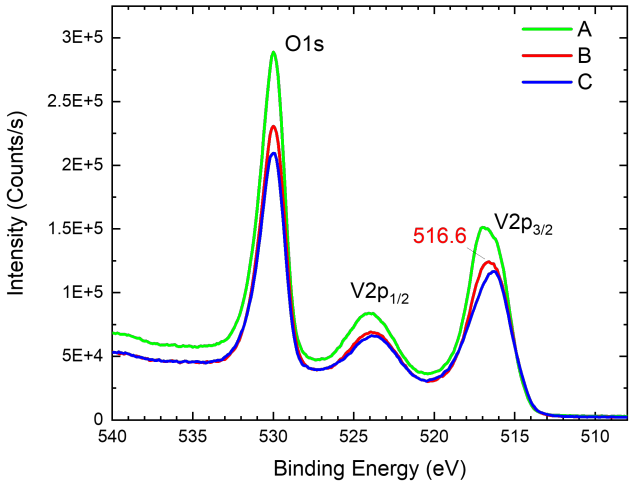

Figure 4.20: Acquired XPS spectra for vanadium oxide samples deposited with varying O_2 pressure. Sample Cs $V2p_{3/2}$ peak at 516.3 eV indicates a purely VO_2 phase.

4.4.2 VO_2 Thickness

VO_2 sample thickness was determined through several complementary methods. Transmission spectra for VO_2 thin film samples in semiconducting phase were taken using a Cary UV-Vis Spectrophotometer. A comparison of the transmittance spectra of three VO_2 films fabricated by PLD at different O_2 partial pressures are shown in Fig. 4.21 to simulated transmittance spectra. The transmittance spectra compare favourably to the simulated spectra, particularly at longer wavelengths, as further characterisation confirms the VO_2 films grown with 20, 30 and 40 μbar O_2 partial pressures produced thin films with 21, 32 and $\sim$ 60 nm respectively. It's noted that the largest changes between transmittance spectra occur for films below 80 nm and from 80 - 100 nm there isn't a significant difference in simulated transmittance spectra. The 90 nm transmittance spectra is depicted in Fig. 4.21 for comparison against the 60 nm case.

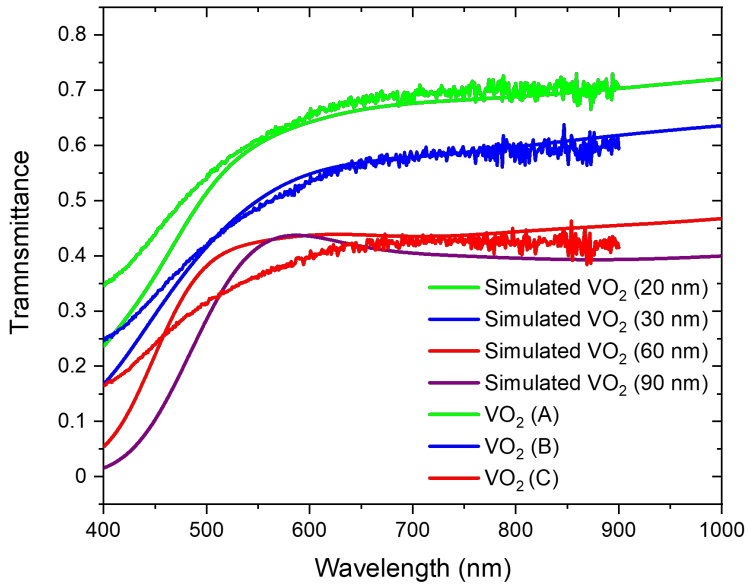

Figure 4.21: Comparison of simulated VO_2 transmittance spectra to VO_2 thin films fabricated with varying O_2 partial pressures.

XRR

X-ray reflectivity is used to determine the thickness of fabricated thickness to high resolution. Similar to the XRD characterisation, a PANalytical X'pert Pro X-ray Diffractometer is used to perform the scan. A scan range of 0.28° - 7° with a scan step size of 0.015° was used to ensure a sufficient a number of oscillations were acquired for fitting. The spectra were fitted using XRR software, with film thickness, roughness and density acting as fitting parameters. A representative example of acquired spectra for fabricated thin films is given in Fig. 4.22 demonstrating the change in oscillation periodicity for a 21 and 32 nm VO_2 thin film. Accurate measurement of film thickness was used to determine the growth rate of films fabricated by PLD allowing for control of the film thickness through deposition time.

It's noted that for VO_2 films with significant roughness such as the VO_2 sample grown at 40 μbar, fitting an XRR curve may not be possible. The thickness of this particular film was confirmed using a focused ion beam (FIB) to cut into the sample surface. In this way the VO_2 sample thickness could be approximately measured from an SEM

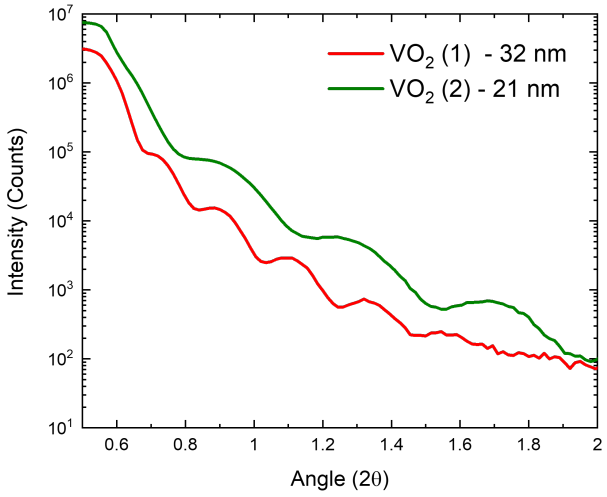

Figure 4.22: XRR scans of VO_2 thin films with 21 and 32 nm thickness demonstrating the characteristic thickness dependent periodicity in the oscillations.

image of the FIB cut as demonstrated in Fig. 4.23.

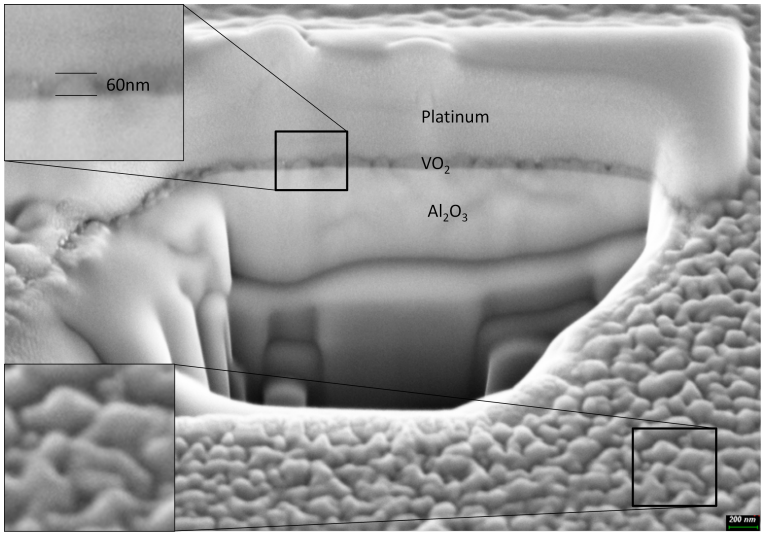

Figure 4.23: SEM image of FIB cut of VO_2 thin film. This film was fabricated by PLD with 40 μbar O_2 partial pressure resulting in significant film roughness.

Ellipsometry

Ellipsometry is employed as an additional tool to measure the thickness of fabricated VO_2 thin films. A J.A. Woollam Alpha-SE ellipsometer is used to scan the surface of VO_2 thin films with the resulting spectra fitted using a model based on the dielectric function of a fabricated 30 nm VO_2 sample in semiconducting phase previously fitted

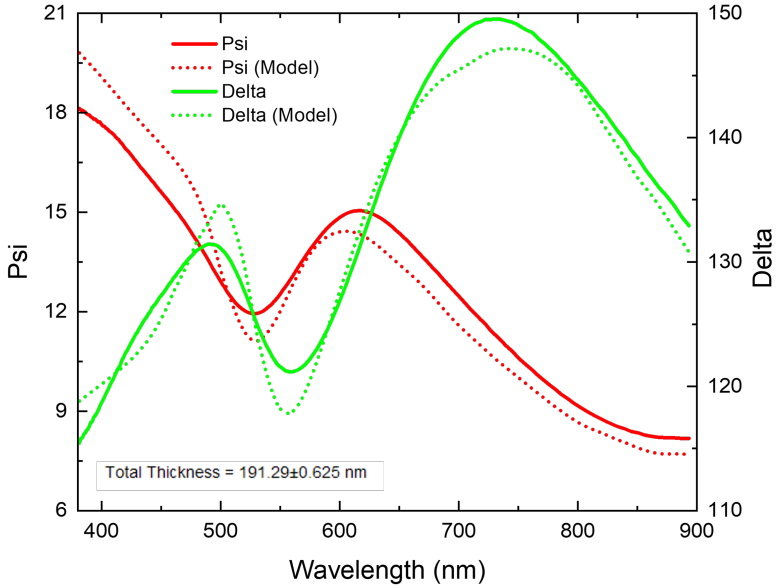

Figure 4.24: Ellipsometry Spectra with fitted model for $\sim 191nm$ VO_2 sample fabricated by reactive sputtering.

using data taken by a Sopra GESP5 ellipsometer. The 30 nm film's thickness was determined by XRR. Measurement and analysis was achieved through the CompleteEASE ellipsometry software. An example of a spectra acquired by ellipsometry with the fitted model based on the VO_2 dielectric function is given in Fig. 4.24. The software uses a standard, iterative, non-linear regression algorithm (Levenberg-Marquardt method) to improve the agreement between the measured and model generated ellipsometry data.

4.4.3 Film Roughness

Roughness of the fabricated VO_2 thin films was an important characteristic as it has a direct effect on the quality of periodic nanostructures fabricated on the VO_2 thin film. Additionally, increased roughness results in an increase in scattered signal from the VO_2 thin film itself, increasing the difficulty of resolving the nanostructure plasmon scattering signal. Film roughness was characterised using a vibrationally isolated MultiMode AFM. Scans were taken of 5×5 μm regions on the surface of each VO_2 sample. A selection of AFM images is shown in Fig. 4.25 with a corresponding table

indicating sample roughness for each AFM image. The Ra and Rq roughnesses are the arithmetic average and the root mean square average given by $Ra = \frac{1}{l_r}\int_0^{l_r} |z(x)|dx$ and $Rq = \sqrt{\frac{1}{l_r}\int_0^{l_r} z(x)^2 dx}$ respectively where l_r is the length of the mean line and z(x) is the deviation at each point along the mean line. The samples depicted in Fig. 4.25 (a), (b) and (c) respectively are taken for samples grown using PLD at different O_2 partial pressure but with an equal deposition time of 30 mins. The AFM image in Fig 4.25 (b) has the same growth parameters as (a) with a reduced laser repetition rate. From the table it's clear that the reduced repetition rate isn't suitable for thin film growth as the roughness of the sample is over three times larger than when a repetition rate of 10 Hz is used.

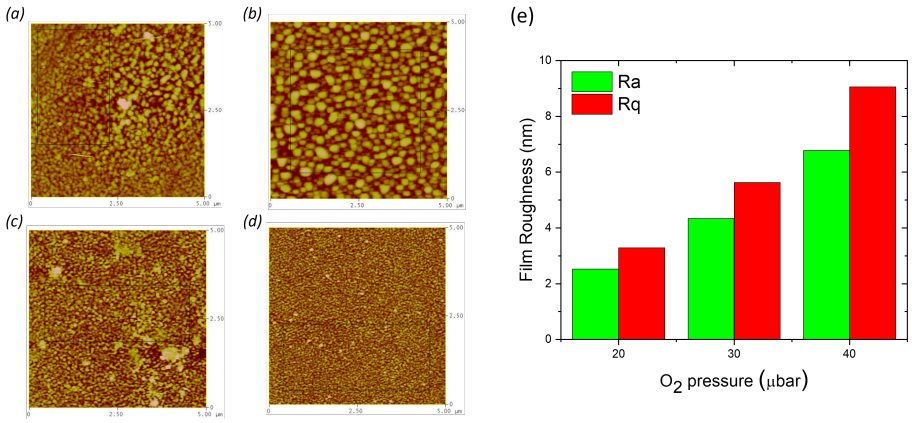

Figure 4.25: AFM images of VO_2 samples prepared by PLD. The O_2 partial pressure and laser repetition rate is indicated for each sample (a) VO_2 (40μ bar, 10Hz) (b) VO_2 (40 μ bar, 5Hz, (c) VO_2 (30 μ bar, 10Hz, (d) VO_2 (20 μ bar, 10 Hz) (e) Bar chart indicating VO_2 thin film roughness (Ra and Rq) as a function of O_2 partial pressure in chamber during film growth. The chart indicates a linear relationship, for this given range, between O_2 partial pressure and film roughness with a decrease in growth pressure, decreasing surface roughness.

	VO_2 (a)	VO_2 (b)	VO_2 (c)	VO_2 (d)
Ra (nm)	6.780	21.195	4.339	2.531
Rq (nm)	9.065	25.825	5.627	3.291

Table 4.3: Table indicating the Ra and Rq roughness of the VO_2 samples depicted in Fig. 4.25.

As indicated previously, a higher partial pressure, results in a thicker film for a given deposition time. A higher partial pressure also results in increased roughness values for both the Ra and the Rq roughness as indicated in the table and Fig. 4.25 (e). VO_2

(d), grown at the lowest O_2 partial pressure, is the best film in terms of roughness. The relationship is determined to be linear within the partial pressure range used in the fabrication of VO_2 samples.

From the characterisation of the VO_2 thin film roughness, it's clear that for fabrication of VO_2 with high quality surface, the O_2 partial pressure within the PLD system should be at the lower bound where growth of the VO_2 oxide phase is favoured with a reduced surface roughness.

4.5 VO_2 Transition

As mentioned previously the VO_2 phase change can be triggered by a range of external stimuli. In this section the change in electrical and optical response induced by the VO_2 phase change is shown when the phase change is actuated through the use of a ceramic heating stage, through the application of a voltage or current by contacting probes onto metallic contacts pads patterned onto the thin film surface and finally through the use of a high power laser incident on the thin film surface.

4.5.1 Thermal induced VO_2 transition

For measurements where the VO_2 phase change was actuated thermally, sample heating was achieved by placing the VO_2 films on ceramic heating stage mounted in a custom 3D printed mount. The heating stage was connected to an ILX Lightwave LDT-5910B temperature control to allow precise control of target temperature. An AD590 transducer monitored the temperature on the stage and allowed for temperature feedback to the controller. The heat stage mount was designed to minimise heat loss to the surrounding environment so that temperatures of approximately 100 $^{\circ}C$, significantly higher than the critical transition temperature (T_c) of the VO_2 films, could be maintained while still allowing for implementation into the microscope stage under various microscope objectives. In addition to this, the heat stage allows room for probes for measurement of electrical resistance and supply of voltage and current

for electrical transition measurements. Electrical probes were connected to a Keithley 2400c source meter which, in conjunction with the heat stage, allowed resistance - temperature graphs for each VO_2 thin film sample to be obtained, as shown in the Fig. 4.26. The VO_2 thin films A,B and C presented in Fig. 4.26 are grown using PLD and represent films grown using 40, 50 and 60 μbar O_2 partial pressure, respectively. The characteristic large change in resistivity/conductivity as the VO_2 films transition from the low temperature monoclinic phase to the high temperature metallic rutile phase is demonstrated in Fig. 4.26(a). From the heating and cooling curves shown in the figure a hysteresis effect in the VO_2 phase transition is evident. The transition temperature for both heating and cooling curves can be seen in Fig. 4.26 (b) showing a plot of $-\delta LogR/\delta T$ as a function of sample temperature. The phase transition is observed to occur close to the T_c value of 68 $^\circ C$ quoted in literature. The phase transition occurs at 71.5 $^\circ C$ upon heating and 66.1 $^\circ C$ on cooling with a hysteresis width of 5.4 $^\circ C$. The hysteresis effect arises from the domains within the thin film VO_2 transitioning at different temperatures.

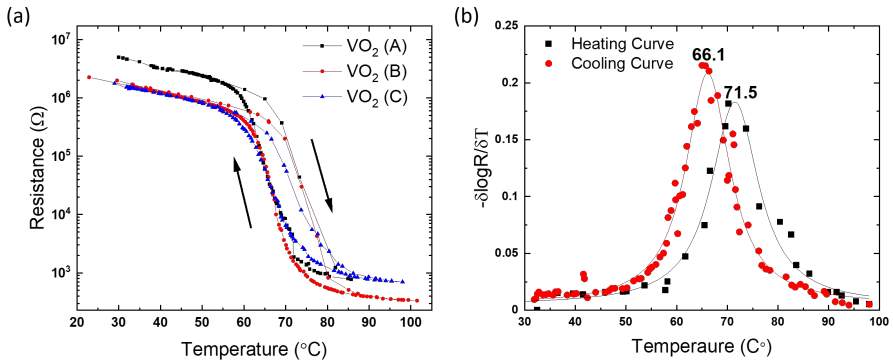

Figure 4.26: (a) Plot demonstrating the temperature dependent resistance for various VO_2 films grown on c-plane Al_2O_3. A significant change of resistance of over 3 order of magnitude is demonstrated for each sample. A, B and C represent films grown by PLD at O_2 partial pressures of 40,30 and 20 μbar, respectively. (b) Plot of -$\delta logR/\delta T$ vs temperature for VO_2 (C) demonstrating a phase transition at 71.5 °C upon heating and 66.1 °C on cooling. A hysteresis width of $\sim$ 5.4 °C is seen.

A comparison of the reflectance spectra of a $\sim$ 40 nm VO_2 sample with simulated VO_2 spectra in Fig. 4.27 shows good agreement, particularly in the wavelength range between 400 - 650 nm. This high level of agreement between simulation and experi-

mental spectra is attributed to the implementation of the dielectric function acquired from ellipsometry within FDTD simulations.

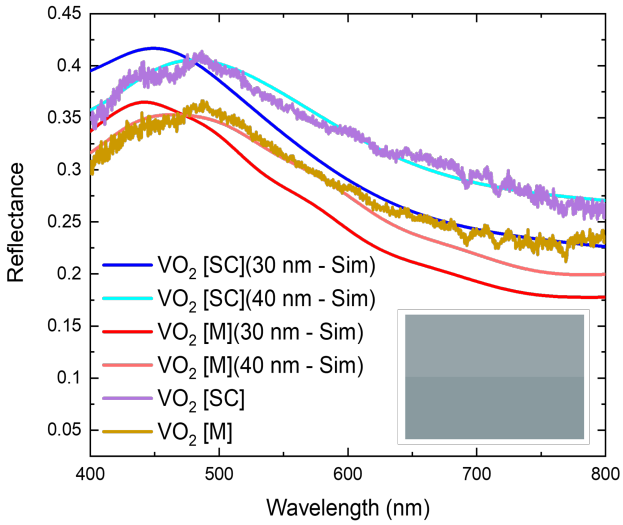

Figure 4.27: Comparison of simulated 30 - 40 nm VO_2 reflectance spectra with VO_2 sample spectra acquired under bright field microscope for VO_2 in semiconducting (SC) and metallic phase (M). The colour generated from the experimental spectra is depicted as an inset.

4.5.2 Electrically induced VO_2 transition

In addition to thermal actuation using the heat stage, the VO_2 phase transition was actuated electrically through application of a voltage across the surface or a current through the VO_2 thin film. This differs from other reported electrical tuning methods in that there is a potential difference across the VO_2 film, i.e. current flows through the VO_2 itself rather than a configuration where current flowing through a top metallic patch is used to heat the VO_2 film through Joule heating as seen in Kim et al.[124] The electric field was applied by a precision controlled probe station with a Keithley 2400c Standard Series Source Measure Unit acting as a voltage or current source. Voltage and current sweep experiments were controlled through the use of National Instruments Labview software, which also controlled data collection.

Initial electrical measurements were performed by placing the contact probes on the VO_2 film surface and increasing the voltage across the film until a characteristic jump

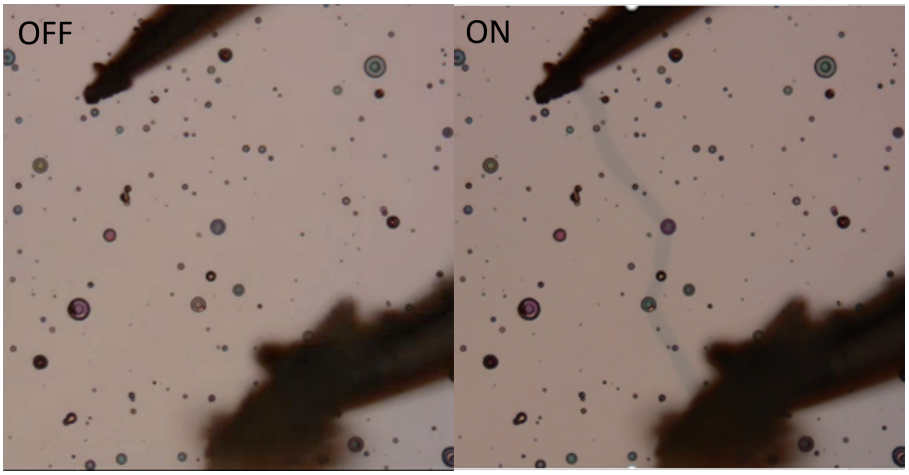

Figure 4.28: Image demonstrating formation of conducting metallic VO_2 channel between metallic probes with an applied voltage.

in current indicated that the VO_2 channel had reached a low resistance metallic phase. This phase transition is accompanied by a drop in reflectance and a visible colour change in the metallic VO_2 channel formed between the probes. From Fig. 4.28, in this case, the metallic VO_2 channel takes a path between large vanadium defects that arise from the deposition process.

To investigate the electrically induced VO_2 phase change electrical contact pads (Ti5nm/Au35nm) were fabricated on the surface of the VO_2 thin film through EBL methods. While a thinner Ti layer is sufficient for Au adhesion, 5 nm is used due to the availability of a weekly free metal deposition using 5 nm Ti. The distance between contacts was set at 5 - 15 μm so that a sufficiently strong electric field could be induced along the VO_2 channel length. For all electrical measurements resistors with resistances of between $3k\Omega$ - $22k\Omega$ are placed in series to limit the increase in current when the VO_2 channel transitions to a low resistance metallic state. The magnitude of the limiting resistor used in each case is dependent on the intrinsic resistance of the VO_2 channel in both states and the channel length.

In the monoclinic phase, VO_2 displays characteristic semiconductor properties for applied voltages lower than the critical voltage. The value of the critical voltage (V_c) is indicated by the sharp jump in the measured current. The IV-curves were converted to the characteristic VO_2 resistance curves using a simple Ohm's law relationship,

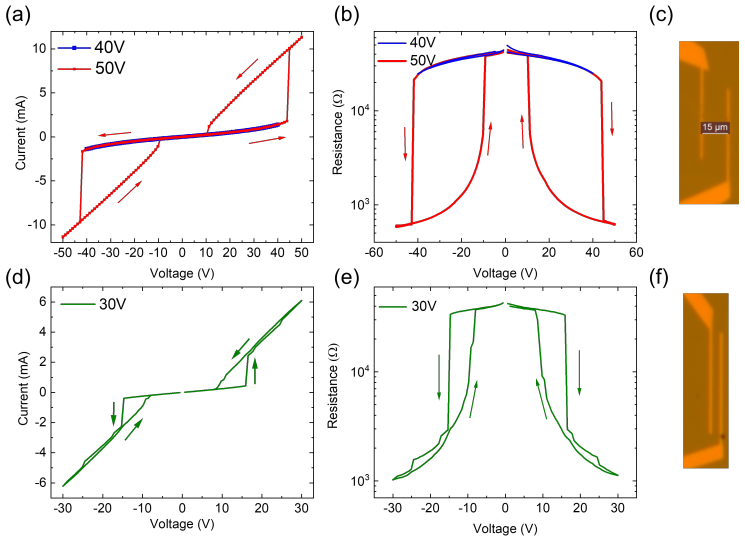

Figure 4.29: (a) 40V (blue) and 50V (red) sweep on a VO_2 sample for a channel length of $15\mu m$. The abrupt jump in current at 42V indicates the phase transition (b) Resistance curves demonstrating the strong switching characteristic at the critical voltage (42V) (c) image of $15\mu m$ channel between Au contacts (d) 30V (green) sweep on a VO_2 sample for a channel length of $5\mu m$. The abrupt jump in current at 15V indicates the phase transition (e) Resistance curves indicating the switching characteristic at the critical voltage (15V) (f) image of $5\mu m$ channel between Au contacts.

subtracting the current limiting resistance.

From the IV curve in Fig. 4.29 (a) it can be seen that for a VO_2 channel length of 15 μm the V_c occurs at $\sim 44V$. When the voltage drop across the limiting resistor ($3.8k\Omega$) is factored in, the V_c across the VO_2 channel becomes $\sim 37.18V$. Using $\frac{V_c}{L}$ where L is the length of the VO_2 channel, gives a critical field of $\sim 2.5 \times 10^6 V/m$ in good agreement with values reported in literature[125] and a full order of magnitude lower than rival PCM options GST and AIST which have threshold fields of $5.6 \times 10^7 V/m$ and $1.9 \times 10^7 V/m$, respectively.[126] When the smaller channel length of 5μ m is considered, the critical voltage occurs at $\sim 15V$ as shown in Fig. 4.29 (d). When the limiting resistor and length of the channel are factored in, the critical field is calculated as $\sim 2.67 \times 10^6$ V/m, slightly higher than for the larger channel.

The response of a VO_2 (20 nm) film with 10 μm wire spacing for voltage and current sweeps are given in Fig. 4.30 (a) and (b) respectively. In each case, three values of limiting resistor (12, 15 and 22 $k\Omega$) are considered. The VO_2 channel has an intrinsic resistance of 19 $k\Omega$ in semiconducting phase. When the IV curves are adjusted for the

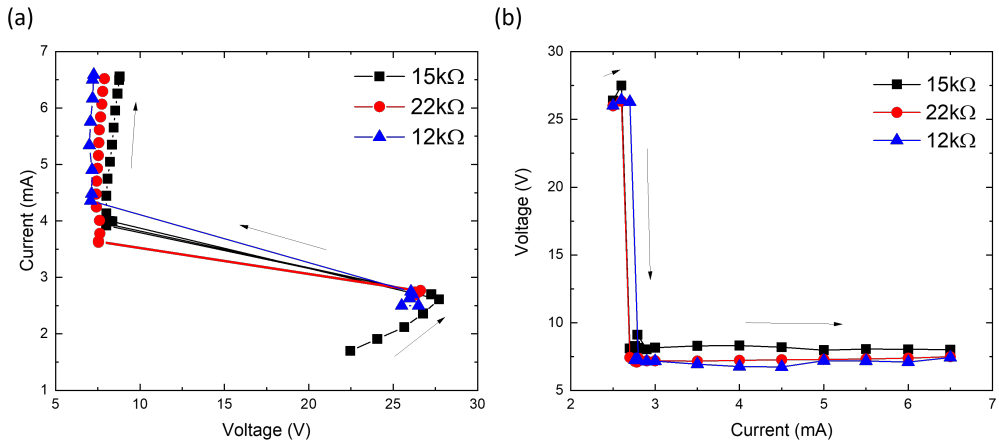

Figure 4.30: (a) Voltage driven VO_2 phase transition for $10\mu m$ channel with a 12,15 and 22 $k\Omega$ limiting resistor in series (b) current driven VO_2 phase transition for 10μ channel with 12,15 and 22 $k\Omega$ limiting resistor in series.

differing limiting resistor i.e. to isolate the response of the VO_2 channel, largely similar behaviour is seen. The current driven transition occurs at ~ 2.7 mA corresponding to a voltage of $\sim 26V$ across the channel length. This V_c corresponds to a critical field of 2.6×10^6 V/m, a value consistent with the previous measurements of 5 μm and 15 μm VO_2 channels.

It's noted that the size of the metallic VO_2 channel is dependent on the magnitude of the applied current or voltage as demonstrated in Fig 4.31. A distinct drop in reflectance in the channel allows easy visualisation of the channel width.

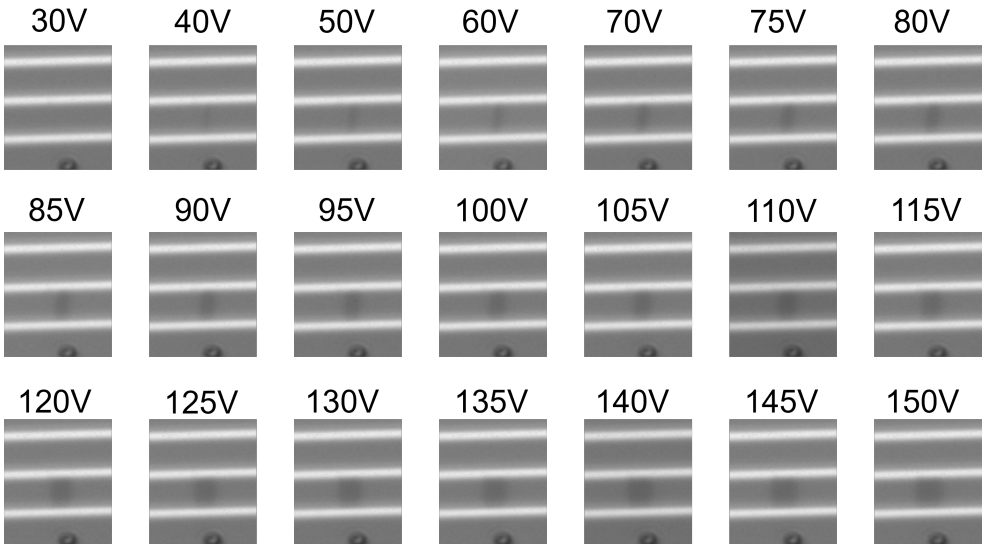

Figure 4.31: Images of a 10 μm channel on 20 nm VO_2 film showing increasing channel width with increasing voltage.

The width of the metallic VO_2 channel was measured by taking the difference between in CCD images of the VO_2 film with the applied voltage/current on and off as indicated in Fig. 4.32 (b). This allowed for easy visualisation of the area where the metallic channel forms as the difference in reflectance is effectively 0 at all other points on the sample. This is demonstrated in Fig. 4.32 (a), where the width of the channel is shown to increase as a function of applied current. From measurements of the width of the metallic VO_2 channel a linear relationship is found between the applied voltage and the channel width (Fig. 4.32 (c).)

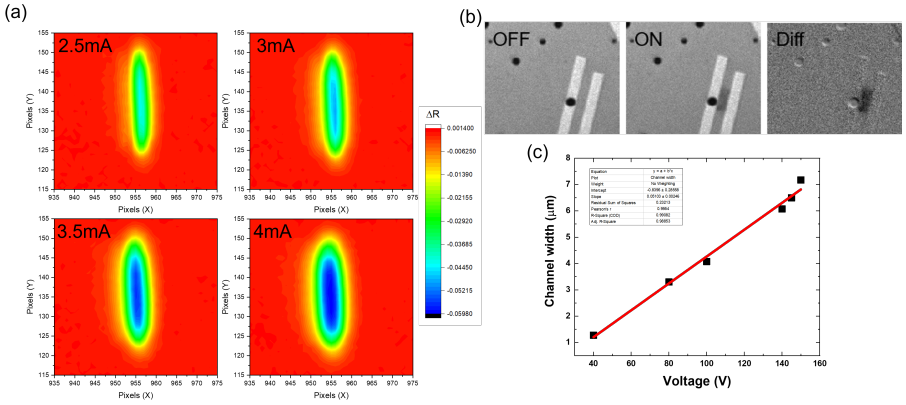

Figure 4.32: (a) Metallic VO_2 channel at various applied currents displaying the difference in reflectance intensity within the channel. (b) Images of VO_2 channel formed between Au wires, the three images show the off state, on state and the difference between the two states. (c) Plot demonstrating the linear relationship between channel width and applied voltage.

4.5.3 Laser induced VO_2 phase transition

In additional to thermal actuation of the VO_2 phase change using a ceramic heater, a Dragon laser M series 980 nm laser source is coupled into a normal reflection setup and used a source of thermal energy to actuate the VO_2 phase change (Fig. 4.33). The optical parameters of this laser are given in the table 4.4.

For laser heating measurements a VO_2 sample fabricated by reactive sputtering (190 nm) is mounted on the ceramic heating stage to facilitate comparison with spectra taken when the sample is heated by the thermal stage. The stage is mounted normal to incident white light illumination and adjusted so the reflected beam is focused onto

Laser	980 ± 10 nm
Power	1 - 2000 mW
Transverse Mode	Multimode
Beam Shape	Square
Beam Diameter	5 * 8 mm
Divergence	<3 mRAD

Table 4.4: Optical Parameters of Dragon laser M Series 980nm Laser

the fibre couple connected to the Andor 230i spectrometer. The focus is adjusted by moving the 40 x objective within the setup along the axis parallel to the direction of the white light propagation. The 980 nm laser beam is positioned so that the beam is incident on the same spot on the VO_2 sample as the white light. The beam is incident on the sample at an oblique angle, as close to grazing as possible to ensure the beam is not cut off by the focusing objective. The objective lens is not placed within the laser path to avoid damage to the lens by the high intensity beam. A schematic of the laser beam coupled into the normal reflectance spectra is given in Fig. 4.33.

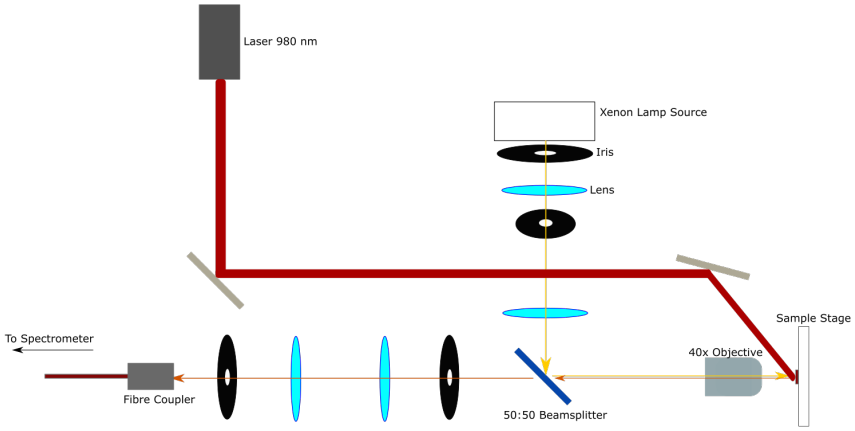

Figure 4.33: Schematic of normal reflection set-up incorporating 980 nm laser source.

Reflectance spectra taken with the laser source off and on are compared to reflectance spectra taken when the ceramic stage temperature is 90 $°C$. The experimental spectra are also compared to simulated reflectance spectra for a 190 nm VO_2 film.(Fig. 4.34) The reflectance spectra show good agreement with the simulated spectra indicating the actuation of the VO_2 phase transition using the laser source. As the incident laser is unfocused, there is a delay in the change in reflectance spectra as the VO_2 sample

is heated to the critical temperature. This time to reach the critical temperature was measured as a function of the laser power as demonstrated in Fig. 4.35 (d).

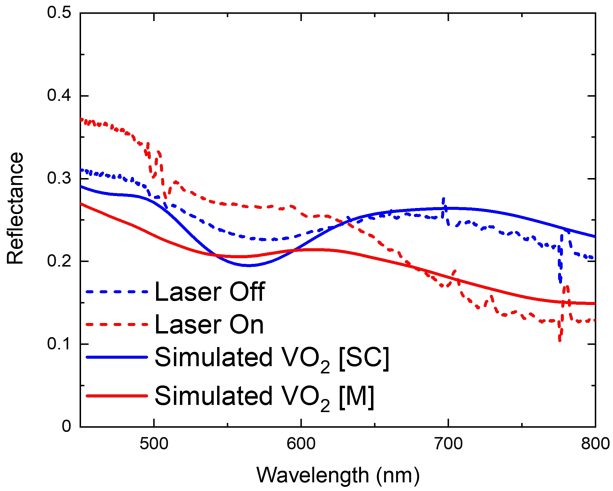

Figure 4.34: Normal reflectance of 190 nm VO_2 sample with laser heating source off and on compared to simulated VO_2 reflectance spectra.

Fig. 4.35 (a-c) depict normalised reflectance spectra taken every 2s from when the laser source is switched on. The spectra are taken for the laser output power at 2.2 W maximum down to 1 W where no phase transition is seen over 180s. The experimental time taken to heat the VO_2 sample to the critical temperature of 68° was taken as the time when the normalised spectra stopped changing between 2s intervals as with reduced power more intermediary spectra were visible. From measurements made using a Thorlabs PM100D Powermeter, the power at the VO_2 sample is found to be reduced to 0.243 times the laser output power. From the spectra depicted in Fig. 4.35 (a) taken for a laser power at the sample of 0.535 W the phase change occurs at $\sim$ 24s. This increases to $\sim$ 42s and $\sim$ 112 s for laser powers of 0.437 W and 0.292 W respectively. Sample heating time measurements were plotted as a function of power dependence. From Fig. 4.35 (d) there is a inverse square dependence on laser power and time to fully transition to metallic phase. It's noted that while these transition time scales are relatively long, the laser spot isn't focused. The beam spot is rectangular with dimension 8 mm * 5 mm. The laser contains multiple TE modes resulting in a rectangular beam spot. For a focused beam, the VO_2 phase transition may be actuated

at a lower power over a shorter timescale facilitating implementation in optoelectronic applications where high switching speeds are needed. It is noted this kind of optical actuation isn't suitable for plasmonic systems as high laser powers can damage metallic nanoparticles.

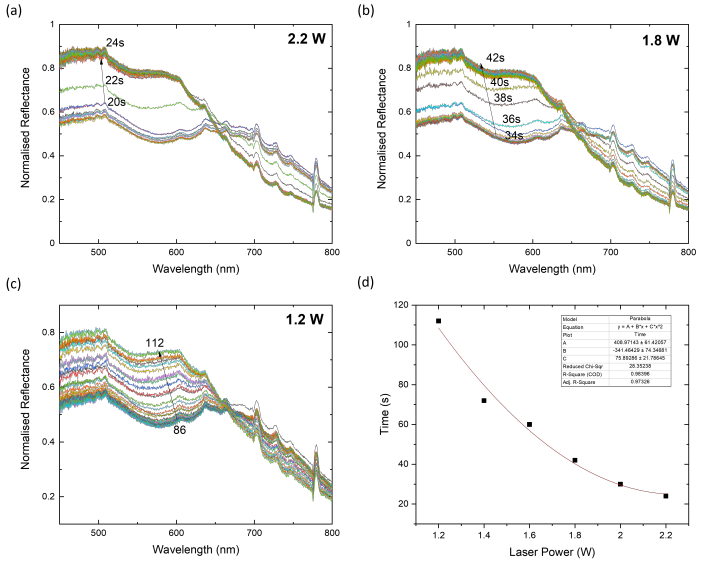

Figure 4.35: (a) Normalised reflectance spectra taken at 2s intervals after 980 nm laser (2.2 W) is switched on indicating VO_2 phase change (b) Normalised reflectance spectra taken at 2s intervals after 980 nm laser (1.8 W) is switched on indicating VO_2 phase change (c) Normalised reflectance spectra taken at 2s intervals after 980 nm laser (1.2 W) is switched on indicating VO_2 phase change (d) Plot of time to full film phase transition vs laser power. The plotted points are fitted with a second order polynomial curve. The spectra are normalised to a maximum value at 893.2 nm, not within the range shown.

4.5.4 Conclusion

This chapter demonstrates, through FDTD simulation, how the optical properties of thin film VO_2 evolve as a function of the film thickness. Calculated spectra demonstrate a range of colours and colour changes over thicknesses up to 200 nm. The change in the thin film reflectance between the VO_2 phases is seen to dramatically increase with the inclusion of a backreflecting metallic layer resulting in a significantly larger colour gamut. Simulations of varying Au inclusion in a VO_2 thin film demonstrate a large range of ΔR profiles between the VO_2 phases. Experimentally the VO_2 phase change was explored through different actuation methods and found to align well with

simulated spectra based on optical constants acquired from ellipsometry. Through the characterisation of fabricated VO_2 films, optimal parameters for deposition were attained allowing films of precise thickness to be fabricated with a strong switching characteristic, an important factor in tuning the properties of the hybrid nanostructures based on VO_2.

5 Metallic nanoparticle - VO_2 structures

5.1 Summary

In this chapter, the modification of the plasmonic response of metallic nanoparticles placed on thin film VO_2 is investigated. Experimental demonstration of shifts in the spectral response of coupled nanostructures, when the phase of the underlying VO_2 layer transitions from semiconducting phase to metallic phase, are shown for a range of nanoparticle morphologies. For these investigations, single nanoparticles and periodic arrays of nanoparticles are fabricated on thin film VO_2 using electron beam lithographic methods (EBL). EBL allows for well- defined uniform arrays of plasmonic nanoparticles to be examined. The spectral response of these structures when VO_2 is in semiconducting and metallic phase was examined under bright and dark field illumination by placing the hybrid structure on a ceramic heating stage within the microscope system. Additionally, arrays are fabricated between metallic contact pads to allow plasmonic tuning through the electrical transition of the underlying VO_2 film.

FDTD simulations of plasmonic structures are used to demonstrate optimal configurations of the hybrid system for large shifts in peak scattering wavelength, large differences in scattering cross-sections and E-field strength at plasmonic hotspots surrounding the metallic nanoparticles. Modification of the scattering and reflectance properties of single nanoparticles and periodic structures are examined and analysed

based on how each parameter in the hybrid system affects the response and the tuning of the response.

5.2 Introduction

In the previous chapter, it is shown that the optical response of planar thin film VO_2 can demonstrate a significant change through the phase transition from semiconducting to metallic phase and the subsequent change in dielectric function. As previously discussed, the inability to tune the response of plasmonic nanostructures, post-fabrication, acts as a limiting factor for implementation in many optoelectronic applications. The optical response of plasmonic nanostructures is largely dependent on factors such as size, shape, material composition and surrounding dielectric medium. On the nanoscale, small changes in these factors can have a significant impact on the response of the nanostructure. Through the implementation of an underlying thin film layer of VO_2, plasmonic tuning across a large wavelength range can be shown and, in particular, a large tunable response in the regime $< 1\ \mu m$ can be demonstrated. Much of the previous work in tunable plasmonics consider the significantly larger changes in dielectric function in the IR spectral region, particularly at 1550 nm[127–130] . However, there is an increasing interest in utilising the smaller but still significant changes in the dielectric function seen in the region below $< 1\ \mu m$ for the development of switchable metasurfaces[131,132] .

5.2.1 Numerical Simulations

The impact of the VO_2 thin film on the tunability of the local surface plasmon resonance (LSPR), scattering cross-section and modification of the spatial E-field for a range of single nanoparticles and dimers is examined through numerical simulations. An example of the configuration used for scattering simulations within Lumerical is shown in Fig. 5.1. The impact of VO_2 thin film thickness on the plasmonic response of single nanoparticle structures is also examined. The first structures considered within

this work are rod and cuboid shaped nanoparticles. Due to their anisotropic shape, these particles allow the excitation of multiple plasmonic features along two major polarization axes, namely the longitudinal plasmon along the long axis and the transverse plasmon along the short axis. The plasmonic response of these particles for VO_2 in both phases is compared to the response seen for metallic nanodiscs, which, due to rotational symmetry, have degenerate resonances at each polarization angle. The noble metallic nanoparticles considered throughout this work are made up of gold (Au) or silver (Ag) with numerical simulations presented in this section consisting of Au nanoparticles as experimentally Ag nanoparticles are well known to suffer from oxidation. In the case of each nanoparticle, the tunability is quantified by three factors:

1. $\Delta\lambda$, the shift in the peak scattering wavelength when the VO_2 film transitions from semiconducting to metallic phase, i.e. $\lambda_{Max_M} - \lambda_{Max_{SC}}$.

2. $\Delta\sigma$, the difference in scattering cross-section at each given wavelength for VO_2 in semiconducting and metallic phase, i.e. $\sigma_M(\lambda) - \sigma_{SC}(\lambda)$.

3. ΔE^2, the difference in electric-field intensity surrounding the nanoparticle in semiconducting and metallic phase, i.e. $E_M^2 - E_{SC}^2$.

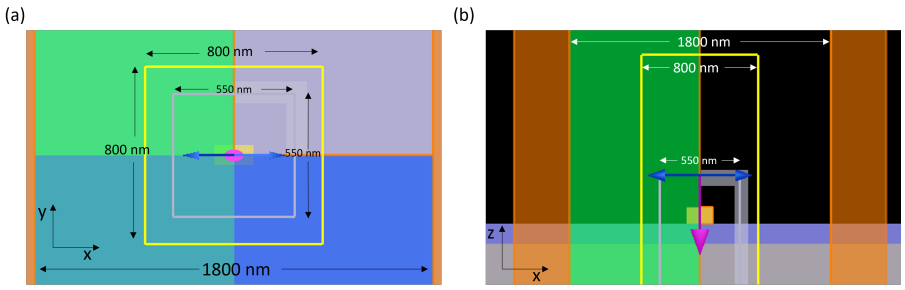

Figure 5.1: Schematics of the configuration used for single particle scattering simulations (a) top down view of nanocuboid with TFSF source and monitor box. Symmetric and anti-symmetric boundary conditions are used to take advantage of nanoparticle symmetry. (b) side view of nanocuboid on VO_2 with an Al_2O_3 substrate. The purple arrow indicates the direction of light propagation from the TFSF source and the blue arrows the polarization direction. The TFSF source has dimensions of 550 nm along the x and y axes and 400 nm along the z-axis. The monitor box is shown in yellow and is set as a cube with a side length of 800 nm. Anti-symmetric boundary is in green perpendicular to the TFSF source polarization. The FDTD simulation volume is set as a cube with side length 1800 nm with the boundaries depicted in orange.

For the nanocuboid case, which demonstrates a large wavelength shift upon the VO_2 phase transition, the impact of the nanocuboid dimensions on the longitudinal and transverse plasmon scattering spectra is examined. To examine the effect of varying the height of the plasmonic nanoparticle, Au nanocuboids with a fixed length and width of 180 nm and 90 nm, respectively, and height varying between 10 - 100 nm on a 10 nm VO_2 thin film, in semiconducting and metallic phase are considered. The impact on the longitudinal plasmon is first considered. As the longitudinal plasmon is excited along the long axis of the nanocuboid (180 nm) the resonance feature is considerably redshifted in comparison to the feature excited along the short axis (90 nm). Increasing the nanoparticle height blueshifts the plasmonic response of the longitudinal polarization for both VO_2 phases, with the larger blueshift occurring for the nanocuboid on semiconducting VO_2 (Fig. 5.2(a)). This results in a smaller shift in peak wavelength between the two VO_2 phases. The resonance blueshift is consistent with known variations in resonance wavelength with aspect ratio in metallic nanoparticles. As the nanocuboid height increases, there is an increase in the induced charge on both sides of the nanoparticle while the separation distance remains fixed. This results in a larger restoring force acting on the displaced charge resulting in the blueshifted response.[133] This decreased wavelength shift is accompanied by an increase in the magnitude of the scattering cross-section, σ, as well as a larger positive $\Delta\ \sigma(\sigma_M - \sigma_{SC})$ in the visible spectral region, as seen in Fig. 5.2 (c). Increasing nanoparticle height also results in the emergence of a plasmonic feature at 600 nm corresponding to oscillation perpendicular to the VO_2 plane. There is no change in the position of this feature after the phase transition due to the significantly smaller difference in VO_2 optical constants in this wavelength range. The peak shift is larger for the nanocuboids with reduced heights as the resonant feature occurs at higher wavelengths, where a larger change in the dielectric permittivity occurs after the VO_2 phase transition. Within the range of interest, below 1500 nm, the plasmon peak wavelengths shifts by 285 nm for the 20 nm high nanocuboid. This peak wavelength shift is decreased to 170 nm for the 100 nm high nanocuboid case. The impact of the nanoparticle height on the transverse

plasmonic response of the Au nanocuboid can also be seen in Fig. 5.2 (b). As in the case of the longitudinal plasmon response, there is a spectral blueshift with increasing height, and a narrowing of the plasmon resonance peak. In this case, once the structure height is greater than 40 nm there is no further impact on the position of the resonant feature near 780 nm. For the transverse case a positive $\Delta\sigma$ can also be seen within the visible spectral range (Fig. 5.2 (d)). However, in this case the magnitude of the scattering and the difference in scattering is significantly smaller than the longitudinal case. From Fig. 5.2 (b) a large overlap in the resonant response in seen for VO_2 in semiconducting and metallic phase. In addition to the regions with increased scattering cross-section in the visible spectral range, the semiconducting to metallic phase transition can modulate the scattering cross-section by a factor of approximately 3 at higher wavelengths.

In Fig. 5.3(a) the impact of increasing width of the Au nanocuboid on the longitudinal resonance feature is examined. The nanocuboid height is fixed at 40 nm with the width varied between 30 nm to 180 nm in 30 nm steps. An increased width results in a blueshifted longitudinal plasmon response. The resonance is blueshifted for similar reasons to the blueshift seen with increasing nanoparticle height. The scattering cross-section similarly increases with width. In the case of the transverse plasmon, (Fig. 5.3(b)), as the width increases the resonance is shifted to longer wavelengths due to the increasing aspect ratio. For both polarizations, the plasmon peak blueshifts, by up to 200 nm, with the phase transition of VO_2. From Fig. 5.3 (c) and (d) an increase in the scattering cross-section for both polarizations is evident. The magnitude of $\Delta\sigma$ is noted to increase with the increased scattering cross-section seen at increased widths. As shown previously, the scattering cross-section can be modulated by a factor of ~ 3 when VO_2 transitions from semiconducting phase to metallic phase.

In the previous cases the impact of altering height and width on the spectral position of the plasmonic feature is considered for a nanocuboid with no rounded edges as this configuration gives the largest wavelength shift when the phase of the underlying VO_2 transitions from semiconducting to metallic phase. However, chemically synthesised

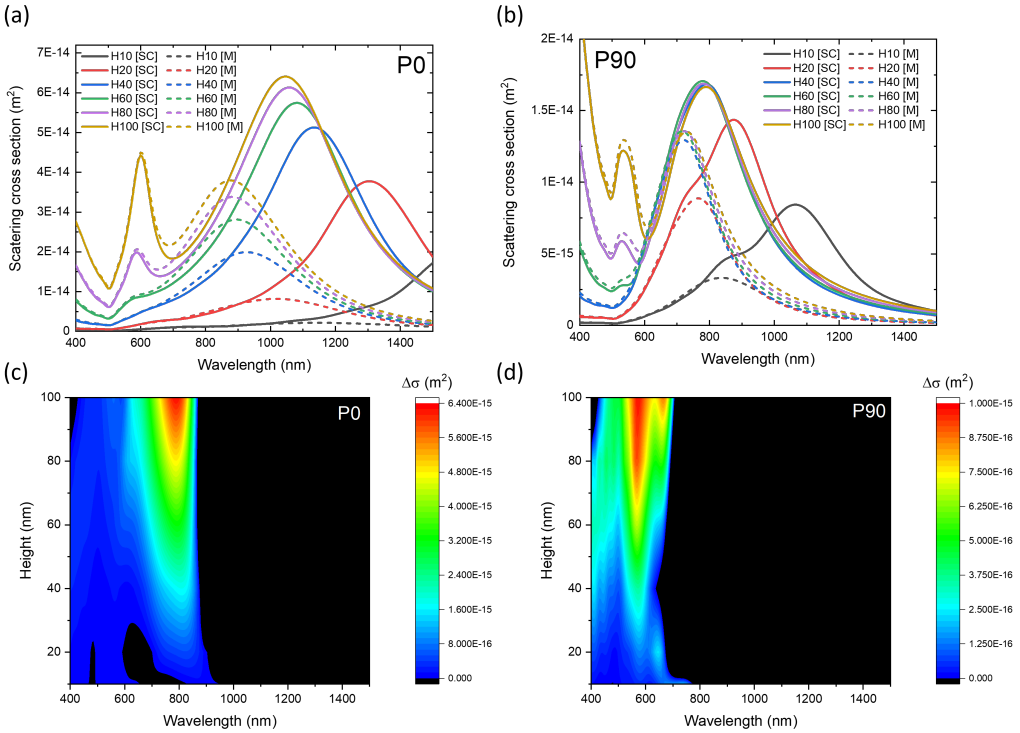

Figure 5.2: Scattering cross-section of Au Nanocuboid (Length = 180 nm, Width = 90 nm, Height = 10, 20, 40, 60, 80, 100 nm) for VO_2 (10 nm) in semiconducting phase (solid line) and metallic phase (dashed line) for (a) excitation polarized along long axis (b) excitation polarized along short axis. Contour maps depicting changes in scattering cross-section $\Delta\sigma$ ($\sigma_M - \sigma_{SC}$) for Au nanocuboid (Length = 180 nm, Width = 90 nm) on VO_2 (10 nm) for (c) excitation along long axis and (d) excitation along short axis. Coloured sections indicate an increase in scattering as VO_2 transitions to its metallic phase. Black regions indicate decreased scattering as VO_2 transitions to its metallic phase. These regions are coloured in black to highlight the regions where there is an increase in scattering.

nanoparticles and those produced through lithography usually have corner tip radii of between 5 - 10 nm. Corner tip radii are limited by the resolution of lithographic techniques. In Fig. 5.4 the scattering cross-section of a Au nanocuboid (Length = 180 nm, Width = 90 nm, Height = 40 nm) on VO_2 (10 nm) is given for edge radii from 0 - 20 nm. From this a redshift can be observed with increasing corner radius in both VO_2 material phases with the magnitude of the redshift significantly higher for the semiconducting phase. For a nanocuboid with no rounded edges a wavelength shift of 210 nm is observed which decreases to 185 nm for a 5 nm edge radius and is reduced to 120 nm for an edge radius of 20 nm.

As Au and Ag are materials most commonly used in plasmonic elements, a comparison

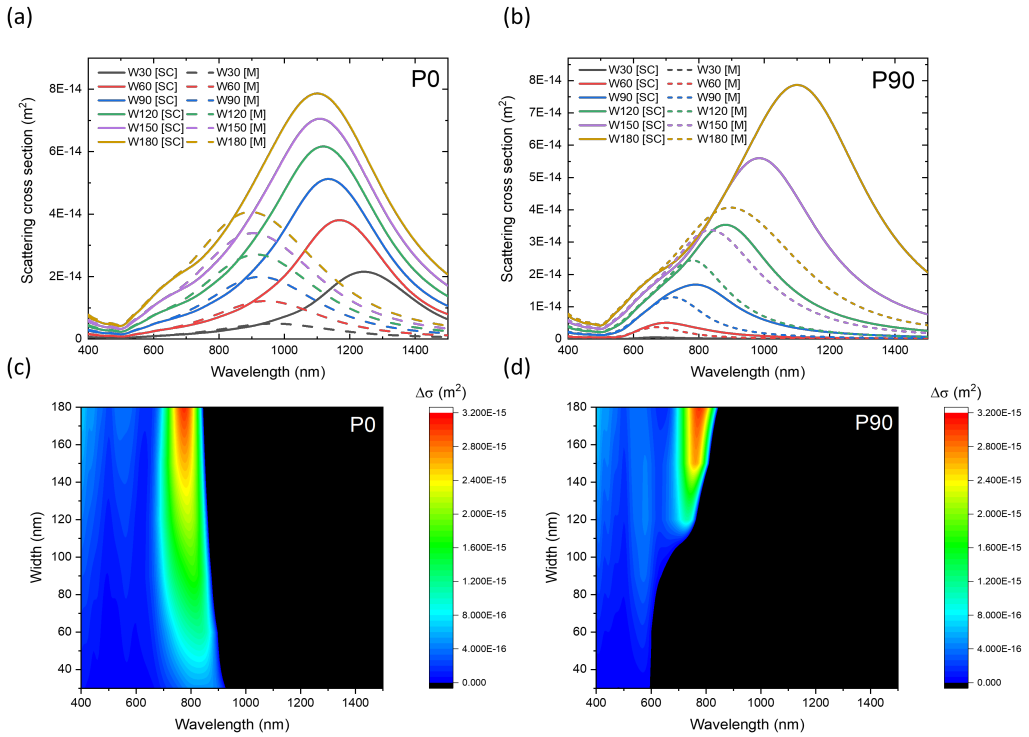

Figure 5.3: Scattering cross-section of Au Nanocuboid (Length = 180 nm, Width = 30, 60, 90, 120, 150, 180 nm, Height = 40 nm) for VO_2 (10 nm) in semiconducting phase (solid line) and metallic phase (dashed line) for (a) excitation polarized along long axis (b) excitation polarized along short axis. Contour maps depicting changes in scattering cross-section $\Delta\sigma$ ($\sigma_M - \sigma_{SC}$) for Au nanocuboid (Length = 180 nm, Height = 40 nm) on VO_2 (10 nm) for (c) excitation along long axis and (d) excitation along short axis. Coloured sections indicate an increase in scattering as VO_2 transitions to its metallic phase. Black regions indicate decreased scattering as VO_2 transitions to its metallic phase.

of the scattering response of metallic nanocuboids (Length = 180 nm, Width = 90 nm, Height = 40 nm) comprising these noble metals on thin film VO_2 is made. Fig. 5.5 compares the scattering response of the Au nanocuboid and Ag nanocuboid for VO_2 in semiconducting phase and metallic phase. It can be seen that in semiconducting phase, the magnitude of the scattering cross-section is equal for the Au and Ag nanoparticles. The Ag nanoparticles also demonstrate a redshifted response when comparted to the Au nanoparticles for VO_2 in semiconducting phase. For the metallic phase, it is noted that the Au nanoparticles display a larger scattering cross-section with minimal differences in the resonant wavelength between the two metals. This results in a larger $\Delta\lambda$ for Ag nanoparticles, however as mentioned previously Ag nanoparticles are susceptible to tarnishing effects.

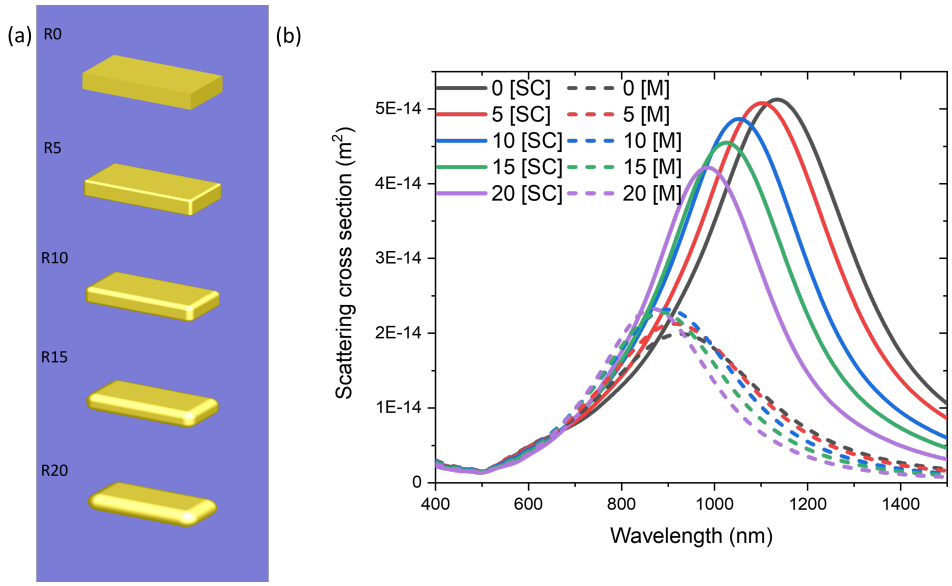

Figure 5.4: (a) Schematic of Au nanocuboid with edge radius between 0 - 20 nm (b) Scattering cross-section of Au Nanocuboid (Length = 180 nm, Width = 90 nm, Height = 40 nm on VO_2 (10 nm) for edge radius between 0 - 20 nm.

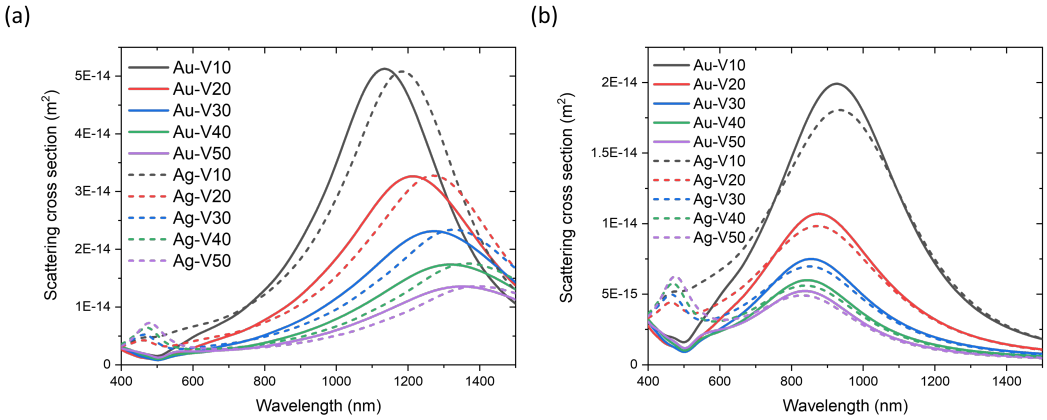

Figure 5.5: Scattering cross-section of Au and Ag Nanocuboid (Length = 180 nm, Width = 90 nm, Height = 40 nm) in (a) semiconducting phase and (b) metallic phase for VO_2 thicknesses between 10 - 50 nm.

The VO_2 thin film thickness has a significant effect on the nanoparticle plasmon resonance. Scattering spectra for a Au nanocuboid (Length = 180 nm. Width = 90 nm, Height = 40 nm) with VO_2 thickness between 10 - 200 nm, are shown in Fig. 5.6. Different trends can be seen for the semiconducting and metallic phases of VO_2. In the semiconducting phase increasing VO_2 thickness initially strongly redshifts the plasmon peak. For thicker films the dampened peak slowly oscillates between 1300 nm and 1400 nm, attributed to the change in VO_2 transmittance spectra between 40 - 90 nm. For

the metallic VO_2, the scattering spectra show a blueshift of the plasmon resonance up to a thickness of 90 nm, after which it is only weakly affected by the film thickness. The opposing spectral shifts result in an average $\Delta\lambda$ ($\lambda_{Max[SC]} - \lambda_{Max[M]}$) of 500 nm with a maximum of $\approx$ 560 nm occurring at 80 nm and 200 nm.

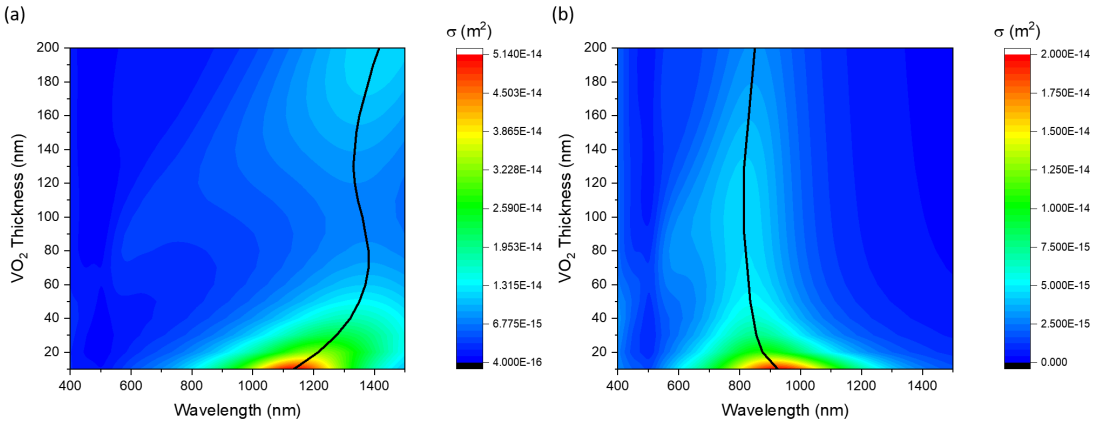

Figure 5.6: Contour maps showing the dependence of the scattering cross-section spectrum, for longitudinal excitation, of a Au nanocuboid (Length = 180 nm, Width = 90 nm, Height = 40 nm), on the VO_2 thickness for VO_2 in (a) semiconducting phase and (b) metallic phase. The scattering peak wavelength is indicated by the black line.

The spectral blueshift seen for all fixed geometries, when the underlying VO_2 layer is transitioned from semiconducting to metallic phase can mainly be attributed to the difference in the real part of the dielectric permittivity. If a simplified case is considered, the polarizability (α) of a small (r « λ) Au sphere surrounded by VO_2 can be obtained by solving the Laplace equation. In the case of dipolar excitation, the polarizability can be given as

$$\alpha(\lambda) = r^3 \frac{\tilde{\varepsilon}_{Au}(\lambda) - \tilde{\varepsilon}_{VO_2}(\lambda)}{\tilde{\varepsilon}_{Au}(\lambda) + 2\tilde{\varepsilon}_{VO_2}(\lambda)} \tag{5.2.1}$$

The resonance condition is when the real part of the denominator vanishes i.e. $\varepsilon_{Au}(\lambda) + 2\varepsilon_{VO_2}(\lambda) = 0$ or $\tilde{\varepsilon}_{Au}(\lambda) = -2\tilde{\varepsilon}_{VO_2}(\lambda)$

The real part of the Au dielectric permittivity is < 0 in the spectral region between 200 - 1000 nm and becomes increasingly negative with increasing wavelength. As the real part of the dielectric permittivity of VO_2 decreases from the semiconducting phase to the metallic phase, the resonance condition is satisfied at a shorter wavelength when

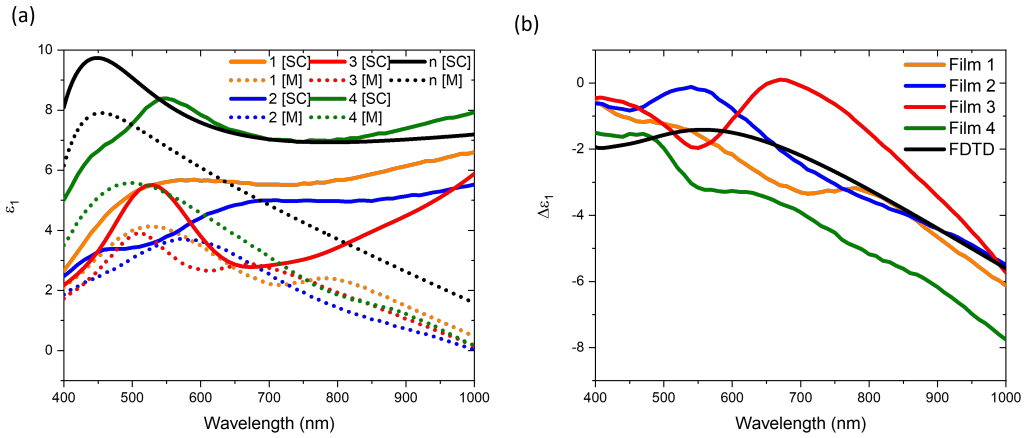

Figure 5.7: (a) Comparison of ε_1 value in semiconducting phase (solid line) and metallic (dotted line) used in numerical simulations (black line) to four from literature.[134] (b) Comparison of $\Delta\varepsilon_1(\varepsilon_1[M] - \varepsilon_1[SC])$ for the values of ε_1 used in numerical simulation (black line) with four from literature.

VO_2 is in its metallic phase. This results in the blueshifted plasmon resonance peak for the metallic phase compared to the semiconducting phase, and a decrease in peak scattering cross-section. Despite the decreased scattering peak, due to the broadness of the resonance, a region of increased cross-section can be observed. As the shift in the wavelength is highly dependent on the difference in the real part of the dielectric function, a comparison of the values used for the numerical simulations was made to four values from literature[134] and is shown in Fig. 5.7. The change is the real part of the dielectric function used in the simulations presented in this work are comparable to others seen in literature[135] and in some cases more conservative.[134]

To examine the impact of nanoparticle shape on the spectral position of the longitudinal scattering peak, three nanoparticle shapes are considered namely nanorods, nanocuboids and nanodiscs. The response of nanorods and nanocuboids with lengths of 180 nm and 230 nm and nanodiscs of diameter 180 nm on a VO_2 thin film of varying thickness were considered. The width and height of the rod and cuboid single nanoparticle structures were fixed at 90 nm and 40 nm, respectively to allow direct comparison between the shapes. In the case of the 180 nm long nanoparticles, for VO_2 in semiconducting phase, the resonance peak of the cuboids is the furthest into the infrared. The cuboid resonance peak is between 1135 - 1415 nm, dependent on the thickness of the

underlying VO_2 layer. The peak resonance response of the nanodisc, in the semiconducting phase, is between 955 - 1270 nm, a blueshift of up to 295 nm compared to the cuboids. The nanorods demonstrate a further blueshift in the semiconducting scattering peak between 870 - 1005 nm. This significant redshift in peak scattering wavelength for nanoparticles with sharper edges is consistent with previous studies.[136] However, upon the VO_2 phase transition to metallic phase, the cuboid scattering peak is significantly less redshifted when compared to the nanodisc and nanorod scattering peak wavelength. The cuboid, disc and rod resonance peak wavelengths lie in the ranges 815 - 925 nm, 755 - 825 nm and 790 - 820 nm, respectively. Averaging the wavelength shift ($\Delta\lambda$) over all VO_2 thicknesses up to 200 nm results in an average $\Delta\lambda$ of 148 nm for the rods, 338 nm for the discs and 501 nm for the cuboid of similar length. in the case of the larger Au nanorods, an average $\Delta\lambda$ of 317 nm is seen. It is noted that not only is the 230 nm length nanorod plasmon peak significantly blueshifted compared to the 180 nm cuboid for VO_2 in semiconducting phase, in metallic phase the 230 nm nanorod plasmon peak is only 40 nm redshifted when compared to the smaller cuboid. This indicated that the rounding of the plasmonic nanostructure has a significant impact on the magnitude of $\Delta\lambda$ when transitioning between the VO_2 phases. This is attributed to the polarization charges being highly localised in the corners of the cuboid structure and therefore having a larger interaction with the VO_2 thin film surface. The resonance feature for the 230 nm long nanocuboid when VO_2 is in semiconducting phase is at 1335 nm for 10 nm VO_2 thickness and redshifts above 1500 nm for thicker VO_2, beyond the range of interest in this work. In the metallic phase the resonance feature again lies in the wavelength range between 800 - 900 nm indicating a plasmon shift of > 600 nm. It is noted that, as for the other nanoparticles, for the semiconducting phase there is a redshift in peak wavelength with increasing VO_2 thickness, while increasing metallic phase VO_2 thickness blueshifts the scattering spectrum. Full scattering spectra of the Au nanoparticles for both VO_2 phases as a function of film thickness are given in the Appendix.

Despite the large shift in the plasmon peak wavelength, a decrease in the scattering

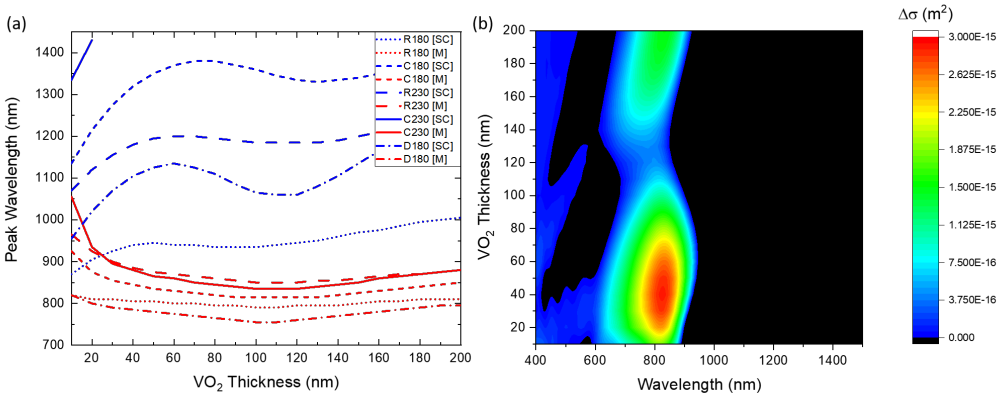

Figure 5.8: The dependence of the plasmon resonance peak wavelength on VO_2 thickness for five Au nanoparticles and VO_2 in semiconducting [SC] and metallic [M] phases under longitudinal excitation. Nanorods of lengths 180 nm and 230 nm are labelled R180 and R230, respectively, nanocuboids of length 180 nm and 230 nm labelled C180 and C230, respectively and nanodiscs of diameter 180 nm are labelled D180. The width and height of the nanorods and nanocuboid are fixed at 90 nm and 40 nm. (b) Contour map depicting change in scattering cross-section $\Delta\sigma$ ($\sigma_M - \sigma_{SC}$) for a Au nanocuboid (Length = 230 nm, Width = 90 nm, Height = 40 nm) with varying VO_2 thickness. Coloured sections indicate an increase in scattering as VO_2 transitions to its metallic phase. Black regions indicate a decrease in scattering as VO_2 transitions to its metallic phase.

cross-section in the metallic phase results in significant spectral overlap of the scattering spectra for the two phases of VO_2 in the visible and NIR. A contour map of the change in scattering cross-section as a function of wavelength and VO_2 film thickness can be seen in Fig. 5.8 (b) for the 230 nm length Au nanocuboid. The map indicates the region where the VO_2 phase transition from semiconducting to metallic results in an overall increase in scattering cross-section. A maximum $\Delta\sigma$ ($\sigma_M - \sigma_{SC}$) occurs at 830 nm for 40 nm VO_2 thickness. A second region of increased $\Delta\sigma$ occurs for thicker VO_2 and, while the plasmonic wavelength shift is larger, increasing VO_2 thickness results in a lower scattering cross-section due to increased quenching making thicker film VO_2 less attractive for implementation in plasmonic devices. Additional studies for nanodisc and nanorod geometries (contour maps given in Appendix) indicate that 30 - 50 nm VO_2 thin films demonstrate an increase in scattering cross-section as VO_2 transitions from semiconducting to metallic phase.

Dimer structures are considered highly advantageous due to the greatly enhanced local

electric field in the gap region between dimer elements. The development of a tunable field enhancement can be employed to provide an enhancement mechanism for coupled quantum emitters. For direct comparison to single nanoparticle structures considered in the previous section, the dimer structures are simulated with similar overall dimensions. A dimer gap of 10 nm is considered in all cases as this is an experimentally feasible dimer gap that allows the placement of a quantum dot (typical radius 6 nm)[137] within the gap.

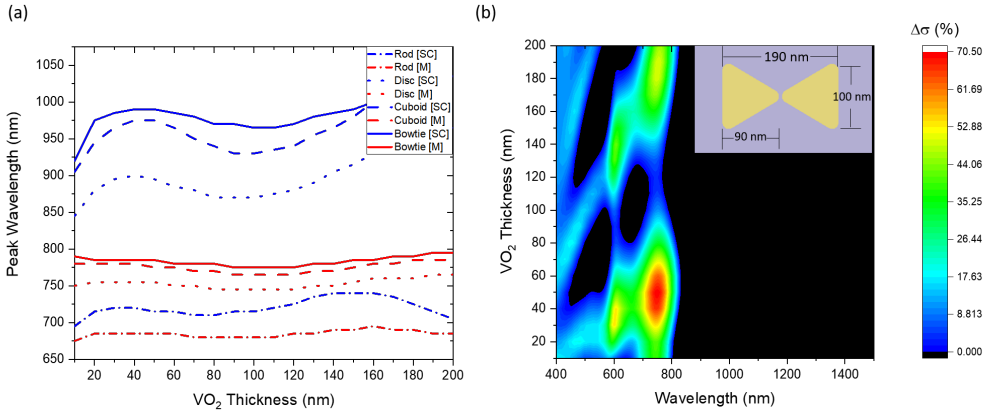

Figure 5.9: Dependence of the plasmon resonance peak wavelength on VO_2 thickness for a Au rod dimer (Rod length = 90 nm, Height = 40 nm, Gap = 10 nm), disc dimer (Disc radius = 45 nm, Height = 40 nm, Gap = 10 nm), cuboid dimer (Length = 90 nm, Height = 40 nm, Gap = 10 nm) and bowtie dimer (Perpendicular bisector = 90 nm, Height = 40 nm, Gap = 10 nm) for semiconducting [SC] and metallic [M] phase VO_2 under longitudinal excitation (b) Contour map depicting $\Delta\sigma(\%)[100 \times \frac{\sigma_M - \sigma_{SC}}{\sigma_{SC}}]$ for the Au Bowtie Dimer (Perpendicular Bisector = 90 nm, Height = 40 nm, Gap = 10 nm). Coloured sections indicate an increase in scattering as VO_2 transitions to its metallic phase. Black regions indicate a decrease in scattering as VO_2 transitions to its metallic phase. A schematic of the bowtie dimer structure is shown in the inset of panel (b).

Fig. 5.9 shows the spectral position of the scattering peak for light polarized along the long axis for a rod dimer (Rod length = 90 nm, Height = 40 nm, Gap = 10 nm), disc dimer (Radius = 45 nm, Height = 40 nm, Gap = 10nm), cuboid dimer (Length = 90 nm, Height = 40 nm, Gap = 10 nm) and bowtie dimer (Perpendicular bisector = 90 nm, Height= 40 nm, Gap = 10nm). Similar to the single nanoparticles, there is a significant redshift of the plasmon peak for increasing thickness of semiconducting phase VO_2. In the metallic phase, only a nominal 20 nm redshift is observed for all structures. Over the range of VO_2 film thicknesses there is an average peak shift of 36

nm, 148 nm, 195 nm and 202 nm for the rod, disc, cube and bowtie dimer structures, respectively, after the VO_2 phase transition. In Fig. 5.9(b) the $\Delta\sigma$ contour plot for longitudinal excitation indicates that a maximum percentage increase of 70% in the scattering cross-section occurs at 750 nm for a 50 nm thick VO_2 film. This region corresponds to a local maximum in $\Delta\lambda$ (205 nm). As before the bottom lobe in Fig. 5.9(b) is more favourable due to the reduced damping with a thinner VO_2 film. In the case of the rod dimer the region of increased scattering is blueshifted to 640 nm with maximum percentage increase of 75% for a 40 nm thick VO_2 film. Additional plots indicating the regions of increased scattering cross-section for disc, cuboid and rod dimer are included in the Appendix.

The major advantage of the bowtie structure is the enhanced electric field intensity concentrated between the pointed triangular elements. For investigation of the E-field enhancement a Au bowtie dimer structure (Perpendicular bisector = 90 nm, Height = 40 nm, Gap = 10 nm) is considered. Fig. 5.10 shows the electric field intensity in the gap region between the dimer elements as a function of wavelength and z-position for a 10 nm film of both VO_2 phases. The plane z = -20 nm indicates the VO_2 - nanostructure interface and z = 20 nm corresponds to the top of the dimer structure. The VO_2 transition blueshifts the maximum E-field intensity from $\sim$ 960 nm to $\sim$ 820 nm as seen in Fig. 5.10. While the transition results in a decrease in the maximum E-field achieved, at particular wavelengths the E-field is increased. The electric field intensity maps at 790 nm are in Fig. 5.10 (c) and (d). The VO_2 phase transition effectively increases the strength of the field between the dimer elements and shifts the region of enhancement closer to the top surface of the dimer. A positive ΔE^2 ($E_M^2 - E_{SC}^2$) of 90 is observed at $\lambda = 820$ nm and an electric field intensity enhancement of >3.6 is observed at λ = 790 nm, indicated in Fig. 5.10. These enhancements are ideal for enhancing the emission of coupled emitters. Additionally, the reshaping of the E-field profile with significant enhancement at the top surface of the nanoparticle has potential applications in enhancing the interactions seen in 2D material - plasmonic hybrid structures.[138]

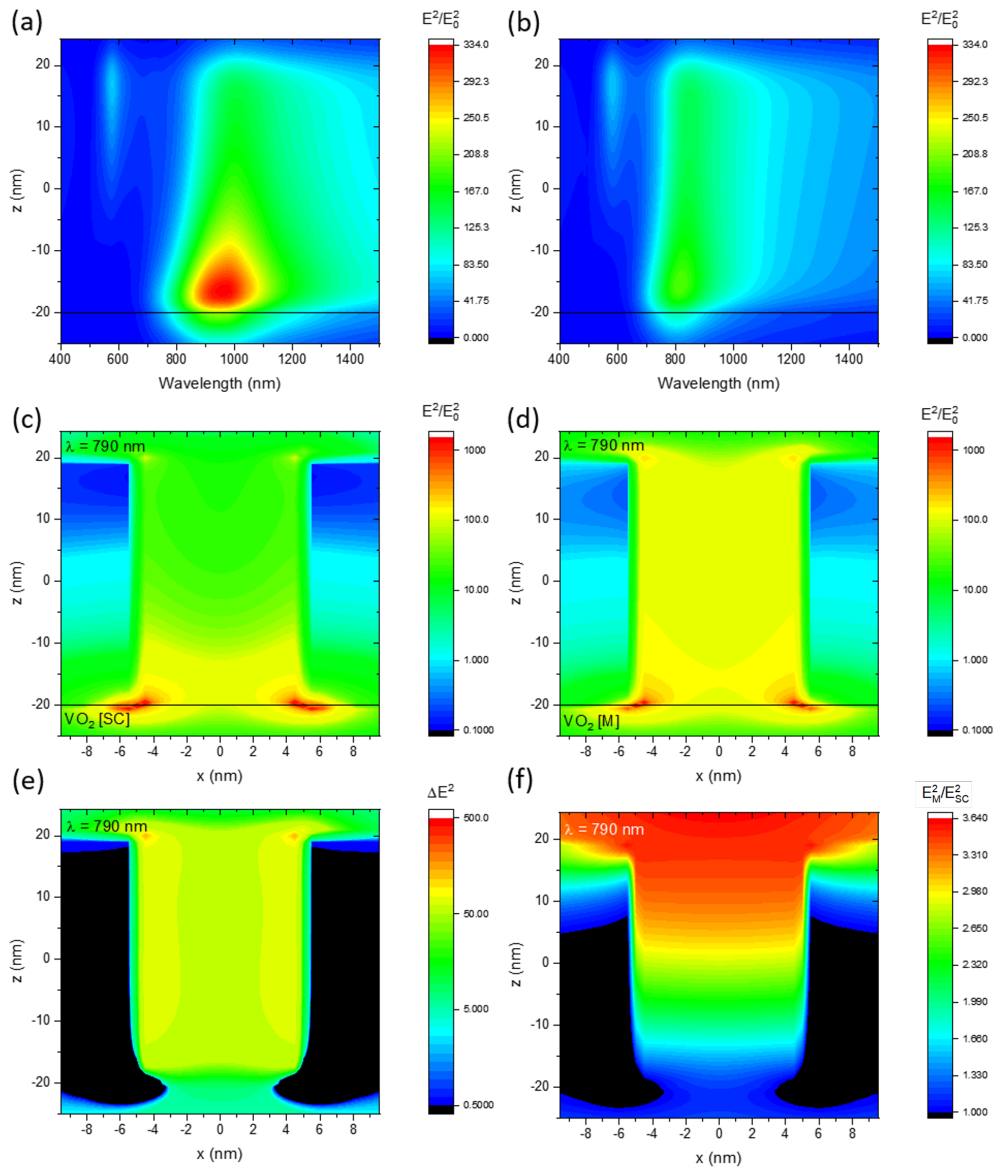

Figure 5.10: Contour maps indicating E-field intensity between the bowtie elements as a function of dimer height (z) for VO_2 (10 nm) in (a) semiconducting phase and (b) metallic phase. The plane z = -20 nm corresponds to the dimer - VO_2 interface. z = 20 nm indicates the top of the dimer structure. The electric field intensity maps for λ = 790 nm between dimer elements as a function of x-position (along dimer axis) and z-position (along dimer height, perpendicular to VO_2 plane) for VO_2 (10 nm) in (c) semiconducting phase and (d) metallic phase. (e) ΔE^2 ($E_M^2 - E_{SC}^2$) between dimer elements as a function of x-position (along dimer axis) and z-position (along dimer height) for λ = 790 nm and 10 nm VO_2 thickness (f) E_M^2/E_{SC}^2 for λ = 790 nm and 10 nm thickness. All maps are calculated for longitudinal excitation along the dimer axis.

When the same structure is considered on a 30 nm VO_2 film, a redshift in the position of the peak E-field enhancement is observed. This is accompanied by a decrease in peak E-field intensity. Despite the reduced E-field intensity in both phases a larger

E-field enhancement of 7.08 is observed. E-field maps for the bowtie structure on 30 nm VO_2 are included in the Appendix.

The E-field enhancement between the VO_2 phases for the cuboid dimer structure (Length = 90 nm, Width= 90 nm, Height = 90 nm, Gap = 10 nm) on VO_2 (10 nm) is similar to the bowtie dimer case with an enhancement of approximately 3.6. However, the ΔE^2 value is reduced as the flat edges of the cuboid structure result in a lower E-field enhancement. E-field maps for the cuboid dimer structure are also included in the appendix.

5.2.2 Au nanoparticles on VO_2 with Au backreflector

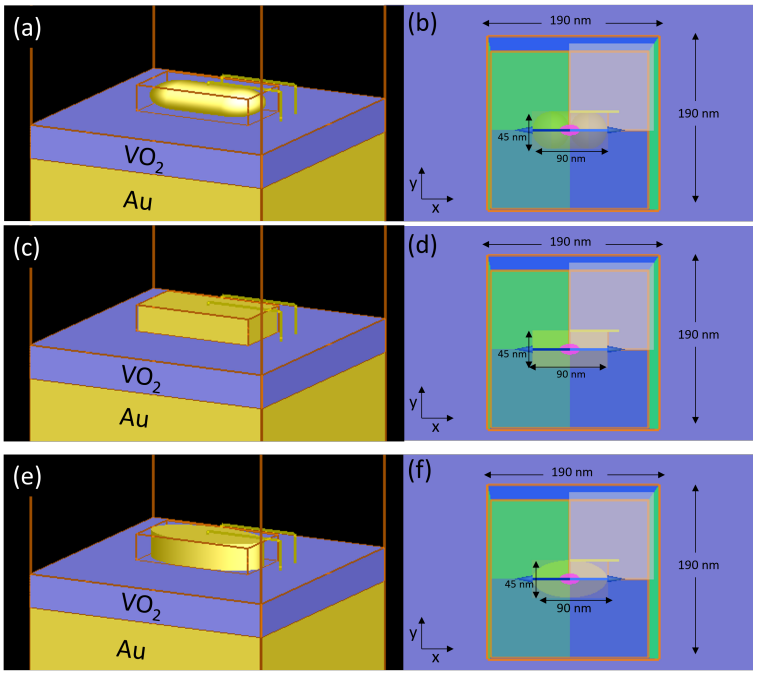

Figure 5.11: FDTD schematic of a unit cell for a periodic array of (a) Au nanorods (c) Au nanocuboids and (e) Au nanoellipses on VO_2 with Au backreflector. XY view of (b) Au nanorod (d) Au nanocuboid and (f) Au nanoellipse (Length = 90 nm, Width = 45 nm, Height = 40 nm) on VO_2 (Thickness = 50 nm). The unit cell has a length and width of 190 nm with periodic boundary conditions. The plane wave excitation source is polarized along the longitudinal axis (x-axis).

In this section the reflectance of hybrid structures comprising of periodic Au nanoparticles coupled to thin film VO_2 on an Au backreflecting layer is calculated and compared to the reflectance seen for periodic Au nanoparticles coupled to thin film VO_2 with no

backreflecting layer and planar VO_2 on a Au backreflector without plasmonic nanoparticles. The impact of Au nanoparticles on the colour switching seen upon the VO_2 transition is examined with and without the backreflecting layer. Additionally, the impact of the backreflecting layer on the enhanced E-field surrounding the plasmonic particle when VO_2 is in semiconducting and metallic phase is considered.

For the investigation, three periodic nanostructures are considered, namely nanorod, nanocuboid and nanoellipse. In each case the reflectance of the hybrid nanostructure is considered for nanoparticle length of 180 nm and 90 nm. The width of these particles is 90 nm and 45 nm, respectively, with height fixed at 40 nm. The unit cell for the periodic structure has a side length of 280 nm in both x and y directions for the larger nanoparticles and 190 nm for the smaller nanoparticles. This periodicity is chosen so that there is a 100 nm gap between adjacent nanoparticles along the longitudinal axis, the direction of excitation within the FDTD simulations. A schematic of the FDTD simulation space with the nanoparticle geometries is shown in Fig. 5.11.

The reflectance spectra of the nanoparticle arrays for 50 nm VO_2 is first considered. From Fig. 5.12 (a) it can be seen that the periodic arrays of nanoparticles with flat tops, i.e. nanocuboid and nanoellipse, show an increased reflectance when compared to the bare VO_2 in both phases with the nanocuboid having the higher reflectance peak ~ 0.4. The addition of the periodic array results an overall decrease in transmittance with a nanoparticle dependent local minimum for VO_2 in semiconducting phase, seen in Fig. 5.12 (b). These minimum values occurs at 885 nm, 825 nm and 670 nm for the cuboid, ellipse and rod, respectively, with the nanocuboid array having the largest transmittance modulation of 0.2 from the plane VO_2 case. For VO_2 in metallic phase similar modulation is seen for the nanocuboid. Fig. 5.12 (c) demonstrates a large change in reflectance due to thin film effects caused by the addition of a backreflecting Au layer. The modulation in reflectance between the two VO_2 phases is significantly greater than for the case seen in Fig. 5.12 (a) with $\Delta R \sim 0.42$ for the nanocuboid case. The local minimum wavelength, seen in the planar VO_2 with a Au backreflecting layer case, is nanoparticle array dependent and is tunable over a broad wavelength range by

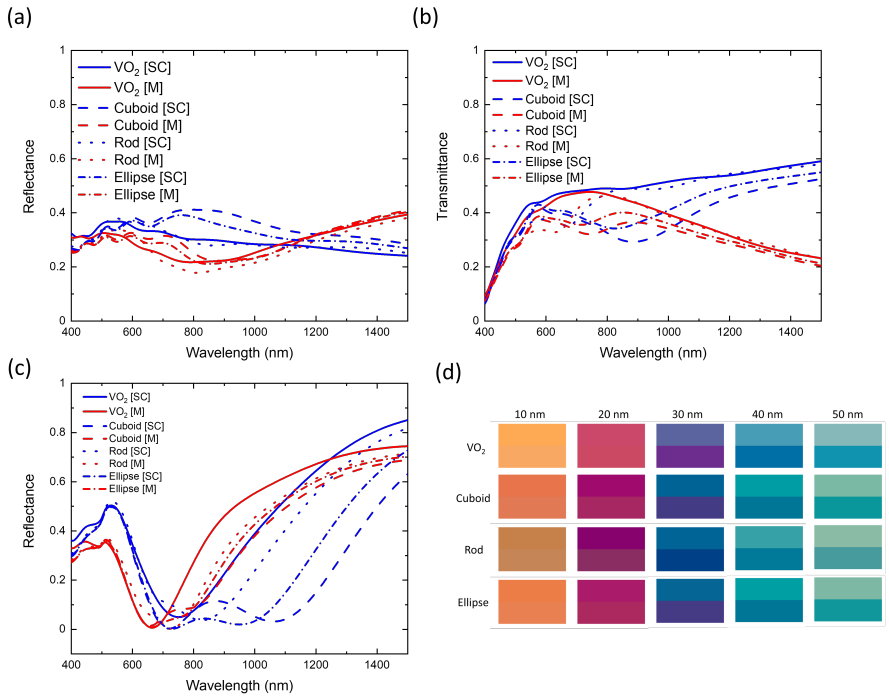

Figure 5.12: (a) Reflectance and (b) transmittance spectra of periodic nanostructures (Length = 90 nm, Width = 45 nm, Height = 40 nm, Period = 190 nm) on VO_2 (Thickness = 50 nm). (c) Reflectance spectra of periodic nanostructures on (Length = 90 nm, Width = 45 nm, Height = 40 nm, Period = 190 nm) on VO_2 (Thickness = 50 nm) with a back-reflecting Au layer (d) CIE colours with VO_2 thicknesses between 10 - 50 nm.

the choice of nanoparticle array when the underlying VO_2 layer is in semiconducting phase. The points of minimum reflectance, with the addition of the nanoparticle array are significantly closer to 0, with a minimum reflectance of approximately 0.28% at 720 nm for the nanocuboid array when VO_2 is in semiconducting phase. The points of minimum reflectance can be translated into points of near perfect absorptance as there is negligible transmittance due to the Au backreflecting layer. A comparison of the CIE colour from the reflectance spectra of the nanoparticle arrays is shown in Fig. 5.12(d) The nanoparticle arrays demonstrate greater colour contrast between the VO_2 phases for thin films, however the colour change is comparable to the planar VO_2 case for film thicknesses > 50 nm.

Next, the reflectance spectra of the nanorod arrays are shown as a function of the thickness of the underlying VO_2 layer (Fig. 5.13). A distinct change in the reflectance for VO_2 in semiconducting and metallic phase is demonstrated for the case with no

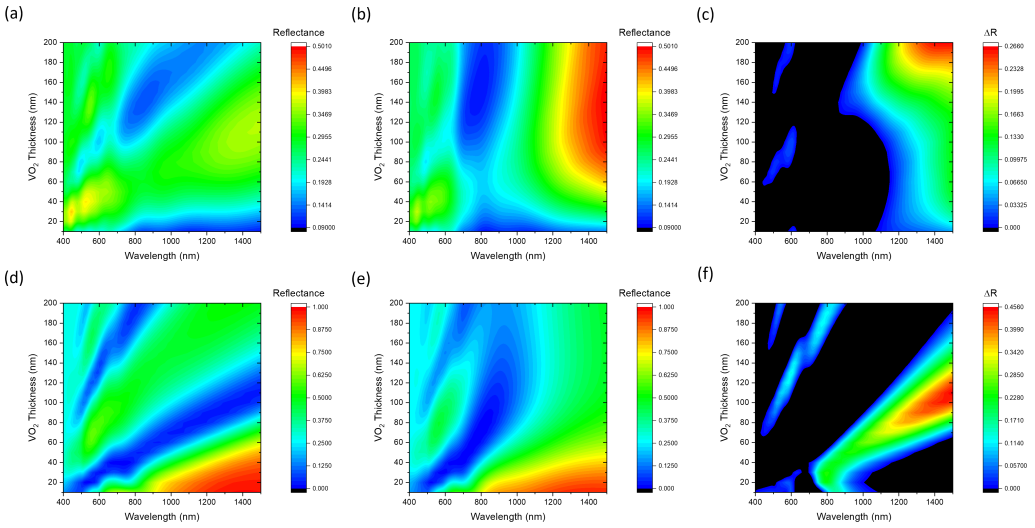

Figure 5.13: Reflectance spectra of a periodic array of Au nanorods (Length = 90 nm, Width = 45 nm, Height = 40 nm, Period = 190 nm) as a function of thin film thickness with no backreflecting metal layer for VO_2 in (a) semiconducting phase and (b) metallic phase. (c) ΔR ($R_M - R_{SC}$) for the periodic nanostructure without a backreflecting layer. Reflectance spectra of the periodic nanorod array with a back reflecting metal layer with VO_2 in (d) semiconducting phase and (e) metallic phase. (f) ΔR ($R_M - R_{SC}$) for the periodic nanostructure with an Au backreflecting layer.

back reflecting layer. It is noted that large ΔR in this case is only seen at longer wavelengths and for thicker VO_2 thin films. Additionally, as seen previously, there is a reflectance $< 50\%$ across all thicknesses. The reflectance spectra with the nanoarray has a similar profile to the case with no nanoarray. A distinct region of increased reflectance when the VO_2 is in metallic phase can be seen in the visible region which redshifts with increasing VO_2 thickness. For comparison, the reflectance spectra for the nanoparticle arrays (Length = 90 nm, Width = 45 nm, Height = 40 nm, Period = 190 nm) are compared to the reflectance spectra acquired from the same nanoparticle shapes with larger dimensions (Length = 190 nm, Width = 90 nm, Height = 40 nm, Period = 280 nm). The larger rods consist of $\sim 20\%$ of the periodic unit cell opposed to the $\sim 11\%$ of the smaller rods. The larger nanoparticle reflectance as a function of VO_2 layer thickness is shown in Fig. 5.14. From this figure it can be seen that the reflectance is redshifted in comparison to the smaller rods. The peak reflectance is near 1500 nm for the smaller rods for VO_2 in semiconducting phase but is redshifted beyond 1500 nm, the simulation limit, in the case of the larger rods. Additional contour maps

for the nanocuboid case and nanoellipse case are given in the Appendix section.

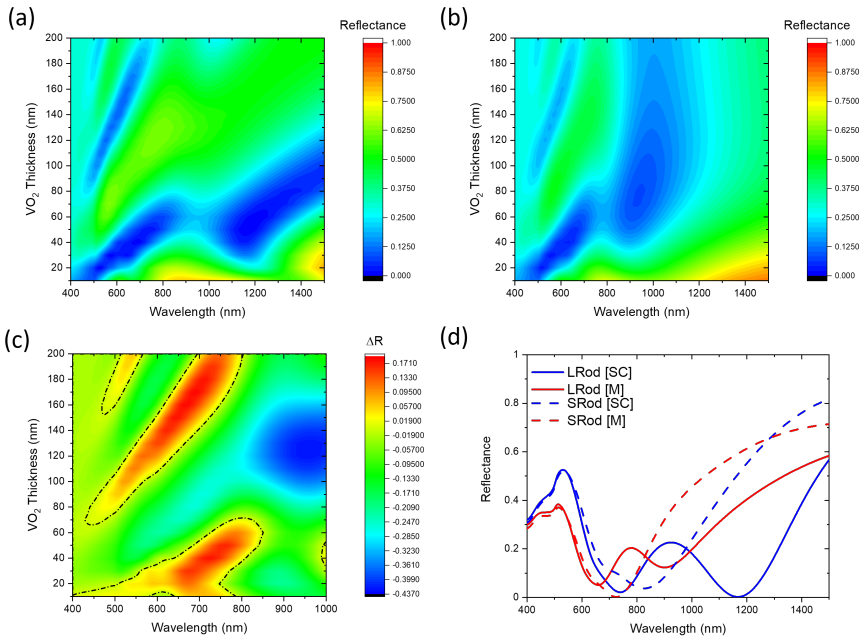

Figure 5.14: Reflectance spectra of a Au nanorod array (Length = 180 nm, Width = 90 nm, Height = 40 nm, Period = 280 nm) for VO_2 in (a) semiconducting phase and (b) metallic phase. (c) ΔR ($R_M - R_{SC}$) spectra for Au nanorod array (d) Comparison between Au nanorod array with larger and smaller array elements on VO_2 (50 nm) called LRod and SRod, respectively. These correspond to Length = 180 nm, Width = 90 nm, Period = 280 nm and Length = 90 nm, Width = 45 nm, Period = 190 nm, respectively.

To conclude this section, the addition of nanoparticles onto thin film VO_2 with a backreflecting Au layer has some impact in shifting the position of minimum reflectance but does not significantly impact the reflectance spectra within the visible regime, as seen from the CIE colour generated. However, as will be shown in the next section, the Au backreflecting layer has a significant impact on the E-field enhancement surrounding the metallic nanoparticles.

E-field

The impact of a Au backreflecting layer on the E-field intensity enhancement surrounding the plasmonic nanoparticles is examined. To simulate this, a 1D DFT monitor is placed 5 nm from the nanoparticle edge in the x-direction perpendicular to the plane of the VO_2 so that it records data in the z-axis along the height of the nanoparticle. For each nanoparticle the dimensions are as in Fig. 5.11 (Length = 90 nm, Width = 45 nm, Height = 40 nm, Period = 190 nm).

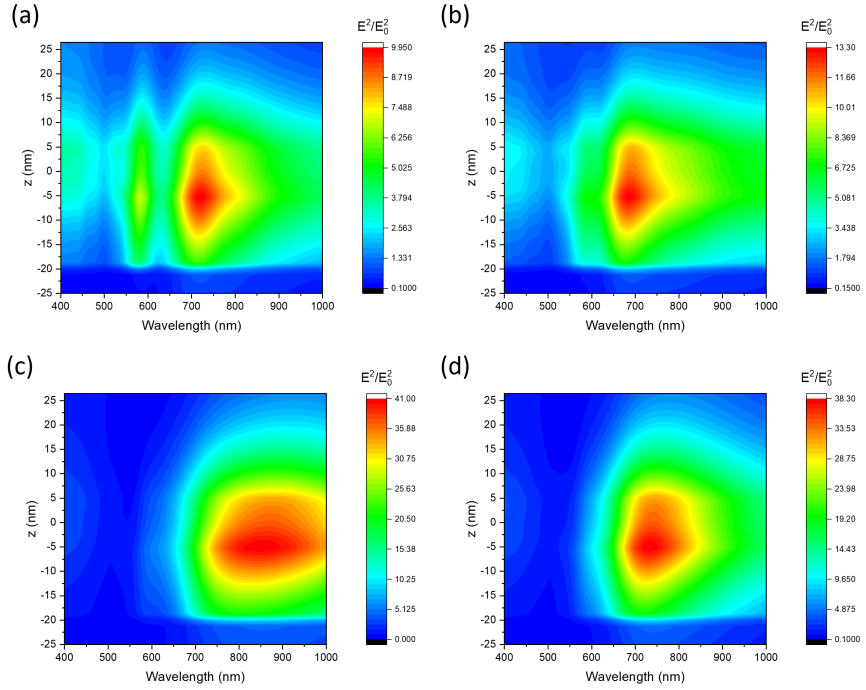

Figure 5.15: E^2/E_0^2 Map for a Au Nanorod array (Length = 90 nm, Width = 45 nm, Height = 40 nm, Period = 190 nm) on VO_2 (Thickness = 50 nm) for VO_2 in (a) semiconducting phase and (b) metallic phase with no Au backreflecting layer and in (c) semiconducting phase and (d) metallic phase with an Au backreflecting layer.

From Fig. 5.15(a) a maximum E-field intensity enhancement of ~ 10 is seen near 720 nm for the nanorod on VO_2 (50 nm) in the semiconducting phase. As with the bowtie dimer structures discussed previously, the peak E-field enhancement blueshifts upon the VO_2 phase transition. For VO_2 in metallic phase (Fig. 5.15 (b)) the peak E-field blueshifts ~ 35 nm to 685 nm with an increase in the peak enhancement to 13. In this case the peak E-field in both phases is at a point 15 nm above the VO_2 film or 5nm below the half height of the nanorod. From Fig. 5.15 (c) the peak E-field intensity at

the nanoparticle edge is seen to increase by a factor of 4, with a distinct redshift where the maximum E-field enhancement is seen. This region is significantly broader and is centred around 860 nm, a 140 nm redshift compared to the same configuration without the Au backreflecting mirror. A marginal decrease in the peak E-field enhancement is seen for metallic phase VO_2 with a 135 nm blueshift in the peak response. The shifts in peak E-field intensity and wavelength result in a ΔE^2 of 6.3 at 665 nm for the VO_2 case and 14.7 at 685 nm for the VO_2 with Au backreflecting layer.

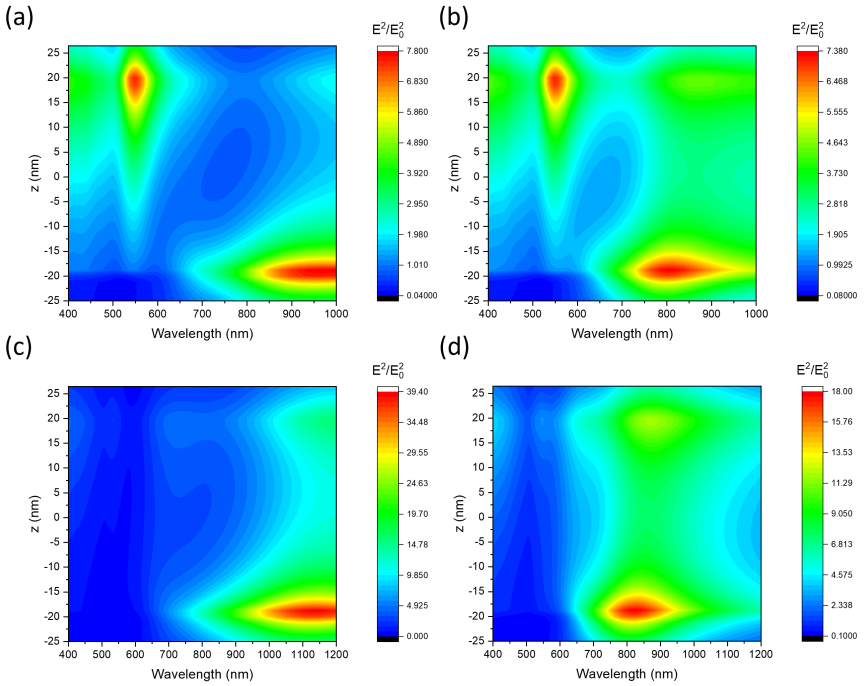

Figure 5.16: E^2/E_0^2 Map for Au Nanocuboid array (Length = 90 nm, Width = 45 nm, Height = 40 nm, Period = 190 nm) on VO_2 (Thickness = 50 nm) for VO_2 in (a) semiconducting phase and (b) metallic phase with no Au backreflecting layer and in (c) semiconducting phase and (d) metallic phase with an Au backreflecting layer.

For the nanocuboids case, the peak E-field enhancement occurs at the top edge and the bottom edge-VO_2 interface. As the E-field hotspots surrounding the nanoparticle are shifted to the edges of the nanostructure, like in the bowtie dimer case, a reshaping of the E-field profile can be observed. Comparing Fig. 5.16 (a) and (b) representing the nanocuboid on semiconducting and metallic VO_2 respectively, the maximum E-field at the top edge of the nanoparticle at 550 nm doesn't change substantially between the VO_2 phases. The maximum E-field at the interface blueshifts from 970 nm to

810 nm as a result of the phase transition. The reshaping of the E-field results in the greatest increase in the E-field occurring at 770 nm at the interface and at 845 nm at the top edge of the nanocuboid. The addition of the Au backreflecting layer redshifts the peak E-field intensity to 1135 nm (Fig. 5.16(c)). The E-field strength is significantly enhanced compared to the case with no Au mirror. It's noted that the strong E-field enhancement at the top edge of the nanocuboid near 550 nm is significantly reduced. For VO_2 in the metallic phase, the peak resonance blueshifts to 925 nm with a significant decrease in intensity (Fig. 5.16(d)). The largest increase in the E-field intensity is located at the top edge of the nanocuboid with a $\Delta E^2 = 7$ at 860 nm. This increase in the E-field strength is twice the magnitude seen without the backreflecting Au layer.

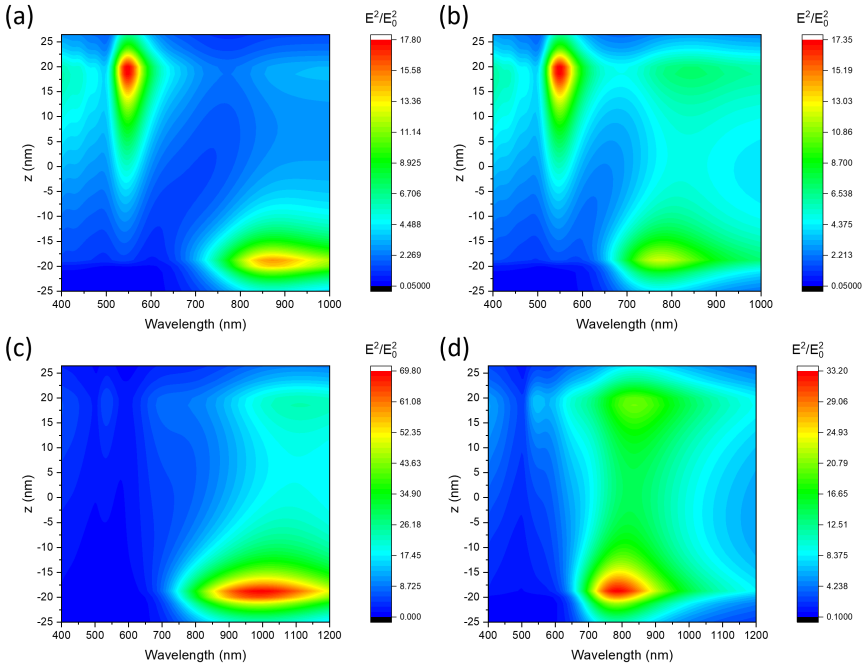

Figure 5.17: E^2/E_0^2 Map for Au Nanoellipse array (Length = 90 nm, Width = 45 nm, Height = 40 nm, Period = 190 nm) on VO_2 (Thickness = 50 nm) for VO_2 in (a) semiconducting phase and (b) metallic phase with no Au backreflecting layer and in (c) semiconducting phase and (d) metallic phase with an Au backreflecting layer.

Next the E-field enhancement around the nanoellipse is considered. The response of the nanoellipse is similar to the nanocuboid due to their similarly well defined edges. However, as demonstrated in Fig. 5.17, the more pointed edge of the nanoellipse results in a stronger E-field at the top edge and at the bottom edge interface. For

the nanoellipse on VO_2 the maximum E-field enhancement at the top edge is 17.8 compared to 7.8 for the nanocuboid. The maximum E-field intensity blueshifts from the 875 nm to 775 nm indicating that the nanoellipse has a larger maximum E-field intensity at shorter wavelengths compared to the nanocuboid. For the VO_2 with the Au backreflecting layer the response is similarly higher and blueshifted compared to the nanocuboid case. An E-field enhancement of ~ 70 can be seen at 995 nm (Fig. 5.17 (c)) In metallic phase the region of maximum E-field is blueshifted to 785 nm. The blueshift and change in E-field profile due to the VO_2 phase transition results in regions where the E-field intensity is substantially in metallic phase. This is highlighted for the three nanoparticle shapes in Fig. 5.18.

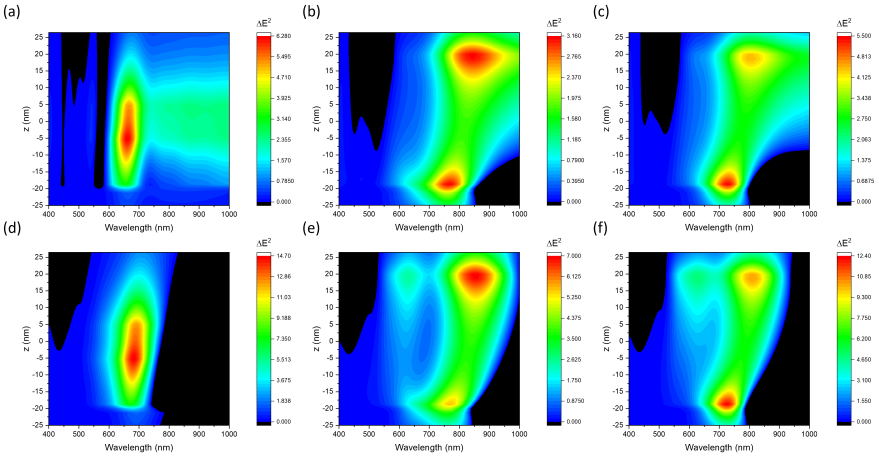

Figure 5.18: $\Delta E^2(\frac{E_M^2}{E_0^2} - \frac{E_{SC}^2}{E_0^2})$ for (a) nanorods (b) nanocuboids (c) nanoellipse on VO_2 (50 nm) and (d) nanorods (e) nanocuboids (f) nanoellipse on VO_2 (50 nm) with a backreflecting Au layer. Black regions indicate negative ΔE^2 i.e. regions where there is a decrease in E^2 as VO_2 transitions to its metallic phase.

From Fig. 5.18 the greatest increase in E-field intensity between the semiconducting and metallic VO_2 phase occurs for the nanorod. Inclusion of the Au backreflecting mirror layer results in a greater E-field intensity and therefore a greater contrast between the two phases. ΔE^2 is increased by a factor of > 2. Inclusion of the Au layer also results in a region at lower wavelengths where there is an increase in E-field intensity not seen when the Au layer isn't present. The greater overall E-field intensity and contrast between the E-field when VO_2 is in semiconducting and metallic phase along with the reshaping of the E-field profile seen makes the hybrid structure ideal

for applications where the enhanced field at higher temperatures can compensate for thermal losses.

Additionally, E-field profiles with VO_2 layers with 30 nm and 10 nm thicknesses are made for comparison. These E-field profiles are shown in the Appendix. A summary of the results for all three thicknesses (10,30,50) given for the nanoparticles on VO_2 with and without a Au backreflecting layer is given in Table. 5.1 and Table. 5.2, respectively.

From the tables clear trends can be seen. The nanoellipse has the greatest enhancement of the E-field in all cases, with the degree of enhancement decreasing with the VO_2 thickness. However, the addition of the Au layer reverses this trend, the degree of E-field enhancement increases with VO_2 thickness. Similar trends are seen for the nanocuboid, with significantly decreased E-field magnitude as discussed previously. In the case of the nanorods an increase in the maximum E-field can be seen upon the VO_2 phase transition. This is not seen for the other nanoparticle shapes as the maximum E-field is at the nanoparticle-VO_2 interface. From these results and Fig. 5.18 it can be seen that the VO_2 phase change can modify the plasmonic hotspots surrounding metallic nanoparticles.

Nanoparticles on VO_2						
VO_2	E^2_{Max}			λ (nm)		
	Rod	Cuboid	Ellipse	Rod	Cuboid	Ellipse
10 nm [SC]	17.54	13.98	29.68	690	840	810
10 nm [M]	19.17	12.58	21.05	670	780	750
30 nm [SC]	10.31	9.38	18.33	720	955	865
30 nm [M]	13.12	7.94	12.98	685	805	770
50 nm [SC]	9.94	7.79	14.94	720	975	875
50 nm [M]	13.25	7.38	12.19	685	805	775

Table 5.1: The maximum E-field intensity and corresponding wavelength for nanoparticles on VO_2

Nanoparticles on VO_2 with Au layer						
VO_2	E^2_{Max}			λ (nm)		
	Rod	Cuboid	Ellipse	Rod	Cuboid	Ellipse
10 nm [SC]	42.27/21.774	38.36/22.02	79.58/26.60	605/870	575/1410	565/1255
10 nm [M]	29.65/25.53	34.22/7.34	72.70/11.68	600/770	570/900	565/860
30 nm [SC]	53.75	33.16	57.77	790	1130	995
30 nm [M]	46.96	15.90	29.75	720	830	790
50 nm [SC]	40.98	39.26	69.62	850	1135	995
50 nm [M]	38.26	17.98	33.13	730	825	785

Table 5.2: The maximum E-field intensity and corresponding wavelength for nanoparticles on VO_2 with a Au layer. There are two values given for 10 nm case accounting for the max E-field at the top edge of the nanoparticle and at the bottom interface.

5.2.3 Experimental Plasmonic Tuning

Within this section, optical measurements of nanoparticle arrays fabricated on thin film VO_2 were performed. These nanoparticle arrays were patterned using a standard electron beam lithography technique as outlined in **Chapter 3**. The fabricated arrays of nanostructures are examined under white light illumination in both bright field and dark field modes, while single nanoparticle structures are examined in dark field. Nanoparticle arrays are then imaged using SEM to measure the dimensions of the fabricated nanoparticles. Measurements of nanoparticle dimensions from the SEM images were taken using the processing software ImageJ. The experimental spectra are compared to simulated spectra based on the average dimensions of the imaged nanoparticles.

To investigate the change in optical response of the fabricated nanostructures by actuation of the VO_2 phase change, the sample was mounted on the custom-built-heating stage and placed under bright field illumination. The sample was heated from room temperature through the critical temperature to 90 °C in steps of 5°C. The temperature was allowed to stabilise between each temperature measurement and the microscope focus adjusted to compensate for defocusing as a result of sample heating. Raw spectra were taken using a 100x objective and were treated in the standard way outlined in **Chapter 2** to give reflectance spectra. In Fig. 5.19 spectra from a Au nanorod array (Length = 160 nm, Width = 82 nm, Height = 40 nm, Period = 260 nm) on a 30 nm

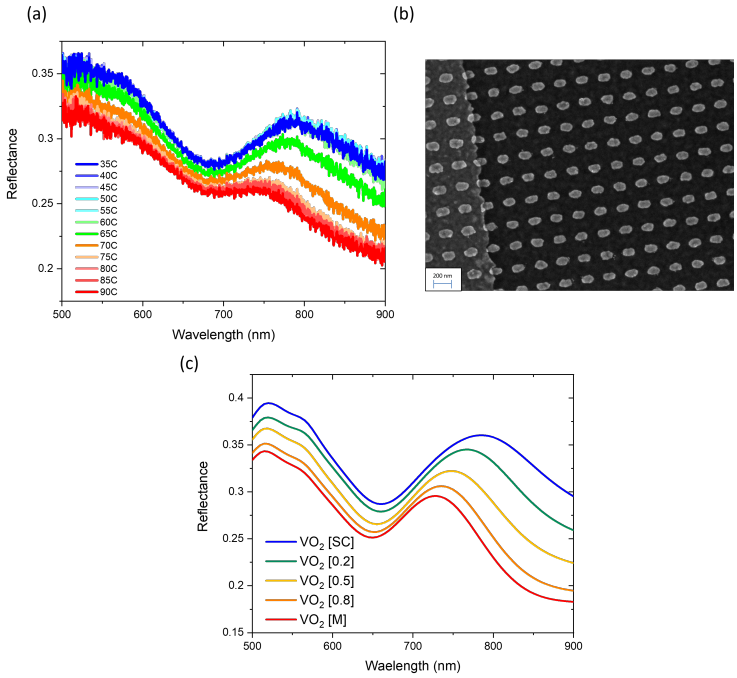

Figure 5.19: (a) Reflectance spectra of a nanorod array (Length = 160 nm, Width = 82 nm, Height = 40 nm, Period = 260 nm) on VO_2 (30 nm) at temperatures between 35 °C - 90 °C. (b) SEM image of nanorod array. (c) Simulated reflectance spectra of nanorod array based on dimension taken from SEM image. Reflectance spectra for VO_2 in semiconducting [SC] and metallic [M] phase with intermediate phases based on 0.2, 0.5 and 0.8 volume fractions of metallic phase VO_2 in semiconducting phase VO_2 are shown.

thick VO_2 are shown at temperatures above and below the VO_2 critical temperature (68 °C). The resonance feature is observed to blueshift from $\sim$ 790 nm to $\sim$ 750 nm upon the VO_2 transition. It is noted that there is no substantial change in reflectance for temperatures between 35 - 60 °C. The spectra taken at 65 and 70 °C show intermediate spectra indicating the VO_2 thin film has not fully made the transition from semiconducting to metallic phase. Spectra taken at 75 - 90 °C demonstrate significant modification indicating the thin film underlying the metallic nanoparticle is in metallic phase. ΔR from the peak response in semiconducting phase to metallic phase is $\sim$ 0.05, a 16% decrease. From the SEM image in 5.19 (b) the average dimensions of the fabricated nanorods are as follows; Length = 160 nm, width = 82 nm, height = 40 nm and period = 260 nm. FDTD simulations of the periodic nanorod array using the real dimensions from the SEM images are compared to the experimental spectra to confirm the shift in the peak resonance for the given VO_2 thickness is reasonable. The simu-

lated spectra are given in Fig. 5.19(c). For the simulated nanostructure the resonance wavelength shifts from 775 nm in semiconducting phase to 730 nm in metallic phase. The resonance of the simulated structure is $\sim$ 15 nm blueshifted in comparison to the experimental resonance. The variation is attributed to the distribution of the nanorod sizes in the real structure and the 5 nm titanium adhesion layer used in the fabricated structure.

To compare the effect of electrically actuated the VO_2 phase change on the nanorod array resonance feature Au contact pads were fabricated on the sample so that the Au wires crossed the nanoarray as shown in Fig. 5.20 (a). The CCD images given in Fig. 5.20 (b) for no applied voltage and 180 V, respectively, indicate a decrease in intensity when VO_2 is in metallic phase. A relatively high potential difference of 180 V was selected to ensure the metallic phase region is large enough to acquire reflectance spectra without interference from regions in semiconducting phase. The pixel range in the y-direction is reduced to diminish signal from the Au wires across the nanoarray.

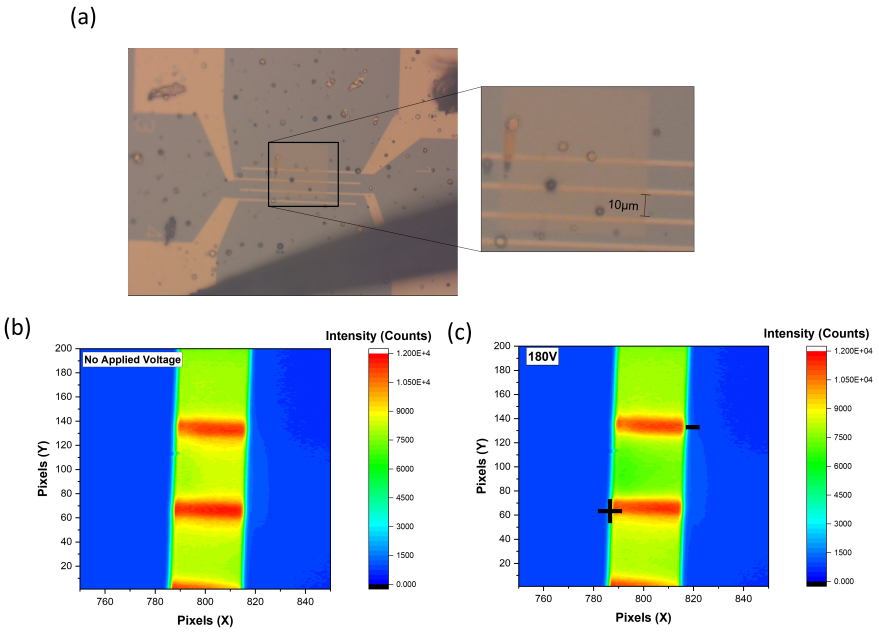

Figure 5.20: (a) Image of Au contact pads patterned over Au array. Inset shows wire spacing of 10 μm. (b) CCD image of nanaoarray with no applied voltage between the Au wires. (c) CCD image with 180 V applied voltage. The plus and minus symbols indicate which wire is at higher potential.

In Fig. 5.21 the reflectance of the plasmonic nanorod array (Length = 140 nm, Width = 140 nm, Height = 40 nm, Period = 200 nm) on VO_2 (30 nm) is compared at 25 °C and 90 °C, when the phase change is thermally actuated and at 0 V and 180 V applied voltage, when the phase change is electrically actuated. For both cases there is a similar blueshift in the resonance response indicating placing the nanoarray between wire elements is a viable way to reversibly tune the plasmonic response of the coupled nanoparticles.

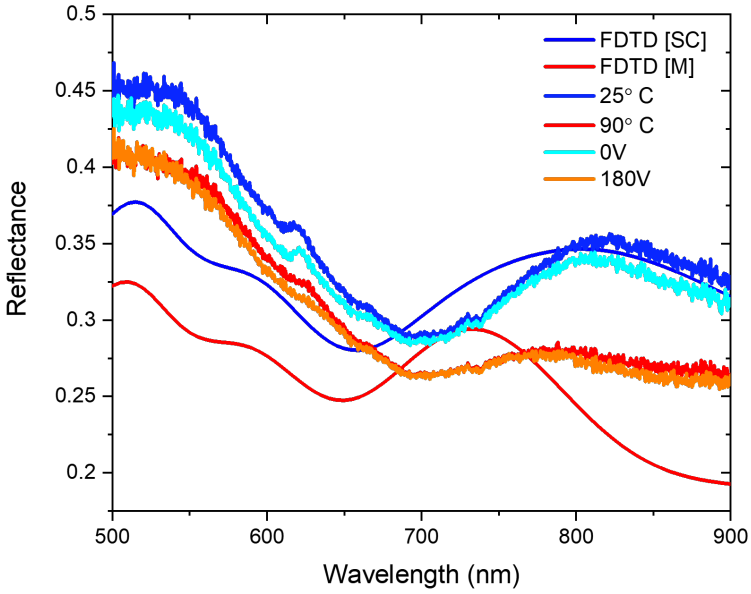

Figure 5.21: Comparison of simulated and experimental spectra for a nanorod array (Length = 140 nm, Width = 50 nm, Height = 40 nm, Period = 200 nm) on VO_2 (30 nm). The spectra are taken at 25°C, 90°C, 0 V and 180 V applied voltage.

Despite the large changes seen in simulations presented earlier in this chapter the resonance shifts seen in experiments are smaller. The smaller changes seen experimentally are attributed to the roughness variation in fabricated VO_2 films that isn't present in the simulated VO_2 thin films. Surface roughness in the VO_2 thin films can be accounted for within simulations by incorporating surface maps of the thin films taken by AFM. Additionally, a damping of the resonance feature with thicker VO_2 increases the difficulty in resolving the resonance feature and this is further exacerbated as the Andor 230i spectrometer is less sensitive at longer wavelengths where the resonance

features of nanoparticles with a large $\Delta\lambda$ lie, particularly the resonance for VO_2 in semiconducting phase.

5.3 Conclusion

In this chapter, single plasmonic nanoparticles and dimer nanostructures coupled to thin film VO_2 to realise widely tunable plasmon resonances are considered. The factors affecting the magnitude of the plasmon blueshift as the underlying VO_2 layer transitions from the low temperature semiconducting phase to the high temperature metallic phase are investigated. Single cuboid nanoparticles show significantly larger average $\Delta\lambda$ than rounded particles of similar dimensions with an average blueshift of 501 nm for the 180 nm long nanocuboid compared to 338 nm for a disc and 148 nm for a rod. For dimer structures, bowtie dimers demonstrate large shifts in the resonance coupled with a large E-field enhancement in the dimer gap rendering this kind of structure an ideal candidate in applications requiring E-field enhancements, as will be further discussed in **Chapter 6**. Additionally, the impact of an Au backreflecting layer on the E-field enhancement is examined. It was found that the Au mirror significantly increases the intensity of the plasmonic hotspot surrounding the nanoparticle coupled to the VO_2 thin film allowing for a greater E-field enhancement induced by the VO_2 phase change. Finally plasmonic tuning of nanoparticles on VO_2 films was experimentally demonstrated with good agreement with simulation. The tunable nanostuctures discussed in this chapter have great potential in many optoelectronic systems as sensing elements or as building blocks for the compensation of thermal quenching at elevated temperatures.

6 Luminescence Enhancement

6.1 Summary

This chapter investigates the modification in the luminescence of quantum emitters coupled to nanoparticles on thin film vanadium dioxide. The photoluminescence model used to determine the degree of enhancement when the VO_2 phase is switched is described in detail. The model allows for separate calculation of the contribution from the modified excitation rate and modified emission rate for emitters with dipole orientations parallel to the x,y and z axis of the simulation space. First the model is applied to calculate the modification to an emitters PL on a bare planar VO_2 with thicknesses up to 150 nm.

The main section of the chapter focuses on the modification of quantum emitters coupled to a Ag nanodisc structure. The impact of varying the various parameters of the system including the disc diameter, height, the choice of coupled emitter and the thickness of the underlying layer of PCM is examined. Additionally the impact of employing a protective silica layer and embedding the quantum emitters within this layer is shown.

The effect on the degree of photoluminescence enhancement for various volume fractions of metallic VO_2 in semiconducting VO_2 is also investigated.

Finally, analysis of the contributions to the enhanced photoluminescence of emitters, placed around a Ag nanodisc, are examined to determine which are most significant.

6.2 Introduction

Nanoscale light manipulation using plasmonic nanostructures has been at the center of scientific interest for past two decades.[139] Among the various applications of plasmonic nanoparticles, methods to modify the luminescence of coupled quantum emitters has been one of the areas of most interest, in particular methods to quench[48,140] , or enhance[48,139] , spectrally reshape[141,142] and modify the directionality of luminescence emission.[143] Various hybrid systems have been reported as candidates for luminescence modification, including single nanoparticles of various shapes ranging from standard morphologies such as spheres,[48] rods,[144] nano-shells[145] to more complex shapes such as nanostars.[146,147] Additionally, nanoparticle assemblies, such as dimers,[148] aggregates of randomly assembled nanoparticles[149] and well-ordered nanoparticles in arrays[150] can also offer luminescence modification.

In general, the photoluminescence of quantum emitters coupled to plasmonic nanostructures can be modified through two mechanisms, modification of the excitation rate and modification of the emission rate. Both mechanisms depend strongly on a number of factors including the spectral overlap of the quantum emitter's absorption and emission with the plasmon modes of the nanostructure, the size and morphology of the nanostructure, the distance between the quantum emitter and the nanostructure, and the orientation of the molecular dipole with respect to the nanostructure. Plasmonic nanostructures allow light to be concentrated in nanoscale regions close to their surface so that the local electric field intensity is substantially higher than the intensity of the incident electric field.[151] An emitter coupled to a plasmonic nanostructure will therefore experience a higher electric field and thus an excitation rate enhancement. Modification of the emission rate can be attributed to the effect of the nanoantenna. Since plasmonic nanostructures modify the local density of states,[152] the presence of the nanostructure in the proximity of an emitting dipole can alter the radiative decay rate and provide new loss mechanism and non-radiative decay pathways for the emitters, such as energy transfer.

While surface enhanced phenomena with nanostructures, such as luminescence modification[153] and surface enhanced Raman Scattering (SERS),[154,155] are well studied, there are few methods to alter or tune these effects via plasmon resonance tuning post fabrication. Previously reported methods rely on changes in the relative position of the emitters with respect to the nanostructure; by conformational changes of ligands attached to both the emitter and the nanostructure,[156] mechanically via manipulation with an AFM[157] tip or with the aid of elastic substrates.[158] However, these methods aren't suitable for photoluminescence (PL) tuning in various optoelectronic devices.

As was demonstrated in the previous chapter the interaction between nanoparticles and VO_2 thin films allows for significant tuning of the optical properties of the coupled nanoparticles and therefore can provide a platform for dynamically tunable photoluminescence of coupled quantum emitters.

For many applications incorporating quantum emitters, a high luminescence efficiency is important. High efficiencies are particularly important for applications in spectral converters for warm white LEDs,[159,160] electroluminescent devices[161] and solar concentrators.[162] The luminescence efficiency has a strong temperature dependence with significant quenching at elevated temperatures which can significantly reduce the efficiencies of devices incorporating quantum emitters. As VO_2 transitions to a metallic phase at elevated temperatures, it can act as the ideal platform for compensation for thermal quenching as the increased photoluminescence seen when VO_2 is in the metallic phase can make up for the thermal losses. By optimisation of the hybrid system, additional enhancement beyond thermal quenching compensation can be realised.

In this chapter, hybrid VO_2 - plasmonic Ag nanoparticle structures coupled to Alexa dye quantum emitters are examined and using a numerical model, the contributions to the modified photoluminescence are determined.

6.3 Photoluminescence Model

From the modelling point of view the photoluminesecence (PL) spectra of the quantum emitters within the hybrid nanosystem can be described by the following equation:

$$PL(\lambda) = I_{inc} N \sigma_{Abs}(\lambda_{Exc}) \cdot \Omega \cdot \eta \cdot f_0(\lambda) \tag{6.3.1}$$

where $f_0(\lambda) = PL_{exp}(\lambda)\frac{1}{\int PL_{exp}(\lambda)d\lambda}$ is the integral-normalised experimental PL spectrum, $PL_{exp}(\lambda)$, of the quantum emitter with $\int f_0(\lambda)d\lambda = 1$, I_{inc} is the incident excitation in W/m^2 and N is the number of emitters. For the purpose of simplification, in this work, the value of N is set to one. $\sigma_{abs}(\lambda_{Exc})$ is the absorption cross-section of the emitter at the laser excitation wavelength and Ω is a function accounting for experimental response function which includes the detection direction, detector area and sensitivity. This is chosen so that the total detected fluorescence radiance, called intensity, $I_{PL} = \int PL(\lambda)d\lambda)$ represents the total number of detected photons per second.

The following parameters, associated with the intrinsic optical properties of the quantum emitters, can be determined experimentally:

1. The molar extinction coefficient $\varepsilon_M(\lambda)$ from which the extinction cross-section $\sigma_{ext}(\lambda) = \ln(10)\frac{10^3}{N_A}\varepsilon_M(\lambda)$ can be calculated, where N_A is the Avogadro constant ($\approx 6.02 \times 10^{23}$). $\sigma_{ext}(\lambda) = \sigma_{Abs}(\lambda) + \sigma_{Scat}(\lambda) \approx \sigma_{Abs}(\lambda)$ since the scattering cross-section $\sigma_{Scat}(\lambda)$ of the emitter is negligible compared with the absorption cross-section $\sigma_{Abs}(\lambda)$, it can be neglected in the first instance.

2. The fluorescence spectra $PL_{exp}(\lambda)$ and the intensity $I_{PL_{exp}} = \int PL_{exp}(\lambda)d\lambda$

3. the fluorescence lifetime τ_{PL} and the quantum yield η of the quantum emitters, which can both be measured in solutions of low emitter concentration.

.

Introducing the total decay rate constant $\gamma_T = \frac{1}{\tau_{PL}}$ and the rate constants γ_R and γ_{NR} for the radiative decay rate and the non-radiative decay rate respectively, the PL lifetime becomes $\tau_{PL} = \frac{1}{\gamma_R + \gamma_{NR}}$. The quantum yield can then be expressed in terms of the radiative and non-radiative rate.

$$\eta = \gamma_R \cdot \tau_{PL} = \frac{\gamma_R}{\gamma_R + \gamma_{NR}} \tag{6.3.2}$$

The radiative rate $\gamma_R = n^2 \gamma_{0R}$ is the modified by the index n of the surrounding medium, while γ_{NR} is not. For the calculation of the modified decay rates in the system, the free space values γ_{0R} and γ_{NR} are needed, so the solvent refractive index n must be considered. To ensure that the calculation of the modified photoluminescence gives realistic results, commercially available quantum dots and dye molecules from the AlexaFluor series are considered. The quantum yields η, lifetimes τ_{PL} and molar extinction coefficients ε_M, which are offered by Thermo Scientific,[163] are given in the table along with the excitation wavelength λ_{Exc} of the laser excitation source considered for each dye (Table 6.1).

Emitter	η	$\tau_{PL}[ns]$	$\varepsilon_M[cm^{-1}M^{-1}]$	$\lambda_{Exc}[nm]$
Alexa Fluor 647	0.33	1	270000	632
Alexa Fluor 700	0.25	1	205000	670
Alexa Fluor 750	0.12	1	290000	705
Alexa Fluor 790	0.12	1	260000	730
Qdot® 800	0.83	20	10600000	730

Table 6.1: Intrinsic optical properties of the quantum emitters: Quantum yields $\boldsymbol{\eta}$, lifetimes $\boldsymbol{\tau_{PL}}$ and molar extinction coefficients $\boldsymbol{\varepsilon_M}$ as well as the excitation wavelength $\boldsymbol{\lambda_{Exc}}$ used with the model. Quantum yield and lifetime measurements were made in water at 22° C.

In order to account for laser excitation of the quantum emitters, an equation describing the excitation rate is introduced.

$$\gamma_{Exc}(\lambda_{Exc}) = \sigma_{Abs}(\lambda_{Exc}) \frac{I_{inc}}{E_{Photon}(\lambda_{Exc})} \cdot |\overrightarrow{\mu_Q} \cdot \overrightarrow{E_{loc}(r, \lambda_{Exc})}|^2 \tag{6.3.3}$$

with $E_{Photon}(\lambda_{Exc}) = \frac{hc}{\lambda_{Exc}}$ the energy of a single exciation photon, $\overrightarrow{\mu_Q}$ is the transition dipole moment of the emitter and the $\overrightarrow{E_{loc}(r, \lambda_{Exc})}$ the local excitation field at the emitter position. In the first instance, it can be assumed the emitter transition dipole $\overrightarrow{\mu_Q}$ is perfectly aligned to the local fields, $\overrightarrow{\mu_Q} \parallel \overrightarrow{E_{loc}(r, \lambda_{Exc})}$.

An excitation modification factor is introduced:

$$\boxed{g_{Exc}(\lambda_{Exc}) = \frac{|\overrightarrow{\mu_Q} \cdot \overrightarrow{E_{loc}(r, \lambda_{Exc})}|^2}{|\overrightarrow{\mu_Q} \cdot \overrightarrow{E_{vac}(r, \lambda_{Exc})}|^2}} \tag{6.3.4}$$

and with $|\overrightarrow{\mu_Q} \cdot \overrightarrow{E_{vac}(r, \lambda_{Exc})}|^2 = 1$, the expression for the excitation rate can be rewritten as

$$\gamma_{Exc}(\lambda_{Exc}) = g_{Exc}(\lambda_{Exc}) N(\lambda_{Exc}) \tag{6.3.5}$$

where $N(\lambda_{Exc}) = \sigma_{Abs}(\lambda_{Exc}) \frac{I_{inc}}{E_{Photon}(\lambda_{Exc})}$. This refers to the number of photons absorbed per unit time by a specific emitter in free space and λ_{Exc} is taken at the wavelength of an appropriate laser excitation source for each emitter. The incident intensity I_{inc} is set to $1 \frac{W}{cm^2}$ which translates to an excitation spot of 1 μm^2 and a laser power of 10 nW. Laser intensities between 50 and 100 times higher are typically used in experiments.[141] Rewriting $I_{PL} = \int PL(\lambda) d\lambda$ yields the known formula for the fluorescence intensity

$$I_{PL} = \gamma_{Exc} \eta \cdot \Omega = \gamma_{Exc} \tau_{PL} \gamma_R \Omega \tag{6.3.6}$$

and for the fluorescence spectrum

$$PL(\lambda) = \gamma_{Exc} \cdot \tau_{PL} \gamma_R \cdot \Omega \cdot f_0(\lambda) \tag{6.3.7}$$

The excitation rate γ_{Exc}, and the quantum yield, η, of an emitter on top of a VO_2 thin film is determined through two separate numerical calculation, namely the calculation of the excitation $g_{Exc}(\lambda_{Exc})$ and the calculation of γ_R and τ_{PL}.

To numerically determine the excitation and emission modification of coupled emit-

ters the Finite Difference Time Domain (FDTD) solver of the commercial software Lumerical Device Suite software is used. The simulation volume is set as a cube with side length 1.5 μm. As the numerical simulations deal with emitters coupled to single nanoparticles the boundary conditions are set to perfectly matched layers (PML) to absorb any electromagnetic radiation leaving the simulation space. For calculation of the modified excitation rate the simulation time was set to 350 fs. This time was increased to 1000 fs for the calculation of the emission modification of the emitters to ensure the simulations ran to completion. For mesh refinement conformal mesh 0 was selected. In all cases the background refractive index was set as 1.

For the calculation of $g_{Exc}(\lambda_{Exc})$ a plane wave total-field scattered-field (TFSF) source was used as an excitation source in the system. The TFSF source is placed at the origin point in the model and the dimensions are set to 302.5 nm in the x,y and z direction so that the source fully encompasses the hybrid nanostructure. As the emission of the Alexa dyes are all in the region below 1 μm the broadband source wavelength was set at 400 - 1000 nm. The source plane wave is injected in the negative z direction from the top face with x-polarization in the coordinate system of the model. In all numerical simulations the plane wave is normally incident on the nanoparticle and substrate.

In the model, the dye molecules and quantum dots are treated as electric dipole emitters and are located at various positions, r, surrounding the nanoparticle. Therefore the excitation modification, $g_{Exc}(\lambda_{Exc}) = \frac{|\overrightarrow{\mu_Q} \cdot \overrightarrow{E_{loc}(r,\lambda_{Exc})}|^2}{|\overrightarrow{\mu_Q} \cdot \overrightarrow{E_{vac}(r,\lambda_{Exc})}|^2}$ can be evaluated at positions r with point monitors placed at these positions. The radiative rate $\Gamma_0[s^{-1}]$ of an isolated electric dipole in the free space is defined as $\Gamma_0 = \frac{P_0}{\hbar\omega}$ where $P_0[W]$ is the total power radiated by the dipole in the whole solid angle (4π steradians). Upon the VO_2 phase transition the optical properties of the material change and consequently the optical properties of the quantum emitter will be modified by the presence of the VO_2 thin film. Numerically, the Purcell Factor $g_{P(Film)} = \frac{\Gamma_{R(Film)}}{\Gamma_0} = \frac{P_{EM}}{P_0}$ is calculated by calculating the total power radiated $P_{EM}[W]$ by an electric dipole in the presence of the VO_2 thin film. As $P_{EM}[W]$ must be calculated for the whole solid angle, in the model $P_{EM}[W]$

is the transmitted power through all faces of a 3D box surrounding the emitter and the system, the substrate and the VO_2 film. The Purcell factor $g_{P(Film)} = \frac{P_{EM}}{P_0} = \sum_{Box} T_i$ can be determined by summing the transmission T_i through each face of the 3D Box surrounding the emitter and the system, shown in Fig. 6.1.

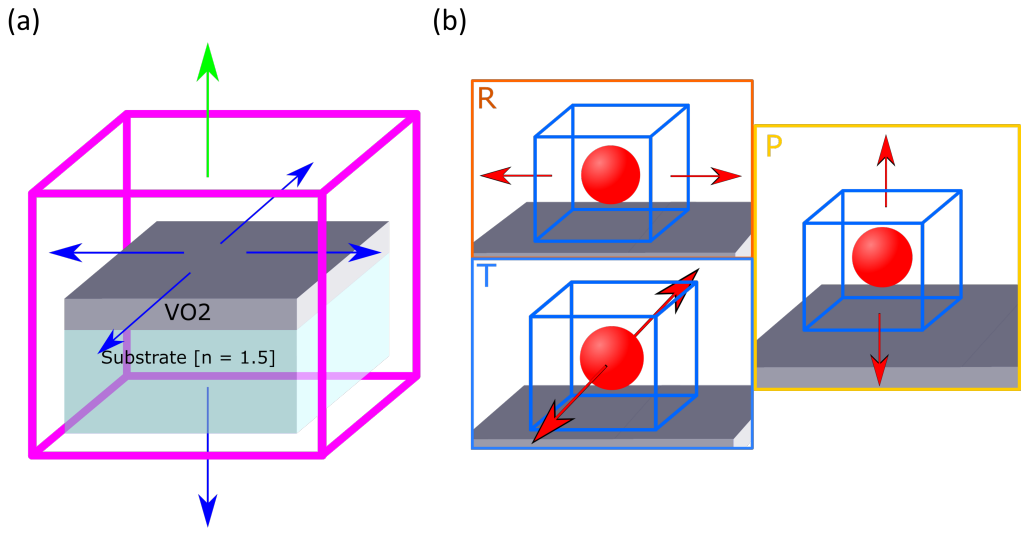

Figure 6.1: (a) Schematic of 3D box surrounding system. The Purcell factor is determined by summing the transmission through each face of the box indicated by the blue and green arrow. (b) The dipole orientation along the x direction is defined as radial (R), the dipole orientation along the y direction is defined as tangential (T), the dipole orientation along the z direction as perpendicular (P).

The modified radiative rate $\gamma_{R(Film)}$ of an emitter on the VO_2 thin film is described by

$$\gamma_{R(Film)} = \gamma_{0R} \int_{400}^{1000} f_0(\lambda) g_{P(Film)} d\lambda \tag{6.3.8}$$

In contrast to conventional dielectric substrates with negligible absorption, the imaginary part of the dielectric functions of the VO_2 film in both phases can't be neglected. This is due to the additional nonradiative decay pathways provided for the quantum emitter in the presence of the VO_2 thin film. These additional nonradiative decay pathways are described by a rate $\gamma_{Loss(Film)}$ accounting for all losses due to the VO_2 thin film.

$$\gamma_{Loss(Film)} = \gamma_{0R} \int_{400}^{1000} f_0(\lambda) g_{Loss(Film)} d\lambda \tag{6.3.9}$$

$g_{Loss(Film)} = \frac{P_{Abs}}{P_0} = \frac{P_{Dip} - P_{EM}}{P_0}$ can be calculated as the total absorbed power in the system. P_{Dip} is the total emitted power by the electric dipole in the presence of the VO_2 thin film. Similar to the calculation of the P_{EM}, P_{Dip} is numerically calculated with the aid of 3D box surrounding the electric dipole.

The modified decay times can be calculated using the following equation

$$\tau_{PL(Film)} = \frac{1}{\gamma_{R(Film)} + \gamma_{Loss(Film)} + \gamma_{NR}} \tag{6.3.10}$$

where γ_{NR} is the unaltered intrinsic nonradiative rate of the real emitter.

As mentioned previously, a function Ω is used to account for the experimental response function, detection direction, detector area and sensitivity, and is chosen so that the total detected fluorescence radiance

$$I_{PL} = \int PL(\lambda) d\lambda = \gamma_{Exc} \tau_{PL} \gamma_R \Omega \tag{6.3.11}$$

I_{PL} is also called the intensity and represents the total number of detected photons per second.

The term $\gamma_R \Omega = \frac{P_{Det}}{P_0} \gamma_{0R}$ is defined as the detection rate g_{Det}, which can be determined by calculating the power transmitted through a planar monitor placed above the hybrid structure outside of the TFSF source box. This mimics the experimental transmission along the detection path.

From the detection rate g_{Det} and the modified photoluminescence lifetime τ_{PL}, the second part of the luminescence modification, the emission modification $g_{em}(\lambda) = \tau_{PL} g_{Det}(\lambda)$ can be determined. The PL spectra simplifies to $PL(\lambda) = \lambda_{Exc(Film)} g_{em}(\lambda) f_0(\lambda)$

and the total number of detected photons $I_{PL} = \gamma_{Exc(Film)} \int g_{em}(\lambda) f_0(\lambda) d\lambda = \gamma_{Exc(Film)} \tau_{PL} \int g_{Det}(\lambda) f_0(\lambda) d\lambda$

The ratio of detected photons to absorbed photons as the detectable quantum yield is defined as $\Phi_{Det} = \frac{I_{PL}}{\gamma_{Exc}}$. The numerical aperture (NA) in the simulation model is 0.707. The calculated luminescence enhancement is sensitive to the NA as an increased NA increases the power transmitted along the detection path.

The photoluminescence emission of the coupled emitter is also highly dependent on the dipole orientation. The dipole orientation parallel to x-axis is defined as radial (R), the orientation parallel to the y-axis is defined as tangential (T) and the orientation parallel to the z-axis is defined as perpendicular (P) as shown in Fig. 7.1(b). For each dipole position considered a separate simulation is done for each orientation and both VO_2 phases.

The same procedure can for applied for calculating the photoluminescence of quantum emitters in the hybrid system comprising of a plasmonic metallic nanoparticle on a VO_2 thin film. In this case the modified photoluminescence lifetime is calculated factoring in the modified radiative and nonradiative rate for the entire hybrid structure.

6.4 Photoluminescence Modification on VO_2

In this section the interaction of dye molecules with the bare VO_2 substrate is numerically calculated. The interaction of four different Alexa Dyes with VO_2 film thicknesses between 10 - 150 nm is considered. The quantum emitters are placed at three different heights above the planar VO_2 film at positions A,B and C which correspond to 5, 20 and 40 nm above the film respectively (Fig. 6.2). For the calculation of the radiative rate (γ_R) and the nonradiative rate (γ_{NR}) the three dipole orientations R, T and P are considered. For planar VO_2, results for the R and T dipole orientations are equal as, in the case of emitters on a bare VO_2 film, these orientations are equivalent.

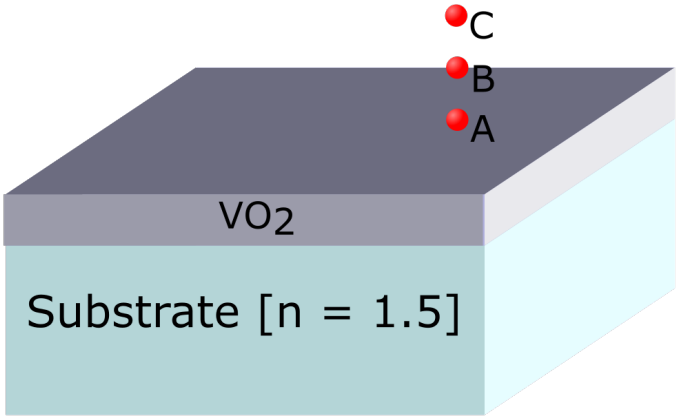

Figure 6.2: Schematic of quantum emitters at positions A,B and C. These positions are 5,20 and 40 nm above the VO_2 thin film surface, respectively.

6.4.1 Planar VO_2 Excitation rate modification (γ_{Exc})

The impact of VO_2 film thickness on γ_{Exc} for coupled emitters is examined by comparing the magnitude of the electric field intensity (E^2/E_0^2) at the three emitter positions as shown in Fig 6.3. From the E-field maps it can be seen as VO_2 transitions from semiconducting to metallic phase there is an increase in the magnitude of the field at each position. It's noted that for positions A and B closer to the VO_2 film the magnitude of the E-field is significantly reduced by the presence of the VO_2 film in both semiconducting and metallic phase. For position C there are regions on the E-field map where the E-field is enhanced by the presence of the VO_2 thin film.

By comparing the ratio of the E-field intensity for VO_2 in the metallic phase to the semiconducting phase at each position the optimal thickness for enhancement of γ_{Exc} is found to between 30 - 50 nm for wavelength range between 630 - 730 nm (Fig 7.4) i.e. the wavelength range where λ_{Exc} for each AlexaFluor dye emitter considered lies. It's noted that for these thicknesses the presence of the VO_2 thin film is still reducing the overall magnitude of the E-field.

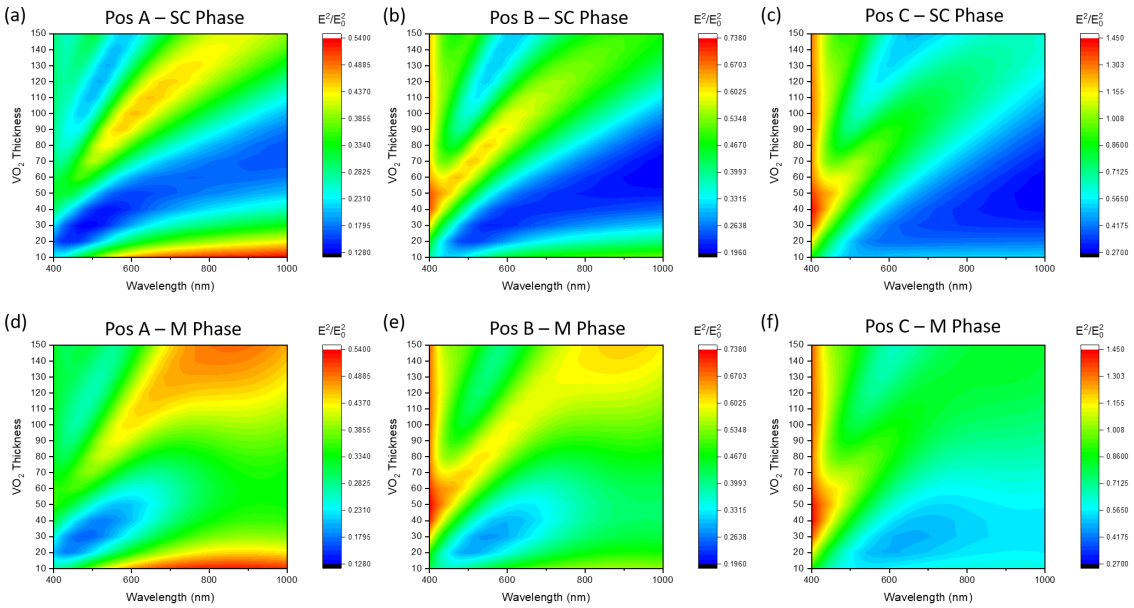

Figure 6.3: E^2/E_0^2 maps for VO_2 films of thicknesses between 10 - 150 nm at three different heights above the VO_2 film: 5 nm (Pos. A), 20 nm (Pos. B) and 40 nm (Pos. C). The VO_2 in semiconducting phase (a-c) and metallic phase (d-f).

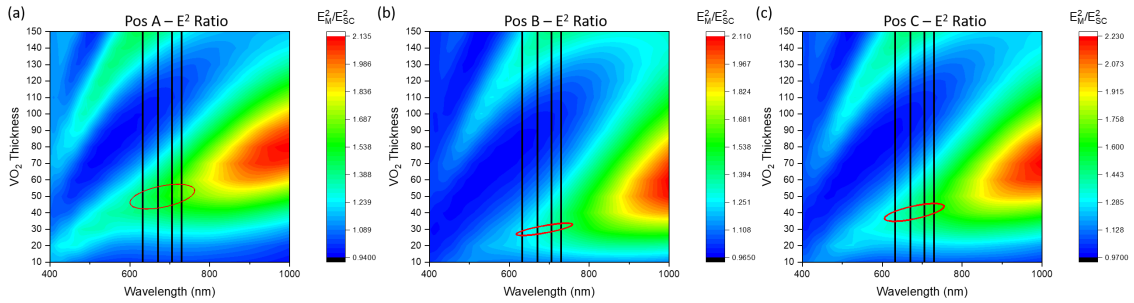

Figure 6.4: E_M^2/E_{SC}^2 Ratio for VO_2 films of thicknesses between 10 - 150 nm for heights (a) 5 nm (Pos. A), (b) 20 nm (Pos. B), and (c) 40 nm (Pos. C) above the VO_2 film. The black lines on each plot indicate the excitation wavelengths (λ_{Ex}) of the Alexa dyes. The encircled area indicates the largest enhancement for the range of the excitation sources.

The ratio of the excitation rate modification in metallic phase to semiconducting phase (E_M^2/E_{SC}^2) at the excitation wavelengths for each of the AlexaFluor dyes at the three positions above the VO_2 film are indicated in Fig. 7.4. As the excitation wavelength redshifts, corresponding to the peak absorption wavelength of the dyes, a marginal increase of 12% in the γ_{Ex} ratio is seen from Alexa647 to Alexa790. Additionally, a 15% increase in the γ_{Ex} ratio moving from an emitter in position C (40 nm above the thin film) to position A (5 nm above the thin film) is seen. The γ_{Ex} ratio for the Alexa

dyes at their appropriate excitation wavelengths is shown in Fig. 7.5. The optimal VO_2 thickness for increased γ_{Ex} ratio for the dye emitters is 30 nm for emitters at position C, 40 nm for emitters at position B and 50-60 nm for emitters at position A closest to the VO_2 thin film.

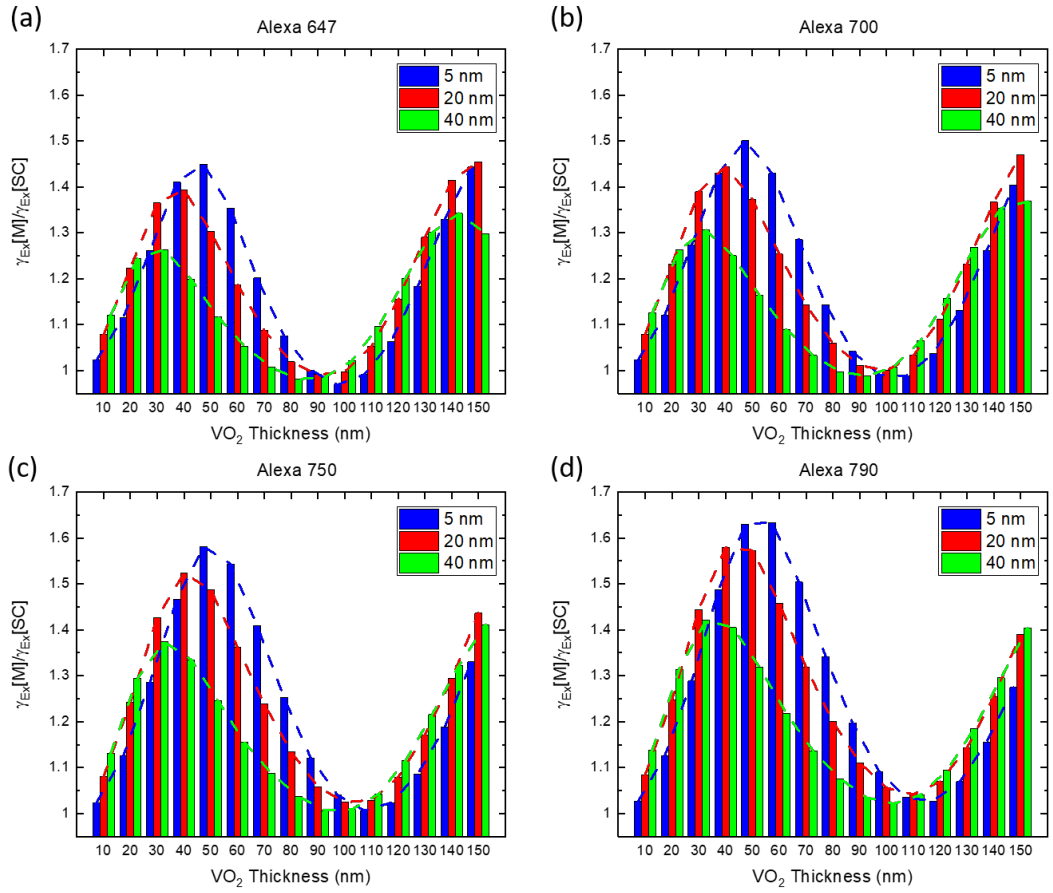

Figure 6.5: $\gamma_{Ex}[M]/\gamma_{Ex}[SC]$ for VO_2 thicknesses between 10 - 150 nm at appropriate excitation wavelengths (λ_{Exc}) for each Alexa dye; (a) Alexa647 ($\lambda_{Exc} = 632nm$), (b) Alexa700 ($\lambda_{Exc} = 670nm$), (c) Alexa750 ($\lambda_{Exc} = 705nm$), (d) Alexa790 ($\lambda_{Exc} = 730nm$)

Additional peaks in the γ_{Ex} ratio can be seen for VO_2 films with thickness around 150 nm. However the increase in γ_{Ex} at large thickness is less readily utilised as in there is a plasmon damping effect to consider when analysis is expanded to nanostructure on VO_2.

6.4.2 Planar VO_2 Radiative rate modification (γ_R)

The impact of VO_2 film thickness on the modified radiative rate of quantum emitters is examined by comparing the transmission through a 3D box around the structure for emitters at positions A,B and C, 5, 20 and 40 nm above the VO_2 film surface respectively. The three dipole orientations (R, T and P) are considered with P parallel to the film normal (perpendicular to the planar VO_2) and the R and T orientations mutually perpendicular and parallel to the VO_2 film. The ratio γ_R for VO_2 in metallic phase to semiconducting is compared for Alexa647, Alexa700, Alexa 750 and Alexa 790, shown in Fig. 6.6. As the figure indicates the R and T dipole orientations are equivalent with a much greater difference between the ratios at each height above the VO_2 film than for the case where the P orientation is considered. In the case of the R and T dipole orientations the transition of the VO_2 film decreases the radiative rate for emitters at all three considered positions. The emitter at position C, 40 nm above the VO_2 film surface shows the least decrease in radiative rate with a γ_R ratio of 0.97 at a VO_2 thickness of 50 nm. The dipole emitters closer to the VO_2 film surface show decreased radiative rate ratios in comparison. However, for the P orientated dipoles there is a small increase (<5%) in the γ_R ratio for VO_2 thicknesses less than 30 nm for all three considered positions. The γ_R ratio for the three dipole orientations for the other Alexa dyes is not depicted as there is no significant deviation from the trend observed in the Alexa647 case.

In Fig. 6.7 the γ_R ratio is averaged for the three dipole orientations. For increasing VO_2 thickness there is a decrease in the average γ_R ratio for each Alexa dye considered. However, for VO_2 thickness below 50 nm this decrease is between 6.5 - 8.5 % for dipoles 5 nm above the film surface and less for dipoles in positions B and C, further from the

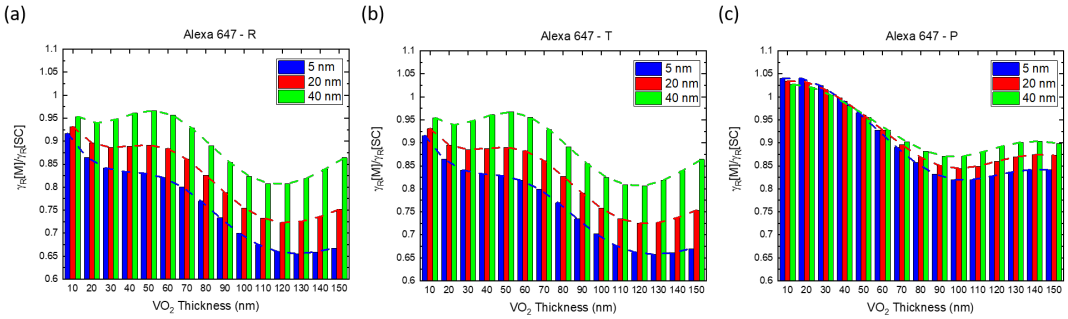

Figure 6.6: $\gamma_R[M]/\gamma_R[SC]$ for Alexa647 dye emitters placed 5, 20 and 40 nm above a VO_2 thin film with thicknesses between 10 - 150 nm for the three dipole orientations (a) R, (b) T and (c) P.

film surface. When averaged over the three dipole orientations the γ_R ratio is <1 for all Alexa dyes considered with no significant difference in the response of the dyes for VO_2 thicknesses < 80 nm.

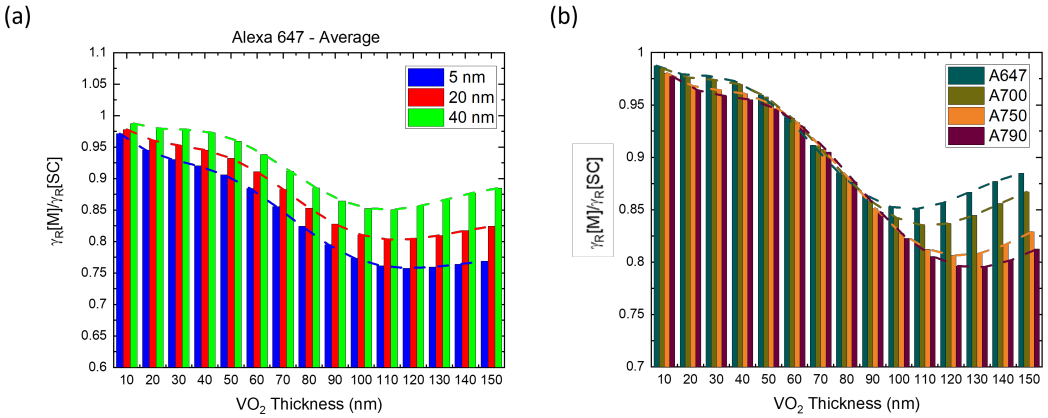

Figure 6.7: (a) $\gamma_R[M]/\gamma_R[SC]$ for Alexa647 dye emitters placed 5, 20 and 40 nm above a VO_2 thin film with thicknesses between 10 - 150 nm averaged over the three dipole orientations (b) $\gamma_R[M]/\gamma_R[SC]$ for Alexa647, Alexa700, Alexa750 and Alexa790 dye emitters placed 40 nm above a VO_2 thin film with thicknesses between 10 - 150 nm averaged over the three dipole positions.

6.4.3 Planar VO_2 Nonradiative rate modification (γ_{Loss})

The impact of the VO_2 film thickness on the modified nonradiative rate of quantum emitters is examined by comparing the difference between transmission through a 3D box around the emitter and a 3D box surrounding the entire structure. Similar to the radiative rate calculation, this was done for emitters at positions 5, 20 and 40 nm above the surface of the VO_2 thin film and for three dipole orientation R, T and P.

As indicated in Fig. 6.8(a), which shows the γ_{Loss} ratio for Alexa647 averaged over the dipole orientations for the positions A, B and C for VO_2 thicknesses between 10 - 150 nm, the thickness of the underlying VO_2 thin film has minimal impact on the γ_{Loss} ratio. However, there is a significant modification in the nonradiative rate upon the VO_2 transition. For VO_2 in metallic phase there is a significant increase in the nonradiative rate, particularly for emitters placed in close proximity to the film where a γ_{Loss} ratio of > 5 is seen. Emitters 20 and 40 nm from the VO_2 thin film surface show γ_{Loss} ratios of 2.56 and 2.35 respectively. Fig. 6.8(b) indicates the γ_{Loss} ratio for the four Alexa dyes considered averaged over VO_2 thicknesses between 10 - 150 nm and each dipole orientation. The graph indicates an increase in the γ_{Loss} ratio with a redshift in the dye emission wavelength, particularly in the case where the emitter is 5 nm from the VO_2 film surface, i.e. has the most interaction. This increased contrast in the nonradiative rate, seen between the VO_2 phases for higher wavelength , is due to the increased difference in the VO_2 optical constants at increased wavelengths.

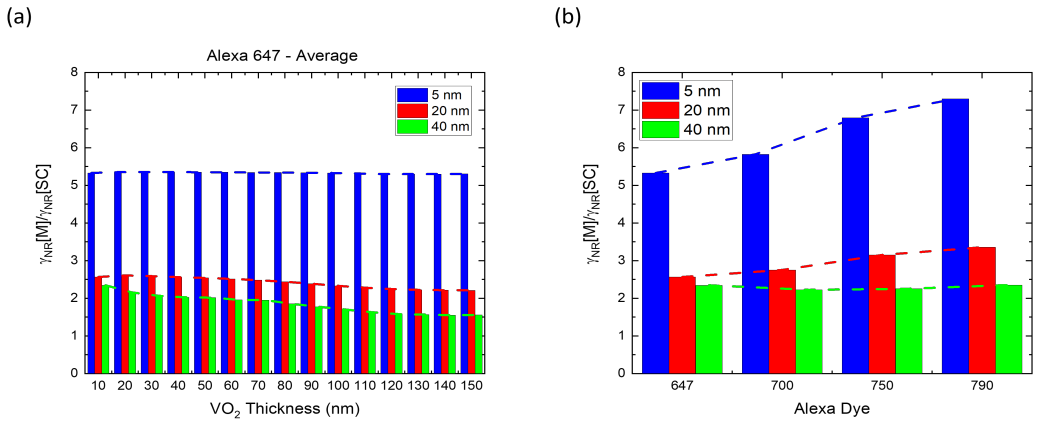

Figure 6.8: (a) $\gamma_{Loss}[M]/\gamma_{Loss}[SC]$ for Alexa647 dye emitters placed 5, 20 and 40 nm above a VO_2 thin film with thicknesses between 10 - 150 nm averaged over the three dipole orientations. (b) $\gamma_{Loss}[M]/\gamma_{Loss}[SC]$ for Alexa647, Alexa700, Alexa750 and Alexa790 emitters placed 5, 20 and 40 nm above a VO_2 thin film. The values displayed are averaged over VO_2 thicknesses between 10 - 150 nm and over the three dipole orientations.

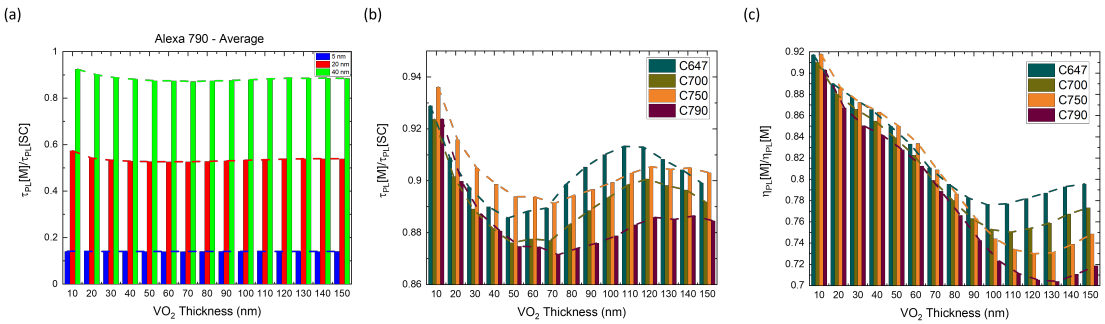

Figure 6.9: (a) $\tau_{PL}[M]\tau_{PL}[SC]$ for Alexa790 dye emitters place 5, 20 and 40 nm above a VO_2 thin film with thicknesses between 10 - 150 nm averaged over the three dipole orientations.(b) $\tau_{PL}[M]\tau_{PL}[SC]$ for Alexa647, Alexa700, Alexa750 and Alexa790 at position C for VO_2 thicknesses between 10 - 150 nm. (c) $\eta_{PL}[M]/\eta_{PL}[SC]$ for Alexa647, Alexa700, Alexa750 and Alexa790 at position C for VO_2 thicknesses between 10 - 150 nm.

6.4.4 Planar VO_2 Photoluminescence modification

The modification of the radiative and nonradiative rate seen in the previous sections results in a modification of the lifetime (τ_{PL}). The significant modification of γ_{NR} results in a highly reduced τ_{PL} ratio for the emitters in position A. For emitters in position B and C, the reduction in the τ_{PL} ratio is lessened due to the decreased interaction with the VO_2 thin film. In the case of Alexa790 the τ_{PL} ratio is 0.14, 0.57 and 0.92 for emitters in positions A, B and C respectively, as shown in Fig. 6.9(a) In Fig. 6.9(b) it is shown that there is some small variation ($< 4\%$) in the τ_{PL} ratio for the different Alexa Dye emitters 40 nm above the VO_2 film with increasing thickness. As η_{PL} is a product of γ_R and τ_{PL} there is a significant decrease in the η_{PL} ratio with increasing VO_2 thickness with a larger decrease in η_{PL} for Alexa dyes emitting at longer wavelengths, as clearly seen in Fig. 6.9(c).

To examine and summarise the overall trends in the interaction of emitters on the VO_2 film, the interaction of Alexa790 dye on a 15 nm VO_2 film is considered, see Fig. 6.10 In this case, the R, T and P dipole orientations are considered with R and T being equivalent. The number of detected photons (I_{PL}) is increased upon the phase transition only at position C, 40 nm above the VO_2 film surface. Proximity to the VO_2 film has a quenching effect when the VO_2 transitions to metallic phase. For all

considered positions there is an increase in γ_{Ex} upon the VO_2 phase transition with a 15 % increase from position A to C. However, as shown in previous discussion of the γ_{Ex} ratio there is an optimal VO_2 film thickness at 50 nm where the emitters closer to the VO_2 film surface demonstrate the largest γ_{Ex} ratio. While γ_{Ex} is larger for emitters at position A, the magnitude of the E-fields themselves is reduced, resulting in decreased photoluminescence intensity. γ_R decreases for R and T dipole orientation and shows a slight increase for the P orientation upon the VO_2 phase transition. This results in an overall decrease when averaged over the three dipole orientations. γ_{Loss}, as discussed previously, demonstrates a large increase upon VO_2 phase transition, particularly at position A, where the dye emitter is heavily quenched by the metallic VO_2 film and an almost 8-fold increase in γ_{loss} is seen. The quantum yield η_{PL} is noted to decrease upon the VO_2 phase transition, particularly for the emitters close to the VO_2 film where γ_{Loss} is highest. However, when the detectable quantum yield is considered, it's noted there is an increase for the R and T emitter orientations at position C where the photoluminescence enhancement is seen.

In conclusion, the VO_2 phase transition from semiconducting phase to metallic phase results in a quenching of the emission of coupled emitters placed in close proximity to the VO_2 film, due to the large increase in γ_{Loss} for the metallic phase VO_2. Emitters at position C, 40 nm away from the VO_2 film surface, show enhancement due to E-field enhancement and reduced γ_{Loss}. These results indicate that coupling emitters to a plasmonic nanoparticle, where the γ_{Ex} ratio can be increased can result in a significant photoluminescence enhancement.

6.5 Photoluminescence Modification on Ag Nanodiscs

In this section the interaction of AlexaFluor dye molecules with a Ag nanodisc on thin film VO_2 is numerically calculated. A Ag nanodisc structure was selected as the rotational symmetry of the structure allows for polarization independence and Ag is

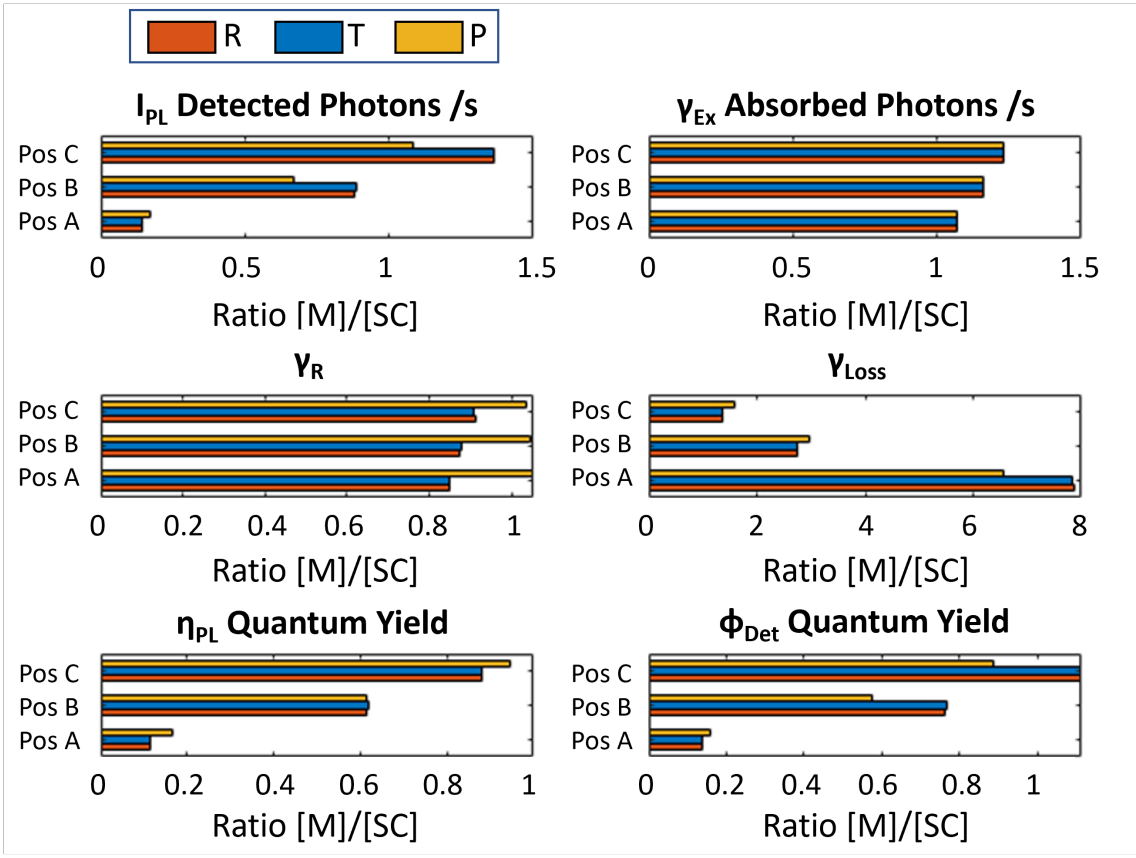

Figure 6.10: Ratio of I_{PL}, γ_{Exc}, γ_R, γ_{Loss}, quantum yield η_{PL} and detectable quantum yield Φ_{Det} for Alexa790 dye emitters, located at the positions A-C, on a 15 nm VO_2 thin film in metallic phase to semiconducting phase.

known to demonstrate a larger plasmonic response in the visible spectrum.[164] The same procedure applied to modelling the photoluminescence on the bare VO_2 film is used to investigate the hybrid system. The schematic of the model used for the excitation modification is dipected in Fig. 6.11(a). The initial investigation of the impact of a Ag nanodisc on γ_R and γ_{Loss} was performed similar to the case on bare VO_2, with three positions A, B and C which are 5, 20 and 40 nm above the VO_2 film surface, respectively. In this case these positions are 5 nm from the surface of a 40 nm high Ag nanodisc with a 120 nm diameter. (Fig 6.11(b)) Emitters are placed at least 5 nm away from the disc as at smaller distances PL quenching via energy transfer becomes dominant. In Fig. 6.11(c) the changes in γ_R and γ_{Loss} of the Alexa790 emitters at position A-C are shown after the introduction of the Ag nanodisc. It's observed that $\gamma_R[NP]$ is up to 20 times larger than $\gamma_R[Film]$ for the R dipole orientation.

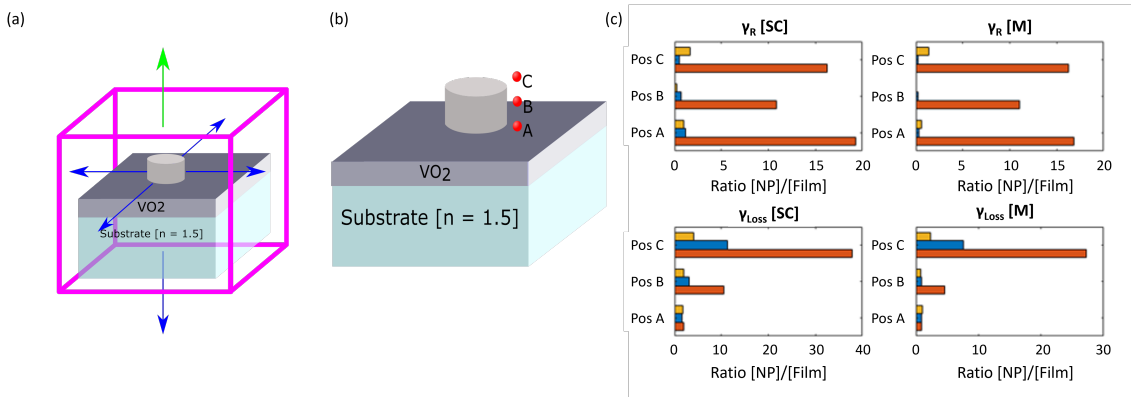

Figure 6.11: (a) Schematic of the model used for the calculation of $g_{Ex}(\gamma_{Ex})$ for the hybrid systems investigated consisting of a Ag nanodisc on a VO_2 film (Thickness = 15 nm) on a substrate with refractive index 1.5. (b) Schematic of the hybrid system with a Ag nanodisc (Height = 40 nm, Diameter = 120 nm) on a VO_2 (Thickness = 15 nm). The Alexa790 dye emitters are positioned at three different heights above the VO_2 film: 5 nm (Pos A), 20 nm (Pos B) and 40 nm (Pos C) and at a distance of 5 nm from the Ag nanodisc sidewall (c) Graphs depicting the modification of the radiative rate (γ_R and non-radiative rate (γ_{Loss}) in both phases for the hybrid Alexa790 Dye - Ag Nanodisc - VO_2 system shown in (b). The changes in γ_R and γ_{Loss} are determined as the ratio of the γ_R and γ_{Loss} in the hybrid system and the γ_R and γ_{Loss} when the emitters are at the positions A-C on the VO_2 film in absence of the nanodisc.

The photoluminescence of the hybrid system is substantially enhanced when compared to the bare VO_2 case as is shown in Table 6.2. It's noted, that while the number of detected photons coming from the emitters at position A in the hybrid system is 2 orders of magnitude greater than $I_{PL}(Film)$, the largest $I_{PL}(NP)$ occurs near the top edge of the nanodisc. To obtain an I_{PL} more representative of a realistic system, a model emulating a thin coating of dye molecules surrounding the system is considered.

	Semiconducting (SC)			Metallic (M)		
	R	T	P	R	T	P
C	8.15	0.97	5.48	18.32	0.9	12.81
B	14.43	1.94	1.74	32.16	1.6	2.08
A	132.08	6.57	8.76	345.53	3.50	13.99

Table 6.2: $I_{PL}[NP]/I_{PL}[Film]$ for Alexa dye emitters at locations A - C and 5 nm away from the surface of a Ag nanodisc (Height = 40 nm, Diameter = 120 nm) on VO_2 (Thicknesss = 15 nm)

To model a thin coating of dye molecules on the Ag nanodisc, similar to one that forms when diluted dye molecules solutions are either drop casted or spin coated on top of

such systems, $g_{em}(\lambda)$ and $g_{Ex}(\lambda_{Ex})$ are calculated at 15 different positions around the plasmonic nanoparticle. 6 of these positions are located along the top of the nanodisc, at 5 nm and 7.5 nm above the nanoparticle and distributed along the nanodisc, i.e. at the centre of the nanodisc, at the half radius of the disc and the at the full radius at the upper edge of the disc. The remaining 9 positions mimic a homogeneous distribution of emitters at the sides of the nanodisc. In the radial direction the emitters are at 5, 7.5, 10 nm from the nanodisc. In the z direction the emitters are distributed at three different distances from the VO_2 thin film, i.e. 5 nm from the VO_2 film surface, a height corresponding to the half-height (20 nm) and a height corresponding to the height of the nanodisc (40 nm), as depicted in Fig. 6.11)

As the phase transition of VO_2 can be induced thermally, optically and electrically, thermal quenching is not included directly in the calculated PL emission. However, as thermally induced phases transition is one of the most common methods used to actuate the VO_2 phase transition, it is important to determine if any increase in emission can compensate for thermally induced luminescence quenching. A figure of merit

$$R = \frac{I_{PL}(M)}{I_{PL}(SC)} \tag{6.5.1}$$

where $I_{PL}(M)$ and $I_{PL}(SC)$ are the PL intensities in the metallic and semiconducting phases respectively, is introduced. Considering the PL quenching rate of dye molecules is in the range of 0.2 - 2% per degree, a value of R = 2 will provide sufficient enhancement of the PL intensity to compensate for thermal losses, and R>2 will correspond to an increase in the emission compared with the low temperature semiconducting phase of VO_2. To determine the best candidates for dynamic PL modification several emitters were considered. Dyes from the Alexa Fluor family are suitable for implementation in the hybrid system due to their strong emission peaks in the visible and NIR spectral region. These are taken by way of example, but the results can equally be applied to quantum dot emitters. In this work Alexa Fluor dyes with PL emission peaks at 670 nm (Alexa647), 720 nm (Alexa700), 780 nm (Alexa750) and 805

nm (Alexa790) are considered. The excitation wavelengths used within the model to calculate emitter excitation rates for these dyes are 632 nm, 670 nm, 705 nm and 730 nm, respectively.

6.5.1 Disc Diameter

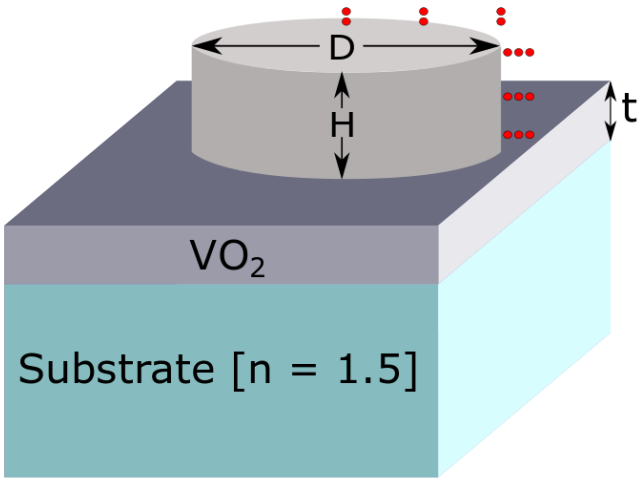

Figure 6.12: Schematic of Emitter - Nanostructure - VO_2 system with Ag nanodisc diameter D, height H and VO_2 thickness t. The schematic indicates the 15 emitters (red circles) positions chosen to emulate a uniform coating of Alexa dye molecules.

For the fluorescence modification in the hybrid system, the dependence on the diameter of the Ag nanodisc is first considered, as the shift in the resonance feature is expected to have a significant impact on any enhancement. A schematic of the structure is given in Fig. 6.12. From the spectra and graph shown in Fig. 6.13(a) and Fig. 6.13(b), respectively, it can be seen that the optimal choice of emitter shifts to increased wavelengths with increasing disc diameter and redshifted plasmon resonance position. For the 120 nm diameter case, the Alexa700 dye demonstrates the largest enhancement, with R = 2.44, when the VO_2 layer transitions from semiconducting to metallic phase. For the 140 nm and 160 nm disc diameter the Alexa750 and Alexa790 dyes show the largest enhancement with fluorescent intensity ratios of 2.69 and 3.1, respectively. The increase in PL ratios can be attributed to the increased overlap of the nanodisc plasmon with the dye excitation and emission when the VO_2 layer is in the metallic phase. For Ag nanodiscs of diameter 120 nm, the PL emission of Alexa700 is spectrally on the blue side of the nanodisc plasmon resonance at 785 nm when the underlying VO_2 layer in the system is in semiconducting phase. Upon transition the nanoparticle resonance shifts to 710 nm which significantly overlaps with the emission of the Alexa700 dye accounting

for the increased emission. The 140 nm diameter Ag nanodisc shows an increased PL ratio for the Alexa700, 750 and 790 dyes. Again, for VO_2 in the semiconducting phase the dye emission is on the blue side of the plasmon resonance with an increased overlap with the resonance peak once VO_2 transitions to the metallic phase. This effect is increased even further for the 160 nm diameter Ag nanodisc with an increase in PL ratio for the longer wavelength emitters. However, it must be noted that the increase in PL intensity ratio seen for discs with increased diameter is accompanied by a decrease in overall emission intensity.

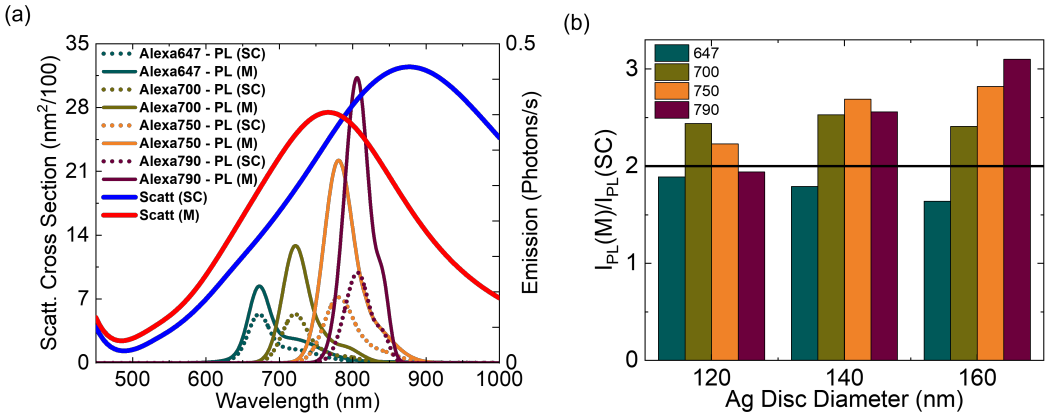

Figure 6.13: (a) Scattering cross-section and PL spectra for Ag nanodiscs (Diameter = 160 nm, Height = 40 nm) on VO_2 (t = 15 nm) in the semiconducting (SC) and metallic (M). In the case of the PL spectra, the dotted and solid lines correspond to the SC and M phases, respectively. (b) $I_{PL}(M)/I_{PL}(SC)$ for Alexa dyes coupled to Ag nanodisc-VO_2 system (Diameter = 120 nm, 140 nm, 160 nm, Height = 40 nm) on VO_2 (t = 15 nm). Ratios above 2 (indicated by the black horizontal line) are considered suitable for compensation of thermal quenching.

6.5.2 Silica Shell

As Ag nanostructures are known to suffer degradation over time due to oxidation, reducing the plasmonic response, thin silica layers are often employed to act as a protective layer. The impact of thin silica shells surrounding Ag nanodiscs on the PL intesity of the coupled emitters is examined. Silica shell thicknesses of 5, 10 and 15 nm are considered with the PL ratios for VO_2 in its metallic phase to semiconducting phase considered for each shell thickness, shown in Fig. 6.14.

The increase in the silica shell thickness has a minor influence on the plasmon resonance,

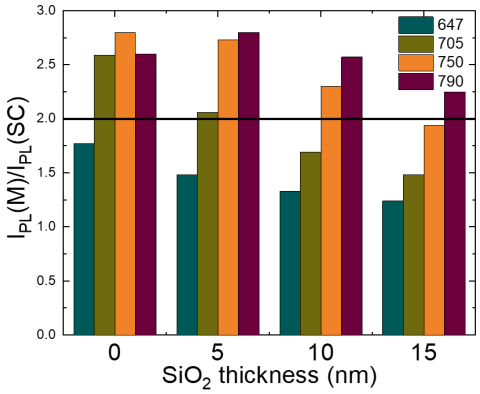

Figure 6.14: $I_{PL}(M)/I_{PL}(SC)$ for Alexa dyes coupled to Ag nanodisc-VO_2 system (Diameter = 120 nm, Height = 40 nm) on VO_2 (15 nm) with varying SiO_2 shell thickness (0 nm, 5 nm, 10 nm, 15 nm).

with a 10 nm redshift for every 5 nm increase in shell thickness. Additionally, increasing shell thickness increases separation between the quantum emitter and the plasmonic nanoparticle, and as a consequence there is a general decrease in both PL intensity and PL intensity ratio, a trend clearly demonstrated in Fig. 6.14. However, it is worth noting that for the Alexa790 dye the emission marginally increases for the 5 nm silica shell, making the 5 nm shell ideal for preventing oxidation of the Ag discs while maintaining strong interaction between the emitter and nanoparticle. While thicker silica shells have been shown in the literature[165,166] to be optimal for emission enhancement due the effect of increased emitter quenching when quantum emitters are in close proximity to the plasmonic nanoparticle, in the case of the Alexa790 dye, the large excitation enhancement seen at close proximity to the nanoparticle results in the increased PL emission for the 5nm thick shell.

6.5.3 Embedded Emitters

As the application of a silica shell, to protect the Ag nanoparticle from oxidation, is known to have an impact on the PL intensity and the intensity ratio, the impact of embedding quantum emitters within the thin silica shell is examined. Spectra indicating the impact of attaching quantum dot emitters, QD800, to the outside of a 15 nm SiO_2 shell surrounding a Ag nanodisc (Diameter = 140 nm, Height = 40 nm) on VO_2

(15 nm) are shown in Fig. 6.15(c), while embedding the QD800 just within the 15 nm shell are shown in Fig. 6.15(d). The structures are depicted in panels (a) and (b), respectively. From these spectra, it can be seen that embedding the QD800 in the SiO_2 shell has the effect of increasing the PL intensity ratio from 1.97 when the emitters are place on the outside of the shell to 2.7 on the inside. While the ratio between the PL intensities increases, however the emission in both phases is severely diminished when the emitters are placed within the silica shell (n = 1.5). This sharp emission reduction for quantum emitters placed within a higher refractive index medium is consistent with literature[167] and the radiative lifetime is inversely proportional to the refractive index of the surrounding medium.[168]

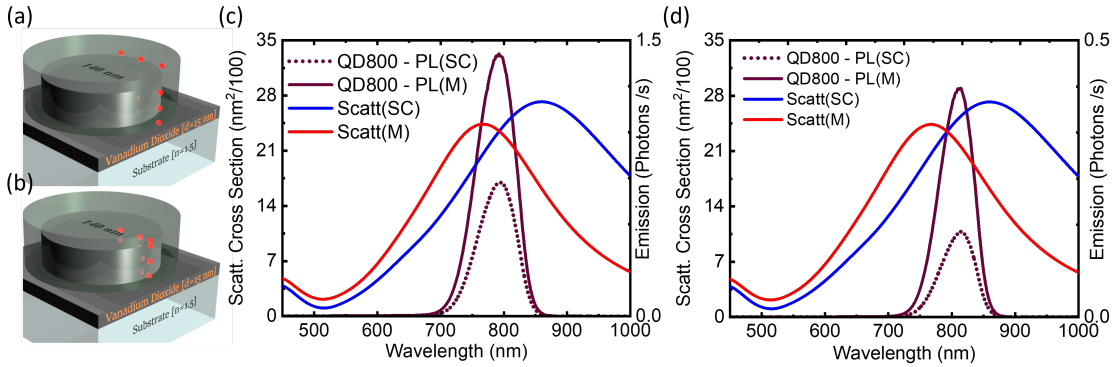

Figure 6.15: Schematic of Ag nanodisc (Diameter = 140 nm, Height = 40 nm) on VO_2 (15 nm) with 15 nm thick silica shell (n = 1.5) with (a) quantum dots (QD800) are attached to the outside of the shell and (b) quantum dots (QD800) embedded within the 15 nm silica shell. Scattering cross-sections and photoluminescence spectra for Ag nanodiscs and QD800 depicted in (a) and (b) are displayed in (c) and (d), respectively. The excitation wavelength $\lambda_{Exc} = 730$ nm.

6.5.4 Disc Height

The next major parameter investigated in this system is the influence of the nanodisc height on the PL of the coupled Alexa dye emitters. As outlined in previous discussion, for the case of emitters on planar VO_2 and coupled to Ag nanodiscs, the magnitude of the nonradiative rate is dominated by the distance from the VO_2 film. The largest contribution to the PL comes from the upper from the upper edge of the nanodiscs, where the largest enhancement to the E-field is concentrated. The total PL is enhanced for

increasing disc height with a substantial increase in PL intensity seen when increasing the nanodisc height from 20 nm to 40 nm. This increase in PL with increasing Ag nanodisc height is attributed to the blueshift in the plasmon resonance. This increased PL is accompanied by a marginal increase in the PL ratio for Alexa647 and Alexa700, however for the dye emitting at the longest wavelength a slight decrease in the enhancement factor is observed. This decrease is also attributed to the blueshift in the plasmon resonance seen with increasing disc height, shifting the wavelength where the maximum excitation rate is seen. Further increase in disc height has no effect on the plasmon resonance, the PL intensities increase slightly, with a marginal decrease in PL ratio for all dye emitters observed, with the exception of the Alexa790 dye which has a marginal increase, as senen in Fig. 6.16.

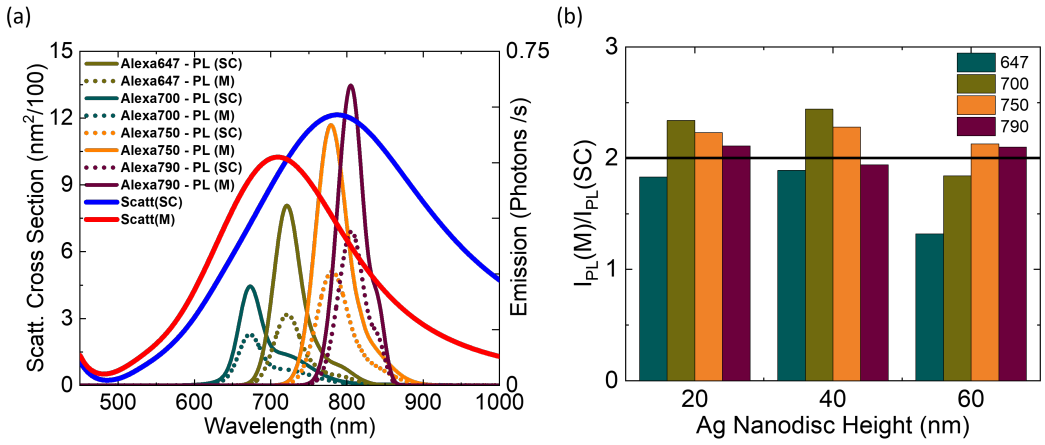

Figure 6.16: (a) Scattering cross-section and PL spectra for Ag nanodiscs (Diameter = 120 nm, Height = 40 nm) on VO_2 (t = 15 nm) in the semiconducting (SC) and metallic (M). In the case of the PL spectra, the dotted and solid lines correspond to the SC and M phases, respectively. (b) $I_{PL}(M)/I_{PL}(SC)$ for Alexa dyes coupled to Ag nanodisc-VO_2 system (Diameter = 120 nm, Height = 20 nm, 40 nm, 60 nm) on VO_2 (t = 15 nm). Ratios above 2 (indicated by the black horizontal line) are considered suitable for compensation for thermal quenching.

6.5.5 VO_2 thickness

As VO_2 is the driving element in tuning the PL emission, numerical simulations are used to investigate the impact of the thickness of the underlying VO_2 layer on the PL intensity and the PL ratio. Increasing the thickness of the VO_2 film has the effect of damping the plasmon resonance which can be seen in the decrease in the scattering

cross-section. While it might be expected that a damping of the plasmon resonance would negatively impact the PL ratio, increasing the VO_2 film thickness from 15 nm to 30 nm results in a dramatic increase in the PL ratio in the case of the Alexa750 and Alexa790 emitters, with an increase in ratio from 1.94 to 4.12 for the Alexa790. The $>$ 4-fold PL enhancement is attributed to the increase in $\Delta\lambda$ or shift in the plasmon resonance peak as the VO_2 film transitions from semiconducting phase to metallic phase. The resonance peak shift of $\Delta\lambda = 125$ nm, from 865 nm in semiconducting phase to 740 nm in metallic phase, is significantly larger than the 75 nm shift seen for the 15 nm thick VO_2 case. Further increase in VO_2 thickness to 60 nm shows no further impact on the magnitude of the plasmon resonance shift and, coupled with the further decrease in scattering cross-section, results in a decreased PL ratio when compared to the 30 nm thick VO_2 film. Examining the case for the Alexa647 dye there is a decrease in PL ratio with increasing VO_2 layer thickness, however the emission demonstrates a different trend. After an initial decrease in the emission moving from 15 nm to 30 nm VO_2 in both phases, when the thickness increases to 60 nm a significant enhancement in the emission is seen, albeit with less contrast between the VO_2 phases. The emission seen in both phases for the 60 nm VO_2 case is larger than the emission on the 15 nm VO_2. For the case of the Alexa700 dye, there is a similar reduction in emission as the VO_2 film thickness is increased from 15 nm to 30 nm. Again emission is increased when VO_2 film thickness is increased to 60 nm, however the emission in this case is lower than that seen on 15 nm VO_2. The Alexa750 shows significantly decreased emission in both phases when the VO_2 film thickness is increased from 15 nm to 30 nm. Further increase to 60 nm demonstrates a slight enhancement of emission in semiconducting phase and slight quenching in metallic phase. Alexa790 demonstrates a similar trend to the Alexa750 with increasing film thickness, with the highest emission occurring for the 15 nm VO_2.

A layer of $VO_2 \sim 30$ nm is therefore an optimal thickness for an increased PL ratio for the longer wavelength emitters as there is a balance between damping effects from increased film thickness and enhancing effects from the increased shift in plasmon

resonance. The scattering cross-section and PL spectra for the Ag nanodisc on 30 nm VO_2 is shown in Fig. 6.17(a) demonstrating the significant $\Delta\lambda$ and large enhancement of the Alexa790 emission. Table. 6.3. shows the tabulated AlexaFLuor dye PL intensity for 15,30 and 60 nm VO_2 indicating that the largest I_{PL} occurs for the 30 nm VO_2 case.

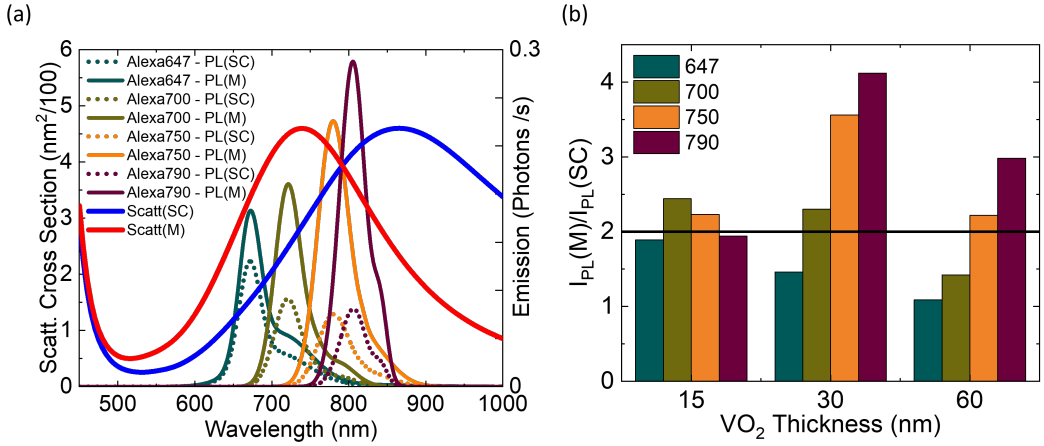

Figure 6.17: (a) Scattering cross-section and PL spectra for Ag nanodiscs (Diameter = 120 nm, Height = 40 nm) on VO_2 (Thickness = 30 nm) in the semiconducting (SC) and metallic (M). In the case of the PL spectra, the dotted and solid lines correspond to the SC and M phases, respectively. (b) $I_{PL}(M)/I_{PL}(SC)$ for Alexa dyes coupled to Ag nanodisc-VO_2 system (Diameter = 120 nm, Height = 40 nm) on VO_2 (Thickness = 15 nm, 30 nm, 60 nm). Ratios above 2 (indicated by the black horizontal line) are considered suitable for compensation for thermal quenching.

	V15			V30			V60		
AlexaFluor	SC	M	Ratio	SC	M	Ratio	SC	M	Ratio
647	7.04	13.32	1.89	6.37	9.30	1.46	14.61	15.91	1.09
700	8.60	21.00	2.44	4.14	9.52	2.30	8.63	12.25	1.42
750	15.08	33.60	2.23	3.286	13.73	3.56	5.97	13.28	2.24
790	16.22	31.46	1.94	3.29	13.55	4.12	3.94	11.74	2.98

Table 6.3: Tabulated AlexaFluor Dye PL intensity for 15,30 and 60 nm VO_2 film thickness in semiconducting and metallic phase. The calculated PL intensity ratio is also shown.

6.5.6 Intermediate Phase

Calculation of PL ratios for intermediary temperatures can be achieved by simulation of the Ag nanodisc structure on VO_2 with dielectric functions calculated using the Maxwell Garnett equation.

$$\varepsilon_{eff} = \varepsilon_m \frac{2\,\delta_i(\varepsilon_i - \varepsilon_m) + \varepsilon_i + 2\varepsilon_m}{2\varepsilon_m + \varepsilon_i - \delta_i(\varepsilon_i - \varepsilon_m)} \tag{6.5.2}$$

where ε_{eff} is the effective dielectric constant of the medium, ε_i the dielectric constant of the inclusions, ε_m the dielectric constant of the matrix and δ_i is the volume fraction of inclusions.

The dielectric functions used for calculation of PL enhancement for three volume fractions (0.2, 0.5, 0.8) of metallic VO_2 in semiconducting VO_2 are shown in Fig. 6.18. The figure shows the PL enhancement for Alexa790 dye on a Ag disc of diameter 120 nm and height 40 nm on a 30 nm VO_2 film using intermediary dielectric functions of VO_2. PL enhancement can be seen for the range of volume fractions corresponding to temperatures when the VO_2 is transitioning from semiconducting to metallic phase. No temperature is assigned to these intermediary phases as the volume fraction is strongly dependent on hysteresis and transition temperature of the VO_2 film.

6.5.7 PL enhancement contributions

Further analysis of the contributions to the PL enhancement for the case of Alexa790 emitters around a Ag nanodisc (Diameter = 140 nm, Height = 40 nm) on VO_2 (Thickness = 15 nm) are presented in Fig. 6.19. In Fig. 6.19(b) the ratio of the excitation rate modification for metallic phase VO_2 relative to the semiconducting phase VO_2 is shown. For almost all emitter positions an enhancement in the modified rate can be seen with the highest enhancement factor corresponding to emitters place at the upper edge of the Ag nanodisc. Averaged over all 15 positions considered an enhancement factor of 2.16 can be seen.

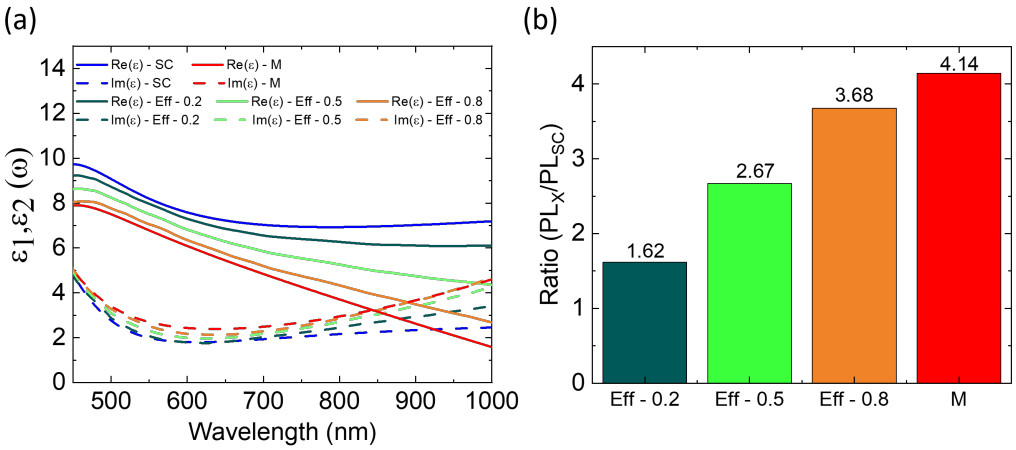

Figure 6.18: Dielectric functions of intermediary VO_2 phases calculated Maxwell Garnett effective media theory. (b)$I_{PL}(X)/I_{PL}(SC)$ for Alexa790 dye coupled to Ag nanodisc-VO_2 system (Diameter = 120 nm, Height = 40 nm) on VO_2 (30 nm). The ratios shown are for VO_2 effective media containing 0.2, 0.5, 0.8 volume fraction metallic VO_2 as well as the fully metallic case.

In contrast the ratio of the modified emission rates, shown in Fig. 6.19(b) demonstrate quenching or enhancement can be observed depending on the dipole position. The dipoles closest to the VO_2 films are most strongly quenched, however those at least 5 nm from the surface of the Ag nanodisc and VO_2 film experience an increase by a factor of approximately 1.4. The average ratio over all considered dipole positions is approximately 1. Comparison of these figures indicates that the main contribution to the PL emission enhancement arises from the increased excitation for metallic phase VO_2.

In Fig. 6.20 (a-c) The values of I_{PL} are shown for the three dipole orientations for Alexa790 emitters couple to Ag nanodics (Diameter = 120 nm, 140 nm, 160 nm) on VO_2 (Thickness = 15 nm). The highest number of detected photons (134.64 Ph/s) occurs for the 120 nm Ag disc on metallic phase VO_2 for emitters with radial (R) orientation, with the high emission mostly stemming from the upper edge of the nanodisc. The regions on the top surface of the disc and close to the VO_2 film surface where the number of photons is low, regardless of disc diameter and VO_2 phase. For the radial orientation, the number of detected photons decreases with increasing disc diameter, but the regions with highest photon numbers are not altered. This is opposite to

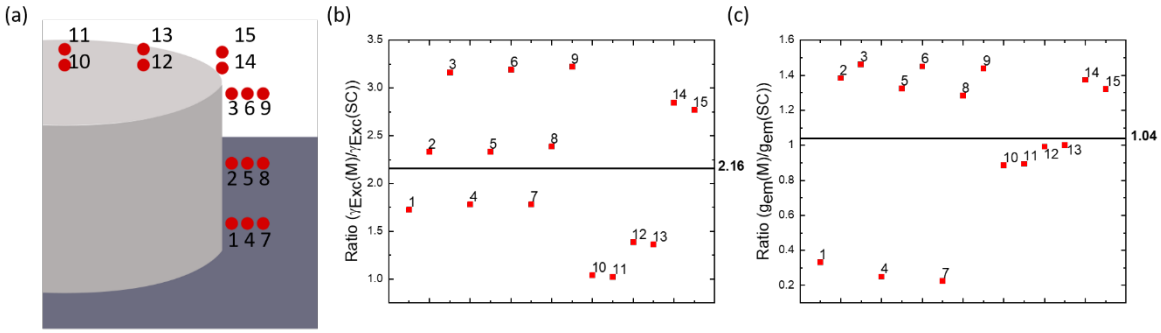

Figure 6.19: (a) Numbered schematic of emitters positions around Ag nanodisc (b) Ratio $\gamma_{Exc}(M)/\gamma_{Exc}(SC)$ for an Ag nanodisc (Diameter = 140 nm, Height = 40 nm) on VO_2 (Thickness = 15 nm). The black line indicates a mean $\gamma_{Exc}(M)/\gamma_{Exc}(SC)$ of 2.16 over the 15 emitter positions (c) Ratio $g_{em}(M)/g_{em}(SC)$ for Alexa790 emitters coupled to Ag nanodisc (Diameter = 140 nm, Height = 40 nm) on VO_2 (Thickness = 15 nm). The black line indicates the mean $g_{em}(M)/g_{em}(SC)$ of 1.04 over the 15 emitter positions.

the case when Alexa790 emitters are tangentially (T) oriented. Although the number of detected photons is substantially smaller, as expected for a dipole with tangential orientation interacting with a plasmonic disc, an increase in disc diameter leads to a slight increase in photon numbers and an alteration of the positions with high detectable emission. In the case of perpendicular (P) dipole orientation, the highest photons emission again comes from the upper edge of the disc with an increased number of regions with low photon emission numbers.

Fig. 6.20 (d) indicates the normalised I_{PL},γ_{Ex},γ_R,γ_{Loss} for Alexa790 emitters around a Ag nanodisc (Height = 40 nm, Diamter = 140 nm) on VO_2 (Thickness = 15 nm) averaged over the three dipole orientations.

Upon the VO_2 phase transition, as noted previously, the γ_{Loss} is substantially increased in the regions 5 nm above the VO_2 film surface leading to a large decrease in PL at these locations. Again, the increase in γ_{Ex} can be seen as the driving contribution to the increased I_{PL} observed when VO_2 is in its metallic phase.

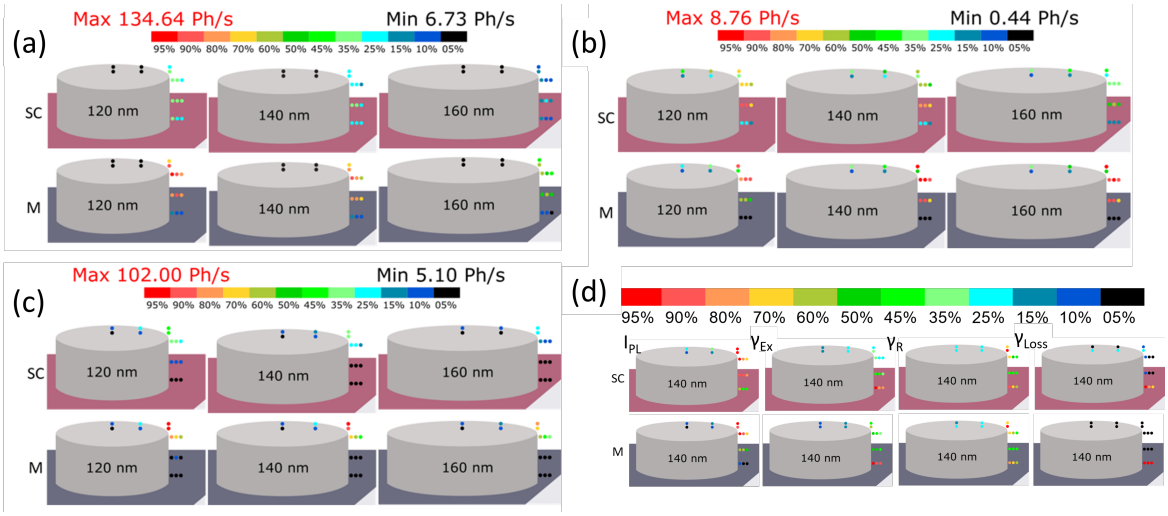

Figure 6.20: (a-c) Detected photons form Alexa790 emitters in the hybrid system comprising of Ag nanodiscs (Height = 40 nm, Diameter = 120 nm, 140 nm, 160 nm) on a VO_2 film (Thickness = 15 nm) in the semiconducting phase (SC) and in the metallic phase (M). In each case $g_{Ex}(\lambda_{Ex})$ is calculated for γ_{Ex} = 730 nm. (a) Detected Photons from Alexa790 emitters with radial (R) dipole orientation. (b) Detected photons from Alexa790 emitters with tangential (T) dipole orientation. (c) detected photons from Alexa790 emitters with perpendicular (P) dipole orientation. (d) Normalised I_{PL},γ_{Ex},γ_R and γ_{Loss} calculated for Alexa790 emitters surrounding a Ag nanodisc (Height = 40 nm, Diameter = 140 nm) on VO_2 (Thickness = 15 nm) for VO_2 in semiconducting (SC) and metallic (M) phase. Before normalisation, the quantities were averaged over the three dipole orientations to model random oriented dipole emitters.

6.5.8 Conclusion

In conclusion, this chapter has demonstrated that coupling Alexa Dye quantum emitters to a plasmonic Ag nanodisc on thin film VO_2 is a promising platform for dynamic tuning of the photoluminescence of quantum emitters with an enhancement factor greater than 4 demonstrated. These enhancements are sufficient to compensate for thermal quenching of emission, making the system ideal in applications where elevated temperatures reduce device efficiency, such as in dye synthesised solar cells and solar concentrators. Additionally, this system is of interest in applications where the VO_2 phase change is induced electrically or optically. In such applications, if ohmic heating effects are negligible, a large range of dynamic tuning of PL enhancement can be exploited.

While, within this chapter, coupling to Ag nanodiscs structures is considered, allowing

emitters to be coupled to other plasmonic particles morphologies such as the nanodisc dimer structures considered in the previous chapter can allow for large PL in both VO_2 oxide phases. Additionally, through emerging methodologies such as two-photon polymerisation, quantum emitters can be placed in the regions surrounding plasmonic particles with the largest E-field enhancement, negating losses arising from emitter proximity to the VO_2 thin film and allowing for large photoluminescence enhancement.

7 Conclusion

In this thesis, the idea of incorporating a phase change material, thin film VO_2, into hybrid nanostructures to dynamically tune their optical properties, particularly within the visible and near infrared spectral region < 1000 nm, is explored. Dynamically tunable hybrid nanostructures consisting of metallic nanoparticles with various morphologies coupled to a thin film of phase change material VO_2 were investigated. In particular, nanoparticle - VO_2, hybrid nanostructures were investigated as a route toward dynamic enhancement of the photoluminescence of coupled quantum emitters through dynamic changes in the plasmonic response of the metallic nanoparticle.

In **Chapter 4**, it was demonstrated how through the VO_2 phase transition, there is a distinct change in the optical properties of films with thicknesses between 10 - 200 nm. A distinct change in reflectance, transmittance and absorptance of the thin films is seen, and the resulting change in reflected and transmitted colour is shown, with a significant dependence on film thickness due to thin film effects.

VO_2 films fabricated through pulsed laser deposition and reactive sputtering techniques are shown to display a strong switching characteristic. a resistance change of over 3 orders of magnitude, indicative of films consisting of purely the VO_2 phase. Investigation of the incorporation of a backreflecting metallic layer demonstrates a significant shift in spectra, particularly reflectance minima and absorbance maxima. This manifests as substantial shifts in colour as demonstrated on the CIE colour maps shown within this section. Within this chapter, it's also demonstrated that the VO_2 phase can be actuated through the application of various stimuli. The reflectance spectra of fabri-

cated samples are compared favourably to the simulated optical properties indicating the films suitability for work done in the succeeding chapters.

In **Chapter 5**, it's seen that for various geometries and dimensions a significantly large blueshift in the peak plasmonic wavelength is achieved through actuating the VO_2 phase change. Additionally, when examining the change in scattering between metallic phase VO_2 and semiconducting phase VO_2, a distinct gain in the scattering cross section is seen at wavelengths close to the visible spectrum. Significant reshaping of the electric field surrounding the plasmonic nanoparticles is also observed, as the E-field can be shown to move up to the top surface of the coupled nanoparticle. Through the VO_2 phase transition, in Au dimer nanostructures, a significant blueshift in the peak electric field intensity results in an enhanced E-field at wavelengths within the visible spectrum. The enhancements in E-field seen are significant and drive the enhancement in photoluminescence further explored within the **Chapter 6**. Additionally the impact of an Au backreflecting layer is again examined, with large changes in spectra and E-field enhancement demonstrated for a range of periodic nanostructures.

Finally, in **Chapter 6**, a model for calculating photoluminescence enhancement of coupled dye emitters was implemented with enhancement factors of > 4 demonstrated for Alexa790 dye coupled to a silver nanodisc on thin film VO_2. This model is used to explore how modification of the nanoparticles dimensions and the thickness of the underlying VO_2 effect the emission of the emitters within the hybrid system. An exploration of the factors contributing to the enhancement are examined with the excitation enhancement appearing to be a driving factor in photoluminescent enhancement over the emission enhancement. With this work, hybrid nanostructures coupled to emitters that can operate at elevated temperatures without thermal quenching losses can be implemented to increase the efficiency of devices that operate at these elevated temperatures. Additionally, as previously mentioned, through tuning of the VO_2 critical temperature and minimising losses by fixing quantum emitters at locations of high E-field intensity, a significantly large photoluminescence enhancement can be achieved

7.0.1 Outlook

The results presented in this work gives insight into the how VO_2 can be implemented into plasmonic devices particularly for those operating in the spectral region below 1 μm. While many metallic nanoparticles morphologies are presented and demonstrate significant plasmon shifts and enhancement of coupled emitters, there is still a large sample space to be explored. For future work, further exploration of the electrically and optically driven VO_2 phase transition is needed as within this work the electrical actuation of the VO_2 phase change appears to be based on a heating effect. The laser induced VO_2 phase transition is similarly using a heating effect to reach the transition temperature. Further consideration of various back-reflector designs, including anti-reflective coatings, could allow for additional applications in optoelectronic devices. To further increase the enhancement of emission, more investigation of the plasmonic tuning capabilities of the hybrid system using a field effect is needed. Exploration of different electronic configurations may allow a larger area of the thin film to be switched potentially increasing possible implementations. Limiting thermal quenching effects in quantum emitters, by decreasing the VO_2 critical temperature, while simultaneously providing an enhanced emission could also expand the potential avenues of implementation within various devices with extremely fast switching speeds.

A further potential avenue to explore with VO_2 based plasmonic devices are as multi-functional sensors. By utilisation of the change in reflected colour within the visible spectra, the shift in the plasmonic scattering peak or increase in coupled emitters photoluminescence through the VO_2 phase change, allows for many avenues for the development of smart devices. The reshaping of the E-field profile and the shift in peak E-field intensity in particular has high potential for implementation in devices. Through the advent of experimental methodologies such as two photon polymerisation (2PP),[169] quantum emitters may be fixed at plasmonic hotspots surrounding a metallic nanoparticle allowing greater enhancement because, as was shown in chapter 6 of this thesis, the average total enhancement is decreased by emitters lying in regions outside

of the optimal E-field enhancement. Future optimisation of the VO_2 material itself through addition of dopants and induced strain has the potential to allow even greater tailoring of the phase transition to suit particular device specification. In particular, large control of the width of the VO_2 hysteresis would make it less challenging to keep the material at a particular volume fraction of metallic VO_2 within semiconducting VO_2 thus achieving full tuning rather than just the OFF/ON states reported in much of the literature. Ultimately VO_2 based hybrid nanostructures demonstrate a wide range of modulation through the VO_2 phase change and further optimisation and experimental confirmation of enhancing effects can pave the way to implementation in optoelectronic devices, particularly ones operating near the critical temperature.

References

[1] Richard P. Feynman. There's plenty of room at the bottom. 1959.

[2] Patricia I. Dolez. Chapter 1.1 - nanomaterials definitions, classifications, and applications. In Patricia I. Dolez, editor, *Nanoengineering*, pages 3–40. Elsevier, Amsterdam, 2015.

[3] Alf Mews. Nanomaterials handbook. edited by yury gogotsi., 2007.

[4] Pedro Gómez-Romero and Clément Sanchez. *Functional hybrid materials*. John Wiley & Sons, 2006.

[5] P Iqbal, JA Preece, and PM Mendes. Supramolecular chemistry. *Nanotechnology: The "Top-Down" and "Bottom-Up" Approaches*, 2012.

[6] Samer Bayda, Muhammad Adeel, Tiziano Tuccinardi, Marco Cordani, and Flavio Rizzolio. The history of nanoscience and nanotechnology: From chemical–physical applications to nanomedicine. *Molecules*, 25(1), 2020.

[7] Regina Luttge. Massively parallel fabrication of repetitive nanostructures: Nanolithography for nanoarrays. *J. Phys. D: Appl. Phys. J. Phys. D: Appl. Phys*, 42:123001–18, 06 2009.

[8] Enlai Gao, Shao-Zhen Lin, Zhao Qin, Markus J. Buehler, Xi-Qiao Feng, and Zhiping Xu. Mechanical exfoliation of two-dimensional materials. *Journal of the Mechanics and Physics of Solids*, 115:248–262, 2018.

[9] Mengqi Zeng, Yao Xiao, Jinxin Liu, Kena Yang, and Lei Fu. Exploring two-dimensional materials toward the next-generation circuits: From monomer design to assembly control. *Chemical Reviews*, 118(13):6236–6296, 2018. PMID: 29381058.

[10] SPIE Europe Ltd. Metalenz meta-optics arrive in time-of-flight sensor.

[11] SPIE Europe Ltd. Optical metamaterials to impact lens market 'within a year'.

[12] Ulf Leonhardt. Invisibility cup. *Nature photonics*, 1(4):207–208, 2007.

[13] Alessia Polemi, Sabrina Wells, Nickolay Lavrik, Michael Sepaniak, and Kevin Shuford. Dispersion characteristics in disk-on-pillar array nanostructures for surface-enhanced raman spectroscopy. *The Journal of Physical Chemistry C*, 115, 06 2011.

[14] Graeme McNay, David Eustace, W. Ewen Smith, Karen Faulds, and Duncan Graham. Surface-enhanced raman scattering (sers) and surface-enhanced resonance raman scattering (serrs): A review of applications. *Applied Spectroscopy*, 65(8):825–837, 2011. PMID: 21819771.

[15] Agnes Purwidyantri, Chih-Hsien Hsu, Chia-Ming Yang, Briliant Adhi Prabowo, Ya-Chung Tian, and Chao-Sung Lai. Plasmonic nanomaterial structuring for sers enhancement. *RSC Adv.*, 9:4982–4992, 2019.

[16] Lorenzo Ferrari, Joseph S. T. Smalley, Haoliang Qian, Atsunori Tanaka, Dylan Lu, Shadi Dayeh, Yeshaiahu Fainman, and Zhaowei Liu. Design and analysis of blue ingan/gan plasmonic led for high-speed, high-efficiency optical communications. *ACS Photonics*, 5(9):3557–3564, 2018.

[17] Xingce Fan, Qi Hao, Teng Qiu, and Paul K. Chu. Improving the performance of light-emitting diodes via plasmonic-based strategies. *Journal of Applied Physics*, 127(4):040901, 2020.

[18] Q. Hao, T. Qiu, and P.K. Chu. 11 - surface plasmon enhanced leds. In JianJang Huang, Hao-Chung Kuo, and Shyh-Chiang Shen, editors, *Nitride Semiconductor*

Light-Emitting Diodes (LEDs), pages 355–367. Woodhead Publishing, 2014.

[19] Anand M Shrivastav, Uroš Cvelbar, and Ibrahim Abdulhalim. A comprehensive review on plasmonic-based biosensors used in viral diagnostics. *Communications biology*, 4(1):1–12, 2021.

[20] Antonio Minopoli, Adriano Acunzo, Bartolomeo Della Ventura, and Raffaele Velotta. Nanostructured surfaces as plasmonic biosensors: A review. *Advanced Materials Interfaces*, 9(2):2101133, 2022.

[21] J. R. Mejía-Salazar and Osvaldo N. Oliveira. Plasmonic biosensing. *Chemical Reviews*, 118(20):10617–10625, 2018.

[22] Chao Zhan, Gan Wang, Jun Yi, Jun-Ying Wei, Zhi-Hao Li, Zhao-Bin Chen, Jia Shi, Yang Yang, Wenjing Hong, and Zhong-Qun Tian. Single-molecule plasmonic optical trapping. *Matter*, 3(4):1350–1360, 2020.

[23] Yuan-Fong Chou Chau, Chung Tin Chou Chao, Hung Ji Huang, Ya-Chih Wang, Hai-Pang Chiang, Muhammad Nur Syafi'ie Md Idris, Zarifi Masri, and Chee Ming Lim. Strong and tunable plasmonic field coupling and enhancement generating from the protruded metal nanorods and dielectric cores. *Results in Physics*, 13:102290, 2019.

[24] Stephen Cunningham, Calin Hrelescu, and A. Louise Bradley. Plasmonic nanodiscs on vanadium dioxide thin films for tunable luminescence enhancement. *Opt. Express*, 29(14):22288–22298, Jul 2021.

[25] Rashid Zia, Jon A. Schuller, Anu Chandran, and Mark L. Brongersma. Plasmonics: the next chip-scale technology. *Materials Today*, 9(7):20–27, 2006.

[26] Chang-Won Lee, Hee Jin Choi, and Heejeong Jeong. Tunable metasurfaces for visible and swir applications. *Nano convergence*, 7(1):1–11, 2020.

[27] Jaekyung Kim, Junhwa Seong, Younghwan Yang, Seong-Won Moon, Trevon Badloe, and Junsuk Rho. Tunable metasurfaces towards versatile metalenses and metaholograms: a review. *Advanced Photonics*, 4(2):024001, 2022.

[28] Mikhail Y Shalaginov, Sawyer D Campbell, Sensong An, Yifei Zhang, Carlos Ríos, Eric B Whiting, Yuhao Wu, Lei Kang, Bowen Zheng, Clayton Fowler, et al. Design for quality: reconfigurable flat optics based on active metasurfaces. *Nanophotonics*, 9(11):3505–3534, 2020.

[29] Kai Guo, Xiaoyu Li, Huifang Ai, Xiya Ding, Lulu Wang, Wei Wang, and Zhongyi Guo. Tunable oriented mid-infrared wave based on metasurface with phase change material of gst. *Results in Physics*, 34:105269, 2022.

[30] Weiling Dong, Yimei Qiu, Xilin Zhou, Agnieszka Banas, Krzysztof Banas, Mark B. H. Breese, Tun Cao, and Robert E. Simpson. Tunable mid-infrared phase-change metasurface. *Advanced Optical Materials*, 6(14):1701346, 2018.

[31] Yuanhang Che, Xiaoting Wang, Qinghai Song, Yabei Zhu, and Shumin Xiao. Tunable optical metasurfaces enabled by multiple modulation mechanisms. *Nanophotonics*, 9(15):4407–4431, 2020.

[32] James A. Dolan, Haogang Cai, Lily Delalande, Xiao Li, Alex B. F. Martinson, Juan J. de Pablo, Daniel López, and Paul F. Nealey. Broadband liquid crystal tunable metasurfaces in the visible: Liquid crystal inhomogeneities across the metasurface parameter space. *ACS Photonics*, 8(2):567–575, 2021.

[33] Andrei Komar, Ramón Paniagua-Domínguez, Andrey Miroshnichenko, Ye Feng Yu, Yuri S. Kivshar, Arseniy I. Kuznetsov, and Dragomir Neshev. Dynamic beam switching by liquid crystal tunable dielectric metasurfaces. *ACS Photonics*, 5(5):1742–1748, 2018.

[34] Sinan Balci, Osman Balci, Nurbek Kakenov, Fatih Bilge Atar, and Coskun Kocabas. Dynamic tuning of plasmon resonance in the visible using graphene. *Opt. Lett.*, 41(6):1241–1244, Mar 2016.

[35] Sergey Lepeshov and Alex Krasnok. Tunable phase-change metasurfaces. *Nature Nanotechnology*, 16(6):615–616, 2021.

[36] Xiya Ding, Qianlong Kang, Kai Guo, and Zhongyi Guo. Tunable gst metasurfaces for chromatic aberration compensation in the mid-infrared. *Optical Materials*, 109:110284, 2020.

[37] Trevon Badloe, Jihae Lee, Junhwa Seong, and Junsuk Rho. Tunable metasurfaces: The path to fully active nanophotonics. *Advanced Photonics Research*, 2(9):2000205, 2021.

[38] Sajjad Abdollahramezani, Omid Hemmatyar, Hossein Taghinejad, Alex Krasnok, Yashar Kiarashinejad, Mohammadreza Zandehshahvar, Andrea Alù, and Ali Adibi. Tunable nanophotonics enabled by chalcogenide phase-change materials. *Nanophotonics*, 9(5):1189–1241, 2020.

[39] Byung Joon Choi, Seol Choi, Yong Cheol Shin, Cheol Seong Hwang, Jin Wook Lee, Jaehack Jeong, Yoon Jung Kim, Sung-Yeon Hwang, and Suk Kyoung Hong. Cyclic pecvd of ge2sb2te5 films using metallorganic sources. *Journal of the electrochemical society*, 154(4):H318, 2007.

[40] Irene Olivares, Luis Sánchez, Jorge Parra, Roberto Larrea, Amadeu Griol, Mariela Menghini, Pía Homm, Lee-Woon Jang, Bart van Bilzen, Jin Won Seo, Jean-Pierre Locquet, and Pablo Sanchis. Optical switching in hybrid vo2/si waveguides thermally triggered by lateral microheaters. *Opt. Express*, 26(10):12387–12395, May 2018.

[41] Kent A Hallman, Kevin J Miller, Andrey Baydin, Sharon M Weiss, and Richard F Haglund. Sub-picosecond response time of a hybrid vo2: silicon waveguide at 1550 nm. *Advanced Optical Materials*, 9(4):2001721, 2021.

[42] Bharathi Rajeswaran, Inyalot Jude Tadeo, and Arun M. Umarji. Ir photoresponsive vo2 thin films and electrically assisted transition prepared by single-step chemical vapor deposition. *J. Mater. Chem. C*, 8:12543–12550, 2020.

[43] MC Larciprete, M Centini, S Paoloni, I Fratoddi, SA Dereshgi, K Tang, J Wu, and K Aydin. Adaptive tuning of infrared emission using vo2 thin films. *Scientific*

reports, 10(1):1–10, 2020.

[44] Shengxiang Wang, Lei Kang, and Douglas H Werner. Hybrid resonators and highly tunable terahertz metamaterials enabled by vanadium dioxide (vo2). *Scientific reports*, 7(1):1–8, 2017.

[45] Yuanyuan Cui, Yujie Ke, Chang Liu, Zhang Chen, Ning Wang, Liangmiao Zhang, Yang Zhou, Shancheng Wang, Yanfeng Gao, and Yi Long. Thermochromic vo2 for energy-efficient smart windows. *Joule*, 2(9):1707–1746, 2018.

[46] Jiadong Zhou, Yanfeng Gao, Zongtao Zhang, Hongjie Luo, Chuanxiang Cao, Zhang Chen, Lei Dai, and Xinling Liu. Vo2 thermochromic smart window for energy savings and generation. *Scientific reports*, 3(1):1–5, 2013.

[47] Vamsi K. Komarala, A. Louise Bradley, Yury P. Rakovich, Stephen J. Byrne, Yurii K. Gun'ko, and Andrey L. Rogach. Surface plasmon enhanced förster resonance energy transfer between the cdte quantum dots. *Applied Physics Letters*, 93(12):123102, 2008.

[48] Pascal Anger, Palash Bharadwaj, and Lukas Novotny. Enhancement and quenching of single-molecule fluorescence. *Phys. Rev. Lett.*, 96:113002, Mar 2006.

[49] Sergei Kühn, Ulf Håkanson, Lavinia Rogobete, and Vahid Sandoghdar. Enhancement of single-molecule fluorescence using a gold nanoparticle as an optical nanoantenna. *Phys. Rev. Lett.*, 97:017402, Jul 2006.

[50] Olga Kulakovich, Natalya Strekal, Alexandr Yaroshevich, Sergey Maskevich, Sergey Gaponenko, Igor Nabiev, Ulrike Woggon, and Mikhail Artemyev. Enhanced luminescence of cdse quantum dots on gold colloids. *Nano Letters*, 2(12):1449–1452, 2002.

[51] V. N. Pustovit and T. V. Shahbazyan. Fluorescence quenching near small metal nanoparticles. *The Journal of Chemical Physics*, 136(20):204701, 2012.

[52] Yikuan Wang, Tianyu Yang, Mark T. Tuominen, and Marc Achermann. Radiative rate enhancements in ensembles of hybrid metal-semiconductor nanostruc-

tures. *Phys. Rev. Lett.*, 102:163001, Apr 2009.

[53] Soroosh Daqiqeh Rezaei, Jinfa Ho, Ray Jia Hong Ng, Seeram Ramakrishna, and Joel K. W. Yang. On the correlation of absorption cross-section with plasmonic color generation. *Opt. Express*, 25(22):27652–27664, Oct 2017.

[54] Jana Olson, Sergio Dominguez-Medina, Anneli Hoggard, Lin-Yung Wang, Wei-Shun Chang, and Stephan Link. Optical characterization of single plasmonic nanoparticles. *Chem. Soc. Rev.*, 44:40–57, 2015.

[55] Peter B Johnson and R-WJPrB Christy. Optical constants of the noble metals. *Physical review B*, 6(12):4370, 1972.

[56] Edward D. Palik. *Handbook of Optical Constants of Solids*. 1985.

[57] David B. Tanner. *The Complex Dielectric Function and Refractive Index*, page 17–29. Cambridge University Press, 2019.

[58] Vincenzo Giannini, Antonio I Fernández-Domínguez, Susannah C Heck, and Stefan A Maier. Plasmonic nanoantennas: fundamentals and their use in controlling the radiative properties of nanoemitters. *Chemical reviews*, 111(6):3888–3912, 2011.

[59] Julia Lawless, Calin Hrelescu, Carolyn Elliott, Lisanne Peters, Niall McEvoy, and A. Louise Bradley. Influence of gold nano-bipyramid dimensions on strong coupling with excitons of monolayer mos2. *ACS Applied Materials & Interfaces*, 12(41):46406–46415, 2020. PMID: 32960560.

[60] Andreas Tittl. Tunable structural colors on display. *Light: Science & Applications*, 11(1):1–2, 2022.

[61] George Gabriel Stokes. Xxx. on the change of refrangibility of light. *Philosophical Transactions of the Royal Society of London*, 142:463–562, 1852.

[62] Robert P. Learmonth, Scott H. Kable, and Kenneth P. Ghiggino. Basics of fluorescence. 2009.

[63] Joseph R. Lakowicz, editor. *Introduction to Fluorescence*, pages 1–26. Springer US, Boston, MA, 2006.

[64] Marcia Levitus. Handbook of fluorescence spectroscopy and imaging. from ensemble to single molecules. edited by markus sauer, johan hofkens and jörg enderlein. *Angewandte Chemie International Edition*, 50(39):9017–9018, 2011.

[65] M.N. Berberan-SantosB. Valeur. *Molecular Fluorescence, Principles and Applications, 2nd ed.*, chapter 1, pages 1–30. (Wiley, Weinheim), 2012.

[66] Michael Kasha. Characterization of electronic transitions in complex molecules. *Discuss. Faraday Soc.*, 9:14–19, 1950.

[67] R. Chang. *Physical Chemistry for the Biosciences.* University Science Books, 2005.

[68] Donald A. McQuarrie and John D. Simon. *Physical chemistry : a molecular approach.* University Science Books, Sausalito, Calif., 1997.

[69] Edinburgh Instruments Ltd. Jablonski Diagram | What is it?, 4 2021.

[70] Wolfgang Becker. *Advanced time-correlated single photon counting applications*, volume 111. Springer, 2015.

[71] J. B. Birks and D. J. Dyson. The relations between the fluorescence and absorption properties of organic molecules. *Proceedings of the Royal Society of London. Series A, Mathematical and Physical Sciences*, 275(1360):135–148, 1963.

[72] S. J. Strickler and Robert A. Berg. Relationship between absorption intensity and fluorescence lifetime of molecules. *The Journal of Chemical Physics*, 37(4):814–822, 1962.

[73] Surajit Chatterjee and Tushar Kanti Mukherjee. Thermal luminescence quenching of amine-functionalized silicon quantum dots: a ph and wavelength-dependent study. *Phys. Chem. Chem. Phys.*, 17:24078–24085, 2015.

[74] Yiming Zhao, Charl Riemersma, Francesca Pietra, Rolf Koole, Celso de Mello Donegá, and Andries Meijerink. High-temperature luminescence quenching of colloidal quantum dots. *ACS Nano*, 6(10):9058–9067, 2012. PMID: 22978378.

[75] Qinggang Zhang, Mengda He, Qun Wan, Weilin Zheng, Mingming Liu, Congyang Zhang, Xinrong Liao, Wenji Zhan, Long Kong, Xiaojun Guo, and Liang Li. Suppressing thermal quenching of lead halide perovskite nanocrystals by constructing a wide-bandgap surface layer for achieving thermally stable white light-emitting diodes. *Chem. Sci.*, 13:3719–3727, 2022.

[76] Lukas Novotny and Bert Hecht. *Quantum emitters*, page 282–312. Cambridge University Press, 2 edition, 2012.

[77] Ute Resch-Genger, Markus Grabolle, Sara Cavaliere, Roland Nitschke, and Thomas Nann. Quantum dots versus organic dyes as fluorescent labels. *Nature methods*, 5:763–75, 10 2008.

[78] John B. Goodenough. The two components of the crystallographic transition in vo2. *Journal of Solid State Chemistry*, 3(4):490–500, 1971.

[79] F. J. Morin. Oxides which show a metal-to-insulator transition at the neel temperature. *Phys. Rev. Lett.*, 3:34–36, Jul 1959.

[80] Abhimanyu Rana, Chuan Li, Gertjan Koster, and Hans Hilgenkamp. Resistive switching studies in volt;subgt;2lt;/subgt; thin films. *Scientific reports*, 10(1):3293, February 2020.

[81] Daniele Di Gioacchino, Augusto Marcelli, Alessandro Puri, Chongwen Zou, Lele Fan, U. Zeitler, and Antonio Bianconi. Metastability phenomena in vo2 thin films. *Condensed Matter*, 2:10, 02 2017.

[82] Fabien Béteille, Léo Mazerolles, and Jacques Livage. Microstructure and metal-insulating transition of vo2 thin films. *Materials Research Bulletin*, 34(14-15):2177–2184, 1999.

[83] Yan Zhang and Shriram Ramanathan. Analysis of "on" and "off" times for thermally driven vo2 metal-insulator transition nanoscale switching devices. *Solid-State Electronics*, 62(1):161–164, 2011.

[84] J. Zemann. Crystal structures, 2nd edition. vol. 1 by r. w. g. wyckoff. *Acta Crystallographica*, 18(1):139–139, 1965.

[85] Sven Westman, Ingvar Lindqvist, Berndt Sparrman, G. Bech Nielsen, H. Nord, and Aage Jart. Note on a phase transition in vo2. *Acta Chemica Scandinavica (1989)*.

[86] Renata M. Wentzcovitch, Werner W. Schulz, and Philip B. Allen. vo_2: Peierls or mott-hubbard? a view from band theory. *Phys. Rev. Lett.*, 72:3389–3392, May 1994.

[87] S. Biermann, A. Poteryaev, A. I. Lichtenstein, and A. Georges. Dynamical singlets and correlation-assisted peierls transition in vo_2. *Phys. Rev. Lett.*, 94:026404, Jan 2005.

[88] Pengfei Guo, Andrew M. Sarangan, and Imad Agha. A review of germanium-antimony-telluride phase change materials for non-volatile memories and optical modulators. *Applied Sciences*, 9(3), 2019.

[89] Vinod E. M., Marcelo Carignano, Ali Kachmar, and K.s Sangunni. Crystallization properties of arsenic doped gst alloys. *Scientific Reports*, 9, 09 2019.

[90] Luca Perniola, Veronique Sousa, Andrea Fantini, Edrisse Arbaoui, Audrey Bastard, Marilyn Armand, Alain Fargeix, C. Jahan, J.F. Nodin, Alain Persico, Denis Blachier, A. Toffoli, Sebastien Loubriat, Emanuel Gourvest, Giovanni Betti Beneventi, Helene Feldis, Sylvain Maitrejean, S. Lhostis, Anne Roule, and Fabien Boulanger. Electrical behavior of phase-change memory cells based on gete. *Electron Device Letters, IEEE*, 31:488 – 490, 06 2010.

[91] Y. C. Her, Hung-Ting Chen, and Yung-Sung Hsu. Effects of ag and in addition on the optical properties and crystallization kinetics of eutectic sb70te30 phase-

change recording film. *Journal of Applied Physics*, 93:10097–10103, 2003.

[92] T.J. Hanlon, J.A. Coath, and M.A. Richardson. Molybdenum-doped vanadium dioxide coatings on glass produced by the aqueous sol–gel method. *Thin Solid Films*, 436(2):269–272, 2003.

[93] W Burkhardt, T Christmann, B.K Meyer, W Niessner, D Schalch, and A Scharmann. W- and f-doped vo2 films studied by photoelectron spectrometry. *Thin Solid Films*, 345(2):229–235, 1999.

[94] B. L. Brown, Mark Lee, P. G. Clem, C. D. Nordquist, T. S. Jordan, S. L. Wolfley, D. Leonhardt, C. Edney, and J. A. Custer. Electrical and optical characterization of the metal-insulator transition temperature in cr-doped vo2 thin films. *Journal of Applied Physics*, 113(17):173704, 2013.

[95] W. Brückner, U. Gerlach, W. Moldenhauer, H.-P. Brückner, B. Thuss, H. Oppermann, E. Wolf, and I. Storbeck. METAL-NONMETAL TRANSITION IN Fe- AND Al-DOPED VO2. *Journal de Physique Colloques*, 37(C4):C4–63–C4–68, 1976.

[96] Shuanglin () Hu, S.-Y. () Li, R. Ahuja, C. G. Granqvist, K. Hermansson, G. A. Niklasson, and R. H. Scheicher. Optical properties of mg-doped vo2: Absorption measurements and hybrid functional calculations. *Applied Physics Letters*, 101(20):201902, 2012.

[97] A. Cavalleri, Cs. Tóth, C. W. Siders, J. A. Squier, F. Ráksi, P. Forget, and J. C. Kieffer. Femtosecond structural dynamics in vo_2 during an ultrafast solid-solid phase transition. *Phys. Rev. Lett.*, 87:237401, Nov 2001.

[98] A. Cavalleri, Th. Dekorsy, H. H. W. Chong, J. C. Kieffer, and R. W. Schoenlein. Evidence for a structurally-driven insulator-to-metal transition in vo_2: A view from the ultrafast timescale. *Phys. Rev. B*, 70:161102, Oct 2004.

[99] Aurelian Crunteanu, Julien Givernaud, Jonathan Leroy, David Mardivirin, Corinne Champeaux, Jean-Christophe Orlianges, Alain Catherinot, and Pierre

Blondy. Voltage- and current-activated metal–insulator transition in vo2-based electrical switches: a lifetime operation analysis. *Science and Technology of Advanced Materials*, 11(6):065002, 2010.

[100] Sukeji Kachi, Kōji Kosuge, and Hideyuki Okinaka. Metal-insulator transition in vno2n1. *Journal of Solid State Chemistry*, 6:258–270, 1973.

[101] M. Demeter, M. Neumann, and W. Reichelt. Mixed-valence vanadium oxides studied by xps. *Surface Science*, 454-456:41–44, 2000.

[102] H. Katzke, P. Tolédano, and W. Depmeier. Theory of morphotropic transformations in vanadium oxides. *Phys. Rev. B*, 68:024109, Jul 2003.

[103] L. A. Ladd and W Palmberg Paul. Optical and transport properties of high quality crystals of v2o4 near the metallic transition temperature. *Solid State Communications*, 7:425–428, 1969.

[104] Vadim A Markel. Introduction to the maxwell garnett approximation: tutorial. *JOSA A*, 33(7):1244–1256, 2016.

[105] Paul Lorrain and Dale R Corson. Electromagnetic fields and waves. 1970.

[106] Heinz Kiessig. Interferenz von röntgenstrahlen an dünnen schichten. *Annalen der Physik*, 402(7):769–788, 1931.

[107] János Schanda. *Colorimetry: understanding the CIE system*. John Wiley & Sons, 2007.

[108] Asim Kumar Roy Choudhury. *Principles of colour and appearance measurement: Object appearance, colour perception and instrumental measurement*. Elsevier, 2014.

[109] R Hobbs. Digital video and hd algorithms and interfaces, 2010.

[110] H.L.M. Chang, H. You, J. Guo, and D.J. Lam. Epitaxial tio2 and vo2 films prepared by mocvd. *Applied Surface Science*, 48-49:12–18, 1991.

[111] Dong ping Zhang, Mao dong Zhu, Yi Liu, Kai Yang, Guang xing Liang, Zhuang hao Zheng, Xing min Cai, and Ping Fan. High performance vo2 thin films growth by dc magnetron sputtering at low temperature for smart energy efficient window application. *Journal of Alloys and Compounds*, 659:198–202, 2016.

[112] Cuicui Cao, Bin Hu, Guoli Tu, Xiaowei Ji, Zhongshao Li, Fang Xu, Tianci Chang, Ping Jin, and Xun Cao. Sputtering flexible vo2 films for effective thermal modulation. *ACS Applied Materials & Interfaces*, 2022.

[113] Byung-Gyu Chae, Hyun-Tak Kim, Sun-Jin Yun, Bong-Jun Kim, Yong-Wook Lee, Doo-Hyeb Youn, and Kwang-Yong Kang. Highly oriented vo2 thin films prepared by sol-gel deposition. *Electrochemical and solid-state letters*, 9(1):C12, 2005.

[114] H Liu, O Vasquez, VR Santiago, L Diaz, AJ Rua, and FE Fernandez. Novel pulsed-laser-deposition—vo2 thin films for ultrafast applications. *Journal of electronic materials*, 34(5):491–496, 2005.

[115] Syed A. Bukhari, Sooraj Kumar, Pawan Kumar, Sarang P. Gumfekar, Hyun-Joong Chung, Thomas Thundat, and Ankur Goswami. The effect of oxygen flow rate on metal–insulator transition (mit) characteristics of vanadium dioxide (vo2) thin films by pulsed laser deposition (pld). *Applied Surface Science*, 529:146995, 2020.

[116] V. G. Tsirelson, M. Yu. Antipin, R. G. Gerr, R. P. Ozerov, and Yu. T. Struchkov. Ruby structure peculiarities derived from x-ray diffraction data localization of chromium atoms and electron deformation density. *physica status solidi (a)*, 87(2):425–433, 1985.

[117] Roger H. French. Electronic band structure of al2o3, with comparison to alon and ain. *Journal of the American Ceramic Society*, 73(3):477–489, 1990.

[118] Thomas A. Mellan and Ricardo Grau-Crespo. Density functional theory study of rutile vo2 surfaces. *The Journal of Chemical Physics*, 137(15):154706, 2012.

[119] Thomas Stirner, ji Sun, and Martin Aust. Ab initio hartree-fock simulation of r-plane sapphire. *Physics Procedia*, 32:635–639, 12 2012.

[120] Guo Yuxian, Haiyan Xu, Chongwen Zou, Zhiyun Yang, Bin Tong, Jiangying Yu, You Zhang, Li Zhao, and Yaling Wang. Evolution of structure and electrical properties with annealing time in solution-based vo2 thin films. *Journal of Alloys and Compounds*, 622:913–917, 2015.

[121] Kunio Okimura, Joe Sakai, and Shriram Ramanathan. In situ x-ray diffraction studies on epitaxial vo2 films grown on c-al2o3 during thermally induced insulator-metal transition. *Journal of Applied Physics*, 107(6):063503, 2010.

[122] Petr Shvets, Olga Dikaya, Ksenia Maksimova, and Alexander Goikhman. A review of raman spectroscopy of vanadium oxides. *Journal of Raman Spectroscopy*, 50(8):1226–1244, 2019.

[123] Mark C. Biesinger, Leo W.M. Lau, Andrea R. Gerson, and Roger St.C. Smart. Resolving surface chemical states in xps analysis of first row transition metals, oxides and hydroxides: Sc, ti, v, cu and zn. *Applied Surface Science*, 257(3):887–898, 2010.

[124] Yonghwi Kim, Pin Chieh Wu, Ruzan Sokhoyan, Kelly Mauser, Rebecca Glaudell, Ghazaleh Kafaie Shirmanesh, Harry A Atwater, and Thomas J Watson. Phase modulation with electrically tunable vanadium dioxide phase-change metasurfaces. *Nano Lett*, 19:3961–3968, 2019.

[125] Weizhen Zhang, Hui Shi, Jianchao Zeng, Hyun-Tak Kim, Byung-Gyu Chae, Doo-Hyeb Youn, Sung-Lyul Maeng, Gyungock Kim, Kwang-Yong Kang, and Yong-Sik Lim. Mechanism and observation of mott transition in vo 2-based two-and three-terminal devices you may also like real-time residual life prediction based on kernel density estimation considering abrupt change point detection mechanism and observation of mott transition in vo 2-based two-and three-terminal devices. *New Journal of Physics*, 6:52, 2004.

[126] Daniel Krebs, Simone Raoux, and Charles T Rettner. Cite as. *Phase change memory technology Journal of Vacuum Science Technology B*, 95:223, 2009.

[127] Himanshu Ranjan Das and Subhash C. Arya. Performance improvement of vo2 and ito based plasmonic electro-absorption modulators at 1550 nm application wavelength. *Optics Communications*, 479:126455, 2021.

[128] Luca Bergamini, Bigeng Chen, Daniel Traviss, Yudong Wang, Cornelis H. de Groot, Jeffrey M. Gaskell, David W. Sheel, Nerea Zabala, Javier Aizpurua, and Otto L. Muskens. Single-nanoantenna driven nanoscale control of the vo2 insulator to metal transition. *Nanophotonics*, 10(14):3745–3758, 2021.

[129] Tongtong Kang, Zongwei Ma, Jun Qin, Zheng Peng, Weihao Yang, Taixing Huang, Shilin Xian, Shuang Xia, Wei Yan, Yucong Yang, Zhigao Sheng, Jian Shen, Chaoyang Li, Longjiang Deng, and Lei Bi. Large-scale, power-efficient au/vo2 active metasurfaces for ultrafast optical modulation. *Nanophotonics*, 10(2):909–918, 2021.

[130] Gregory Beti Tanyi, Miao Sun, Christina Lim, and Ranjith Rajasekharan Unnithan. Design of an on-chip plasmonic modulator based on hybrid orthogonal junctions using vanadium dioxide. *Nanomaterials*, 11(10), 2021.

[131] Jin-Kyu Yang and Hyeon-Seok Jeong. Switchable metasurface with vo2 thin film at visible light by changing temperature. *Photonics*, 8(2), 2021.

[132] Jingqi He, Meng Zhang, Shiwei Shu, Yan Yan, and Mingxiang Wang. Vo2 based dynamic tunable absorber and its application in switchable control and real-time color display in the visible region. *Opt. Express*, 28(25):37590–37599, Dec 2020.

[133] John Henson, Jeff DiMaria, and Roberto Paiella. Influence of nanoparticle height on plasmonic resonance wavelength and electromagnetic field enhancement in two-dimensional arrays. *Journal of Applied Physics*, 106(9):093111, 2009.

[134] Chenghao Wan, Zhen Zhang, David Woolf, Colin M. Hessel, Jura Rensberg, Joel M. Hensley, Yuzhe Xiao, Alireza Shahsafi, Jad Salman, Steffen Richter,

Yifei Sun, M. Mumtaz Qazilbash, Rüdiger Schmidt-Grund, Carsten Ronning, Shriram Ramanathan, and Mikhail A. Kats. On the optical properties of thin-film vanadium dioxide from the visible to the far infrared. *Annalen der Physik*, 531(10):1900188, 2019.

[135] Gang Xu, Yong Chen, Masato Tazawa, and Ping Jin. Surface plasmon resonance of silver nanoparticles on vanadium dioxide. *The Journal of Physical Chemistry B*, 110(5):2051–2056, 2006. PMID: 16471782.

[136] T. V. Raziman and Olivier J. F. Martin. Polarisation charges and scattering behaviour of realistically rounded plasmonic nanostructures. *Opt. Express*, 21(18):21500–21507, Sep 2013.

[137] Ora Bitton, Satyendra Nath Gupta, and Gilad Haran. Quantum dot plasmonics: from weak to strong coupling. *Nanophotonics*, 8(4):559–575, 2019.

[138] Siqi Yan, Xiaolong Zhu, Jianji Dong, Yunhong Ding, and Sanshui Xiao. 2d materials integrated with metallic nanostructures: fundamentals and optoelectronic applications. *Nanophotonics*, 9(7):1877–1900, 2020.

[139] K. George Thomas and Prashant V. Kamat. Making gold nanoparticles glow: enhanced emission from a surface-bound fluoroprobe. *Journal of the American Chemical Society*, 122(11):2655–2656, 2000.

[140] E. Dulkeith, A. C. Morteani, T. Niedereichholz, T. A. Klar, J. Feldmann, S. A. Levi, F. C. J. M. van Veggel, D. N. Reinhoudt, M. Möller, and D. I. Gittins. Fluorescence quenching of dye molecules near gold nanoparticles: Radiative and nonradiative effects. *Phys. Rev. Lett.*, 89:203002, Oct 2002.

[141] M. Ringler, A. Schwemer, M. Wunderlich, A. Nichtl, K. Kürzinger, T. A. Klar, and J. Feldmann. Shaping emission spectra of fluorescent molecules with single plasmonic nanoresonators. *Phys. Rev. Lett.*, 100:203002, May 2008.

[142] Jiani Huang, Gleb M. Akselrod, Tian Ming, Jing Kong, and Maiken H. Mikkelsen. Tailored emission spectrum of 2d semiconductors using plasmonic nanocavities.

ACS Photonics, 5(2):552–558, 2018.

[143] T.H. Taminiau, F.D. Stefani, Franciscus B. Segerink, and N.F. van Hulst. Optical antennas direct single-molecule emission. *Nature photonics*, 2(4):234–237, 2008. Including cover story.

[144] Tian Ming, Lei Zhao, Zhi Yang, Huanjun Chen, Lingdong Sun, Jianfang Wang, and Chunhua Yan. Strong polarization dependence of plasmon-enhanced fluorescence on single gold nanorods. *Nano Letters*, 9(11):3896–3903, 2009. PMID: 19754068.

[145] Rizia Bardhan, Nathaniel K. Grady, Joseph R. Cole, Amit Joshi, and Naomi J. Halas. Fluorescence enhancement by au nanostructures: Nanoshells and nanorods. *ACS Nano*, 3(3):744–752, 2009. PMID: 19231823.

[146] Edward S. Allgeyer, Adam Pongan, Michael Browne, and Michael D. Mason. Optical signal comparison of single fluorescent molecules and raman active gold nanostars. *Nano Letters*, 9(11):3816–3819, 2009. PMID: 19827758.

[147] Battulga Munkhbat, Johannes Ziegler, Hannes Pöhl, Christian Wörister, Dmitry Sivun, Markus C. Scharber, Thomas A. Klar, and Calin Hrelescu. Hybrid multilayered plasmonic nanostars for coherent random lasing. *The Journal of Physical Chemistry C*, 120(41):23707–23715, 2016. PMID: 27795752.

[148] Deep Punj, Raju Regmi, Alexis Devilez, Robin Plauchu, Satish Babu Moparthi, Brian Stout, Nicolas Bonod, Hervé Rigneault, and Jérôme Wenger. Self-assembled nanoparticle dimer antennas for plasmonic-enhanced single-molecule fluorescence detection at micromolar concentrations. *ACS Photonics*, 2(8):1099–1107, 2015.

[149] Ron Gill, Lijin Tian, Walter R. C. Somerville, Eric C. Le Ru, Herbert van Amerongen, and Vinod Subramaniam. Silver nanoparticle aggregates as highly efficient plasmonic antennas for fluorescence enhancement. *The Journal of Physical Chemistry C*, 116(31):16687–16693, 2012.

[150] Reuben M Bakker, Vladimir P Drachev, Zhengtong Liu, Hsiao-Kuan Yuan, Rasmus H Pedersen, Alexandra Boltasseva, Jiji Chen, Joseph Irudayaraj, Alexander V Kildishev, and Vladimir M Shalaev. Nanoantenna array-induced fluorescence enhancement and reduced lifetimes. *New Journal of Physics*, 10(12):125022, dec 2008.

[151] Martin Bauch, Koji Toma, Mana Toma, Qingwen Zhang, and Jakub Dostalek. Plasmon-enhanced fluorescence biosensors: A review. *Plasmonics*, 9(4):781–799, August 2014. Funding Information: Acknowledgments This work was partially supported by the Austrian NANO Initiative (FFG and BMVIT) through the NILPlasmonics project within the NILAustria cluster (www.NILAustria.at) and by the Austrian Science Fund (FWF) through the project ACTIPLAS (P 244920-N20).

[152] Caner Guclu, Ting Shan Luk, George T. Wang, and Filippo Capolino. Radiative emission enhancement using nano-antennas made of hyperbolic metamaterial resonators. *Applied Physics Letters*, 105(12):123101, 2014.

[153] Signe Damm, N. Craig Carville, Michele Manzo, Katia Gallo, Sergio G. Lopez, Tia E. Keyes, Robert J. Forster, Brian J. Rodriguez, and James H. Rice. Surface enhanced luminescence and raman scattering from ferroelectrically defined ag nanopatterned arrays. *Applied Physics Letters*, 103(8):083105, 2013.

[154] Qing Liu, Koen Vanmol, Sylvia Lycke, Jürgen Van Erps, Peter Vandenabeele, Hugo Thienpont, and Heidi Ottevaere. Sers using two-photon polymerized nanostructures for mycotoxin detection. *RSC Adv.*, 10:14274–14282, 2020.

[155] Yangyang Li, Qiaolin Wei, Fei Ma, Xin Li, Fengyong Liu, and Min Zhou. Surface-enhanced raman nanoparticles for tumor theranostics applications. *Acta Pharmaceutica Sinica B*, 8(3):349–359, 2018.

[156] Xue-Ling Cao, Hong-Wei Li, Yuan Yue, and Yuqing Wu. ph-induced conformational changes of bsa in fluorescent auncs@bsa and its effects on ncs emission.

Vibrational Spectroscopy, 65:186–192, 2013.

[157] Daniel Ratchford, Farbod Shafiei, Suenne Kim, Stephen K. Gray, and Xiaoqin Li. Manipulating coupling between a single semiconductor quantum dot and single gold nanoparticle. *Nano Letters*, 11(3):1049–1054, 2011. PMID: 21280639.

[158] Chung Wei Chen, Chung-Hsiang Wang, Chih-Ming Wei, and Fu-Yuan Chen. Tunable emission based on the composite of au nanoparticles and cdse quantum dots deposited on elastomeric film. *Applied Physics Letters*, 94, 02 2009.

[159] Eunjoo Jang, Shinae Jun, Hyosook Jang, Jungeun Lim, Byungki Kim, and Younghwan Kim. White-light-emitting diodes with quantum dot color converters for display backlights. *Advanced Materials*, 22(28):3076–3080, 2010.

[160] J. Lee, V. C. Sundar, J. R. Heine, M. G. Bawendi, and K. F. Jensen. Full color emission from ii–vi semiconductor quantum dot–polymer composites. *Advanced Materials*, 12(15):1102–1105, 2000.

[161] Kyung-Sang Cho, Eun Kyung Lee, Won-Jae Joo, Eunjoo Jang, Tae-Hee Kim, Sang Lee, Soon-Jae Kwon, Jai Han, Byung-Ki Kim, Byoung Choi, and Jong Kim. High-performance crosslinked colloidal quantum-dot light-emitting diodes. *Nature Photonics*, 3:341–345, 05 2009.

[162] Jana Bomm, Andreas Büchtemann, Amanda J. Chatten, Rahul Bose, Daniel J. Farrell, Ngai L.A. Chan, Ye Xiao, Lenneke H. Slooff, Toby Meyer, Andreas Meyer, Wilfried G.J.H.M. van Sark, and Rolf Koole. Fabrication and full characterization of state-of-the-art quantum dot luminescent solar concentrators. *Solar Energy Materials and Solar Cells*, 95(8):2087–2094, 2011. Photovoltaics, Solar Energy Materials Thin Films, IMRC 2009-Cancun.

[163] Michelle TZ Spence and Iain D Johnson. *The molecular probes handbook: a guide to fluorescent probes and labeling technologies*. Life Technologies Corporation, 2010.

[164] Younan Xia and Naomi J Halas. Shape-controlled synthesis and surface plasmonic properties of metallic nanostructures. *MRS bulletin*, 30(5):338–348, 2005.

[165] Eunil Hahm, Ahla Jo, Sang Hun Lee, Homan Kang, Xuan-Hung Pham, and Bong-Hyun Jun. Silica shell thickness-dependent fluorescence properties of sio2@ag@sio2@qds nanocomposites. *International Journal of Molecular Sciences*, 23(17), 2022.

[166] Wonseok Yang, Sandeep Kaur, Yong Duk Kim, Jung-Mu Kim, Seung Hee Lee, and Dong-Kwon Lim. Precise control over the silica shell thickness and finding the optimal thickness for the peak heat diffusion property of aunr@sio2. *J. Mater. Chem. B*, 10:364–372, 2022.

[167] Kelvin Chung and Snjezana Tomljenovic-Hanic. Emission properties of fluorescent nanoparticles determined by their optical environment. *Nanomaterials*, 5(2):895–905, 2015.

[168] Sander F. Wuister, Celso de Mello Donegá, and Andries Meijerink. Local-field effects on the spontaneous emission rate of cdte and cdse quantum dots in dielectric media. *The Journal of Chemical Physics*, 121(9):4310–4315, 2004.

[169] Dandan Ge, Sylvie Marguet, Ali Issa, Safi Jradi, Tien Hoa Nguyen, Mackrine Nahra, Jéremie Béal, Régis Deturche, Hongshi Chen, Sylvain Blaize, Jérôme Plain, Céline Fiorini, Ludovic Douillard, Olivier Soppera, Xuan Quyen Dinh, Cuong Dang, Xuyong Yang, Tao Xu, Bin Wei, Xiao Wei Sun, Christophe Couteau, and Renaud Bachelot. Hybrid plasmonic nano-emitters with controlled single quantum emitter positioning on the local excitation field. *Nature Communications*, 11(1), jul 2020.

A1 Appendix

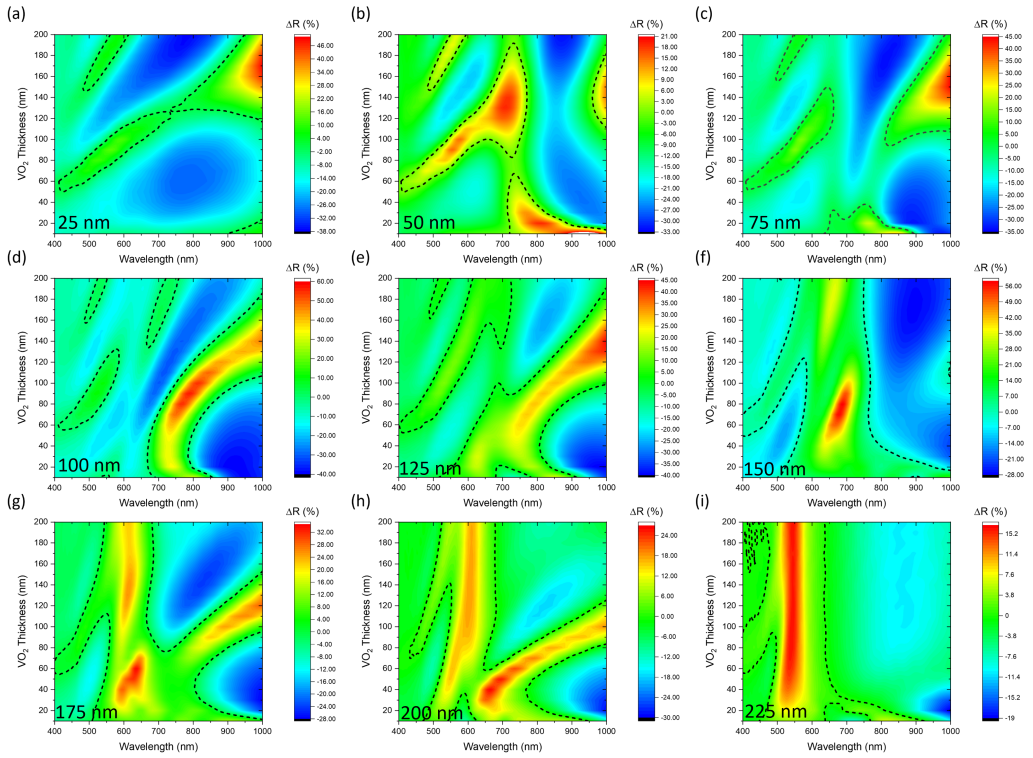

Figure A1.1: (a-i) VO_2 - Au film $\Delta R(R_M - R_{SC})$ for varying film thickness and side length of the embedded Au. Black dashed line represents region where $\Delta R = 0$, therefore the bounded areas represent an increased reflectance for VO_2 in metallic phase.

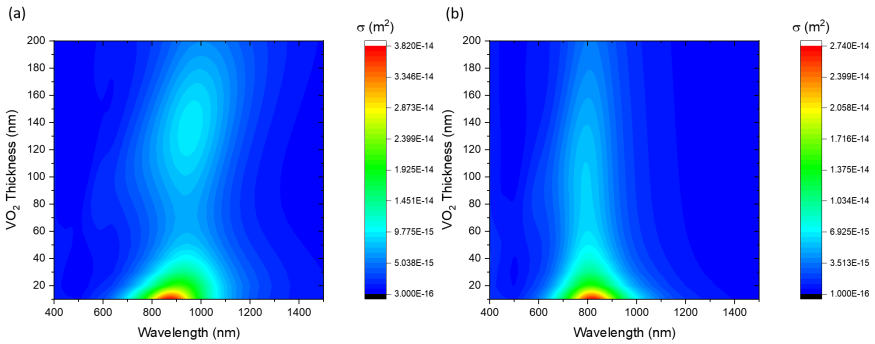

Figure A1.2: Contour maps depicting the dependence of the scattering cross-section spectrum, for longitudinal excitation, of a Au nanorod (Length = 180 nm, Width = 90 nm, Height = 40 nm), on the VO_2 film thickness for VO_2 in (a) semiconducting phase and (b) metallic phase.

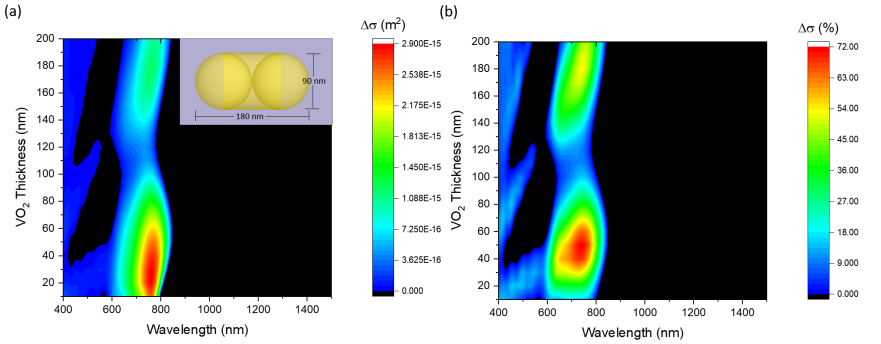

Figure A1.3: Contour maps depicting (a) $\Delta\ \sigma(\sigma_M - \sigma_{SC})$ and (b) $\Delta\sigma(\%)[100 \times \frac{\sigma_M - \sigma_{SC}}{\sigma_{SC}}]$ for Au Nanorod (Length = 180 nm, Width = 90 nm, Height = 40 nm) under longitudinal excitation. Coloured sections indicate an increase in scattering as VO_2 transition to metallic phase. Black regions indicate a decrease in scattering as VO_2 transitions to metallic phase. A schematic of the Au nanorod structure is included as an inset to (a).

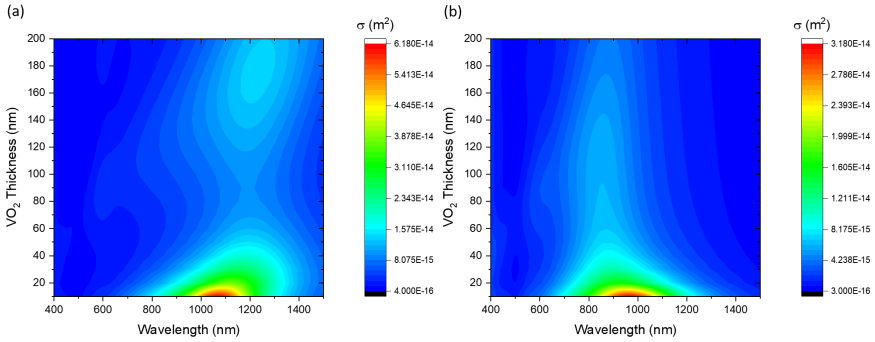

Figure A1.4: Contour maps depicting the dependence of the scattering cross-section spectrum, for longitudinal excitation, of a Au nanorod (Length = 230 nm, Width = 90 nm, Height = 40 nm), on the VO_2 film thickness for VO_2 in (a) semiconducting phase and (b) metallic phase.

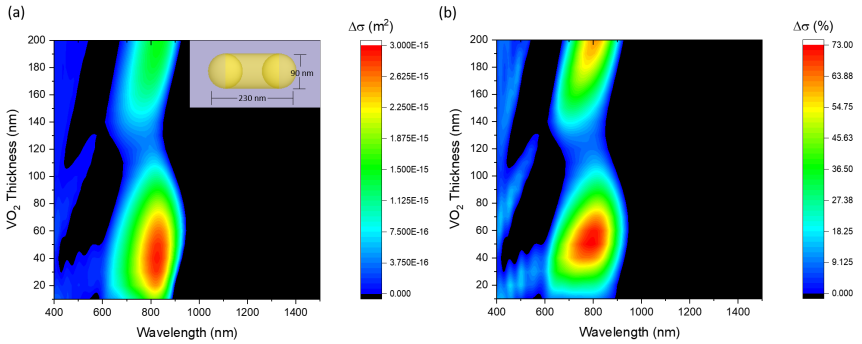

Figure A1.5: Contour maps depicting (a) $\Delta\ \sigma(\sigma_M - \sigma_{SC})$ and (b) $\Delta\sigma(\%)[100 \times \frac{\sigma_M - \sigma_{SC}}{\sigma_{SC}}]$ for Au Nanorod (Length = 230 nm, Width = 90 nm, Height = 40 nm) under longitudinal excitation. Coloured sections indicate an increase in scattering as VO_2 transition to metallic phase. Black regions indicate a decrease in scattering as VO_2 transitions to metallic phase. A schematic of the Au nanorod structure is included as an inset to (a).

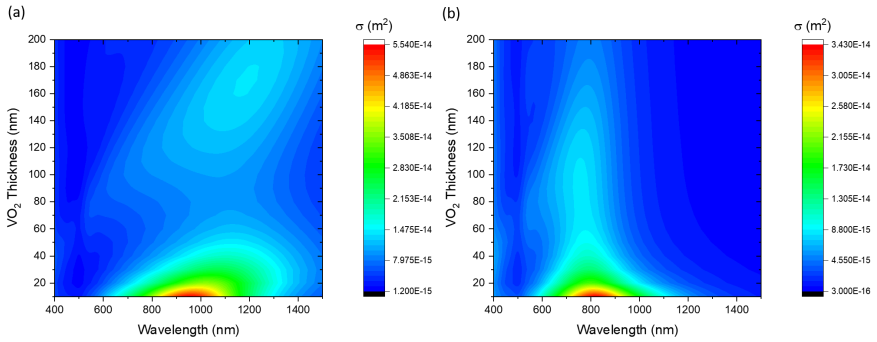

Figure A1.6: Contour maps depicting the dependence of the scattering cross-section spectrum, for longitudinal excitation, of a Au nanorod (Radius = 90 nm, Height = 40 nm), on the VO_2 film thickness for VO_2 in (a) semiconducting phase and (b) metallic phase.

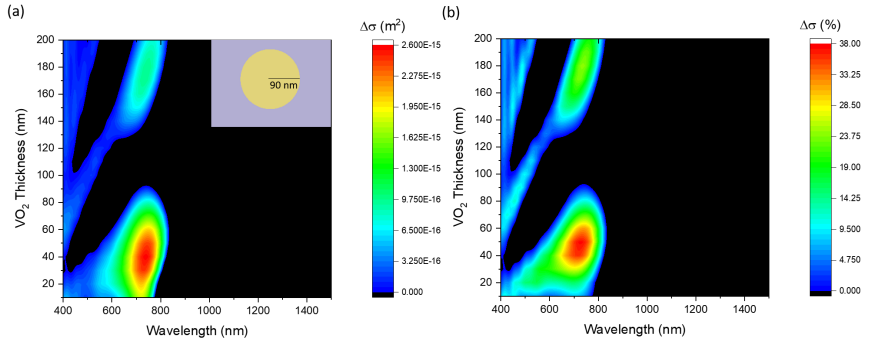

Figure A1.7: Contour maps depicting (a) $\Delta\ \sigma(\sigma_M - \sigma_{SC})$ and (b) $\Delta\sigma(\%)[100 \times \frac{\sigma_M - \sigma_{SC}}{\sigma_{SC}}]$ for Au Nanorod (Radius = 90 nm, Height = 40 nm) under longitudinal excitation. Coloured sections indicate an increase in scattering as VO_2 transition to metallic phase. Black regions indicate a decrease in scattering as VO_2 transitions to metallic phase. A schematic of the Au nanorod structure is included as an inset to (a).

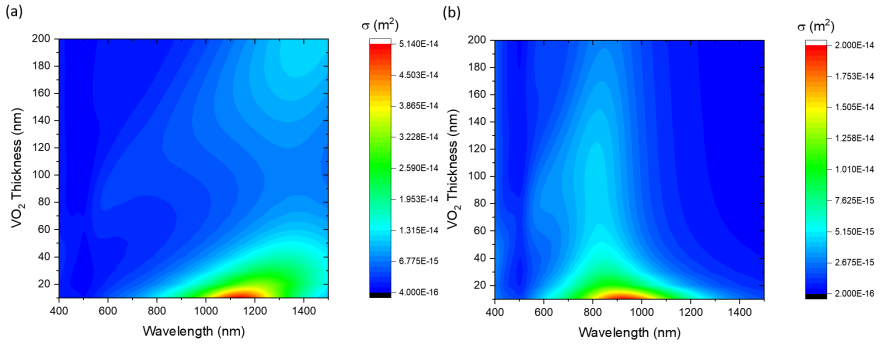

Figure A1.8: Contour maps depicting the dependence of the scattering cross-section spectrum, for longitudinal excitation, of a Au nanorod (Length = 180 nm, Width = 90 nm, Height = 40 nm), on the VO_2 film thickness for VO_2 in (a) semiconducting phase and (b) metallic phase.

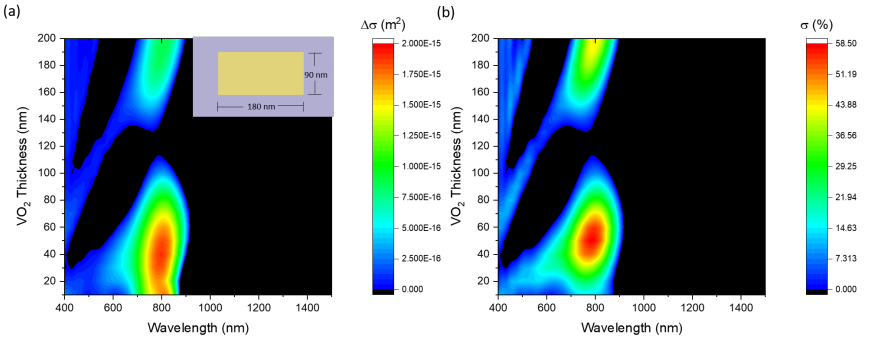

Figure A1.9: Contour maps depicting (a) $\Delta\ \sigma(\sigma_M - \sigma_{SC})$ and (b) $\Delta\sigma(\%)[100 \times \frac{\sigma_M - \sigma_{SC}}{\sigma_{SC}}]$ for Au Nanorod (Length = 180 nm, Width = 90 nm, Height = 40 nm) under longitudinal excitation. Coloured sections indicate an increase in scattering as VO_2 transition to metallic phase. Black regions indicate a decrease in scattering as VO_2 transitions to metallic phase. A schematic of the Au nanorod structure is included as an inset to (a).

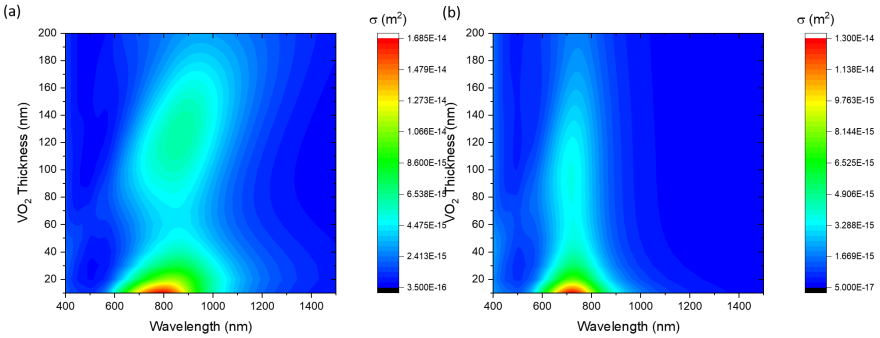

Figure A1.10: Contour maps depicting the dependence of the scattering cross-section spectrum, for transverse excitation, of a Au nanorod (Length = 180 nm, Width = 90 nm, Height = 40 nm), on the VO_2 film thickness for VO_2 in (a) semiconducting phase and (b) metallic phase.

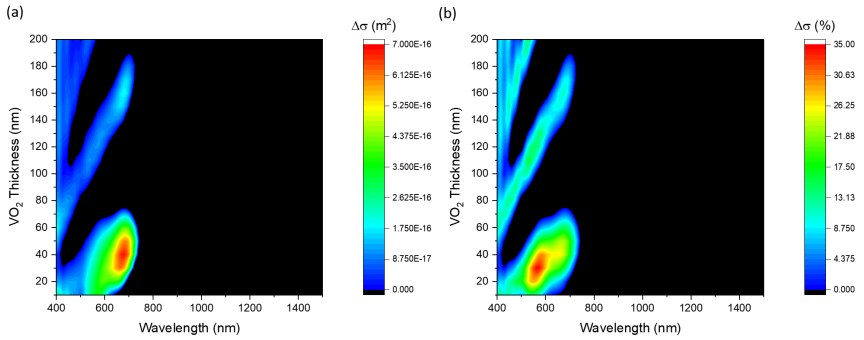

Figure A1.11: Contour maps depicting (a) $\Delta\ \sigma(\sigma_M - \sigma_{SC})$ and (b) $\Delta\sigma(\%)[100 \times \frac{\sigma_M - \sigma_{SC}}{\sigma_{SC}}]$ for Au Nanorod (Length = 180 nm, Width = 90 nm, Height = 40 nm) under transverse excitation. Coloured sections indicate an increase in scattering as VO_2 transition to metallic phase. Black regions indicate a decrease in scattering as VO_2 transitions to metallic phase. A schematic of the Au nanorod structure is included as an inset to (a).

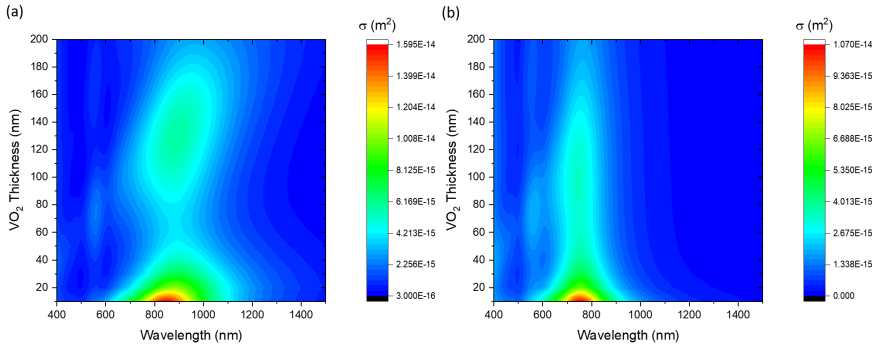

Figure A1.12: Contour maps depicting the dependence of the scattering cross-section spectrum, for longitudinal excitation, of a Au Disc Dimer (Radius = 45 nm, Height = 40 nm, Gap = 10 nm), on the VO_2 film thickness for VO_2 in (a) semiconducting phase and (b) metallic phase.

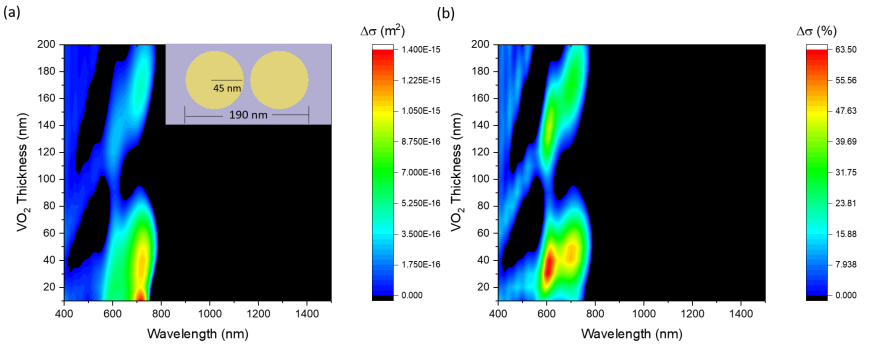

Figure A1.13: Contour maps depicting (a) $\Delta\ \sigma(\sigma_M - \sigma_{SC})$ and (b) $\Delta\sigma(\%)[100 \times \frac{\sigma_M - \sigma_{SC}}{\sigma_{SC}}]$ for Au Nanodisc Dimer (Radius = 45 nm, Height = 40 nm, Gap = 10 nm) under longitudinal excitation. Coloured sections indicate an increase in scattering as VO_2 transition to metallic phase. Black regions indicate a decrease in scattering as VO_2 transitions to metallic phase. A schematic of the Au nanorod structure is included as an inset to (a).

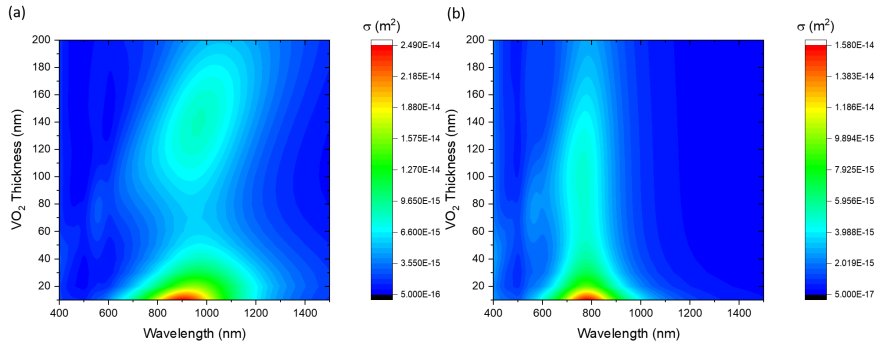

Figure A1.14: Contour maps depicting the dependence of the scattering cross-section spectrum, for longitudinal excitation, of a Au Cuboid Dimer (Length = 90 nm, Width = 90 nm, Height = 40 nm, Gap = 10 nm), on the VO_2 film thickness for VO_2 in (a) semiconducting phase and (b) metallic phase.

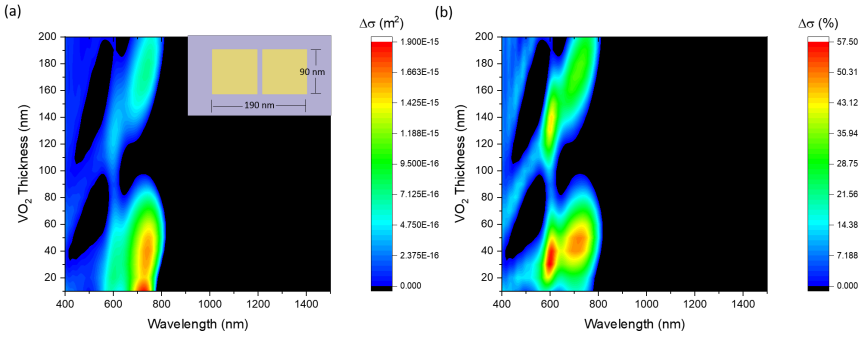

Figure A1.15: Contour maps depicting (a) $\Delta\ \sigma(\sigma_M - \sigma_{SC})$ and (b) $\Delta\sigma(\%)[100 \times \frac{\sigma_M - \sigma_{SC}}{\sigma_{SC}}]$ for Au Cuboid Dimer (Length = 90 nm, Width = 90 nm, Height = 40 nm, Gap = 10 nm) under longitudinal excitation. Coloured sections indicate an increase in scattering as VO_2 transition to metallic phase. Black regions indicate a decrease in scattering as VO_2 transitions to metallic phase. A schematic of the Au nanorod structure is included as an inset to (a).

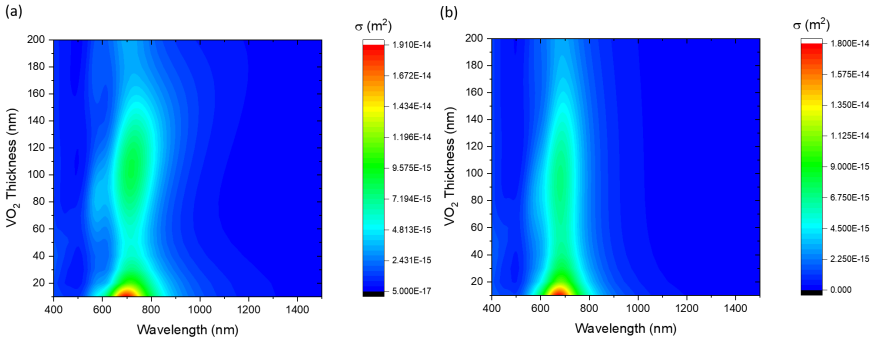

Figure A1.16: Contour maps depicting the dependence of the scattering cross-section spectrum, for longitudinal excitation, of a Au Rod Dimer (Length = 90 nm, Width = 90 nm, Height = 40 nm, Gap = 10 nm), on the VO_2 film thickness for VO_2 in (a) semiconducting phase and (b) metallic phase.

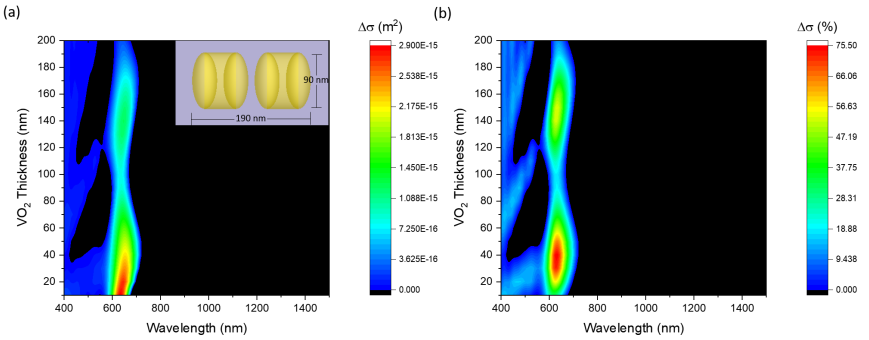

Figure A1.17: Contour maps depicting (a) $\Delta\ \sigma(\sigma_M - \sigma_{SC})$ and (b) $\Delta\sigma(\%)[100 \times \frac{\sigma_M - \sigma_{SC}}{\sigma_{SC}}]$ for Au Rod Dimer (Length = 90 nm, Width = 90 nm, Height = 40 nm, Gap = 10 nm) under longitudinal excitation. Coloured sections indicate an increase in scattering as VO_2 transition to metallic phase. Black regions indicate a decrease in scattering as VO_2 transitions to metallic phase. A schematic of the Au nanorod structure is included as an inset to (a).

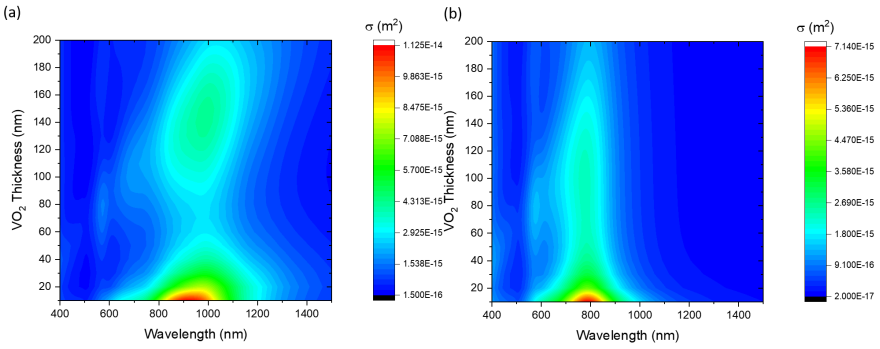

Figure A1.18: Contour maps depicting the dependence of the scattering cross-section spectrum, for longitudinal excitation, of a Au Bowtie Dimer (Perpendicular Bisector = 90 nm, Side Length = 100 nm, Height = 40 nm, Gap = 10 nm), on the VO_2 film thickness for VO_2 in (a) semiconducting phase and (b) metallic phase.

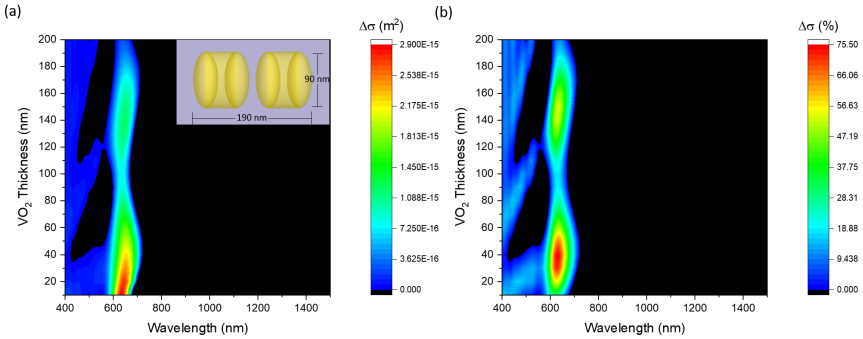

Figure A1.19: Contour maps depicting (a) $\Delta\ \sigma(\sigma_M - \sigma_{SC})$ and (b) $\Delta\sigma(\%)[100 \times \frac{\sigma_M - \sigma_{SC}}{\sigma_{SC}}]$ for a Au Bowtie Dimer (Perpendicular Bisector = 90 nm, Side Length = 100 nm, Height = 40 nm, Gap = 10 nm) under longitudinal excitation. Coloured sections indicate an increase in scattering as VO_2 transition to metallic phase. Black regions indicate a decrease in scattering as VO_2 transitions to metallic phase. A schematic of the Au nanorod structure is included as an inset to (a).

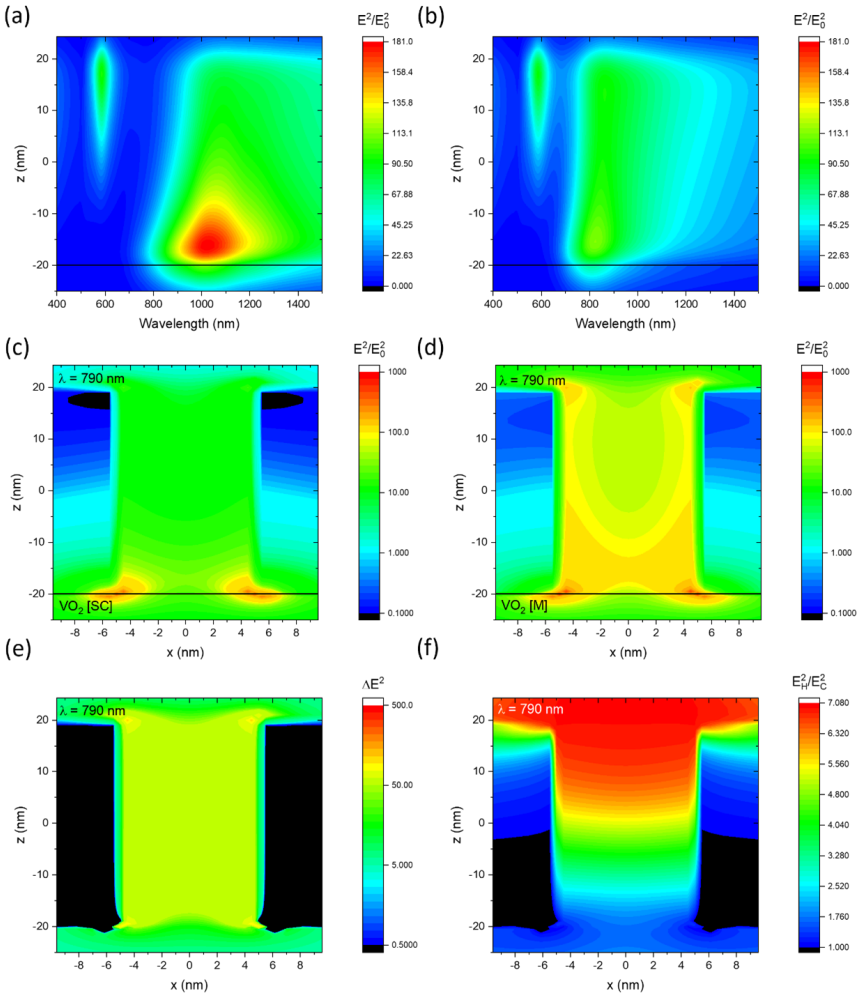

Figure A1.20: Contour maps indicating E-field intensity between the bowtie dimer elements as a function of dimer height (z) for VO_2 (10 nm) in (a) semiconducting phase and (b) metallic phase. The plane z = -20 nm corresponds to the dimer - VO_2 interface. z = 20 nm indicates the top the dimer structure. The electric field intensity maps for λ = 790 nm between dimer elements as a function of x-position (along dimer axis) and z-position (along dimer height, perpendicular to VO_2 plane) for VO_2 (30 nm) in (c) semiconducting phase and (d) metallic phase. (e) $\Delta E^2(E_M^2 - E_{SC}^2)$ between dimer elements as a function of x-position (along dimer axis) and z-position (along dimer height) for λ = 790 nm and 10 nm VO_2 thickness. (f) E_M^2/E_{SC}^2 for λ = 790 nm and 10 nm thickness. All maps are calculated for longitudinal excitation along the dimer axis.

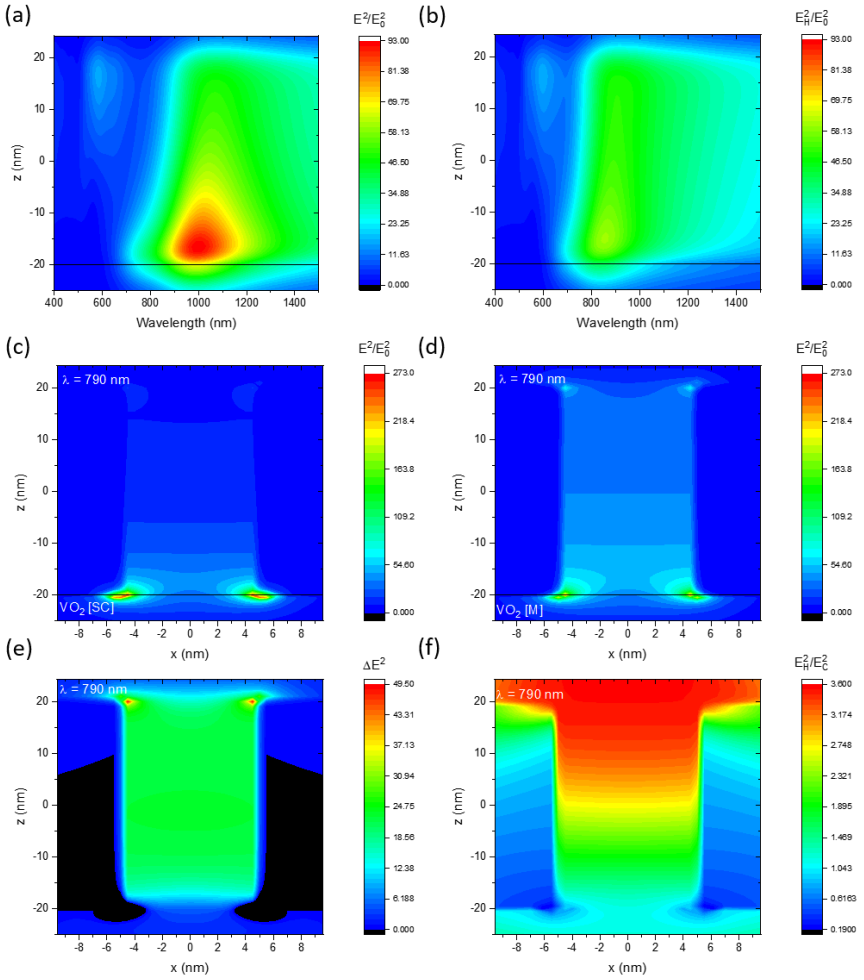

Figure A1.21: Contour maps indicating E-field intensity between the cuboid elements as a function of dimer height (z) for VO_2 (10 nm) in (a) semiconducting phase and (b) metallic phase. The plane z = -20 nm corresponds to the dimer - VO_2 interface. z = 20 nm indicates the top the dimer structure. The electric field intensity maps for λ = 790 nm between dimer elements as a function of x-position (along dimer axis) and z-position (along dimer height, perpendicular to VO_2 plane) for VO_2 (10 nm) in (c) semiconducting phase and (d) metallic phase. (e) $\Delta E^2(E_M^2 - E_{SC}^2)$ between dimer elements as a function of x-position (along dimer axis) and z-position (along dimer height) for λ = 790 nm and 10 nm VO_2 thickness. (f) E_M^2/E_{SC}^2 for λ = 790 nm and 10 nm thickness. All maps are calculated for longitudinal excitation along the dimer axis.

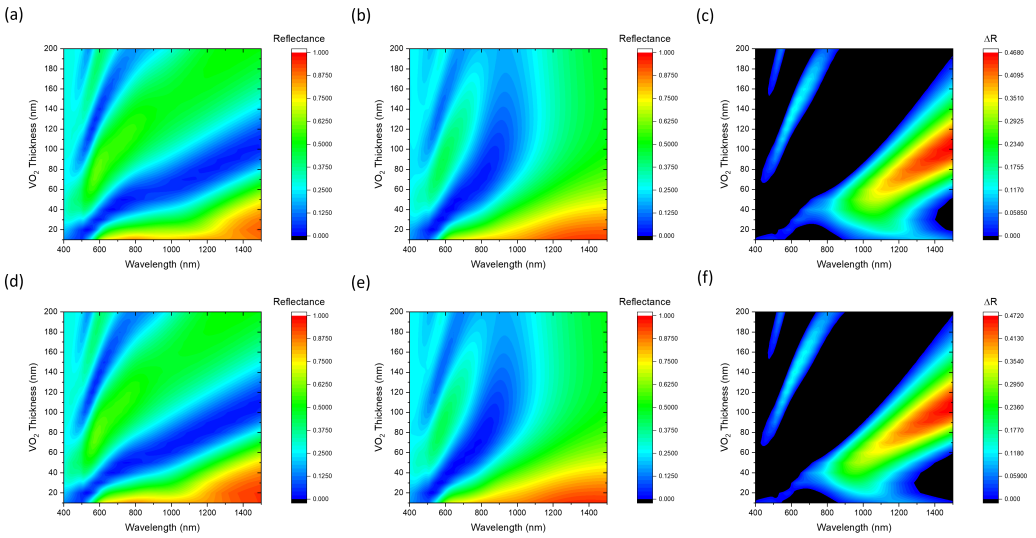

Figure A1.22: ΔR $(R_M - R_{SC})$ for the periodic nanostructure without a backreflecting layer. Reflectance spectra of the periodic nanocuboid array with a back reflecting metal layer with VO_2 in (a) semiconducting phase and (b) metallic phase. (c) ΔR $(R_M - R_{SC})$ for the periodic nanostructure with an Au backreflecting layer. Reflectance spectra of the periodic nanoellipse array with a back reflecting metal layer with VO_2 in (d) semiconducting phase and (e) metallic phase. (f) ΔR $(R_M - R_{SC})$ for the periodic nanostructure with an Au backreflecting layer.

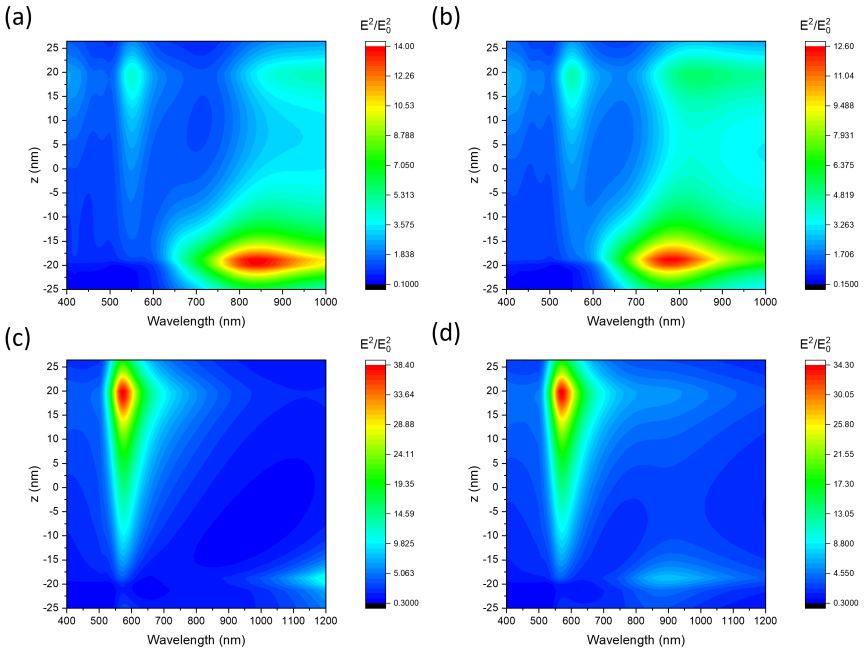

Figure A1.23: E^2/E_0^2 Map for a Au Nanorod array (Length = 90 nm, Width = 45 nm, Height = 40 nm, Period = 190 nm) on VO_2 (Thickness = 10 nm) for VO_2 in (a) semiconducting phase and (b) metallic phase with no Au backreflecting layer and in (c) semiconducting phase and (d) metallic phase with an Au backreflecting layer.

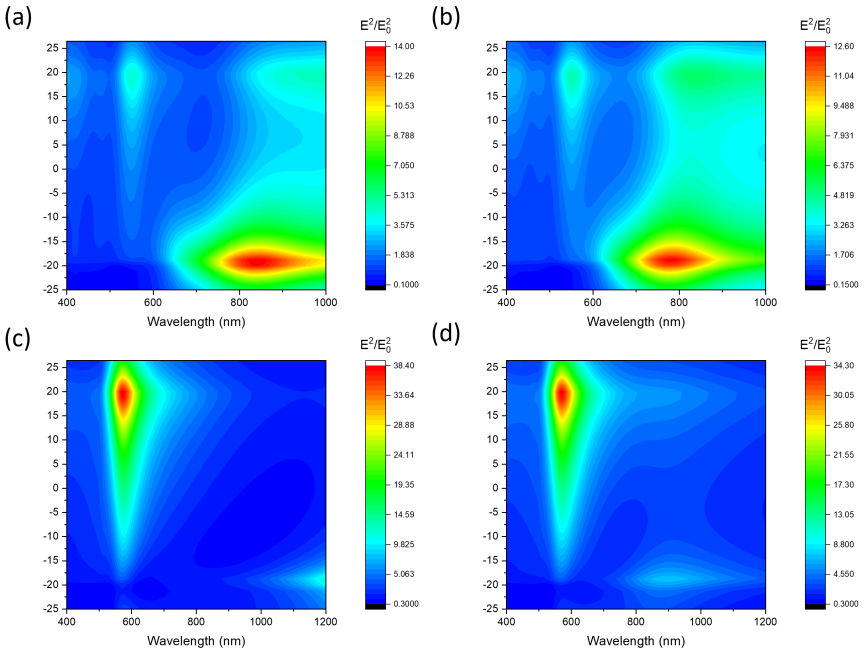

Figure A1.24: E^2/E_0^2 Map for a Au Nanocube array (Length = 90 nm, Width = 45 nm, Height = 40 nm, Period = 190 nm) on VO_2 (Thickness = 10 nm) for VO_2 in (a) semiconducting phase and (b) metallic phase with no Au backreflecting layer and in (c) semiconducting phase and (d) metallic phase with an Au backreflecting layer.

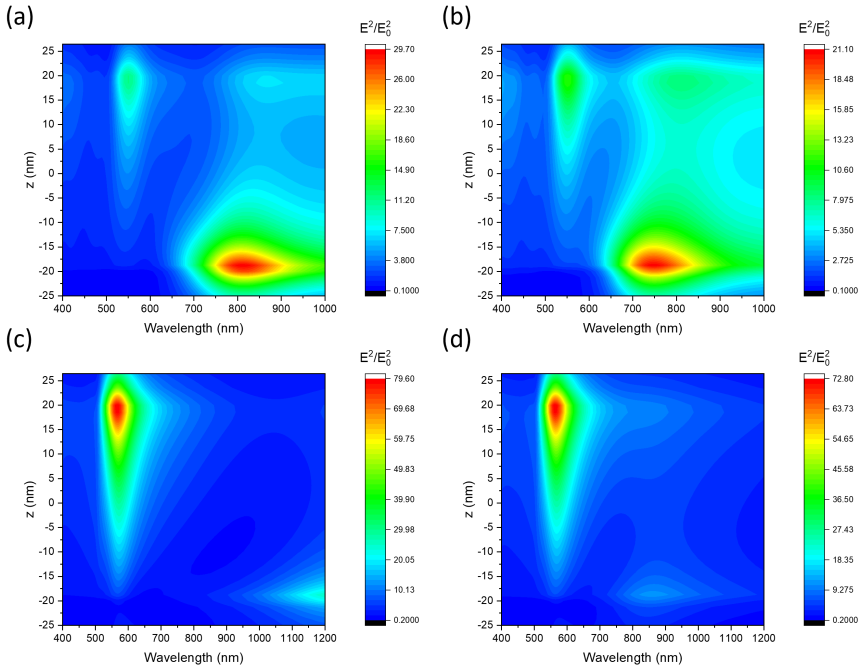

Figure A1.25: E^2/E_0^2 Map for a Au Nanoellipse array (Length = 90 nm, Width = 45 nm, Height = 40 nm, Period = 190 nm) on VO_2 (Thickness = 10 nm) for VO_2 in (a) semiconducting phase and (b) metallic phase with no Au backreflecting layer and in (c) semiconducting phase and (d) metallic phase with an Au backreflecting layer.

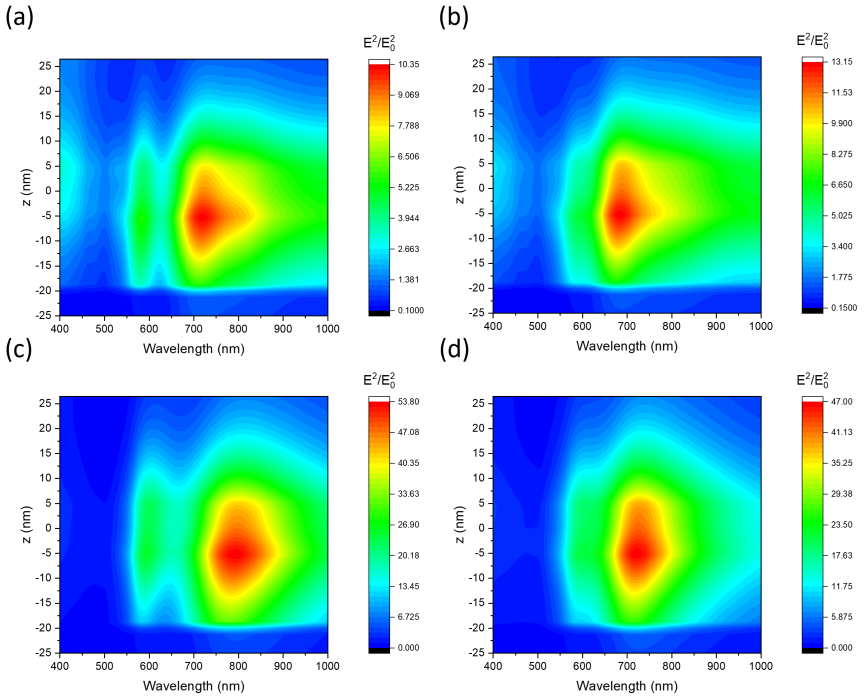

Figure A1.26: E^2/E_0^2 Map for a Au Nanorod array (Length = 90 nm, Width = 45 nm, Height = 40 nm, Period = 190 nm) on VO_2 (Thickness = 30 nm) for VO_2 in (a) semiconducting phase and (b) metallic phase with no Au backreflecting layer and in (c) semiconducting phase and (d) metallic phase with an Au backreflecting layer.

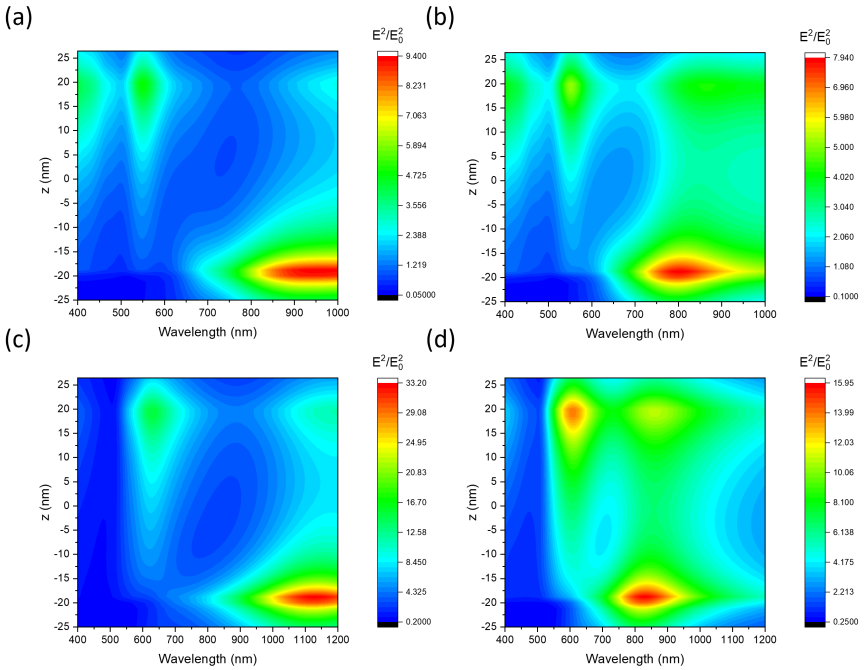

Figure A1.27: E^2/E_0^2 Map for a Au Nanocuboid array (Length = 90 nm, Width = 45 nm, Height = 40 nm, Period = 190 nm) on VO_2 (Thickness = 30 nm) for VO_2 in (a) semiconducting phase and (b) metallic phase with no Au backreflecting layer and in (c) semiconducting phase and (d) metallic phase with an Au backreflecting layer.

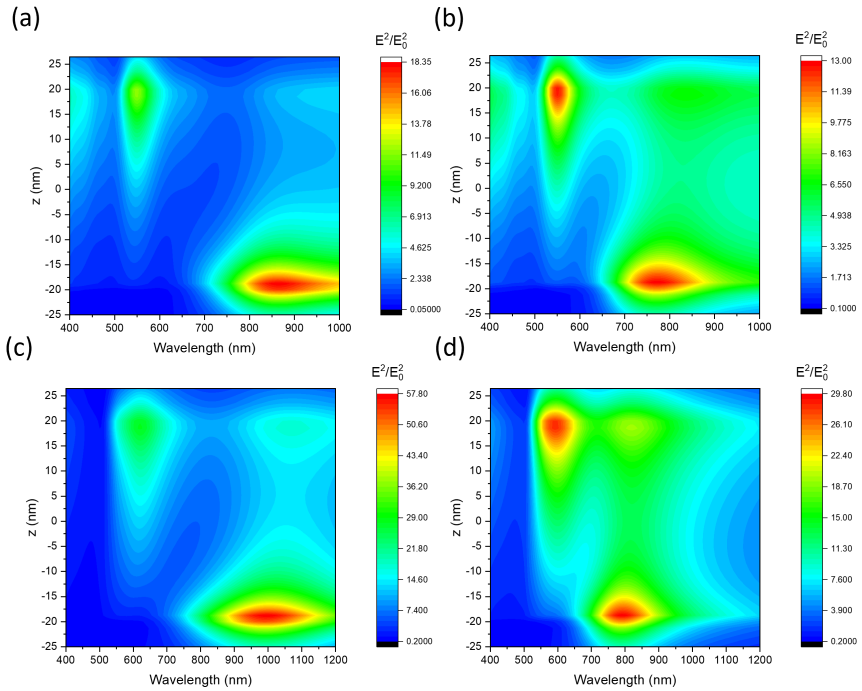

Figure A1.28: E^2/E_0^2 Map for a Au Nanoellipse array (Length = 90 nm, Width = 45 nm, Height = 40 nm, Period = 190 nm) on VO_2 (Thickness = 30 nm) for VO_2 in (a) semiconducting phase and (b) metallic phase with no Au backreflecting layer and in (c) semiconducting phase and (d) metallic phase with an Au backreflecting layer.